Fundamental nuclear properties of indium isotopes measured with laser spectroscopy

A thesis submitted to the University of Manchester for the degree of Doctor of Philosophy in the Faculty of Science and Engineering

2021

Christopher M. Ricketts

Department of Physics and Astronomy in the School of Natural Sciences
The University of Manchester

Contents

List of Figures

List of Tables

Abbreviations

AI	**A**uto-**I**onising state
BBO	**B**eta-**B**arium **B**orate
CEC	**C**harge **E**xchange **C**ell
CLS	**C**ollinear **L**aser **S**pectroscopy
COLLAPS	**COL**linear **LA**ser **SP**ectroscopy
CRIS	**C**ollinear **R**esonance **I**onisation **S**pectroscopy
CRISIS	**CRIS** **I**on **S**ource
CW	**C**ontinuous **W**ave
DFT	**D**ensity **F**unctional **T**heory
FWHM	**F**ull **W**idth at **H**alf **M**aximum
FS	**F**ield **S**hift
GPS	**G**eneral **P**urpose **S**eparator
HFS	**H**yper**F**ine **S**tructure
HRS	**H**igh **R**esolution **S**eparator
IP	**I**onisation **P**otential
ISCOOL	**IS**OLDE **COOL**er-buncher
ISOL	**I**sotope **S**eparator **O**n-**L**ine
ISOLDE	**I**sotope **S**eparator **O**n-**L**ine **DE**vice
LIST	**L**aser **I**on **S**ource and **T**rap
LMFIT	Non-Linear **L**east-Square **M**inimization and Curve-**FIT**ting for Python
MCMC	**M**arkov **C**hain **M**onte **C**arlo
MCP	**M**icro**C**hannel **P**late
MOT	**M**agneto **O**ptical **T**rap
MS	**M**ass **S**hift
NMR	**N**uclear **M**agnetic **R**esonance

NMS	**N**ormal **M**ass **S**hift
NUTS	**N**o-**U**-**T**urn **S**ampler
PBS	**P**olarizing **B**eam **S**plitter
PDL	**P**ulsed **D**ye **L**aser
PID	**P**roportional **I**ntegral **D**ifferential
PMT	**P**hoto-**M**ultiplier **T**ube
PSB	**P**roton **S**ynchrotron **B**ooster
PYMC3	**PY**thon **M**onte **C**arlo **3**
RFQ	**R**adio **F**requency **Q**uadrupole
RILIS	**R**esonance **I**onisation **L**aser **I**on **S**ource
RIS	**R**esonance **I**onisation **S**pectroscopy
SATLAS	**S**tatistical **A**nalysis **T**oolbox for **LA**ser **S**pectroscopy
SHG	**S**econd **H**armonic **G**eneration
SMS	**S**pecific **M**ass **S**hift
TDC	**T**ime-to-**D**igital **C**onverter
THG	**T**hird **H**armonic **G**eneration
ToF	**T**ime **o**f **F**light
TTL	**T**ransistor-**T**ransistor **L**ogic
UHV	**U**ltra **H**igh **V**acuum
UV	**U**ltra **V**iolet
YAG	**Y**ttrium-**A**luminium **G**arnet

Abstract

The primary focus of this thesis is the analysis and interpretation of spectroscopic measurements of the neutron-deficient indium isotopes, $^{101-115}$In, in order to evaluate the evolution of nuclear structure towards the heaviest self-conjugate doubly-magic nucleus, ^{100}Sn. These measurements were performed at the Collinear Resonance Ionisation Spectroscopy experiment at the ISOLDE facility at CERN. Two laser excitations were separately employed: between the $5s^2\ 5p\ ^2P_{1/2}$ and $5s^2\ 8s\ ^2S_{1/2}$ atomic states and between the $5s^2\ 5p\ ^2P_{3/2}$ and $5s^2\ 9s\ ^2S_{1/2}$ states. Both excitations were followed by non-resonant laser ionisation before ion detection.

The work resulted in new nuclear-model-independent measurements of magnetic dipole moments, electric quadrupole moments, nuclear spins and changes in mean-squared charge radii. These properties were determined for the first time in three nuclear ground states, ^{101,102,103}In, and in a number of isomeric states. Comparisons to nuclear theory were performed using predictions of the shell model, droplet model and density functional theory.

Previous predictions of simple single-particle behaviour in the $I^\pi = 9/2^+$ states of the mid-shell indium isotopes are brought further into question by these new results, due to variation in the measured magnetic dipole moments. Confidence in the ^{100}Sn shell closure is reinforced by newly measured quadrupole moments, confirming the similar strength of $N = 82$ and $N = 50$ at $Z = 50$. Density functional theory calculations predict the moments relatively well, while finite-range droplet model calculations underestimate the quadrupole-deformation parameters.

Declaration of Authorship

I, Christopher M. Ricketts, confirm that no portion of the work referred to in the thesis has been submitted in support of an application for another degree or qualification of this or any other university or other institute of learning.

Copyright statement

Acknowledgements

I have been very fortunate to have had the opportunity to work with such a knowledgeable and supportive group of people throughout my PhD. Firstly, I would like to thank my project supervisors, Kieran Flanagan and Ronald Fernando Garcia Ruiz, for giving me the opportunity to be involved in this project and for all the guidance throughout the journey.

Thanks also to the whole CRIS team, without whom none of this work would have been possible, including Adam, Fred, Shane, Agi, Ruben, Cory, Holly, Ben, Jordan, Thomas, Gerda, Xiaofei and everyone else I've worked with and relied on.

I'd particularly like to thank Adam, Cory, Shane and Jordan for your insightful and detailed comments on this thesis.

Thanks to everyone in the ISOLDE community for creating such an exciting and welcoming work place, and for making these experiments possible.

Finally, I would never have got to this point without the unwavering support of my family and my partner Ro, thanks for everything you have given me, I rely on you more than you know.

Chapter 1

Introduction

Nuclear physics, in the most general sense, investigates how the protons and neutrons at the centre of atoms interact to form the nuclei we observe in nature today. The understanding of this process gradually developed from the start of the 20th century, from Rutherford's pioneering work and the inception of the shell model by Mayer and Jensen [1–3], through to state-of-the-art ab initio, no-core shell model and collective theories attempting to reproduce the most intricate details of nuclear structure and interactions [4–6].

Laser spectroscopy, and more recently laser spectroscopy of short-lived radio-isotopes at ion-beam facilities, has and continues to perform a critical role in the development of understanding of nuclear structure. Measurements of hyperfine structure allow for the extraction of nuclear-model-independent observables in low-lying nuclear states, such as nuclear electromagnetic moments and charge radii, providing a reliable benchmark in the development of nuclear theories. These concepts are introduced in Chapter 2. Early work focussed on the more easily accessible stable and long-lived isotopes where a simple shell-model picture performed well. However, with the advent of radioactive-beam facilities, where more exotic isotopes could be studied, unexpected behaviours started to appear. It became clear that a more complete understanding of nuclear structure required a wider breadth of measurements to encompass a wider variety of phenomena.

With this aim in mind, laser spectroscopy collaborations are continuously striving to increase measurement precision, sensitivity and selectivity. A major advance in the early 2000s was the introduction of radio-frequency quadrupole cooler bunchers at beam facilities. These are ion traps filled with helium gas which group the radioactive ions into discrete bunches, allowing for the removal of background signal outside the arrival time of the ion bunch [7, 8]. This led to orders of magnitude increase in sensitivity for

collinear measurements, allowing for the measurement of exotic isotopes with production rates down to $\sim 1000\,\text{ions}\,\text{s}^{-1}$.

Building on this progress, the Collinear Resonance Ionisation Spectroscopy (CRIS) experiment at ISOLDE, CERN, where the measurements in this thesis were performed, was envisioned in 2008 [9, 10]. With the introduction of the buncher, CRIS could now work to improve the sensitivity of collinear laser spectroscopy further by switching from photon detection, after resonant atomic excitation and decay, to an ion-detection technique. The resultant background reduction and efficiency increase led to some of the most sensitive collinear measurements ever performed in the copper isotopes, with a measured production rate of $\sim 10\,\text{ions}\,\text{s}^{-1}$ [5, 11, 12]. Laser spectroscopy techniques including CRIS are introduced and discussed in Chapter 3.

This thesis focusses on the indium case, a single proton hole in the $Z = 50$ shell closure, and investigates the evolution of collective and single-particle behaviour towards the doubly-magic ^{100}Sn and ^{132}Sn. Historically, the odd-mass indium isotopes with paired neutrons have been considered to be a textbook example of single-particle behaviour, with only small variations in the magnetic moments of the nuclear ground states observed in the isotopes close to stability. However, even in these early studies, unexplained behaviours such as the variation in $I^\pi = 1/2^-$-state magnetic moments had already started to suggest that the underlying structure was more complex than first thought. Measurements of nuclear properties closer to the doubly-magic nuclei, the cornerstones of the nuclear shell model, were needed to start to unpack this underlying structure. Chapter 4 describes one such experiment, performed on the neutron-deficient indium isotopes in the range $^{101-115}$In. The chapter details the experimental configuration, data analysis and the extraction of results. The nuclear physics implications and comparisons to nuclear theories are discussed in Chapter 5.

The aim of improved sensitivity applicable to a wide variety of elemental cases continues to guide the development of the CRIS experiment, leading to some of the improvements described in this thesis in Chapter 3 and Chapter 6. Chapter 6 also discusses atomic-physics results in the stable indium isotopes, primarily a new determination of the ionisation potential of ^{115}In, which arose from this development work.

Chapter 2

Nuclear observables from atomic spectroscopy

Atomic-spectroscopy experiments, when applied to nuclear physics, focus on the measurement of a number of microscopic and macroscopic nuclear observables, including changes in mean-square charge radii between elemental isotopes, and electromagnetic moments. The evolution of these observables across elemental chains can be extracted directly from measured spectra without dependence on any particular nuclear model. These observables can then be compared to predictions of independent particle or collective models.

In general, collective and independent-particle nuclear models are differing interpretations of the Schrödinger equation arising from the nuclear many-body problem. The Hamiltonian for a nucleus with A nucleons can be written as [13],

$$H = \sum_{i=1}^{A} t_i + \frac{1}{2} \sum_{i,j=1}^{A} V_{i,j} + ..., \tag{2.1}$$

where t_i is the kinetic energy of a nucleon indexed by i and $V_{i,j}$ are the two-body interaction potentials. Higher-order interactions including three or more nucleons are often neglected to simplify the calculations. This Hamiltonian is often written in terms of a sum of one-body mean-field Hamiltonians, H_0, plus a residual interaction between nucleons, $H_{\text{res.}}$ [13],

$$H = H_0 + H_{\text{res.}} = \left(\sum_{i=1}^{A} t_i + U_i \right) + \left(\frac{1}{2} \sum_{i,j=1}^{A} V_{i,j} - \sum_{i=1}^{A} U_i \right), \tag{2.2}$$

where U_i is the mean-field potential. Models generally start by neglecting $H_{\text{res.}}$ then include it later as a perturbation. Specific approaches to this problem, including the shell model and density functional theory, are introduced in Section 5.1. The resultant states are then used to predict the nuclear parameters described in the following sections.

2.1 Nuclear electromagnetic moments

Two electromagnetic moments are typically accessible in laser spectroscopy experiments: the magnetic dipole moment, μ, and the electric quadrupole moment, Q. These arise from the intrinsic spin, orbital angular momentum, and current and charge distributions of the constituent nucleons.

The magnetic dipole moment, defined as the expectation value of the magnetic dipole operator in the state aligned with the spin axis [13], is dependent on the spin and orbital angular momenta, and the current distribution. In units of nuclear magnetons, for a nucleus of A nucleons with nuclear spin I,

$$\mu \equiv \left\langle I, m = I \left| \sum_{i=1}^{A} g_l(i) l_z(i) + \sum_{i=1}^{A} g_s(i) s_z(i) \right| I, m = I \right\rangle, \tag{2.3}$$

where $g_l(i)$ and $g_s(i)$ are the gyromagnetic ratios of the nucleons, and $l_z(i)$ and $s_z(i)$ are the projections of the orbital and spin angular momentum operators on the nuclear spin axis.

Applying this definition to a state dependent on a single nucleon, we come to what are known as the single-particle Schmidt moments,

$$\mu_{s.p.}(j = l + 1/2) = j g_l + (g_s - g_l)/2, \tag{2.4}$$

$$\mu_{s.p.}(j = l - 1/2) = j g_l - \frac{j(g_s - g_l)}{2(j+1)}, \tag{2.5}$$

where j is the single-particle total angular momentum. For the orbital part, values for protons and neutrons are typically taken as $g_l^{\pi} = 1$ and $g_l^{\nu} = 0$ respectively due to the lack of neutron charge. The spin gyromagnetic ratios are derived from the measured magnetic moments of the free neutron and proton. For more complex nuclei, where the magnetic moment doesn't follow a pure single-particle behaviour but can be treated as such in a shell-model picture, effective values can be taken for the gyromagnetic ratios to take into account the effect of the surrounding 'core' nucleons (not explicitly included in the calculation) on the valence particle. The values taken are typically some fraction of the free proton or neutron values [13]. An example calculation from Heyde et

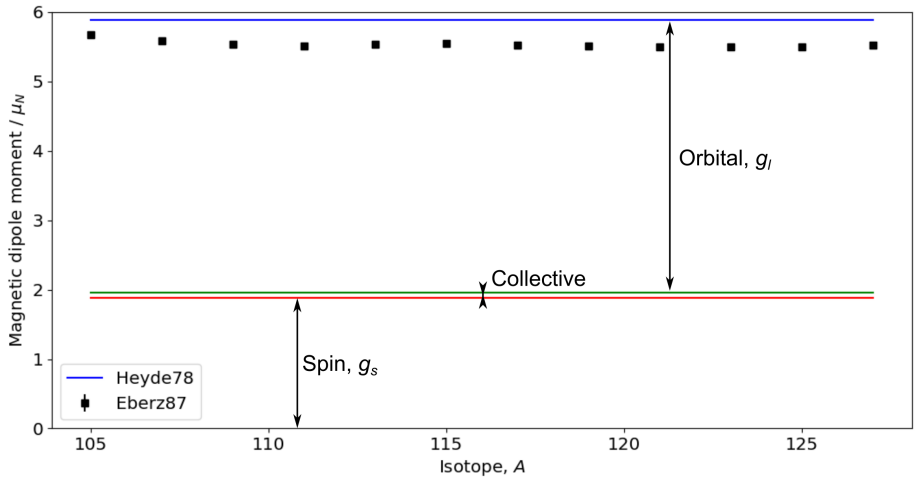

FIGURE 2.1: Magnetic moments of the $I^\pi = 9/2^+$ ground states in the odd proton-even neutron indium isotopes. Experimental values from Eberz et al. [15] are shown as black points (error bars are too small to be seen). The individual contributions to the theoretical magnetic moments from Heyde et al. [14] (blue line) are shown. The spin and orbital contributions are from Equation 2.4 with $g_s^{\text{eff.}} = 0.7 g_s^{\text{free}}$, while the small collective-admixture contribution is from additional excitations of the even-even tin core.

al. [14] using these equations for the indium odd-even isotopes is shown in Fig. 2.1, with $g_s^{\text{eff.}} = 0.7 g_s^{\text{free}}$. Here an additional shell-model collective contribution from the residual Hamiltonian is also included, but it is small relative to the Schmidt orbital and spin components.

The electric quadrupole moment operator is defined as,

$$\hat{Q} \equiv \sum_{i=1}^{A} 3z_i^2 - r_i^2, \tag{2.6}$$

where z_i and r_i are the axial and radial coordinates of each nucleon respectively, giving a measure of the axial deformation of the nucleus, visualised in Fig. 2.2 [16]. The expectation value of this operator is known as the intrinsic quadrupole moment, Q_0. The experimentally accessible value, known as the spectroscopic quadrupole moment, is given by the expectation value of this operator in the spin-aligned state,

$$Q \equiv \langle I, m = I | Q_z | I, m = I \rangle \equiv \sqrt{\frac{I(2I-1)}{(2I+1)(2I+3)(I+1)}} \langle I || Q_z || I \rangle \,, \tag{2.7}$$

where we have written Q as a function of the reduced matrix element $\langle I||Q_z||I\rangle$ using the Wigner-Eckart theorem [16].

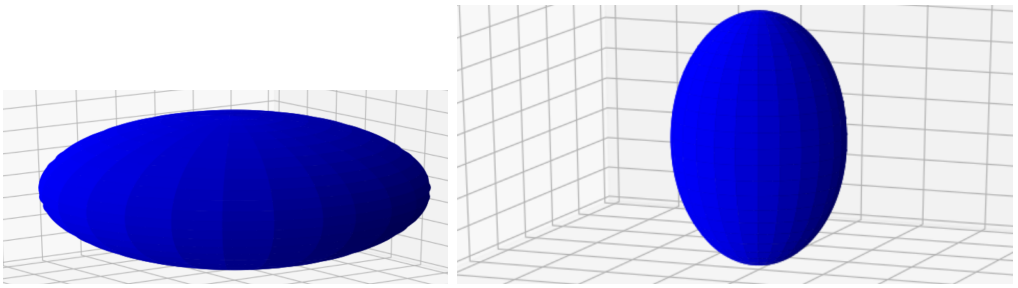

(A) Oblate deformation when $Q < 0$ (B) Prolate deformation when $Q > 0$

FIGURE 2.2: Nuclear axial deformation based on the electric quadrupole moment, Q.

Again, applying this to a state dependent on a single nucleon or hole results in the single-particle value for the quadrupole moment [16],

$$Q_{s.p.} = -e_i \frac{2j-1}{2j+2} \left\langle r_i^2 \right\rangle , \tag{2.8}$$

where a hole for a certain orbit is given the negative charge (e_i) of an equivalent particle. In the more complex picture of a non-pure single-particle state, we can use an effective charge to take into account the effect of the 'core' on the quadrupole moment, the effective charge being some fraction of the unit charge for a valence proton or neutron.

In well deformed nuclei, the measured spectroscopic quadrupole moment, Q, can be related to the intrinsic quadrupole moment of the nucleus, Q_0, through the projection [16, 17],

$$Q = \frac{3K^2 - I(I+1)}{(I+1)(2I+3)} Q_0, \tag{2.9}$$

where K is the projection of the total nuclear spin I onto the deformation-symmetry axis of the nucleus.

2.2 Electronic structure of atoms

To first order, the energy levels of electrons within atoms can be determined by solving the Schrödinger equation given a central potential created by the nucleus and inner-shell electrons. Perturbations can then be introduced to deal with the residual non-central part of the electrostatic interaction between electrons, and the magnetic interaction between the total spin of the electrons, $\vec{S}$, and their total orbital angular momentum, $\vec{L}$. This breaks the degeneracy of $\vec{L}$, $\vec{S}$ and the total electron angular momentum, $\vec{J} = \vec{L} + \vec{S}$, resulting in sub-levels known as the fine-structure. For some heavier systems, $\vec{L}$ and $\vec{S}$ are no longer good quantum numbers and an alternative total-angular-momentum coupling must be considered. $\vec{L}$ and $\vec{S}$ remain good quantum numbers for the indium case.

2.2.1 Hyperfine structure

As a further perturbation, we must also consider nuclear effects. These cause a further energy-level splitting of the fine-structure levels into a sub-structure known as the hyperfine structure. The first contribution arises due to the magnetic moment of the nucleus introduced in Section 2.1 above, present in non-zero spin nuclei. By analogy to the quantum-mechanical spin and orbital moments of the electron, we can write the nuclear magnetic moment in terms of a dimensionless nuclear g-factor, g,

$$\vec{\mu} = g\mu_{\mathrm{N}}\vec{I}, \tag{2.10}$$

where μ_{N} is the nuclear magneton, related to the Bohr magneton μ_{B} [18] by the ratio of the proton and electron masses,

$$\mu_{\mathrm{N}} = \mu_{\mathrm{B}}\frac{m_e}{m_p}. \tag{2.11}$$

The nuclear magnetic moment interacts with the magnetic field created by the orbiting electrons at the position of the nucleus. This magnetic field is proportional to the total electron angular momentum $\vec{J}$, meaning the resultant perturbations to the fine-structure energy levels are a vector coupling of $\vec{I}$ and $\vec{J}$,

$$\Delta E(\mu) = A_{\mathrm{hf}}\left\langle \vec{I}\cdot\vec{J}\right\rangle = \frac{A_{\mathrm{hf}}}{2}K, \tag{2.12}$$

where $K = F(F+1) - J(J+1) - I(I+1)$ and a new quantum number for the hyperfine structure has been defined,

$$\vec{F} = \vec{I} + \vec{J}. \tag{2.13}$$

A_{hf} is the magnetic-dipole hyperfine structure parameter,

$$A_{\mathrm{hf}} = \frac{\mu B_e}{IJ}, \tag{2.14}$$

and B_e is the magnetic field created by the electrons at the position of the nucleus. This magnetic field varies a small amount between isotopes of the same element due to hyperfine-anomaly effects (see Section 2.2.2).

The nuclear quadrupole moment, Q, can also couple to the electric field generated by the electrons, resulting in an additional energy perturbation proportional to the gradient of that electric field along the symmetry axis z,

$$\Delta E(Q) = B_{\mathrm{hf}}\frac{3K(K+1) - 4I(I+1)J(J+1)}{8I(2I-1)J(2J-1)}, \tag{2.15}$$

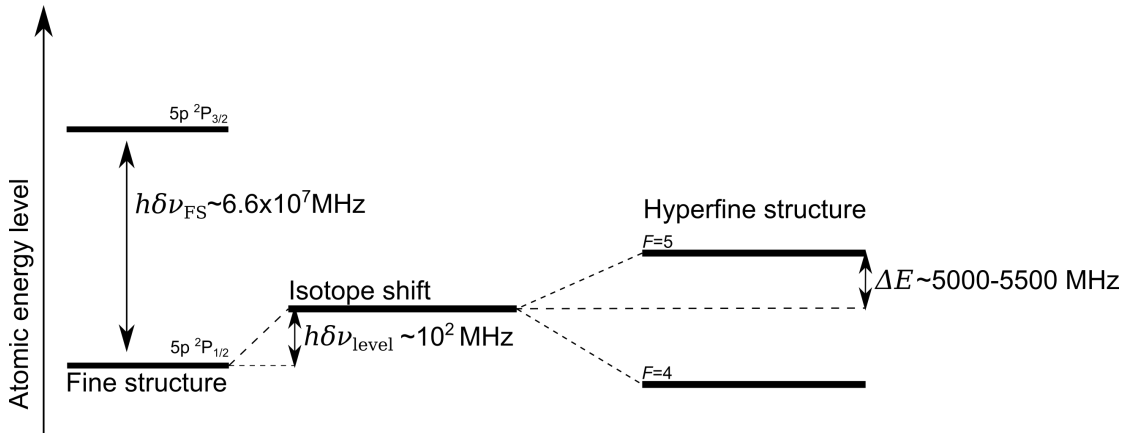

FIGURE 2.3: Schematic of the contributions to the final atomic energy levels with values for the lower atomic states in the $I^\pi = 9/2^+$ states discussed in this thesis (not to scale). The fine-structure energy levels are shifted between isotopes by the mass and field shifts. The shifts in the lower and upper atomic states result in a change in the final transition energy, the spectroscopic isotope shift, given by $h\delta\nu_i = h\delta\nu_{\text{upper}} - h\delta\nu_{\text{lower}}$. The fine-structure levels for non-zero-spin nuclei are also divided into sub-levels known as the hyperfine structure.

where the electric-quadrupole hyperfine structure parameter is given by,

$$B_{\text{hf}} = eQ\frac{\partial^2 V}{\partial z^2}, \tag{2.16}$$

with V as the electric potential. These two terms are the leading order parts of the hyperfine structure and the only terms considered in this work. Allowed dipole-electronic transitions between the resultant hyperfine-structure F-state components follow the selection rules,

$$\Delta F = F' - F = 0, \pm 1 \;\text{ excluding }\; F = 0 \rightarrow F' = 0. \tag{2.17}$$

Fig. 2.3 shows a schematic summary of the possible splittings and their magnitudes for the indium case.

2.2.2 Hyperfine anomaly

The hyperfine anomaly is a modification to the electron magnetic field, B_e, and therefore the magnetic hyperfine structure parameter, Equation 2.14, due to the non-zero spacial extent of a nucleus [19]. The nuclear size modifies the point-like A_{hf} in two ways: firstly, via the Breit-Rosenthal correction, ϵ_{BR}, from the modification of the electron wavefunction due to the extent of the nuclear charge distribution, and secondly via the Bohr-Weisskopf effect, ϵ_{BW}, from the extent of the nuclear magnetisation. The total modification can be written as,

$$A_{\text{hf}} = A_{\text{hf}}^{\text{point}}(1 + \epsilon_{\text{BR}})(1 + \epsilon_{\text{BW}}). \tag{2.18}$$

These correction factors vary between isotopes of the same element. Given the fact that the ϵ correction factors are small, taking the ratio of hyperfine-A parameters (Equation 2.14) for two isotopes (indexed as 1 and 2) gives,

$$\frac{A_1^{\mathrm{hf}}}{A_2^{\mathrm{hf}}} \approx \frac{\mu_1}{\mu_2}\frac{I_2}{I_1}(1+\Delta_{1,2}^{\mathrm{BW}})(1+\Delta_{1,2}^{\mathrm{BR}}), \tag{2.19}$$

where $\Delta_{1,2}^{\mathrm{BW}} = \epsilon_1^{\mathrm{BW}} - \epsilon_2^{\mathrm{BW}}$ and $\Delta_{1,2}^{\mathrm{BR}} = \epsilon_1^{\mathrm{BR}} - \epsilon_2^{\mathrm{BR}}$. The $\Delta_{1,2}^{\mathrm{BW}}$ values generally dominate, except where the nuclei have almost identical structure where the $\Delta_{1,2}^{\mathrm{BR}}$ values dominate [19]. In the absence of either correction being significant, the hyperfine ratio should be constant for any combination of isotopes of the same element in a given atomic fine-structure state.

2.2.3 Isotope shifts

The energy levels of atomic states shift when moving between isotopes in an elemental chain. This is known as the isotope shift and is caused primarily by two effects: one due to the changing mass of the nucleus, and the other due to the changing size and shape of the nuclear charge distribution.

The finite mass of the nucleus results in a recoil motion where both the nucleus and electrons orbit around their common centre of mass. Ignoring relativistic effects (valid for low- to medium-mass nuclei), the nuclear motion can be incorporated as an extra mass-shift (MS) term in the Hamiltonian [20],

$$H_{\mathrm{MS}} = H_{\mathrm{NMS}} + H_{\mathrm{SMS}} = \frac{1}{2m_A}\sum_i^{N_e}\sum_j^{N_e}\vec{p_i}\cdot\vec{p_j}, \tag{2.20}$$

where m_A is the nuclear mass, $\vec{p_i}$ are the electronic momenta, and N_e is the number of electrons. The mass shift Hamiltonian is divided into two terms: the normal mass shift (NMS), containing the single-electron terms,

$$H_{\mathrm{NMS}} = \frac{1}{2m_A}\sum_i^{N_e}\vec{p_i}^{\,2}, \tag{2.21}$$

and the specific mass shift (SMS), containing the two-electron terms (caused by correlation effects between electrons),

$$H_{\mathrm{SMS}} = \frac{1}{m_A}\sum_j^{N_e}\sum_{i<j}\vec{p_i}\cdot\vec{p_j}. \tag{2.22}$$

Together these mass-shift effects result in a shift in the transition frequency (i.e. the energy difference between the lower and upper atomic states divided by Planck's constant) between isotopes with mass numbers A and A' given by

$$\delta\nu_{\mathrm{MS}} = \frac{A' - A}{A'A} M = \frac{M}{\mu_{A',A}}, \tag{2.23}$$

where the mass-shift factor $M = M_{\mathrm{NMS}} + M_{\mathrm{SMS}}$ and $\mu_{A',A}$ is the mass-modification factor [21]. Assuming the absolute transition frequencies, ν, are approximately equal to the value obtained with $m_A \to \infty$ [22], H_{NMS} gives,

$$M_{\mathrm{NMS}} \approx \nu_{\mathrm{FS}} \frac{m_e}{m_n}, \tag{2.24}$$

where ν_{FS} is the optical transition frequency and m_n is the nucleon mass. The specific mass shifts, M_{SMS}, can be calculated from H_{SMS} through perturbation theory [23].

The second contribution to the isotope shift comes from the changing overlap of the nuclear and electron wavefunctions, due to changes in nuclear volume and surface between isotopes or nuclear states. Electronic states which have increased probability density inside the nucleus for a particular isotope increase in energy as they are more loosely bound [24]. The resultant transition-frequency shift can be written in terms of the change in mean-square nuclear charge radius, $\delta \left\langle r^2 \right\rangle_{A',A}$,

$$\delta\nu_{\mathrm{FS}} = F \delta \left\langle r^2 \right\rangle_{A',A}, \tag{2.25}$$

where the field-shift factor, F, is the expectation value within the electronic wavefunction,

$$F = \left\langle \frac{\delta V_A(r)}{\delta \left\langle r^2 \right\rangle} \right\rangle, \tag{2.26}$$

and $V_A(r)$ is the nuclear potential at the electron position [21].

The mass and field shift factors for an atomic transition are given by the difference between the values for the lower and upper atomic states,

$$F_i = F_{i,l} - F_{i,u}, \quad M_i = M_{i,l} - M_{i,u}, \tag{2.27}$$

where the labels l and u give the values for the lower and upper atomic states of the transition, indexed by i.

The total isotope shift for a transition is therefore,

$$\delta\nu_i = \delta\nu_i^{\mathrm{MS}} + \delta\nu_i^{\mathrm{FS}} = M_i \frac{A' - A}{A'A} + F_i \delta \left\langle r^2 \right\rangle, \tag{2.28}$$

giving changes in mean-square nuclear charge radii, $\delta\langle r^2\rangle$, from measurements of isotope shifts, $\delta\nu_i$, if the field- and mass-shift factors for a particular transition can be accurately determined from atomic theory, or if they can be determined experimentally.

2.3 Extracting nuclear observables

2.3.1 King plots

Accurate calculations of atomic specific-mass-shift and field-shift factors have only recently started to become available [25]. Instead of relying on explicit calculations of these factors, another method can be used for the extraction of nuclear charge radii. If measurements of absolute nuclear charge radii exist for at least three isotopes of the element of interest (for example from muonic atom spectroscopy [26]), we can plot a subset of the measured isotope shifts against the available changes in charge radii after both have been multiplied by the mass-modification factors, $\mu_{A',A} = A'A/(A'-A)$ (see Equation 2.23). This relationship is linear according to Equation 2.28, with gradient F_i and intercept M_i, allowing for the extraction of these parameters from a linear fit. Once F_i and M_i have been determined, they can be used to determine the charge radii changes for isotopes where only isotope-shift measurements exist. The uncertainties on the final charge radii changes are determined from those on the fitted F_i and M_i (a systematic uncertainty affecting all radii in the same way), and from the uncertainties on the individual measured isotope shifts.

Alternatively, if isotope-shift measurements have also been performed for a second transition j, the two instances of Equation 2.28 can be combined to eliminate the dependence on $\delta\langle r^2\rangle$ giving,

$$\mu_{A',A}\delta\nu_i = \frac{F_i}{F_j}\mu_{A',A}\delta\nu_j + \left(M_i - M_j\frac{F_i}{F_j}\right). \tag{2.29}$$

This is another linear relationship, this time between the modified isotope shifts of the two transitions, with gradient, F_i/F_j, and intercept, $M_i - M_jF_i/F_j$. Therefore, if the field and mass shift factors for one transition are known, the values for the other transition can be determined and used as above in Equation 2.28. Fig. 2.4 shows an example application of this method to previously measured isotopes shifts of the indium isotopes from Eberz et al. [15].

2.3.2 Electromagnetic moments

Given nuclear spins, measured hyperfine parameters, A_{hf} and B_{hf}, and calculated atomic structure parameters, B_e and $\partial^2V/\partial z^2$, the magnetic dipole and electric quadrupole

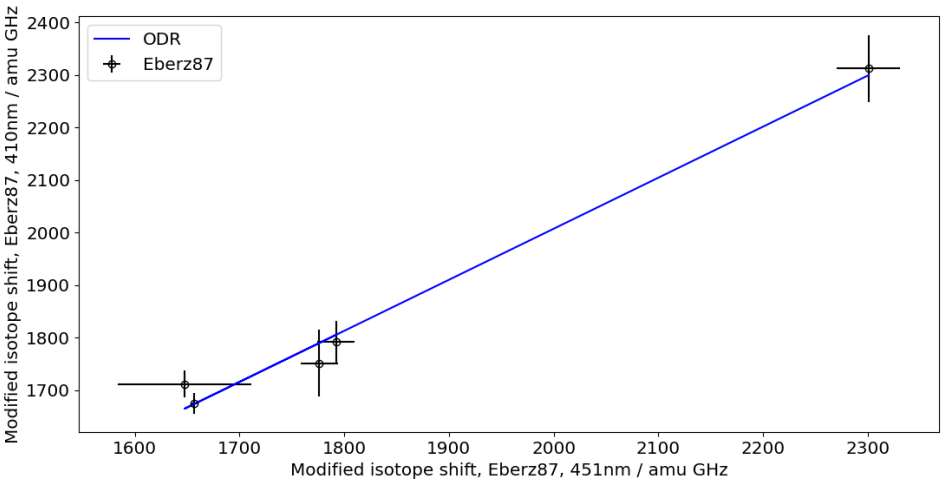

FIGURE 2.4: Example King plot using indium isotope shift data from Eberz et al. [15] (black points). Modified isotope shift values from the two measured transitions are plotted against each other, with the 5p $^2P_{3/2}$ to 6s $^2S_{1/2}$ transition at 451 nm on the x-axis and the 5p $^2P_{1/2}$ to 6s $^2S_{1/2}$ transition at 410 nm on the y-axis. Equation 2.29 can be used with an orthogonal distance regression fit (blue line) to extract the field and mass shift ratios.

moments of the nucleus can be determined from Equations 2.14 and 2.16 respectively. However, in practice, accurately calculating the atomic structure parameters is complex, requiring state-of-the-art techniques in atomic theory. Theoretical calculations of hyperfine parameters have been performed, for example in the indium isotopes in [27], using relativistic coupled-cluster approaches.

To simplify the determination of the nuclear moments, a ratio method can be used instead to remove the dependence on the electromagnetic field created by the electrons. In cases where this field has no significant variation between isotopes (i.e. the hyperfine anomaly introduced in Section 2.2.2 is small), if a measurement exists for the magnetic-dipole moment of a reference isotope (indexed by n), the magnetic moment of a second isotope (indexed by m) can be determined from

$$\frac{\mu_m}{\mu_n} = \frac{I_m}{I_n}\frac{A_m^{\mathrm{hf}}}{A_n^{\mathrm{hf}}}. \tag{2.30}$$

Similarly, a reference quadrupole moment can be used to extract an unknown quadrupole moment through measurements of hyperfine-B values with

$$\frac{Q_m}{Q_n} = \frac{B_m^{\mathrm{hf}}}{B_n^{\mathrm{hf}}}. \tag{2.31}$$

Direct measurements of magnetic-dipole moments of stable and near-stable isotopes

often exist from nuclear-magnetic-resonance (NMR) experiments [28–30]. The high precision of NMR measurements typically means that the uncertainties on resultant exotic magnetic moments are dominated by the measurement uncertainties on $A^{\mathrm{hf}}_{n,m}$. In contrast, a direct measurement technique for electric-quadrupole moments has only recently been developed [31,32], meaning measurements only exist for a small subset of elements. Therefore for quadrupole moments, we must often either rely on theoretical calculations of reference quadrupole moments, or on atomic theory for calculations of the electromagnetic field of the electrons in nuclei.

2.3.3 Nuclear spins

Hyperfine structure studies can also lead to firm determinations of nuclear spin under certain conditions. If we label the lower and upper atomic states of the measured transition for a particular isotope as l and u, taking the ratio of the two instances of Equation 2.14 removes the dependence on the nucleus in the absence of a significant hyperfine anomaly (see Section 2.2.2), giving,

$$\frac{A^{\mathrm{hf}}_u}{A^{\mathrm{hf}}_l} = \frac{B^e_u}{B^e_l}\frac{J_l}{J_u}. \tag{2.32}$$

Similarly, for Equation 2.16 we get,

$$\frac{B^{\mathrm{hf}}_u}{B^{\mathrm{hf}}_l} = \frac{\partial^2 V_u/\partial z^2}{\partial^2 V_l/\partial z^2}. \tag{2.33}$$

These two quantities are constant between isotopes of the same element, provided that the correct nuclear spin I has been chosen for the particular nuclear state when fitting the hyperfine structure. Any deviation of a nuclear state's A or B ratio from a reference value therefore indicates an incorrect nuclear spin assignment. If only one spin is consistent with the reference ratio for a particular state, this is the 'measured' spin for that state.

Chapter 3

Experimental techniques

In high-resolution laser spectroscopy, narrow-linewidth lasers are used to determine the energies of electronic transitions in atoms and molecules by resonantly exciting them. The simplest description of the collinear resonance ionisation spectroscopy (CRIS) technique, employed in the work described in this thesis, is that it is a combination of two previously well-established laser spectroscopy techniques: collinear laser spectroscopy (CLS) and resonance ionisation spectroscopy (RIS). Both of these techniques have been commonly used for the extraction of changes in mean-square charge radii [33–35] and nuclear moments [36–38], through measurements of fine-structure centroids and hyperfine structure respectively, using the methods described in Chapter 2. A comparative summary of the three techniques is given in Table 3.1, alongside in-gas-jet RIS and in-magneto-optical-trap laser spectroscopy which are also outlined in this chapter.

The CRIS measurements described in the later chapters of this work were performed on ion bunches created using the isotope separation on-line (ISOL) technique, due to the large ion production rates which this technique offers when compared to other beam-production facility types [39]. Later sections introduce CERN's ISOL facility (ISOLDE), describe the ion bunching and cooling required for sensitive CLS measurements, and give further details on elements of the CRIS experiment.

3.1 Laser spectroscopy techniques

3.1.1 Collinear laser spectroscopy

Typically in a collinear laser spectroscopy experiment, a single laser is overlapped with a bunched beam of atoms or ions, which has been accelerated to a few tens of keV in a singly-charged ionic state and optionally neutralised in-flight. The laser is tuned to the

	RIS in-source	CLS Fluorescence	CRIS	Gas jet	MOT
Linewidth / MHz	1000	10	10	500	0.05
Minimum yield / s^{-1}	0.01	1000	10	< 100	10^6
Decay detection	Yes	No	Yes	Yes	Yes

TABLE 3.1: Comparison of key parameters for the laser spectroscopy techniques discussed here: in-ion-source Resonance Ionisation Spectroscopy (RIS), Collinear Laser Spectroscopy (CLS) with fluorescence detection, Collinear Resonance Ionisation Spectroscopy (CRIS), in-gas-jet laser spectroscopy [40] and magneto-optical trap (MOT) laser spectroscopy.

Doppler-shift-corrected excitation frequency of an electronic transition in the element of interest. This lab-frame transition frequency, ν_{lab}, of a particle with kinetic energy, E, and mass, m, is Doppler shifted relative to the rest-frame frequency, ν_{rest}, according to,

$$\nu_{\text{lab}} = \sqrt{\frac{1+\beta}{1-\beta}}\nu_{\text{rest}}, \tag{3.1}$$

when the direction of travel is collinear with the laser. Here the particle speed, β, relative to the speed of light, c, is

$$\beta = \sqrt{1 - \left(\frac{mc^2}{E+mc^2}\right)^2}. \tag{3.2}$$

Taking the leading-order terms of the expansions of the derivatives of Equation 3.1 and Equation 3.2 around $E = \beta = 0$ (i.e. in the non-relativistic limit which is valid in this energy regime) gives,

$$\frac{d\nu_{\text{lab}}}{dE} = \left(\frac{d\beta}{dE}\right) \cdot \left(\frac{d\nu_{\text{lab}}}{d\beta}\right) \approx \left(\frac{1}{\sqrt{2mc^2E}}\right) \cdot (\nu_{\text{rest}})\,. \tag{3.3}$$

During the acceleration through a well-defined electrostatic potential, the original kinetic energy spread of the particle ensemble, dE, remains constant. This means that the inhomogeneous Doppler lineshape broadening of the measured atomic transition, proportional to the velocity spread, decreases with increasing beam energy. In Fig. 3.1, plots of this relationship are shown for different masses and energies, given a typical $\nu_{\text{rest}} = 1 \times 10^9\,\text{MHz}$ and $dE = 0.1\,\text{eV}$. At 40 keV, the Doppler contribution to the linewidth is less than 10 MHz, similar to the natural linewidth of transitions typically studied. Atomic transitions are chosen such that they possess sufficient sensitivity to the nuclear observables of interest, typically having resolved hyperfine-structure components. This leads to improved precision in the extraction of nuclear moments and changes in mean-square charge radii when compared to other techniques, including in-ion-source resonance ionisation spectroscopy in most cases.

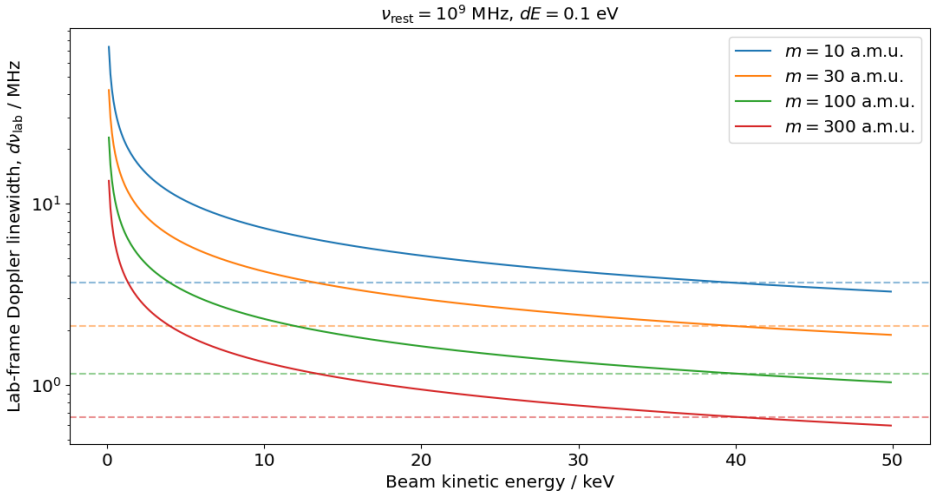

FIGURE 3.1: Approximate Doppler linewidth of a $\nu_{\text{lab}} \approx \nu_{\text{rest}} = 1 \times 10^9$ MHz resonant transition, probed in collinear geometry, at various masses and beam energies given a $dE = 0.1$ eV energy spread. The linewidth scale (y-axis) is logarithmic. The linewidth at 40 keV is indicated by the dashed lines for the different colour-coded masses. The linewidth decreases with increasing mass and energy, beginning to saturate above around 20 keV.

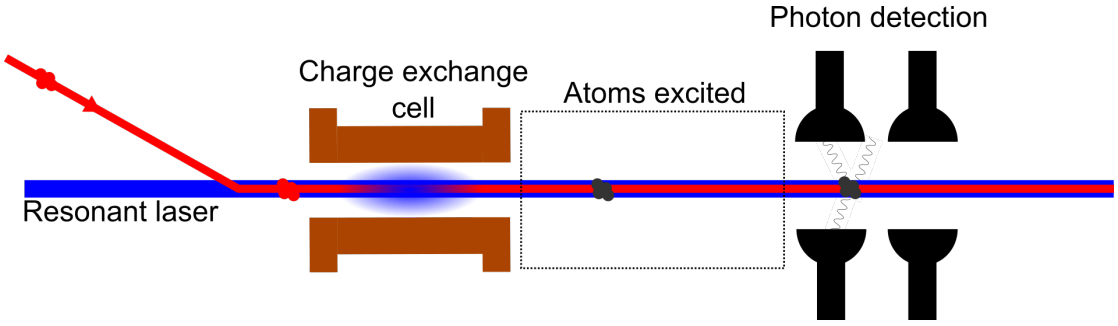

FIGURE 3.2: Schematic layout of a collinear laser spectroscopy experiment using fluorescence detection. Singly-charged ion bunches arrive at the apparatus from a beam production facility and are deflected into the main straight section of beamline. The ions can be neutralised to study atomic levels using a charge exchange cell or the ionic levels can be probed. The ions/atoms are resonantly excited by a single laser. The excited ions/atoms then spontaneously decay, emitting a photon which is detected. The energy of the ion beam (or the laser frequency) is varied to produce a spectrum of photon counts versus rest-frame laser frequency.

In experiments such as the COLlinear LAser SPectroscopy (COLLAPS) experiment at ISOLDE [41], the BECOLA experiment at NSCL [42] and the IGISOL CLS beamline [43], once the electronic transition has been excited, the ions/atoms pass into a region surrounded by photo-multiplier tube (PMT) detectors (see Fig. 3.2). These detect the isotropic photo-emission (fluorescence) of the excited ions/atoms when they decay back to a lower-lying state. The laser frequency in the rest-frame of the ions/atoms is scanned by varying the acceleration voltage of the particle bunch or by changing the lab-frame laser frequency. The photo-multiplier counts are then recorded as a function of this rest-frame laser frequency to determine the hyperfine spectrum.

Experiments employing this fluorescence detection technique are limited by two factors. Firstly, the detection efficiency of the PMTs (25% for ultra-violet photons, decreasing to 5% for infra-red) and their solid angle coverage (maximum 10%) [44] are relatively low. Secondly, the technique can also suffer from a high background counting rate from laser light scattered into the PMTs, fluorescence light from collisions of beam atoms with remaining gas particles, and dark counts. Various techniques, such as ion bunching and cooling [45] (see Section 3.2.3), have been employed to mitigate these effects and in ideal cases, such as in neutron-rich calcium [33], isotopes with yields down to a few hundred ions per second have been measured. However, typically collinear laser spectroscopy with fluorescence detection is limited to cases with yields of $> 10^4$ ions s^{-1} when bunched beams are utilised [46].

3.1.2 Resonance ionisation spectroscopy

Resonance ionisation spectroscopy (RIS) combines the resonant-excitation laser used in CLS with subsequent processes to finally ionise the atomic species. This can be achieved via a number of routes following the resonant laser excitation. The first option is direct non-resonant excitation of the electron into the continuum using a high-power laser (typically a pulsed fixed-wavelength Nd:YAG system with high pulse energy to maximise the rate of this low cross-section process), provided the photons have sufficient energy to overcome the ionisation potential (IP). A second option is to add additional resonant laser steps to reach a high-lying Rydberg state close to the IP. The highly excited atoms can then be thermally ionised or field ionised by the application of a strong electric field of the order of $10^3\,\mathrm{V\,cm}^{-1}$. Finally, if a known auto-ionising (AI) state exists for the element, this can be used instead of brute-force non-resonant ionisation. Resonant excitation has a much larger cross-section than non-resonant ionisation, meaning much less laser power is required to saturate the process; exciting to an AI has typically been found to be more efficient for this reason despite the lower available photon energy densities of tunable lasers (see for example [47]).

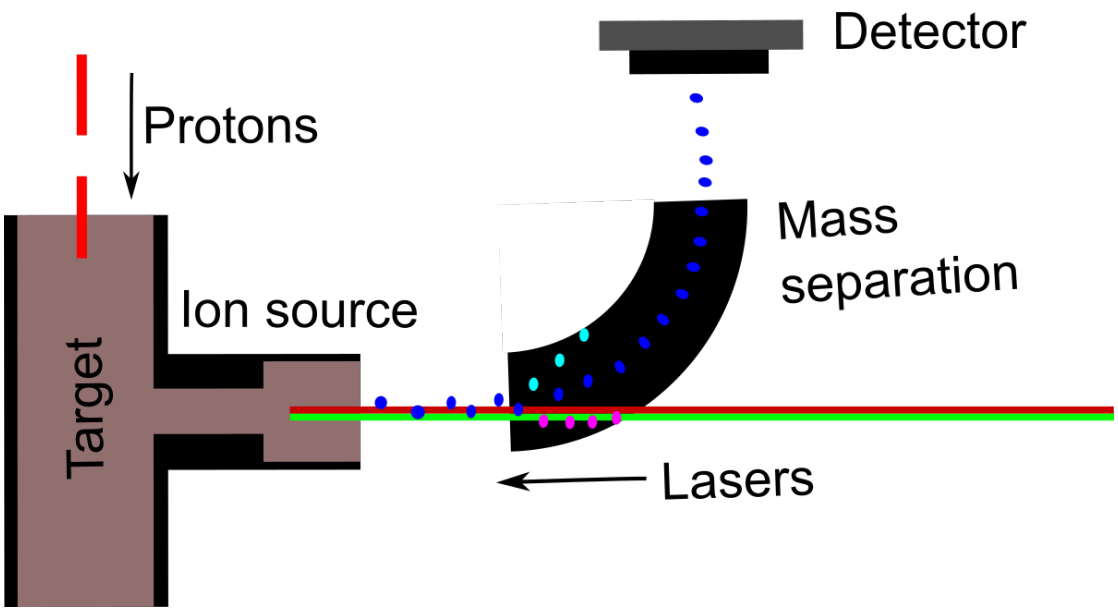

FIGURE 3.3: Schematic representation of in-ion-source Resonance Ionisation Spectroscopy (RIS). The isotopes of interest are resonantly excited and ionised by multiple lasers inside the ion source volume. After extraction and acceleration, the products are mass separated and the resultant ions are detected using either a Faraday cup, a charge-multiplication-like ion detector, a multi-reflection time-of-flight system or through radioactive-decay detection. The detected counts are recorded as a function of the excitation-laser frequency to form a spectrum.

If the ionisation was performed inside an ion source volume (see Fig. 3.3), the ions can then be extracted and mass selected (see Section 3.2.2) before being destructively detected using a Faraday cup or some other ion-detection technique. Ion detection can be performed with very high efficiency, >80% [48], and with no solid-angle limitation, a significant advantage of RIS over fluorescence detection.

Alternatively, if a large isobaric contamination is present at the mass-to-charge ratio of the isotope of interest, one of two isobaric-separation techniques can be used (for example see [49, 50]). In decay-detection mode, the extracted ions are implanted at a decay-detection point surrounded by the relevant alpha, beta or gamma detectors, depending on the decay mode of the isotope of interest. The radioactive-decay signal, gated on the expected decay energy, is then used as the ion-counting signal, thereby removing background signal from stable contaminants (and decay-energy-resolved contaminants) and improving the selectivity of the technique. Another technique which is becoming more common is the use of multi-reflection time-of-flight mass spectrometers for RIS detection. These are a type of electrostatic ion trap which extend the flight distance of the ions by many orders of magnitude before detection, thereby separating species with varying masses in time of detection [51, 52]. The mass resolution of these devices has been measured to be $m/\Delta m \geq 10^5$ [51, 52], meaning isobaric-contaminant counts can normally be removed.

In all modes, the frequency of a resonant-step laser is scanned and the number of ion counts is recorded as a function of this frequency to extract a spectrum. The scanned transition does not have to be the first excitation step, an advantage of RIS relative to fluorescence detection.

Resonant excitation and ionsation inside an ion-source volume (a hot cavity, gas cell or atomic beam unit) is the most common RIS mode as it maximises the number of atoms the lasers interact with and reduces complexity. For this reason, RIS can be performed on isotopes produced in very small quantities, much less than one atom per second in some cases [53], well below the limits of CLS with fluorescence detection. However, as described in Section 3.2, the ion-source volume typically reaches a few thousand degrees Kelvin [54], meaning there is a large Doppler spread (and a significant pressure-dependent broadening contribution to the linewidth of each atom). The velocities of the atoms of mass, m, and temperature, T, in the ion source approximately follow a Maxwell-Boltzmann distribution. Rearranging Equation 3.1 for β and taking the leading-order term of the Taylor expansion about $\nu_{\text{lab}} = \nu_{\text{rest}}$ (valid in this non-relativistic velocity regime) gives the lab-frame laser-frequency distribution,

$$P(\nu_{\text{lab}})d\nu_{\text{lab}} = P(\beta)\frac{d\beta}{d\nu_{\text{lab}}}d\nu_{\text{lab}} = \frac{d\nu_{\text{lab}}}{\nu_{\text{rest}}}\sqrt{\frac{mc^2}{2\pi k_B T}}\exp\left[-\frac{mc^2}{2k_B T}\frac{(\nu_{\text{lab}}-\nu_{\text{rest}})^2}{\nu_{\text{rest}}^2}\right], \quad (3.4)$$

which is a Gaussian distribution with standard deviation,

$$\sigma\left(\nu_{\text{lab}}\right) = \sqrt{\frac{k_B T}{mc^2}}\cdot\nu_{\text{rest}}. \quad (3.5)$$

Fig. 3.4 gives values for this equation given various masses and temperatures and a transition with rest-frame frequency, $\nu_{\text{rest}} = 1\times10^9\,\text{MHz}$, as above. As can be seen from the figure, the Doppler-broadening effect when performing resonant laser excitation in-source is significantly larger than that observed when performing collinear laser spectroscopy. This limits the applicability of standard in-source HFS RIS measurements to the few cases where hyperfine splittings are large enough for precise measurement; these cases are typically found in the heavy elements. Development work is also ongoing on a variety of techniques attempting to reduce or remove this large Doppler-broadening contribution in in-source measurements. An example is the use of two-photon spectroscopy, where two anti-collinear laser pulses excite a two-photon transition in the element of interest, cancelling the Doppler shift for each atom [55].

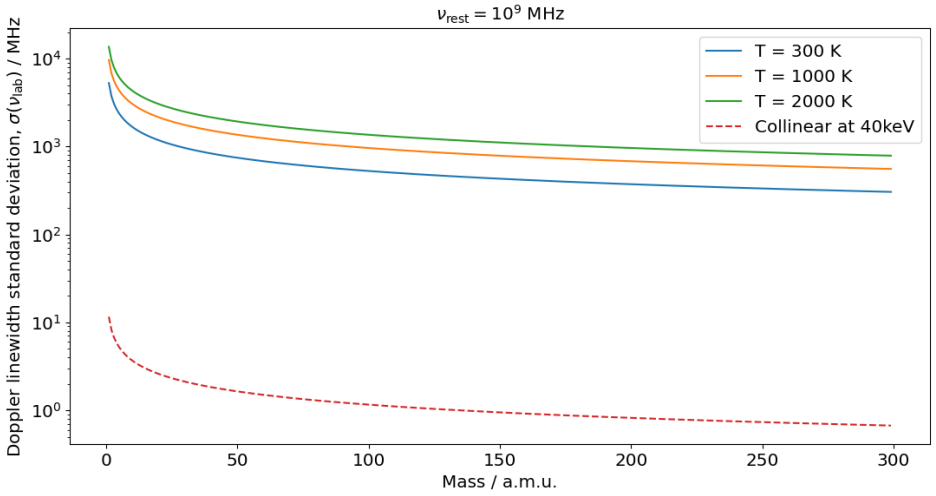

FIGURE 3.4: Ion mass vs. calculated standard deviation of Gaussian broadening caused by the Doppler effect, when exciting a resonant laser transition with rest-frame frequency, $\nu_{\text{rest}} = 1 \times 10^9$ MHz, inside a hot-cavity ion source according to Equation 3.5. Values are given for a variety of ion-source temperatures and are compared to the expected Doppler broadening if an equivalent sample was instead measured in a Collinear geometry at 40 keV and 0.1 eV energy spread. The broadening at 40 keV is consistently three orders of magnitude lower than the in-source spread.

3.1.3 In-gas-jet spectroscopy

A high-resolution laser spectroscopy technique which has been recently developed is the probing of atomic species in an expanding gas-jet [40, 56]. Here the nuclear reaction products are created, thermalised and neutralised inside a gas cell filled with inert noble gas at 500 mbar pressure. The gas cell is connected to a vacuum beamline via a supersonic nozzle; the reaction products follow the gas flow out of the nozzle and form part of a supersonic jet. The atoms of interest are then probed using RIS while inside this gas jet. The resultant temperature reduction from the expansion and acceleration significantly reduces the Doppler lineshape broadening relative to in-source RIS. Measurements have been performed on actinium isotopes [40], and on copper isotopes with a measured spectral linewidth of 450 MHz [57]. The technique, like in-gas-cell RIS, is especially suited to the study of highly-reactive elements such as the actinides [58]. This is because these elements would bind to the target material and would be difficult to extract in atomic form from a thick-target ISOL facility (see Section 3.2), typically the radioisotope source of choice for other laser spectroscopy techniques.

3.1.4 Atom and ion trapping techniques

Another possible environment to probe atomic structure with lasers that could be considered is a magneto-optical atom trap (MOT) or an ion trap. While ion traps utilise the

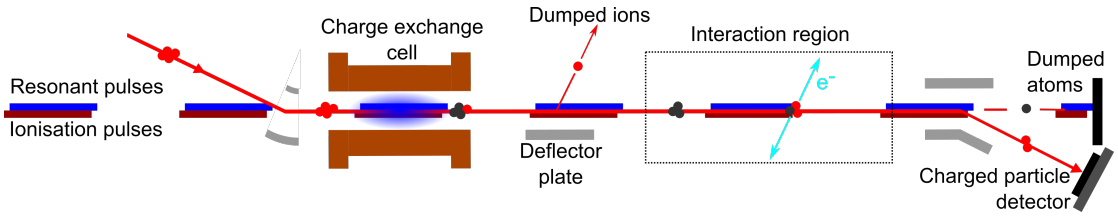

FIGURE 3.5: A simplified schematic view of the CRIS technique. Ions at keV energies are deflected into the main section of beamline and are neutralised into atomic states. The remaining ions are removed through electrostatic deflection. The atoms are excited and ionised with multiple collinear laser steps in an interaction region. The created ions are deflected into a charged-particle detector. The detected counts are recorded as a function of the excitation laser frequency to form a spectrum.

ion charge to trap the particles in three dimensions using some combination of electric and magnetic fields, atom traps must rely on more complex techniques. MOTs confine atoms in three dimensions using laser light incoming from six directions. The frequency of the light is detuned relative to an atomic transition meaning atoms moving towards any of the lasers are Doppler shifted into resonance, absorb photons, and are therefore damped. This laser-cooling effect (which can also be added to ion traps) allows for the cooling of trapped particles to sub-Kelvin temperatures [59], meaning high precision can be achieved in laser-spectroscopy experiments, such as in Wang et al. [60] where the isotope shift of ^{6}He relative to ^{4}He was measured with an uncertainty of 56 kHz. However, MOTs have only been used in limited cases for isotope-shift spectroscopy [39] and have required large atom yields of the order of $10^{6}\,\mathrm{s}^{-1}$ from the ion source due to their complexity [60].

3.1.5 Collinear resonance ionisation spectroscopy

The CRIS technique was first suggested by Kudriavtsev and Letokhov in 1982 [61] as a way to measure rare isotopes with ultra-low relative abundance (isotopic fraction of $< 10^{-10}$). More recently, the application of the technique has become more feasible with the introduction of ion bunching and cooling (see Section 3.2.3) and the development of pulsed-laser technology (see Section 3.3.2).

The aim of the CRIS technique is to combine the kinematic reduction in Doppler broadening found in CLS with the high sensitivity of in-source RIS. Laser excitation is performed on atoms in-flight in a collinear geometry as in conventional CLS. However, unlike CLS, after resonant excitation the atoms are ionised through one of the processes described in Section 3.1.2. The ions can then be separated from the remaining neutral atoms using electrostatic bending plates and detected using a charged-particle detector, such as a microchannel plate (MCP) or a similar style electron amplification detector [9, 10].

This has two main advantages over CLS with fluorescence detection: Firstly, ion detection has a much higher total efficiency than photon detection (>80% [48] instead of <1% when the solid-angle coverage is considered [39]), meaning if the ionisation process is close to saturation (i.e. all of the excited atoms are ionised), the overall efficiency of the technique in ion-detection mode is orders of magnitude greater. The second advantage is the very low rate of background counts when using ion detection. This is because only ions produced in the region between neutralisation and electrostatic deflection are observed. One of the main sources of background is the ionisation of isobaric contamination and the species of interest through collisions with residual gases in this interaction region. The interaction region is kept at ultra-high vacuum, $< 10^{-9}$ mbar, to minimise this effect. Other sources of background exist, such as multi-photon non-resonant ionisation of isobaric contaminants, but these processes typically occur at rates orders of magnitude lower than the background-signal level seen in fluorescence detection experiments. Furthermore, if the ion detection is performed on an event-by-event basis (now routinely achieved at the CRIS experiment at ISOLDE [27]), background can be further reduced by rejecting ion counts outside the arrival-time window of the ion bunches.

Unlike fluorescence detection, CRIS also separates the ionised signal particles in space from the remaining neutral atoms in the final electrostatic deflection. This means that, like conventional RIS, CRIS can be combined with decay detection, where the ion detector is replaced with an implantation point surrounded by silicon or scintillator detectors, allowing for the radioactive decay of the signal-beam components to be measured. If the energy resolution of the detectors is sufficient, or a background contaminant is stable, this allows for further separation of unwanted counts from the decay signals of the nuclear state of interest [4, 62].

3.2 The ISOLDE facility

The Isotope Separator OnLine DEvice (ISOLDE) at CERN has been producing radioactive isotopes of a variety of elemental species for over 50 years. Now in its fourth iteration, ISOLDE is comprised of two target stations serving a number of experimental beamlines with radioisotopes at low (up to 60 keV) or high (up to 10 MeV/u) energy. The two target stations receive up to 2 μA of proton current at 1.4 GeV from the CERN Proton Synchrotron Booster (PSB) accelerator [63] (see Fig. 3.6). The proton beam is pulsed, with 10^{13} protons per pulse, 900 ns pulse length and pulses separated by a varying multiple of 1.2 s [64]. Approximately half the proton pulses circulated in the PSB are sent to ISOLDE, while the others are sent to other CERN accelerators and experiments.

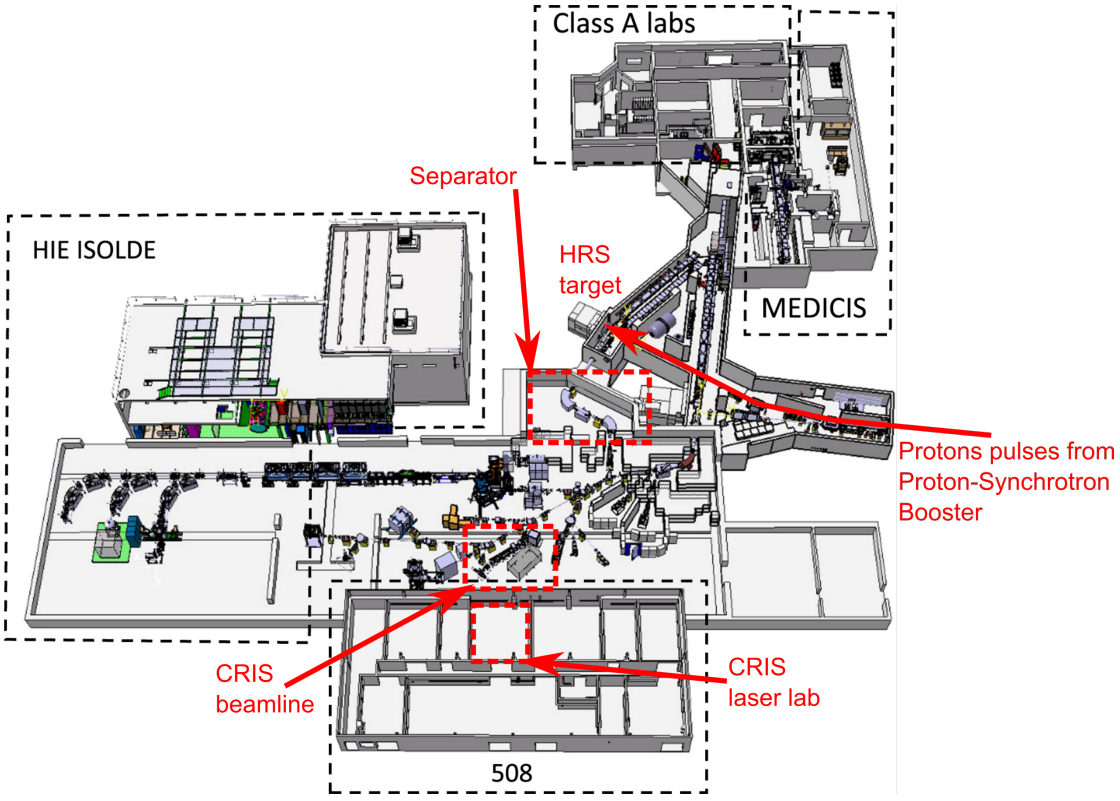

FIGURE 3.6: 3D drawing of the ISOLDE hall and surrounding facilities with additional labels. 1.4 GeV proton pulses are directed from the CERN Proton Synchrotron Booster accelerator into the ISOLDE HRS target. Products are passed through the mass separator and on to the CRIS beamline. Some laser beams are produced in the CRIS laser lab in CERN building 508 and are then transported to the CRIS beamline. Others are produced in the vicinity of the beamline in the CRIS laser cabin. Reproduced from [63].

The two target stations use targets with identical mechanical design. These are comprised of a 20 cm long cylinder of target material, often uranium-carbide (UC_x) [65], connected to an ion source via a tube known as a transfer line (see Fig. 3.7). The proton beam interacts with this target material inducing a variety of nuclear reactions, such as fission, fragmentation and spallation, to produce an assortment of nuclear species, which then collide with the surrounding target material and thermalise. The target material and transfer line are independently heated. This heating allows for the rapid diffusion of the reaction products out into the transfer line and ion source. Depending on the materials used, the target can reach up to 2000 °C [54, 66].

The high proton intensity and target thickness means ISOLDE produces large yields of radioactive products when compared to in-flight separation and in-gas-cell production facilities [39]. However, the requirement for diffusion through the target before extraction from the ion source can be performed means that reaction products which chemically bind to the target material at its high temperature take a long time to be released (relative to their decay lifetime) so are challenging to study at ISOLDE.

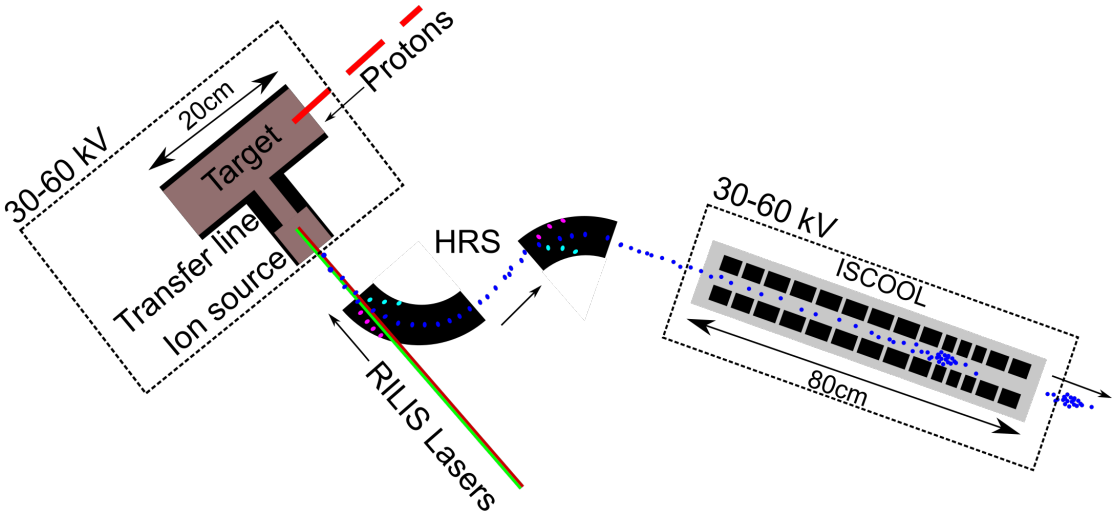

FIGURE 3.7: Schematic of part of the ISOLDE facility (not to scale). During radioactive beam experiments at CRIS, proton bunches impinge on a thick target attached to the HRS ion source via a transfer line. Lasers from the RILIS resonantly excite and ionise the element of interest to selectively enhance the current of that species. The two coupled dipole magnets of the HRS select the mass of interest after acceleration to 30-60 keV. The ISOLDE helium-filled Paul trap, ISCOOL, traps the beam to bunch it and reduce the energy spread. The ion bunches are then electrostatically transported to the CRIS beamline.

3.2.1 Ion sources

A variety of ion-source types can be used at ISOLDE. Firstly, electron-impact ionisation can be used to ionise atoms inside an ion source. In this ion-source type, electrons are emitted from a heated cathode and form a plasma after acceleration through a few hundred volts. The created ions are confined within this plasma, meaning wall collisions leading to re-neutralisation are minimised. These plasma ion sources are generally very efficient, with $> 50\,\%$ ionisation efficiency, but are not chemically selective given the broad range of electron energies leading to the ionisation of most atoms and molecules [67]. The exception is for the noble gas elements. In these cases, the source can be combined with a cooled transfer line so that other elements are adsorbed onto the walls before reaching the source and relatively pure beams of the noble-gas element of interest can be formed.

Secondly, surface ionisation in a hot cavity can be used directly to produce positively-charged ions of elements with a low first ionisation potential (IP). This is where the species released from the target interact with the high-temperature ion-source material and a transfer of an electron occurs, producing either a positive or negative ion. The equilibrium ratio between the number of neutral atoms (n_0) and positive ions (n_i^+) of a

particular element at the hot-cavity surface is given by the Langmuir equation [67],

$$\frac{n_i^+}{n_0} = \frac{g_i^+}{g_0} \exp\left(\frac{\varphi - W_i}{k_B T}\right), \tag{3.6}$$

where g_i^+ and g_0 are the statistical degeneracy of the ionic and atomic ground states respectively, φ and T are the work function and temperature of the ion-source surface respectively, and W_i is the IP of the element of interest. To increase the efficiency of positive-ion production, materials with high work function and high melting point (for high temperature operation), such at tantalum, are typically used to to construct the hot cavity in a positive-ion surface source [54].

Where the element of interest has a much lower IP than the isobaric contamination, such as in the alkali metals, surface ionisation can be chemically selective and efficient [67]. However, in most elemental cases, adding resonant laser ionisation improves both of these factors [68]. In resonance-ionisation laser ion sources, RIS is performed on atoms in the surface-ion-source region. Because the RIS process only excites electronic transitions between atomic levels in a very narrow range of energies, this process is inherently chemically selective (being typically unique to a single element), especially when a number of atomic transitions are excited in sequence before ionisation. Given sufficient laser power to excite all of the atoms of interest, and a large thermal population of the probed atomic state, this process can also be highly efficient, of the order of 10 % [69]. However, surface ionisation from the hot ion source also occurs, introducing ions of elements with a low IP which can contaminate the ion beams. When utilised, the high-power ionisation laser can also cause heating at the back of the transfer line (where the laser power is dumped) enhancing the rate of surface ionisation at this position. These laser ion sources, managed by the ISOLDE Resonance Ionisation Laser Ion Source (RILIS) collaboration, are typically used when running CRIS experiments and are in fact the most commonly used ion sources at ISOLDE in general [70].

Another ion source type developed to reduce the isobaric contamination present in RIS-enhanced ion sources is the laser ion source and trap (LIST). These ion sources add a positively-charged repeller electrode and a quadrupole ion guide to the outside of the hot cavity [71]. Surface ions are prevented from entering the ion guide region by the repeller, while neutral atoms diffuse into the quadrupole and are subsequently laser ionised, trapped and extracted. The ISOLDE LIST ion sources have been shown to suppress the rate of extraction of surface ions by $> 10^5$, while reducing the rate of laser ionisation by only a factor of 20-50 [71].

The target and ion source assembly is held at 30-60 kV; after ionisation, the ions are accelerated through this potential difference and are focussed into a beam using a number

of electrostatic elements.

3.2.2 Mass selection

After extraction from RIS-enhanced ion sources, ISOLDE beams contain a variety of laser- and surface-ionised nuclear-reaction products. To select only the isotope of interest, tunable C-type dipole magnets with a bending radius of 1 m [63], along with a series of collimating slits, select beam components within the mass-resolution range of the system. Connected to one of the two target stations, the ISOLDE High Resolution Separator (HRS) has two of these magnets in sequence, one bending through 90 ° and the other through 60 °, with a combined mass resolving power measured to be up to $m/\Delta m = 6000$ [63]. This is sufficient to select a single isotope of any element of interest, but isobaric contaminants can form a significant part of the final beam, especially in cases where they are produced and emitted from the ion source at rates orders of magnitude higher than the isotope of interest. The first magnet is located on a direct line-of-sight from the ion source, with a laser window opening allowing for RILIS laser access to the ion source. This target station is always used for CRIS experiments due to the improved mass-resolving power (compared to the lower-resolution General Purpose Separator (GPS)) and the presence of the ISOLDE ion trap, ISCOOL, on this line.

3.2.3 Bunching and cooling

The quasi-continuous mass-selected ion beam from the HRS is then decelerated and trapped in ISCOOL, a helium-filled linear Paul trap (see Fig. 3.7) [7]. The continuous ion beam is here converted into discrete bunches in time. This process is crucial for CRIS experiments for two main reasons. The first is that the high-instantaneous laser power required to saturate the laser excitation and ionisation processes is easier to achieve with pulsed laser systems with low repetition rates of the order of 100 Hz. Using 100 Hz pulsed lasers without ion bunching would result in a reduction in total experimental efficiency of 10^3, assuming a 40 keV, 100 u beam and a 3 m interaction length. Secondly, as mentioned in Section 3.1.5, ion bunching means ion counts can be gated in time, accepting counts around the arrival time of each 4(1) μs-wide bunch. This reduces the utilised recording time of the detector by a factor of 10^4, reducing the sum of the time-independent background-signal contributions (such as local radioactive decay) proportionally.

Linear Paul traps generate a rotating electric-potential well in the transverse direction to trap the ions radially (see Fig. 3.8a). This is achieved by applying radio-frequency (RF) sine- or square-wave electric potentials to four longitudinal rods arranged symmetrically

around the beam axis, with adjacent rod voltages out of phase by 180°. The resultant ion equations of motion in the two transverse dimensions, x_i, for time, t, are a special case of the Mathieu equation [72],

$$\frac{d^2x_i}{d\tau^2} - 2q\cos(2\tau)\,x_i = 0, \tag{3.7}$$

where we have written the equations in terms of the dimensionless parameters,

$$q = q_{x_1} = -q_{x_2} = \frac{4eU_{\mathrm{RF}}}{m\omega_{\mathrm{RF}}^2 r_0^2}, \tag{3.8}$$

and,

$$\tau = \frac{\omega_{\mathrm{RF}}t}{2}. \tag{3.9}$$

Here m is the ion mass and r_0 is the internal radius of the rods (i.e. the perpendicular distance between each rod surface and the beam axis). U_{RF} and ω_{RF} are the amplitude and angular frequency of the RF voltage respectively. q is known as the trapping stability parameter.

Stable oscillatory solutions (i.e. without rod collisions) to this equation occur when $|q| < 0.91$ [7], fixing the maximum stable value of the ratio $U_{\mathrm{RF}} : \omega_{\mathrm{RF}}^2$ for a given mass and internal radius. To solve the differential equation, Equation 3.7, the motion of the ions can be divided into the sum of two parts: a low-frequency, high-amplitude macro-motion (dominating the proportional term), and a high-frequency, low-amplitude micro-motion (dominating the differential term). Setting the maximum of the macro-motion to the internal radius, r_0, gives a maximum stable transverse energy

$$D = \frac{qU_{\mathrm{RF}}}{4} \tag{3.10}$$

meaning for optimal acceptance, the amplitude of the applied RF voltage must be maximised within the bounds of stable q. The internal radius for the ISOLDE trap, ISCOOL, is $r_0 = 20\,\mathrm{mm}$ [7]. Both RF parameters are varied to maintain $19\,\mathrm{eV} < D < 25\,\mathrm{eV}$ at $q = 0.5$, a typical stable operating point for linear Paul traps (see for example [8]). Typical values for $m = 100\,\mathrm{u}$, for example, are $f_{\mathrm{RF}} = \omega_{\mathrm{RF}}/2\pi = 300\,\mathrm{kHz}$ and $U_{\mathrm{RF}} = 185\,\mathrm{V}$, giving $D = 23.23\,\mathrm{eV}$ [7].

The ISCOOL device is composed of four RF electrodes surrounded by axial DC electrodes for longitudinal trapping. The DC segments are separated by insulators up to a total length of 800 mm. DC voltages are applied individually to these segments to create a static potential well along the beam axis, causing simple harmonic motion of the ions in this dimension and thereby trapping the ions in three dimensions. A schematic layout of ISCOOL is seen in Fig. 3.9.

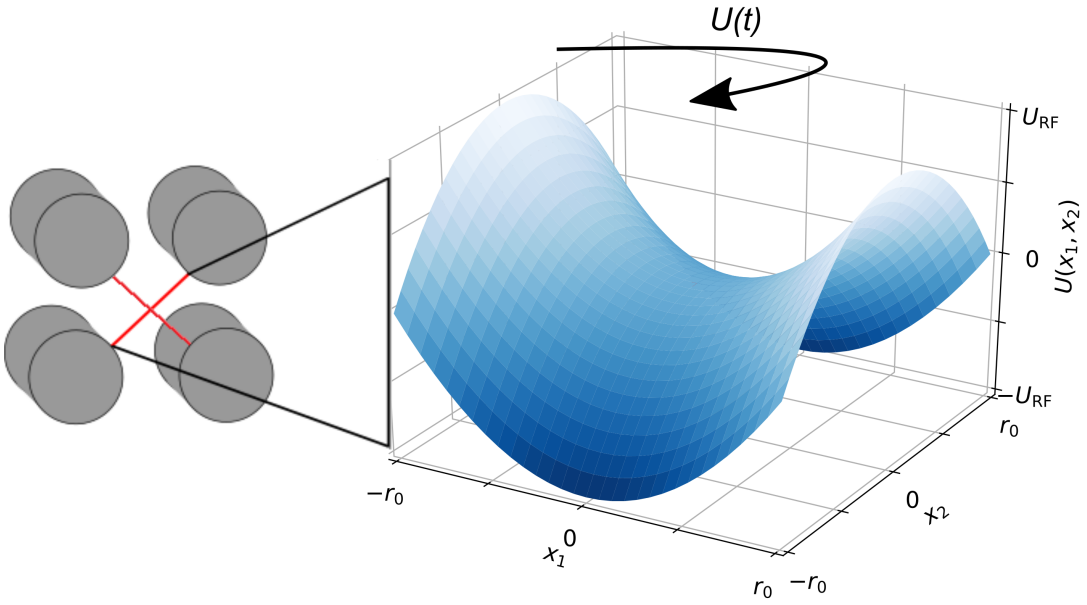

(A) Saddle radial potential created by the RF voltage applied to the rods.

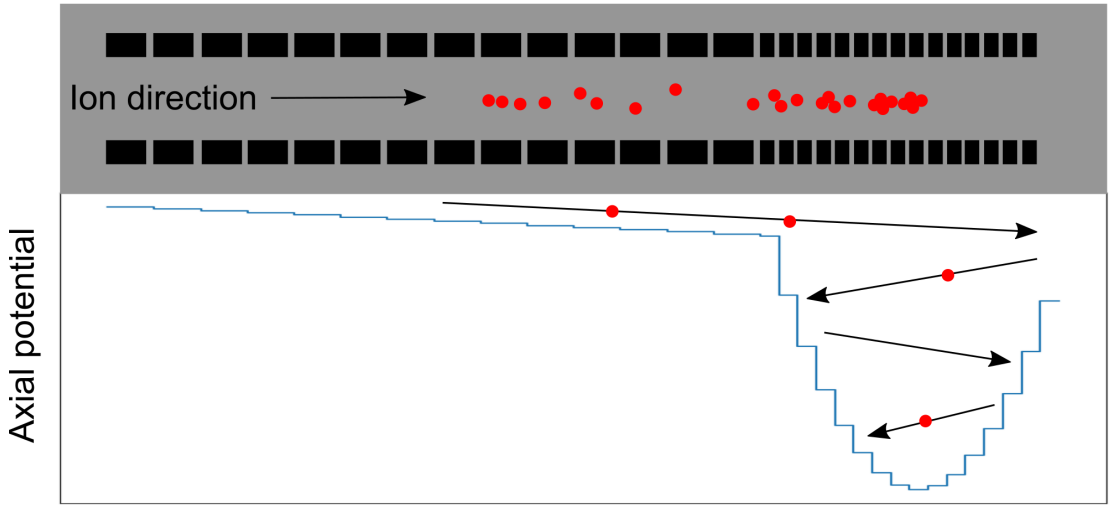

(B) Possible axial DC potential layout of a linear Paul trap.

FIGURE 3.8: The radial and axial voltages of a linear Paul trap. The saddle rotates in time in phase with the applied RF, creating a pseudo-potential well in both dimensions with depth D (Equation 3.10). The longitudinal potential well is static until the bunch release, when the downstream parabolic voltages decrease rapidly to allow the bunch to escape with a narrow time width.

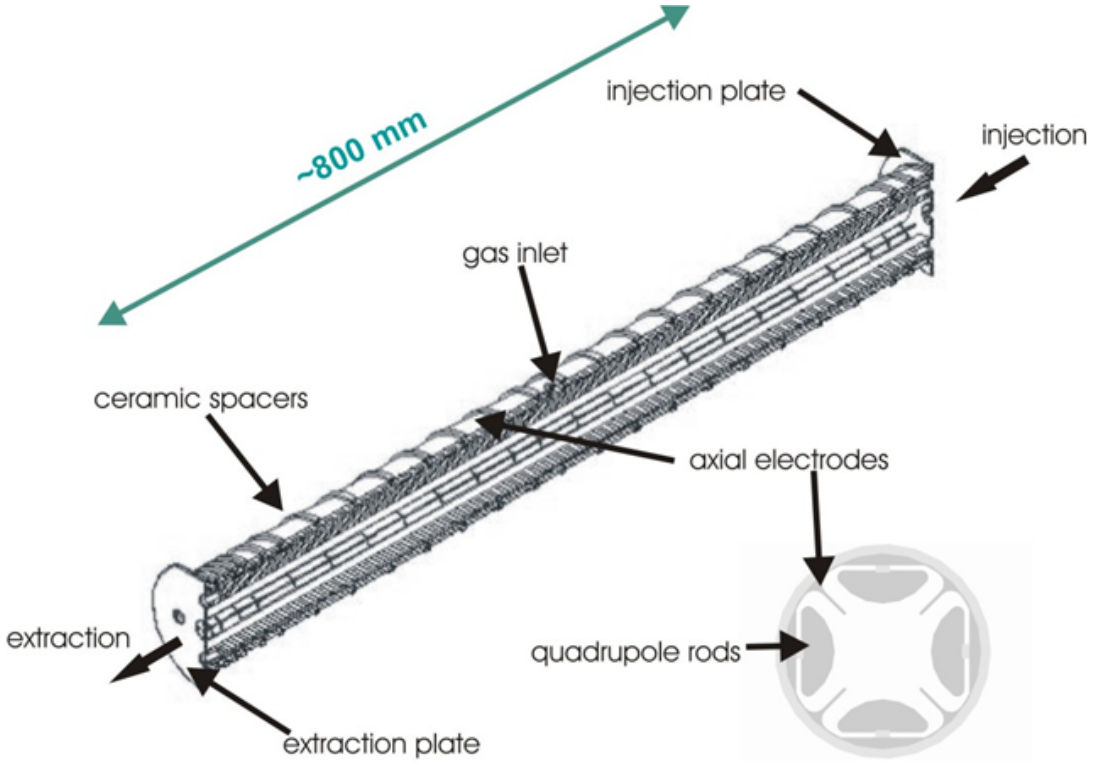

FIGURE 3.9: The interior electrodes of the ISCOOL ion trap cooler buncher, showing the quadrupole rods for the application of the RF radial trapping field and the segmented axial electrodes for the DC longitudinal trapping field. Reproduced from [7].

Helium is constantly injected into the trap to maintain an internal pressure of approximately 0.1 mbar. The trapped ions collide with this inert, light "buffer" gas, kinematically cooling the ions. Macroscopically, this can be added as a viscous damping term in the radial equations of motion (Equation 3.7) and in the longitudinal equation of motion, resulting in an exponentially reducing amplitude of oscillation. More precisely, in simulations for example, probabilistic elastic collisions between the buffer gas atoms and the trapped ions (often modelled as hard spheres) can be used, but the overall damping result is the same.

The DC voltages applied to the rod segments on the downstream end of ISCOOL are periodically and rapidly decreased to create a ramp potential to ground, removing one side of the longitudinal potential well. This releases a discrete bunch of ions from the trap with a temporal width in the range 2 to 5 μs. These ions also have a small energy spread (<0.1 eV) and transverse emittance (3π mm mrad) relative to those upstream of the trap due to the kinematic cooling [45]. During CRIS experiments, the timing of the release is synchronised with the 100 Hz repetition rate of the CRIS lasers, meaning the ions are trapped for up to 10 ms. After the release time of the radioactive products from the target, this is one of the main limitations on the lifetime of nuclear states which can be probed with CRIS, as the population of shorter-lived states can decrease below the

yield threshold here. After release from ISCOOL, the ion bunches are guided through a series of electrostatic bending and focussing elements to the experimental beamlines.

The design, simulation and construction of an alternative independent ion trap cooler-buncher specifically for the CRIS experiment is being performed. This project is detailed and motivated in Section 6.2.

3.3 The CRIS experiment

The following sections describe the specific implementation of the CRIS technique at the ISOLDE facility. A set of CF-flanged stainless-steel vacuum chambers are connected to the central ISOLDE vacuum system downstream of ISCOOL. After passing through an electrostatic quadrupole triplet, the ion beam is deflected through 34 ° into the main 3-m-long section where neutralisation and spectroscopy are performed. The laser-entry vacuum window is located at this bend. This is a Kurt J Lesker DUV DN35CF CF-flanged quartz viewport. After the main section, the ions are deflected again through 20 ° into the final beamline section where they are impinged directly onto an ETP MagneTOF detector after another 1 m of flight. The laser exit window (of the same type as the entry) is located at this bend.

Remotely insertable Faraday cups are located at various positions along the beamline (see Fig. 3.11, labelled FC0, 2 and 3) to monitor the atom and ion beam currents, primarily for the adjustment of electrostatic-element potentials in the optimisation of ion-beam transport efficiency in preparation for experiments. A pair of manually adjustable irises are also located in the main section of beamline; these are used to optimise the overlap of the ion and laser paths by ensuring both are collinear with the central axis.

Ultra-high vacuum is maintained throughout the vacuum beamline using a set of Edwards Vacuum nEXT and Agilent (Varian) TV301 Navigator turbomolecular pumps, backed by Edwards Vacuum nXDS Dry-scroll pumps (with a $10\,\mathrm{L\,s^{-1}}$ pumping rate) in addition to a SAES Capacitorr D 1000 non-evaporable getter pump (with a $1000\,\mathrm{L\,s^{-1}}$ pumping rate). The beamline is divided into sections separated by gate valves so that maintenance can be performed on individual vented sections without compromising the vacuum pressure of the entire beamline.

The poorest vacuum is found in the charge-exhange cell (CEC) section (see the following Section 3.3.1), where the pressure is typically 10^{-8} mbar. The interaction region, the section where the atom bunches and laser pulses are overlapped to perform the spectroscopy, has the best vacuum, reaching 10^{-9} or 10^{-10} mbar. The pressure differential

between these two sections is maintained when the valves are open through a pair of differential-pumping stages in a third independently valved section. These are cylindrical apertures aligned with the beam axis, each 10 mm in diameter and 20 mm long [73], restricting the gas flow between the regions. A section upstream of the CEC containing the quadrupole triplet and a section downstream of the interaction region containing the ion detector are also independently valved.

3.3.1 Neutralisation

Probing the electronic level structure of neutral atoms at CRIS is typically much easier in a practical sense than probing the structure of ions. This is due to the fact that elements have a much larger second ionisation potential (IP) than their first IP meaning more lasers at deeper ultra-violet (UV) wavelengths are needed, adding complexity, reducing laser-pulse powers and inevitably reducing ionisation efficiency. The electronic structure of ions is also generally less well studied than atoms, meaning fewer resonant-excitation routes can be found in databases. Additionally, it is more difficult to separate ions in two charged states, 1^+ and 2^+, than it is to separate neutral atoms and charged ions. It is therefore advantageous to convert the incoming 1^+ ion bunch into neutral atoms before performing spectroscopy.

This is achieved at the CRIS experiment through the use of a Charge-Exchange Cell (CEC) (see Fig. 3.10). This consists of a 200-mm long, 10-mm internal radius wire-mesh tube, aligned with the beam axis and surrounded by solid alkali metal. This is encased in a copper chamber, approximately 100 mm in diameter, surrounded by Nichrome heating cable [24]. High-current AC is passed through the Nichrome wire to heat the cell and the alkali metal. Thermocouples monitor the temperature of the centre and ends of the cell. As the CEC is heated, an alkali vapour forms in the centre of the cell in the path of the ion bunches. The beam ions interact with the alkali atoms and electrons are transferred, neutralising part of the bunch into a variety of atomic states [74]. Alkali metal is used because the atoms each contain a single weakly-bound electron with a low ionisation potential outside a closed atomic shell, meaning the probability of a charge-exchange reaction occuring in each interaction is maximised. The ends of the cell are air cooled using a CPU fan and an internal vacuum-sealed cooling circuit, condensing the vapour into the wire mesh [24]. The liquid metal can then recirculate via surface-tension flow within the mesh, extending the operational lifetime of the cell before refilling is required and reducing its impact on the vacuum pressure of the surrounding beamline. The metal, either sodium (Na) or potassium (K), is selected to maximise the population neutralised into the probed state as well as the total neutralisation efficiency. The metal is loaded

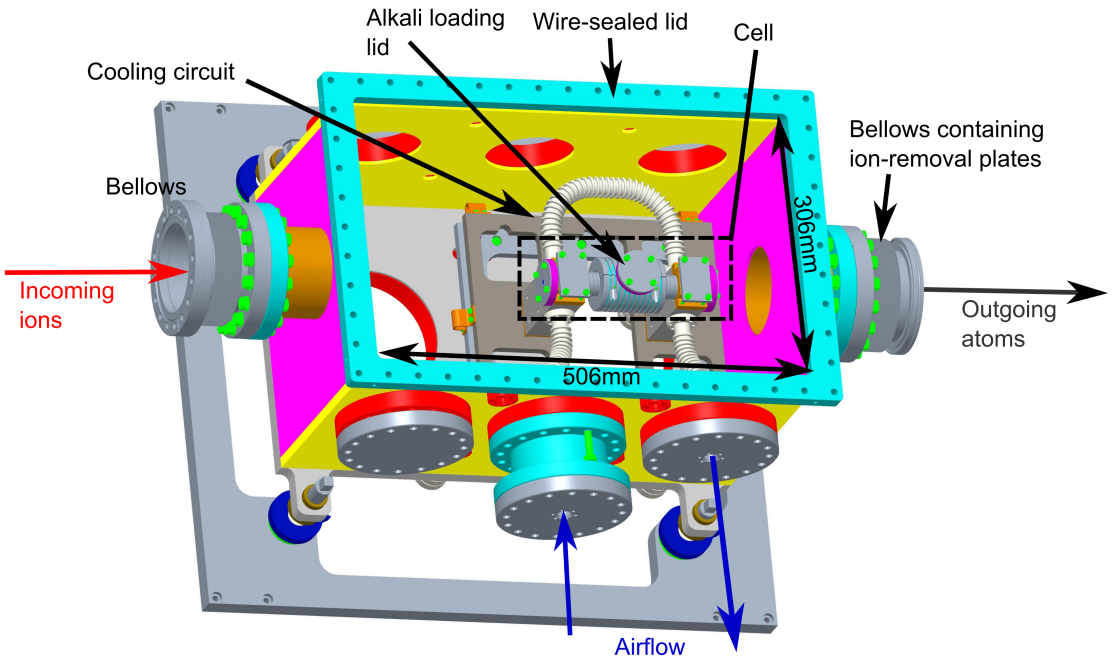

FIGURE 3.10: Top view of a CAD drawing of the CRIS Charge Exchange Cell (CEC). The ion beam enters through the bellows on the left side and exits through the bellows on the right. The exit bellows contains the two oppositely-charged electrostatic plates for the removal of the remaining ions and highly-charged atoms. The internal cell containing the wire-mesh tube for neutralisation is shown. The alkali is loaded in from above when the chamber is vented with argon. Air is continuously circulated through the sealed cooling pipes (connected to the cell mount ends) through the use of a CPU cooling fan connected to an exterior port in atmosphere. This cools the ends of the cell, increasing the condensation of the alkali vapour by adding to the temperature gradient created by the mounting arrangement. The chamber lid is vacuum wire sealed and is pumped by a $1000\,\mathrm{Ls}^{-1}$ turbomolecular pump from below.

from above when the chamber is vented with argon to minimise oxidation. The chamber is pumped by a large $1000\,\mathrm{Ls}^{-1}$ turbomolecular pump from below.

The ions remaining in the bunch after it passes through the cell are removed using a set of electrostatic deflection plates. These include a pair of opposing plates with opposite-polarity high voltage applied ($\approx 5\,\mathrm{kV}$), generating a high-field region after the cell. This high electric-field region ionises and removes atoms neutralised into high-lying Rydberg states, which may otherwise contribute to a non-resonant ionisation background if ionised in the final electrostatic bender (see Fig. 3.11 and Table 4.2).

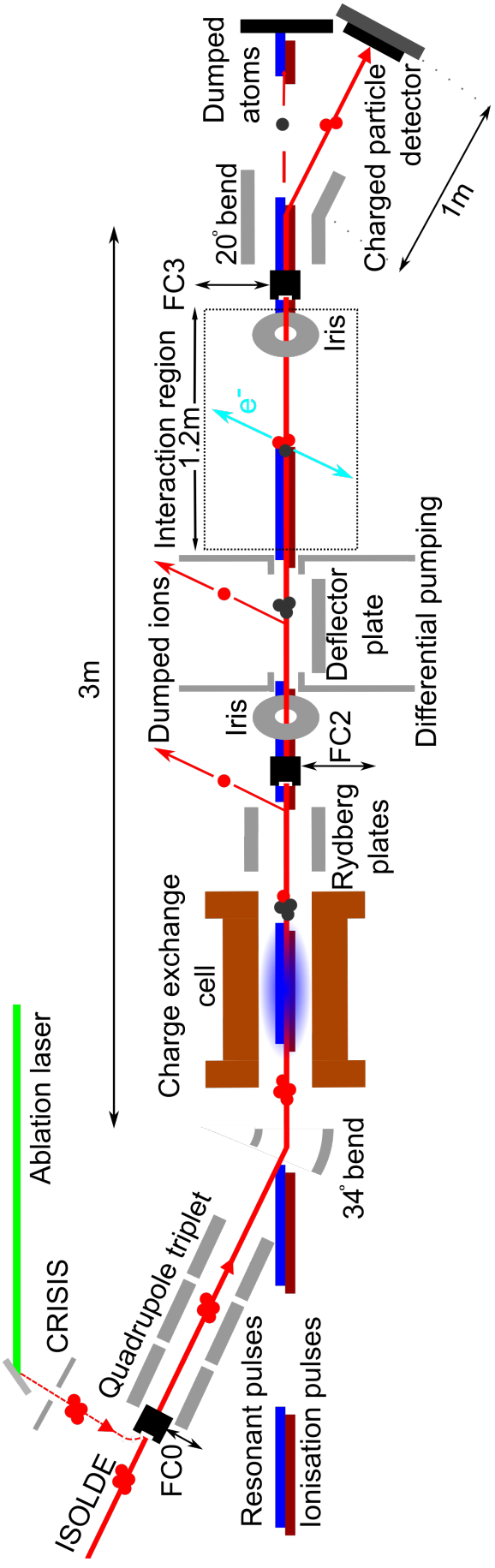

FIGURE 3.11: Schematic of the CRIS beamline. Ion bunches from ISOLDE are refocussed using a quadrupole triplet before being guided through the charge exchange cell for neutralisation. The remaining ions (red circles) are then deflected out of the beam before multiple laser pulses excite and ionise the atoms (black circles) in the UHV interaction region. The resultant ions are detected after deflection. Removable Faraday cups (FC0, 2, 3) are used before the experiment to maximise ion-beam transport efficiency and are then removed. Irises are used for laser alignment and ion-beam collimation. The CRISIS can be used instead of ISOLDE to produce bunched beams of stable isotopes through laser ablation of solid targets.

3.3.2 Laser systems

The elements studied at CRIS come with a variety of electronic configurations and therefore transition frequencies. This means a diverse range of laser systems are needed to satisfy the requirements of all experiments. A schematic connection diagram of the laser systems present at CRIS in the temperature-controlled CRIS laser lab and the CRIS laser cabin is shown in Fig. 3.14. The first and possibly most important systems to describe are the narrow-linewidth titanium-sapphire (Ti:Sa) commercial ring laser systems, the SolsTiS from M-Squared and the Matisse 2 TS from Sirah. These are pumped by 532-nm continuous-wave (CW) Nd:YAG lasers and both use a series of frequency-selective and cavity-locking devices inside the lasing cavity, alongside the Ti:Sa crystal, to produce continuous-wave light at tunable wavelengths (see Fig. 3.12). The linewidth of both lasers is $< 50\,\text{kHz}$ and the tuning ranges are similar (see Table 3.2), with wavelength-dependent maximum output powers of the order of 1 W.

In the Matisse 2 TS specifically, a mirror set with a limited wavelength-reflectivity range acts as the most coarse frequency-selective element, followed by the birefringent filter which reduces the range of frequencies down to a few 100 GHz. The combination of the piezo-driven thick etalon and solid-state Fabry-Perot etalon result in a final spacing between modes of 160 MHz for the cavity [75]. Light is partially transmitted through an output coupler and a small fraction is sampled into the evacuated reference cavity. This contains two opposing mirrors forming an optical resonator, connected and stabilized by an Invar rod (a metal with an extremely low thermal-expansion coefficient). The intensity of the light transmitted through the reference cell, measured on a photodiode, forms an Airy-function spectrum as a function of the laser-output frequency. The cavity's fast piezo can then be moved in a feedback loop attempting to fix the intensity of the photodiode signal to a position on the side of an Airy-function fringe, thereby locking the laser-output frequency to a fixed value.

Back propagation of light around the lasing cavity is prevented by the unidirectional device. This consists of a terbium-gallium garnet crystal placed in a magnetic field, which rotates the polarization of the light. When combined with the geometrical rotation of polarization from a mirror out of the plane of the rest of the laser, the effect is cancelled out for light propagating anti-clockwise. The rotation increases for light travelling in the opposite direction, meaning this light is dissipated [76].

The SolsTiS laser uses a single mirror set for the entire Ti:Sa tuning range, meaning any wavelength can be reached remotely and without modification of the laser cavity. This is a significant advantage of this laser in terms of time saved in setup. The specific internals of this laser are proprietary, but it likely uses similar frequency selection and locking

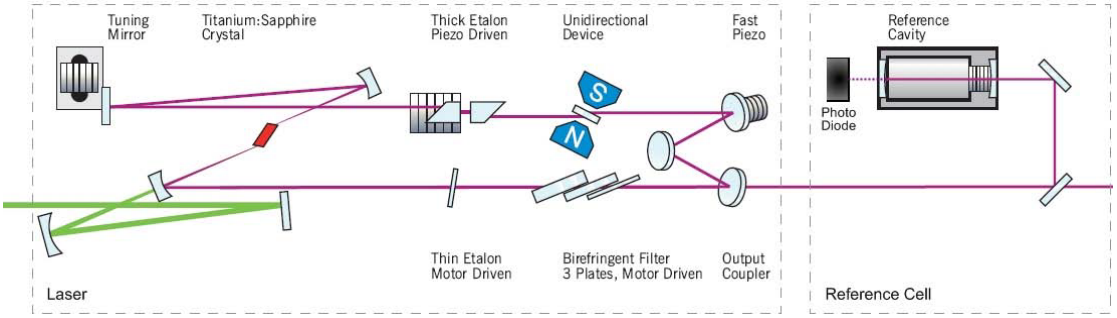

FIGURE 3.12: Schematic layout of the Matisse 2 TS laser. 532-nm light (green) from the pump laser is brought to focus in the Ti:Sa crystal. The stimulated emission is frequency selected using the birefringent filter, thin etalon and thick etalon. The unidirectional device uses the Faraday effect to ensure the lasing mode propagates in the anti-clockwise direction only [76]. After passing through the output coupler, the output light is sampled into the reference cell resonator. The Airy-function spectrum of the resonator is observed on a photodiode and used to lock the cavity fast piezo through side-of-fringe intensity stabilization. The tuning mirror is used to keep the fast piezo in the centre of its dynamic range and for coarse scanning [75]. Reproduced from [75].

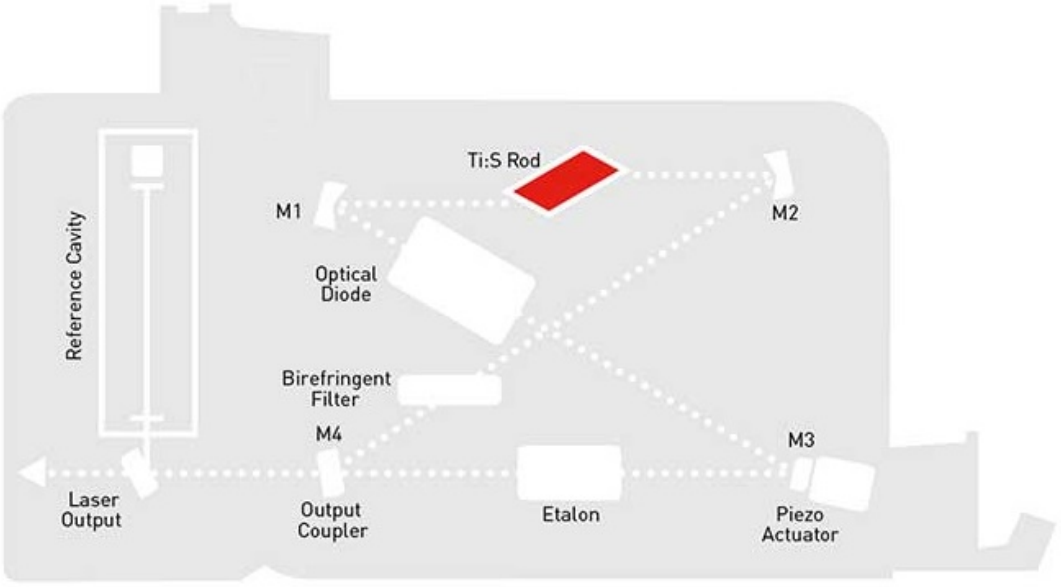

FIGURE 3.13: Schematic layout of the M-Squared SolsTiS laser. The stimulated emission is frequency selected by the birefringent filter and the etalon. The optical diode prevents back propagation of light around the cavity. The output light is sampled into a reference cell, which is likely used to lock the cavity piezo actuator. Reproduced from [77].

techniques to the Matisse. A basic layout of the cavity found on the M-Squared website is shown in Fig. 3.13. This contains a birefringent filter, an etalon, a piezo-actuated mirror, an optical diode, and a reference cavity, similar to the Matisse.

These lasers can be used directly to scan atomic transitions, remotely tuning the lasing frequency in steps to gradually pass over the location of the resonance. However, the CW nature of the laser light means that, without modification, the atoms would continuously interact with the light (when at the resonant wavelength) after neutralisation and before ionisation occurs. Once excited, atoms can decay to any of a number of allowed states with lower excitation energy, with probabilities determined by the transition Einstein-A coefficients [76]. Due to the narrow linewidth of the excitation laser relative to the energy spacing between atomic levels, only the initially probed state can be re-excited, meaning atoms which decay to other states (known as 'dark' states) are lost. The decay lifetimes of excited states chosen for CRIS studies are typically 50-1000 ns. Given the 0.93 m distance between the CEC and the interaction region [78], the flight time of 100-u 40-keV atoms from neutralisation to re-ionisation would be approximately 3 μs, meaning multiple excitation and decay cycles would occur with CW-laser excitation before ionisation. This would result in a significant drop in the number of laser ionised atoms due to the movement of atoms into 'dark' states [79].

This effect is mitigated by intensity modulating the excitation laser periodically to match the repetition rate of the ionisation laser and the ion-bunch release from ISCOOL. Using this method, pulses of excitation laser light are delivered to the CRIS beamline when the atom bunches are in the UHV interaction region. The ionisation-laser pulses are timed to follow these excitation pulses with a delay of the order of 100 ns [79], minimising the decay and loss of atoms to 'dark' states.

The intensity modulation of the CW lasers can be achieved using a Pockels cell [79]. A Pockels cell rotates the polarization of light entering the device when high-voltage is applied. A polarizing beam splitter (PBS) is placed after the cell, reflecting light of one linear polarization and transmitting light with the other. A Behlke high-voltage switch is then used as the voltage source for the Pockels cell to modulate the output polarization and therefore the transmission through the PBS, following a trigger time-synchronised to the rest of the experiment from one of the Quantum Composers units described in Section 3.3.5. The transmitted light is transported to the CRIS beamline and the deflected light is dumped. This technique was utilised in a number of CRIS experimental campaigns including in [80]. A schematic representation of this technique is shown in Fig. 3.16.

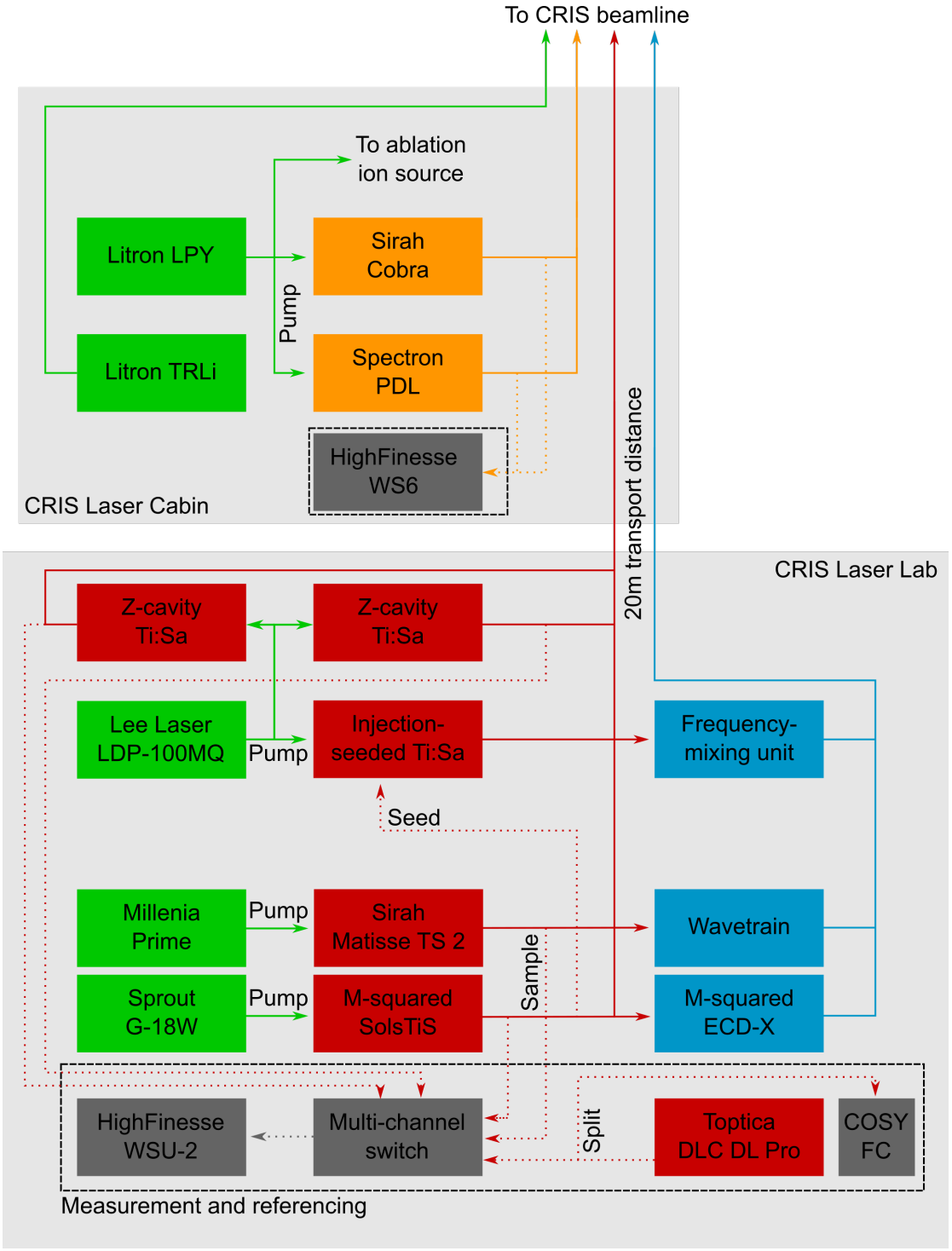

FIGURE 3.14: Schematic connection diagram of the laser systems and surrounding equipment present in the CRIS laser laboratory and in the CRIS laser cabin. Nd:YAG 532-nm systems (green) pump Ti:Sa lasers in the laser lab (red) and dye lasers in the laser cabin (orange). Pick-off mirrors sample the output laser beams. The samples are then transported via optical fibre (dotted lines) for frequency measurement in one of the two HighFinesse wavelength meters. Seed light is also transported to the injection-seeded Ti:Sa from the Matisse or SolsTiS via fibre. Frequency mixing units are shown in blue (see Fig. 4.4). A Toptica diode laser is locked with an external absorption cell (COSY) and is also measured. Light is transported in free space over a distance of 20 m between the laser lab and laser cabin before entering the beamline.

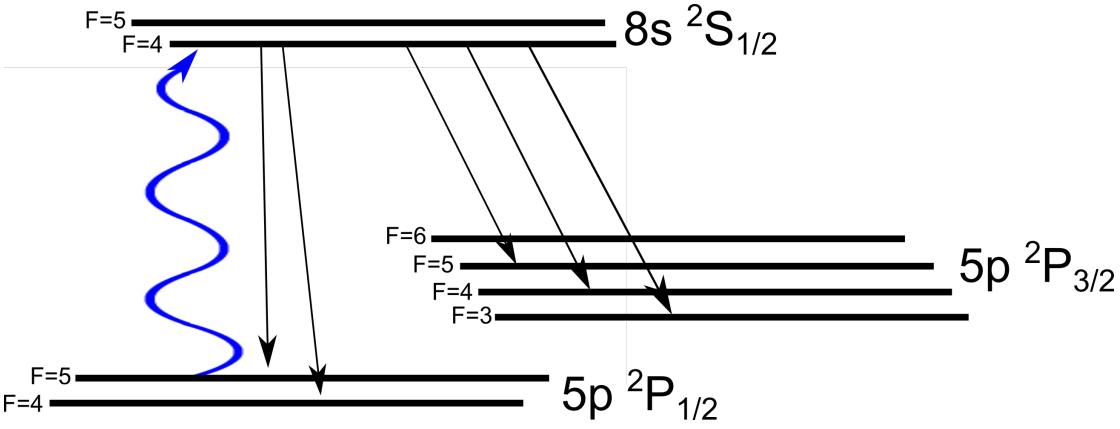

FIGURE 3.15: An example of dark states in an $I^\pi = 9/2^+$ indium nuclear state. If photons continuously excited the transition between the $^2P_{1/2}$ $F = 5$ state and the $^2S_{1/2}$ $F = 4$ state, some excited atoms would decay to the $^2P_{3/2}$ states and the $^2P_{1/2}$ $F = 4$ state (the 'dark' states) and would be lost, reducing experimental efficiency.

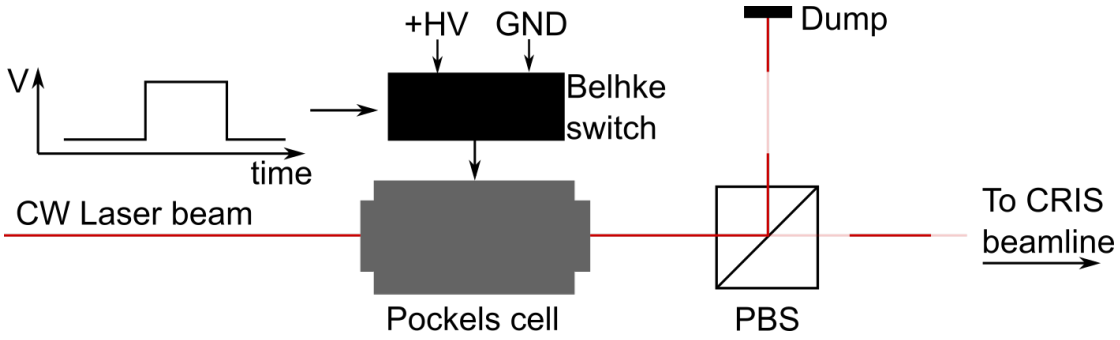

FIGURE 3.16: Intensity modulation of the high-resolution CW lasers. A low voltage pulse drives a Behlke switch, switching between ground and a high-voltage terminal. This activates a Pockels cell, rotating the polarization of a section of the incoming laser light, allowing it to traverse a polarizing beam splitter (PBS) cube.

Alternatively, a few mW of the CW light can be used to 'seed' an injection-locked Ti:Sa system also present in the CRIS laser lab, schematically shown in Fig. 3.17. This bow-tie shaped cavity follows the wavelength of the seed laser via a dither-locking technique. The stimulated emission caused by the seed light is partially transmitted through one of the cavity mirrors and is measured using a photodiode. This photodiode signal is sent to a TEM Laselock Lock-in amplifier which also dithers a piezo connected to another cavity mirror. The dither produces resonances in the photodiode signal where the cavity length matches one of the longitudinal modes of the seed light. The piezo is then moved in a proportional-integral-differential (PID) control locking loop, attempting to maintain a constant photodiode signal at a position on the side of one of these resonances, thereby locking the cavity [81].

The Ti:Sa crystal is pumped using a pulsed Lee Laser LDP-100MQ Nd:YAG laser at 532 nm and variable repetition rate in the range 1-10 kHz. In this arrangement, the spontaneous emission from the Ti:Sa crystal after the pump pulses would saturate the

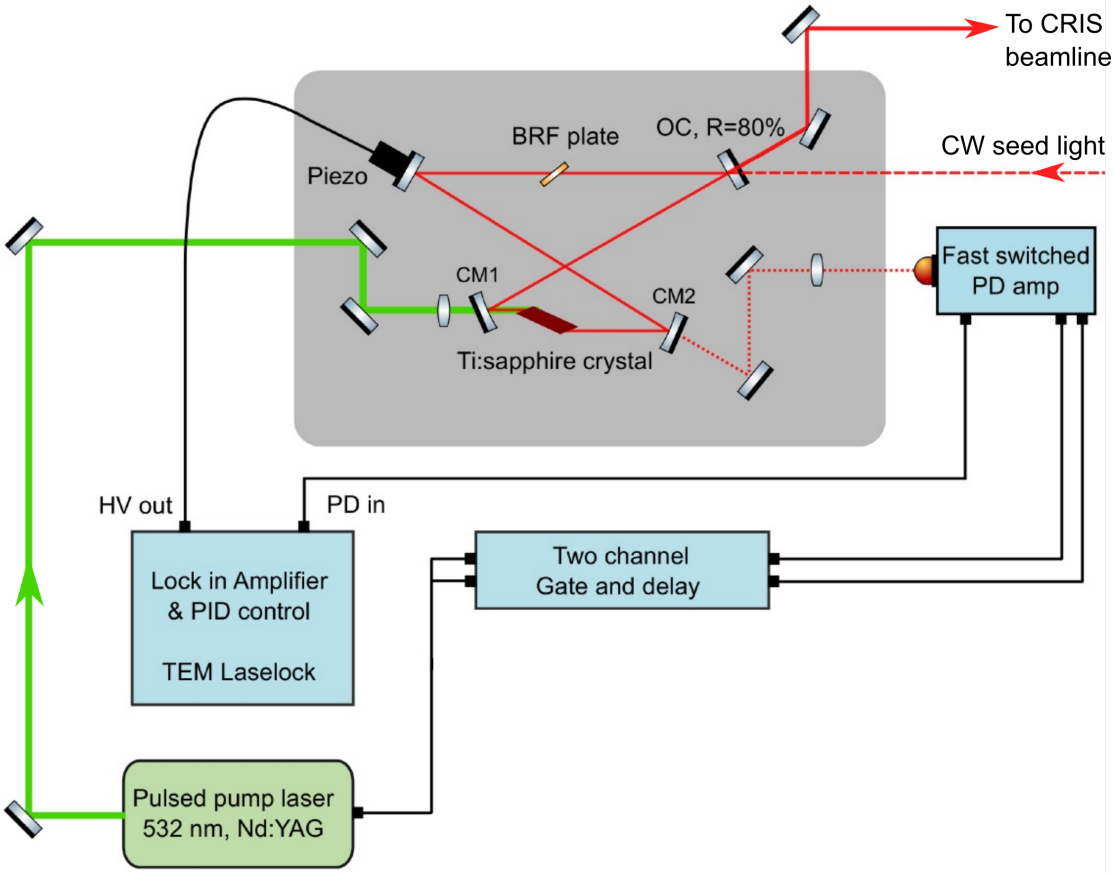

FIGURE 3.17: Schematic outline of the injection-seeded laser cavity. Seed light from a high-resolution CW laser induces spontaneous emission from the excited Ti:Sa crystal. Part of the resultant cavity light is observed behind one of the curved focussing mirrors (CM2) with a photodiode. The amplified photodiode signal is used in a PID loop to dither a piezo mirror and lock the cavity to a single mode. The photodiode is grounded in phase with the pump laser trigger signal, routed through a gate and delay apparatus, to prevent saturation of the photodiode during the pump laser pulse. The resultant pulses pass through an output coupler mirror (OC) and are transported to the CRIS beamline [81]. Adapted from [81].

photodiode. To prevent this (to maintain the cavity lock), the photodiode is grounded during the pump pulse, timed using the pump-laser trigger signal routed through a gate and delay circuit [81].

The output is pulsed, matching the repetition rate of the pump laser, and follows the wavelength of the seed laser, albeit with an increased spectral linewidth of about 20 MHz [82]. The time-averaged power of the output is generally lower than that of the CW seed lasers (see Table 3.2) but the instantaneous photon density during the pulse is approximately four orders of magnitude larger, meaning an atomic excitation step is more likely to be saturated using the injection-locked system compared to an intensity-modulated CW setup.

As described in Section 3.1.2, following this first excitation, resonance ionisation spectroscopy requires options for further resonant excitation to higher-lying atomic states. CRIS has a number of laser systems available to perform this role (see Fig. 3.14). Firstly, a pair of Z-cavity Ti:Sa lasers are present in the CRIS laser lab, also pumped by the Lee Laser Nd:YAG system. These contain an etalon and a birefringent filter for wavelength selection. They have a spectral linewidth of 6-10 GHz and a wavelength tuning range of 680-960 nm [83]. Secondly, a pair of dye lasers, a Spectron Spectrolase 4000 pulsed dye laser (PDL) and a Sirah Cobra, are located near the experimental beamline in what is known as the CRIS laser cabin. These can use a variety of dye compounds in (typically ethanol) solution to produce light over a wide range of wavelengths (approximately 500 - 800 nm). The dye lasers are pumped by 532-nm light from a Litron LPY 601 50-100 PIV system, pulsed at 100 Hz repetition rate. This unit has two independent outputs from two Nd:YAG lasers, each with 8 ns pulse width [73]. The unit can be configured to output fundamental light at 1064 nm with 80 mJ pulse energy, or frequency-doubled light at 532 nm and 50 mJ pulse energy.

The CRIS laser cabin also contains the laser used for non-resonant ionisation of excited atoms. This is a Litron Nano TRLi HR 250-100 pulsed Nd:YAG laser system, operating at 100 Hz repetition rate. This laser can be operated at 1064 nm, 532 nm or 355 nm through the use of detachable higher-harmonic generation units which fix to the front of the laser. The wavelength is chosen to provide the minimum required photon energy to ionise the excited atoms. This ensures that the ionisation efficiency is maximised, while minimising the unwanted non-resonant ionisation of lower-lying states in the atoms of interest and in contaminants.

A summary of all the lasers available at CRIS is given in Table 3.2, with approximate laser powers, spectral linewidths and scanning ranges.

3.3.3 Higher-harmonic generation

As can be seen from Table 3.2, scanning wavelengths can be produced at CRIS in the approximate range 500 - 900 nm using the fundamental output light of the available lasers. To access higher-energy atomic transitions with shorter wavelengths, we must employ higher-harmonic generation. Higher-harmonic generation is a process by which laser photons are combined within an anisotropic crystal at a certain angle relative to the symmetry axis, thereby producing photons at the sum or difference of the input photon frequencies [76]. In second-harmonic generation for example, two photons of the same frequency are combined inside the crystal to produce a single photon with double

Scanning lasers	Wavelength(s) / nm	Linewidth / MHz	Rep. rate / Hz	Power / mW
M-Squared SolsTiS	725 - 960 [77]	< 0.05	CW	6×10^3
Sirah Matisse TS	690 - 1020 [75]	< 0.05	CW	1×10^3
Injection-seeded Ti:Sa	740 - 860	20	1×10^3	150 - 300
Z-cavity Ti:Sa	690 - 940	3×10^3	1×10^3	200 - 250
Spectron PDL	500 - 800	1×10^4	100	50-400
Sirah Cobra	500 - 800	1.8×10^3	100	100
Fixed-wavelength lasers				
Lee Laser	532		1×10^3	7×10^3
Litron LPY	532		100	5×10^3
Litron TRLi	1064/ 532 / 355		100	1×10^4

TABLE 3.2: Summary of the CRIS lasers, detailing the covered wavelength ranges, spectral linewidths, laser pulse repetition rates ('Rep. rate') and time-averaged laser powers [78]. The lasers are separated into those used for scanning atomic transitions and those used for pumping, laser ablation and non-resonant ionisation.

the frequency. The intensity of the resultant light, $I(2\omega)$, follows,

$$I(2\omega) \propto I^2(\omega) L^2 \,\mathrm{sinc}^2\left(\Delta k L/2\right), \tag{3.11}$$

where L is the crystal length, ω is the angular frequency of the incoming beam and Δk is the phase mismatch,

$$\Delta k = k_{2\omega} - 2k_{\omega} = \frac{2\omega}{c}(n_{2\omega} - n_{\omega}). \tag{3.12}$$

The input angle relative to the symmetry axis is therefore adjusted to minimise the difference between the effective refractive indices, $n_{2\omega}$ and n_{ω}, to maximise the intensity of the second-harmonic light [76].

Typically, very high input photon densities are required to produce a usable beam of higher-harmonic light [76]. Pulsed lasers are now typically used at CRIS in a frequency-mixing unit (see Fig. 4.4) for harmonic generation for this reason, with type-I sum second- (SHG) and third-harmonic generation (THG) of light from the injection-seeded system being relatively routine. SHG is also often performed on light from the dye lasers. Alternatively, SHG can be performed on light from the CW SolsTiS or Matisse

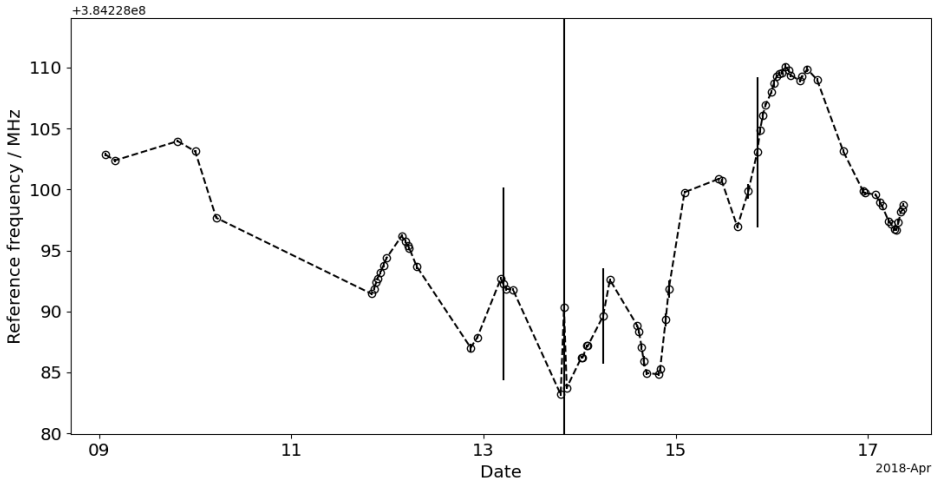

FIGURE 3.18: Variation in the recorded Toptica reference laser frequency over time in the CRIS indium experiment reported in this work. The points show the mean and standard deviation of reference frequencies for each scan. The point with the large error bar shows when the diode laser lost lock during the experiment.

laser inside an M-squared ECD-X or Sirah Wavetrain 2 CW cavity respectively. These contain cavity mirrors which are highly reflective for the fundamental wavelength but highly transmissive for the second harmonic. The cavity is locked to a single mode of the fundamental light to produce the required photon density. More details on higher-harmonic generation at CRIS can be found in [78].

3.3.4 Laser frequency measurement

To construct the hyperfine spectra, precise and accurate frequency monitoring of the scanning lasers is required. This monitoring is performed at CRIS using a pair of High-Finesse wavelength meters (see Fig. 3.14 for further connection details). These use proprietary Fizeau-style interferometers for frequency measurement. The first is a WSU2 model, with 2 MHz specified absolute accuracy [78], which can be used to simultaneously measure up to four laser frequencies in the CRIS laser lab through a four-channel switch. This is primarily used to measure sampled light from one of the CW seed lasers to monitor the resonant excitation frequency when scanning resonances.

A Toptica DLC DL PRO 780 diode laser is simultaneously measured by the WSU2 and is used as a reference. This is frequency-stabilized by locking to a Doppler-free hyperfine absorption line of atomic caesium, potassium or rubidium in a compact saturation absorption cell (COSY FC-CS+RB+K) [78], thereby providing a constant reference wavenumber for later correction of any wavelength-meter measurement drift in the measurement of the scanning lasers.

The second wavelength meter is a WS6 model used to measure the frequency of one of the dye lasers in the CRIS laser cabin, with 200 MHz quoted absolute accuracy in the dye laser wavelength range [84]. The wavenumber values from both wavelength meters are continuously recorded to .csv files with timestamps while scanning.

3.3.5 Timing

The lasers used in CRIS experiments are typically pulsed at repetition rates above 100 Hz. It is therefore necessary to precisely control the temporal overlap of the ion bunches and the laser pulses, in addition to the sequencing of the excitation and ionisation laser steps. At the CRIS experiment, this is controlled by a set of Quantum Composers 9520 digital-delay pulse generators. These pulse generators provide digital trigger signals with 250 ps timing resolution. The 1 kHz Q-switch transistor-transistor logic (TTL) pulse of the Lee Laser system is used as the 'master' trigger for the experiment; the pulse generators, connected in sequence, are triggered on this signal, adding some delay before releasing the ion bunch, initialising the data acquisition and firing the laser pulses. More details on the specific timing arrangement for the indium experiment are given in Section 4.1.3.

3.3.6 The CRIS ion source

In addition to the ISOLDE ion sources described in Section 3.2.1, CRIS can also receive ion beams from an independent ion source (CRISIS) located at the entrance to the CRIS beamline. This is placed at 90° relative to the main line (see Fig. 3.11 and Fig. 3.19); when in use an electrostatic bend is inserted to deflect the ions into the main line. The CRISIS can be operated either as a surface ion source, where the source material is heated to form a vapour before it is ionised via collisions with the heated cavity casing (resistive heating with a 25 V, 40 W DC current), or as an ablation source.

When in ablation mode, a high-power pulsed laser is focused onto the surface of the material, creating plumes of atoms and ions due to the high fluence. The 1^+ state can then be selected with the electrostatic transport. The ablation laser is typically one head of the Litron LPY Nd:YAG system described in Section 3.3.2, pulsed at a repetition rate of 100 Hz. In both cases, the ion source is floated at a high potential of 20-30 kV, accelerating ions through electrostatic focusing and bending elements to the beam energies required for collinear laser spectroscopy. In surface-ionisation mode the ion beam is continuous, while in ablation mode the ion beam is pulsed following the repetition rate and timing of the ablation laser, controlled using the Quantum Composers (see Section 3.3.5) to precede the spectroscopy lasers.

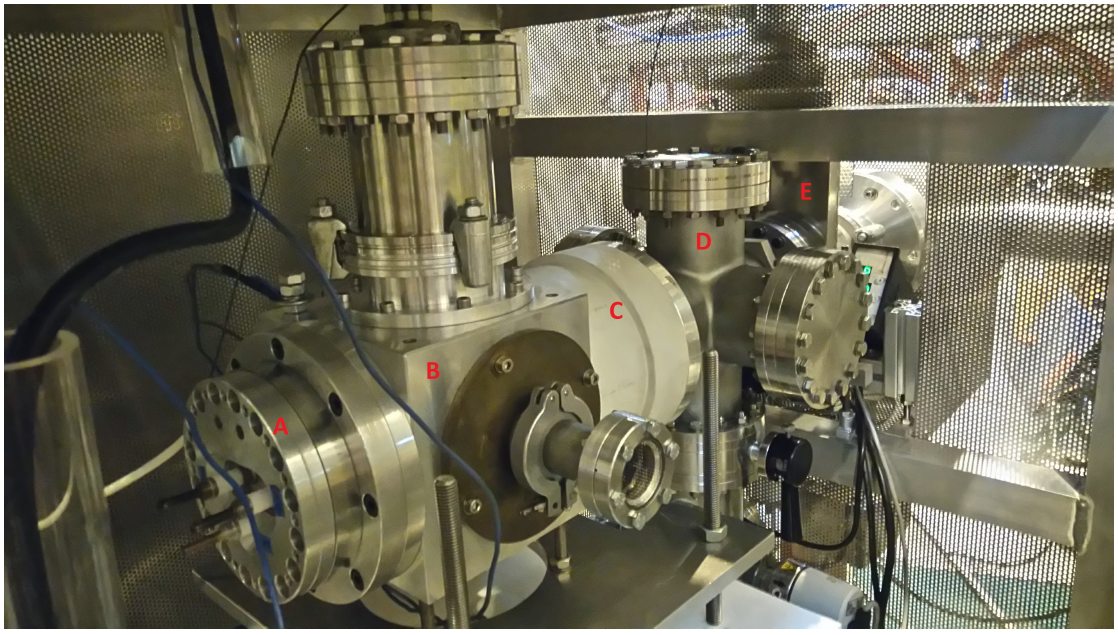

(A) Vacuum assembly and Faraday cage: A - surface ion source, B - chamber with laser windows containing the ablation target, C - ceramic voltage isolation piece separating the grounded and 20-30 kV chambers, D - 6-way cross with turbomolecular pump, E - gate vacuum valve to isolate the ion source volume when not in use. Reproduced from [85].

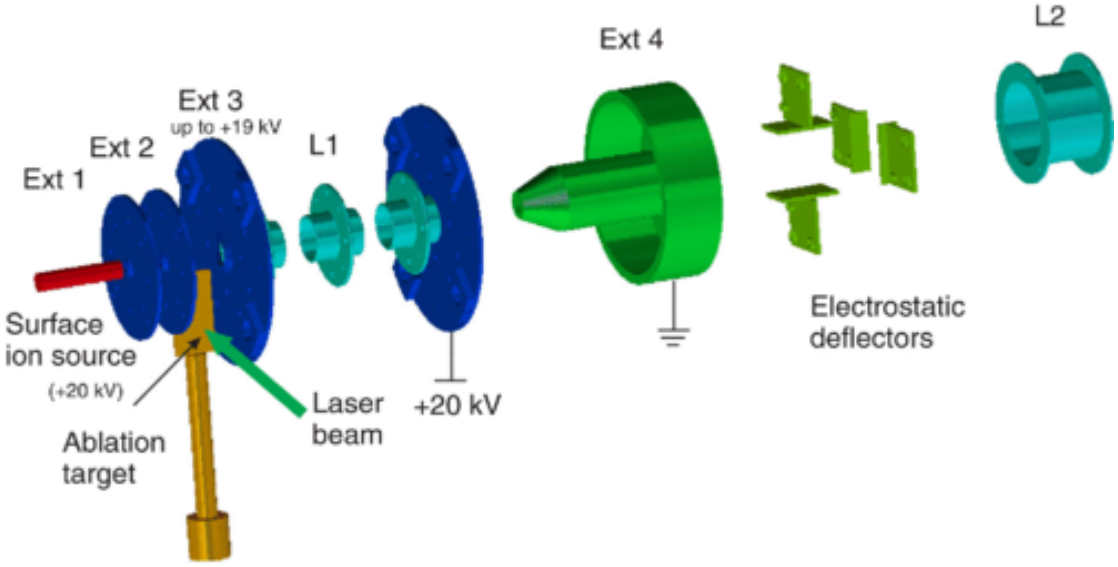

(B) Electrostatic elements: L1 - central Einzel lens electrode, Ext 4 - Grounded acceleration electrode, L2 - external Einzel lens electrode. Figure reproduced from [27].

FIGURE 3.19: CRIS ion source (CRISIS).

In both modes, macroscopic samples of the elemental species of interest are required, meaning only stable or long-lived isotopes can be studied. Target material containing the natural isotopic abundances for the particular element is typically used, and as no magnetic mass selection is present in this mode, the ion beam neutralised and probed with the lasers contains all the stable isotopes in their natural relative abundances. Depending on the range of masses present, some mass selection can be possible through the differences in time of flight of the beam components, seen as separate arrival-time bunches in the event-by-event ion-counting data acquisition system. However, this selection method is limited due to the short flight distance ($\approx 4\,\mathrm{m}$) of the ions relative to their energy and the width of arrival time peaks ($2(1)\,\mu\mathrm{s}$). When distinct arrival time peaks are present, their masses can be approximately determined through the use of a second charged-particle detector, present in the main section of beamline after the charge exchange cell. The distance, L, between this detector and the main CRIS detector is known, meaning the difference in recorded arrival time on the detectors, Δt, for the particular beam component can be used in,

$$m = 2E\left(\frac{\Delta t}{L}\right)^2, \tag{3.13}$$

to determine the approximate mass given the ion kinetic energy, E.

All other aspects of the operation of the CRIS beamline, through neutralisation, laser excitation and ionisation, and detection, are identical to the operation of an experiment using ion beams from the ISOLDE HRS ion source.

Chapter 4

Laser spectroscopy of neutron-deficient indium

A CRIS experimental campaign was carried out between the 9th and 16th April 2018 on the neutron-deficient indium isotopes. The isotopes studied covered the mass-number range between ^{101}In and the stable ^{115}In. The isotopes ^{112}In and ^{114}In were not studied due to time constraints and because these had been measured in previous work [15, 24]. Two nuclear states were observed in each isotope, a ground state and a single long-lived isomeric state, except for in ^{101}In and ^{102}In, where only one state was observed, and for ^{115}In, where the proton beam was turned off so only the stable ground state was observed. The measured intensity ratio of the isomeric $I^{\pi} = 1/2^{-}$ states in the odd-even indium isotopes relative to the ground states varied between 0.01 and 0.03. This was determined by comparing the sum of peak counting rates for all resonances belonging to each nuclear state. The ratio for the odd-odd indium isomeric states varied between 0.1 and 0.2, generally decreasing with neutron number. Periodic measurements of ^{115}In were taken throughout the campaign so that the centroid and hyperfine parameters in this isotope could be used as a reference, to correct for measurement drifts in data analysis (see Section 4.2.1).

This chapter details the specific experimental configuration used during the neutron-deficient indium campaign, including specific operational details concerning the ISOLDE facility (Section 4.1.1), the laser schemes employed (Section 4.1.2), and efficiency considerations (Section 4.1.4). This is followed by a full account of the analysis process (Section 4.2), working from the raw data to the final reported nuclear observables.

4.1 Experimental configuration

4.1.1 ISOLDE

To produce indium ions, a 1.4 GeV beam of protons from the CERN PSB was impinged on a thick LaC_2 target (target number 640) at the ISOLDE HRS, inducing spallation reactions [86]. The proton beam was pulsed, with pulses separated by 1.2 s. Between 9 and 13 pulses were sent to the HRS target in a super-cycle of 24 or 31 pulses. The time-averaged proton current varied between 1.22 μA and 1.9 μA, with between 2.7×10^{13} and 3.3×10^{13} protons per pulse, through the course of the experiment. The target was heated with 520 A current and the transfer line was heated with 270 A current. The resultant indium ions diffused through the heated target ($\approx$ 2000 °C) to be released into the transfer line and ion source; the expected release efficiency of indium isotopes with >5 s half-life (true for all isotopes measured in this work [87]) was estimated to be >85 % [86]. The indium ions were then resonantly excited and ionised by the RILIS lasers in the following arrangement.

A Credo dye laser containing DCM dye in ethanol solution was used for the first resonant excitation step, alongside a tunable Z-cavity Ti:Sa laser. 100 mW of light at 325 nm was produced after frequency doubling the dye laser. This was used to excite the atoms from the $5s^2\ 5p\ ^2P_{3/2}$ metastable state in indium to the $5s^2\ 5d\ ^2D_{5/2}$ state (see Fig. 4.1). The Ti:Sa laser was frequency tripled to produce light at 304 nm with 100 mW power, which was then used to excite from the $5s^2\ 5p\ ^2P_{1/2}$ ground state to the $5s^2\ 5d\ ^2D_{3/2}$ state. Following this, a Lumera Blaze Nd:YVO4 40 W laser at 532 nm was used to non-resonantly ionise the excited indium atoms. All the lasers were pulsed at 10 kHz repetition rate.

Due to the target heating, indium and beam contaminants were also surface ionised. Table 4.1 shows the enhancement effect on the overall ion-beam current using resonant ionisation over surface ionisation alone. Exciting from both atomic metastable states resulted in an overall RILIS enhancement factor of 30 (relative to when only the ionisation laser was present) when measured for ^{115}In. The table also shows the non-resonant background effect of the lasers, due to the increase in surface ionisation from localised laser heating of the transfer line.

The ions were then accelerated to 40 keV and the mass of interest was selected using the HRS (see Section 3.2) [63]. The mass-selected ions were then trapped in the ISCOOL radio-frequency quadrupole cooler buncher. The platform voltage of ISCOOL was continuously monitored using a PTB voltage divider, connected to a National instruments analog-to-digital converter, in turn connected to the CRIS data acquisition system via

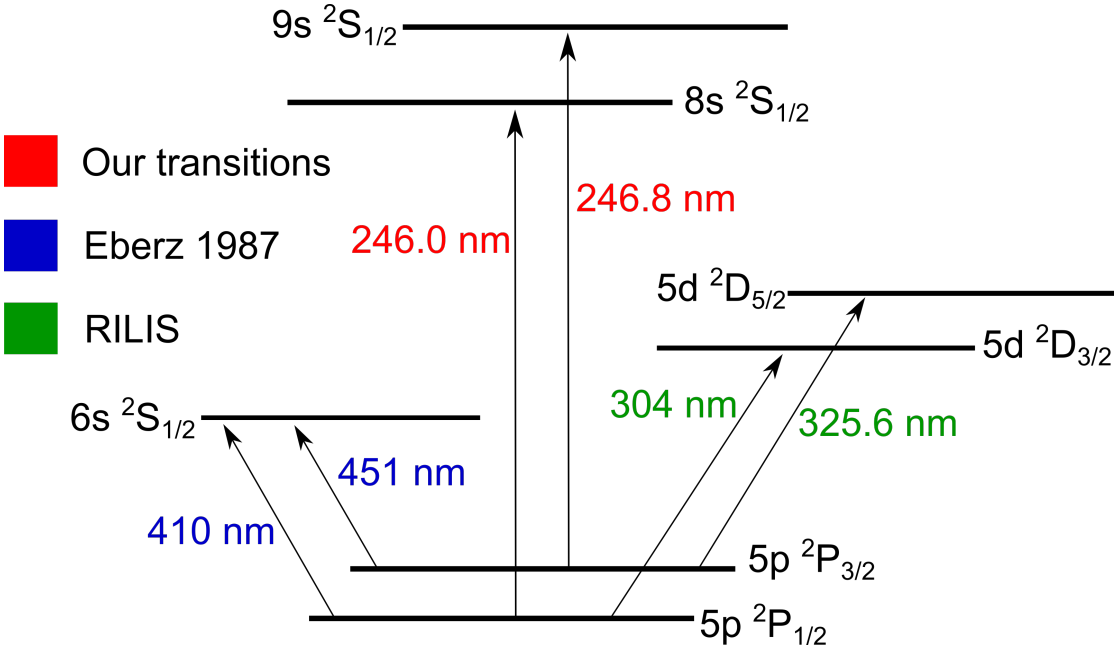

FIGURE 4.1: Resonant laser excitation schemes used in this work and in literature to excite indium atoms, showing the level configurations and transition wavelengths. The transitions labelled in green were used simultaneously by the RILIS collaboration for resonant excitation inside the ISOLDE ion source. The transitions labelled in red were probed in high resolution in the CRIS beamline to extract the hyperfine structures of the levels. The blue transitions were used for hyperfine structure studies of indium by Eberz et al. [15].

Ti:Sa	Dye	Nd:YVO4	Ion beam current, YHRS.FC490 / pA
No	No	No	4
Yes	No	No	12
No	No	Yes	24
No	Yes	Yes	440
Yes	No	Yes	650
Yes	Yes	Yes	800

TABLE 4.1: Total ion-beam current measured after ^{115}In mass selection with different RILIS laser configurations. Significant non-resonant background is caused by the Blaze Nd:YVO4 40 W laser and the Z-cavity Ti:Sa. A factor 30 increase in beam current is seen using resonant excitation. Exciting from both atomic metastable states in indium (Ti:Sa + dye) results in a 24 % enhancement of beam current over exciting from the ground state alone (Ti:Sa).

TCP/IP connection where values were recorded to .csv files with timestamps. The uncertainty on the recorded values was ± 1 V at 40 kV from the systematic uncertainty on the voltage-divider ratio. The ions were periodically released at 100 Hz repetition rate (chosen to match the repetition rate of the CRIS Litron in Section 4.1.2) forming bunches of ions with temporal width of 1.6(2) μs (mean and standard deviation of measured Gaussian TOF profiles). Further details on ISCOOL and the HRS are given in Section 3.2.

4.1.2 CRIS lasers

For this work, two different first-step atomic transitions in indium were used based on results of studies of the stable isotopes with the CRISIS [27] and were the same as those used in an experiment on the neutron-rich isotopes [24]. The transition between the ground $5s^2\ 5p\ ^2P_{1/2}$ state and the $5s^2\ 8s\ ^2S_{1/2}$ state (see Fig. 4.1) at 246.0 nm, was chosen due to its relatively small HFS splitting, $A_{\mathrm{hf}}^{115}(5p^2P_{1/2}) = 2281.9501(4)$ MHz [88] and $A_{\mathrm{hf}}^{115}(8s^2S_{1/2}) = 243.85(31)$ MHz [27], allowing for the full structure to be scanned for each isotope within a manageable amount of time. The typical time required for a scan of this transition varied significantly between isotopes, being approximately 15 minutes for ^{115}In and two hours for ^{101}In. Additionally, in the odd-mass isotopes, a clear separation was observed between the nuclear ground states with $I^\pi = 9/2^+$ and the isomeric states with $I^\pi = 1/2^-$. This meant the resonances were more clearly resolved so the hyperfine parameters and centroids for the isomeric states could be more accurately extracted, resulting in more accurate values for the magnetic moments and changes in mean-square charge radii. An example spectrum in this transition for ^{113}In is shown in Fig. 4.2.

The second transition employed, between the metastable $5s^2\ 5p\ ^2P_{3/2}$ state and the $5s^2\ 9s\ ^2S_{1/2}$ state, was at 246.8 nm. This also had a relatively small HFS splitting and similar scanning times but, unlike the first transition, it had sensitivity to the nuclear quadrupole moments through the hyperfine-B splitting of the lower $J = 3/2$ state.

For both transitions, the fundamental light from the M-squared SolsTiS Ti:Sa CW laser system, sampled to 1 mW laser power, was used to seed the injection-locked laser cavity [82] described in Section 3.3.2. The laser used to pump the injection-locked cavity was an LDP-100MQ Lee Laser doubled-Nd:YAG at 532 nm, 1 kHz pulse-repetition rate and 1.3 mJ pulse energy.

The emitted pulses from the injection-locked cavity were then passed through the unit schematically shown in Fig. 4.4 to produce the third-harmonic light. The tripling was

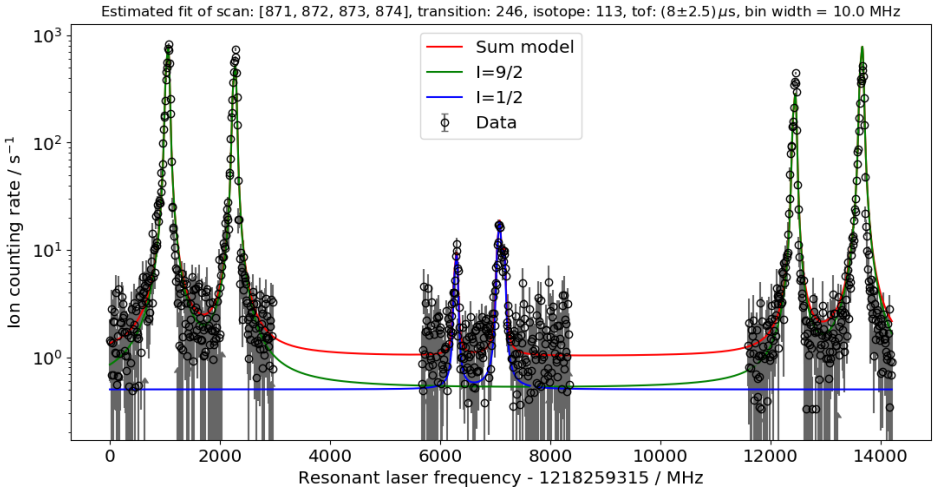

FIGURE 4.2: Example scanning-laser frequency vs ion counting rate data for ^{113}In measured with the $5s^2\ 5p\ ^2P_{1/2}$ to $5s^2\ 8s\ ^2S_{1/2}$ transition (experimental data as black points). An estimated model (unfitted, red line) is also plotted, containing the sum of resonances from the $I^\pi = 9/2^+$ nuclear ground state (green line) and the $I^\pi = 1/2^-$ isomeric state (blue line). The ground- and isomeric-state peaks are clearly separated, allowing for accurate fitting of the lower-rate isomeric HFS. The laser frequency plotted is offset from the true rest-frame value by the value given in the x-axis label.

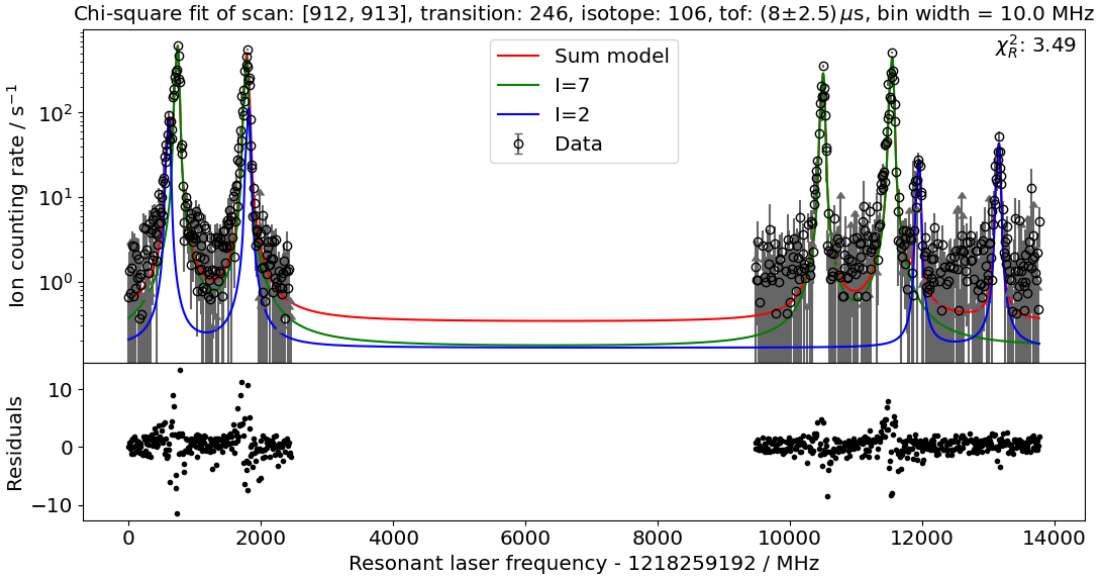

FIGURE 4.3: An example fitted spectrum of the 246.0-nm transition ($5s^2\ 5p\ ^2P_{1/2}$ to $5s^2\ 8s\ ^2S_{1/2}$) for ^{106}In. The $I^\pi = 2^+$ HFS (blue line) is convoluted with the $I^\pi = 7^+$ HFS (green line). The binned data (black points) are fitted to the sum of the two models (red line). The residuals are shown in the lower pane as black points. The reduced chi-square of the fit is $\chi^2_R = 3.49$. The fitted Gaussian FWHM was $\Gamma_G = 35.3(12)$ MHz and the fitted Lorentzian FWHM was $\Gamma_L = 15.3(6)$ MHz.

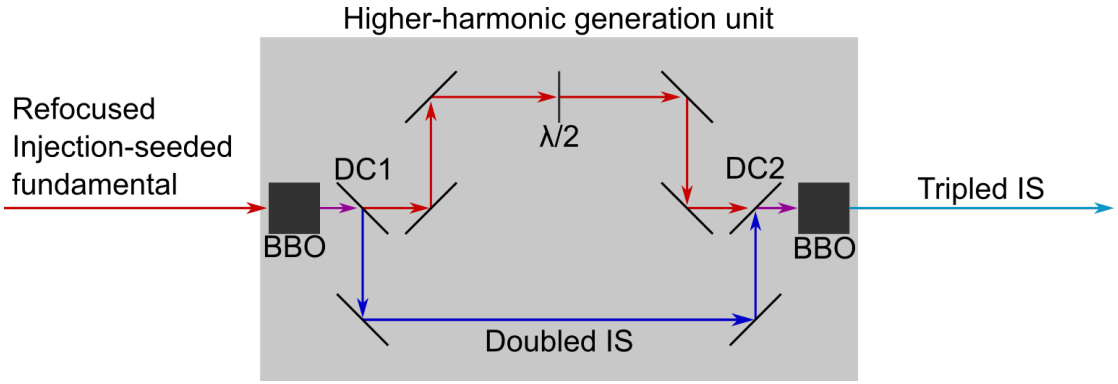

FIGURE 4.4: Diagram of the third-harmonic generation unit used in the indium experiment. The doubled light was produced by passing the fundamental injection-seeded light through a BBO crystal. The two components were separated using a dichroic mirror (DC1). The fundamental light was passed through a tunable half-wave plate ($\lambda/2$) to phase-match the two components. The components were then recombined using a second dichroic mirror (DC2) and sent into a second BBO crystal to produce the tripled light.

achieved by first frequency doubling the pulsed light using a non-linear beta-barium-borate (BBO) crystal at the correct phase-matching angle. The fundamental and second-harmonic components were then separated using a dichroic mirror and the polarisation of the fundamental was rotated using a half-wave plate, $\lambda/2$, to match that of the second harmonic. The two beams were then recombined in another BBO crystal to produce the third-harmonic light at the desired scanning wavelength [78]. The laser-power conversion-efficiency ratios for the experiment were approximately $3\nu : 2\nu : \nu = 1 : 20 : 70$. The tripling unit was developed as part of the work described in [78] but the specific configuration for the indium experiment formed part of this work.

Atoms excited into the higher-lying states were non-resonantly ionised using 1064 nm pulses from a Litron TRLi 250-100 Nd:YAG laser at 100 Hz pulse repetition rate and 10 mJ pulse energy, measured after passing through the CRIS beamline.

4.1.3 CRIS beamline

The ion bunches from ISCOOL were electrostatically focussed and guided into the main section of the CRIS beamline where they were neutralised with sodium vapour in the CEC. The CEC temperature varied between 300 °C and 340 °C during the experiment. The atom bunches were next overlapped with the injection-seeded laser and 1064 nm laser pulses (see Section 4.1.2) in the interaction region. The pressure in this region was $1.95(5) \times 10^{-9}$ mbar during the experiment.

Ions produced in the interaction region were then deflected through the final 20 ° bend and impinged directly onto an ETP MagneTOF detector. This ion detector uses an

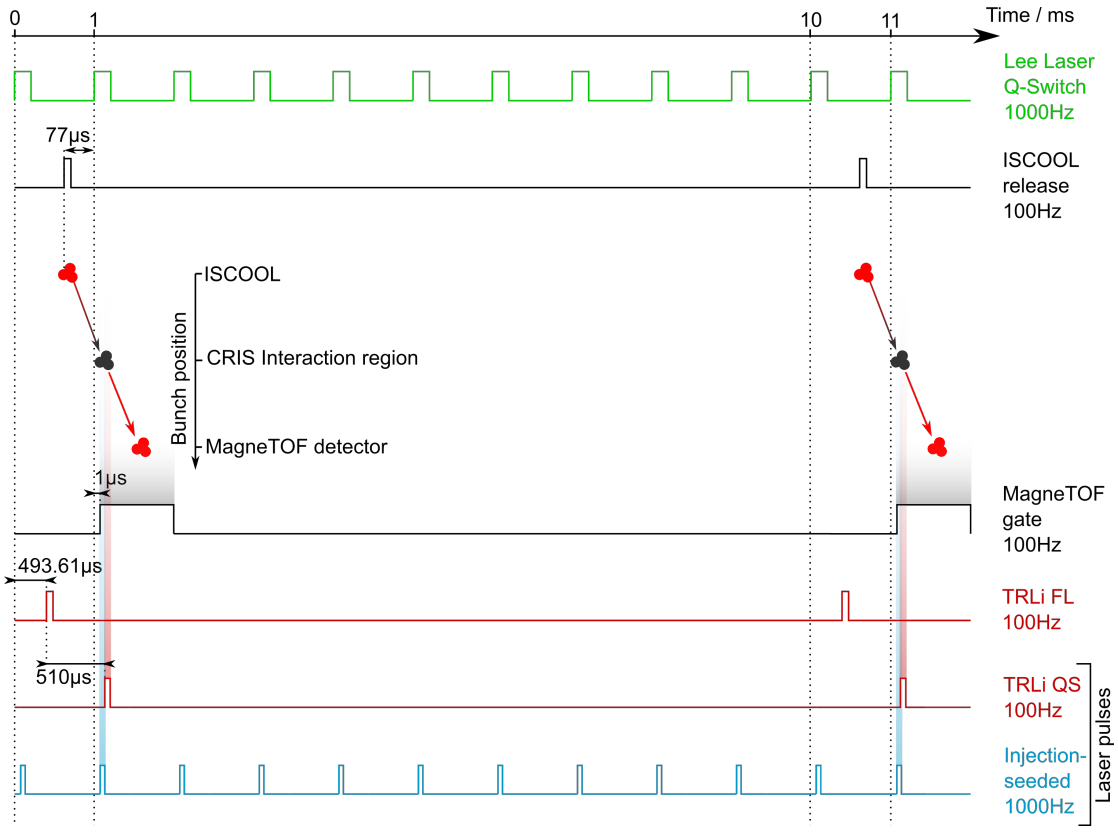

FIGURE 4.5: Time synchronisation during the indium CRIS experiment described in this work. The Lee Laser Q-switch was used as the master trigger, defining time zero, t_0. The ISCOOL ion-release trigger was 77 μs before the following Lee Laser pulse so that the atoms were in the CRIS interaction region when the next injection-seeded pulse fires. The fixed 510 μs offset between the Litron TRLi flashlamp (FL) trigger and Q-switch (QS) defined the 493.61 μs delay of the flashlamp relative to t_0, so that this laser also fired when the atoms were in the interaction region. The Data acquisition started recording 1 μs after the second Lee Laser pulse to collect the ionised bunch atoms.

electron-multiplier-style design to produce signal pulses from the detection of single ions with a quoted FWHM of < 1 ns [48]. The ion pulses were then amplified using a NIM module and used to trigger an AC-coupled stop channel on a Cronologic TimeTagger4-2G-PCIe time-to-digital converter (TDC). This digitised and recorded the individual ion signals to .csv files with a timing resolution of 500 ps and low pulse-to-pulse deadtime of 1 ns.

The Lee Laser Q-switch trigger TTL signal was used to trigger the time-synchronisation Quantum composers unit in the CRIS laser lab, defining time zero, t_0. This unit was connected via coaxial cable to the two similar units next to the experimental beamline in series. A single pulse in ten adjacent t_0 pulses was used to initiate the ion-bunch release from ISCOOL, the data-acquisition PCIe card and the TRLi Nd:YAG ionisation laser. The bunch release was delayed 923 μs relative to t_0 so that the ion bunch was present in the CRIS interaction region when the subsequent resonant-excitation laser

pulse arrived. The time offset between the flashlamp and the Q-switch in the Litron TRLi ionisation laser was defined at 510 μs by the manufacturer to allow for sufficient population inversion build-up. The flashlamp was therefore delayed by 493.61 μs relative to t_0, allowing for the ionisation pulse to enter the beamline after the excitation step, 3.61 μs after the second Lee Laser Q-switch signal. The delay between the excitation and ionisation steps was set using a photodiode connected to an oscilloscope, triggered by one of the Quantum Composers units, showing the laser pulses. Unfortunately the precise final delay between the two laser pulses was not recorded. The data-acquisition start signal was delayed 1001 μs relative to t_0, allowing for the collection of ion signals from the ion bunch. A schematic layout of these timing signals is shown in Fig. 4.5.

4.1.4 Efficiency and background

When estimating the total efficiency of the CRIS experiment, ε, defined as the rate of resonantly-ionised ions detected on the MagneTOF divided by the ion current delivered to the beamline, we must consider a number of factors. These are primarily: electrostatic transmission through the beamline ε_t, neutralisation efficiency ε_n, the relative population of the atomic state of interest after neutralisation ε_p, laser-ionisation efficiency ε_L, and final ion-detection efficiency ε_d. As an equation, this becomes

$$\varepsilon = \varepsilon_t \varepsilon_n \varepsilon_p \varepsilon_L \varepsilon_d \tag{4.1}$$

The ion-transport efficiency, ε_t, is difficult to determine precisely. The differing design of the ISOLDE and CRIS Faraday cups means the captured ion currents cannot be accurately compared. Estimated currents indicated an optimised transport efficiency from after the ISOLDE HRS separator to the CRIS interaction region of $\varepsilon_t \approx 80\,\%$.

The total efficiency of neutralisation from ions to atoms was measured at the start of the experiment. This was done using a Faraday cup after the CEC and an electrostatic deflector, but before the 20 ° bend. With voltage applied to the deflector, only the secondary electrons caused by the impact of the atoms on the Faraday cup contributed to the recorded current. Without this voltage, the direct ion current and secondary electrons caused by these ions also contributed to the current. Assuming the number of secondary electrons produced per ion and atom impact was 2 and 3 respectively, the neutralisation efficiency was estimated to be $\varepsilon_n = 20\,\%$ at 300 °C. The relative population of the $5s^2\ 5p\ ^2P_{1/2}$ and $5s^2\ 5p\ ^2P_{3/2}$ states relative to the total neutral-atom number is predicted (from simulation) to be $\varepsilon_p = 37\,\%$ and $\varepsilon_p = 57\,\%$ respectively [74], as shown in Fig. 4.6.

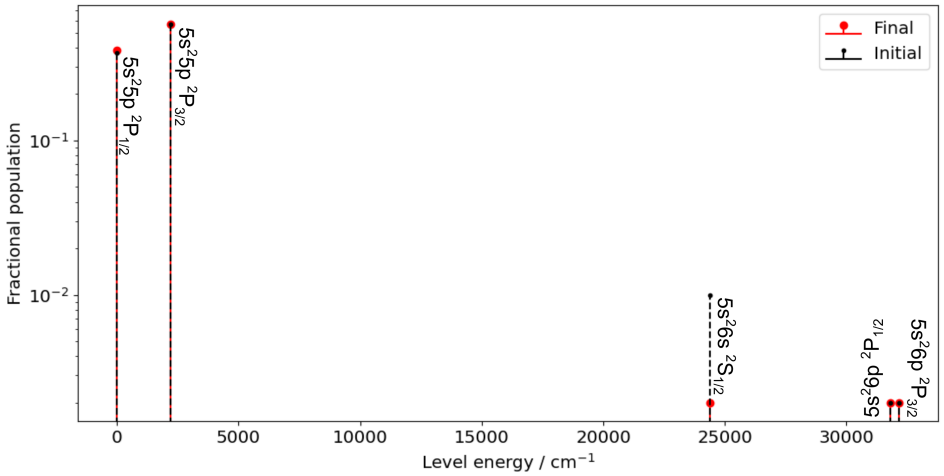

FIGURE 4.6: Logarithmic plot of the simulated fractional population of labelled atomic states in indium after neutralisation. The black stems show the initially populated states, while the red stems show the predicted final population after 1.2 m of further flight, i.e. when the atoms have reached the interaction region. Values taken from [74].

The detection efficiency of the ETP MagneTOF ion detector is specified as $\varepsilon_d = 80\,\%$, with main losses coming from the electrostatic-field-grid transmission and those expected from Poisson counting statistics [48].

When at the resonant laser frequency of the 246.8 nm laser step with ^{115}In, no significant effect was observed on the ion-counting rate of reducing the power of the 1064 nm ionisation laser by 50 %, indicating that the non-resonant ionisation process was saturated. Unfortunately, a similar power reduction was not performed for the first step laser meaning the efficiency of the excitation step is not known. Assuming the laser excitation and ionisation efficiency is close to saturation, i.e. that $\varepsilon_L \approx 100\,\%$, combining the efficiency factors results in $\varepsilon(246.0\,\text{nm}) = 3.0\,\%$ and $\varepsilon(246.8\,\text{nm}) = 4.6\,\%$.

The main part of the observed background in the CRIS experiment arises from unwanted ionisation of neutral particles in the region between the electrostatic deflectors after the CEC and the 20 ° bend. This can occur due to collisions with residual gas in this region, through non-resonant laser ionisation or through field ionisation of high-lying electronic states in the strong electric-field region around the 20 ° bend. Smaller contributions to the background include dark counts or the decay of nearby radioactive species triggering the detector.

Table 4.2 shows the recorded variation in background rate for ^{115}In under different conditions. Introducing the scanning and ionisation lasers to the beamline seem to have no significant effect on the background, indicating that collisional and/or field ionisation are the dominant background sources. Furthermore, applying a strong electric field after

Ti:Sa	1064 nm	Transverse voltage / V	Background rate / s^{-1}
On	Off	0	30
Off	On	0	30
On	On	0	30
On	On	4000	21
On	On	5000	19

TABLE 4.2: Effect of the CRIS lasers and transverse voltage on the scanning background rate (gated on the TOF bunch) for ^{115}In at the start of the experiment, with 3.5 pA beam current at the entrance to the CRIS beamline. 'On' indicates the lasers present in the beamline. The scanning Ti:Sa laser was 460 MHz $\approx$ 20 FWHM away from resonance. There was no laser on/off effect on the background rate for either laser, meaning the background is not caused by non-resonant ionisation at this mass. However, applying a large transverse field to the ion beam after the CEC reduces the background by a factor of 1/3, indicating that this background is caused by neutral particles residing in high-lying electronic states which can be field-ionised.

the CEC reduces the observed background rate by a factor of a third, indicating that part of the background species can be field ionised.

An additional background contribution which was observed in scans of ^{101}In formed resonant structures in the spectra found to not arise from a radiogenic source. It has been suggested that these resonances could have arisen from the excitation of transitions in stable molecular components of the ion beam close in frequency to the indium excitation transitions. The identification of the ^{101}In resonances is discussed in more detail in Section 4.2.5.

An attempt was made to measure ^{100}In in this experiment. However, it was found that the lanthanum-carbide target used in the experiment mistakenly contained a large sample of molybdenum for prior testing purposes. Molybdenum has a stable isotope at $A = 100$ which formed a large isobaric contaminant. Two-photon non-resonant ionisation of the molybdenum was possible with the UV first-step excitation laser; this process formed the main background contribution at $A = 100$ and meant spectroscopic measurement of ^{100}In was impossible.

For future experiments, it is also worth considering non-beam related background effects such as the decay of nearby radioactive contamination in the beamline. Fig. 4.7 quantifies this background contribution, showing the variation in background recorded per second of scanning time per micro-second of recording time outside the time-of-flight (ToF) window around the arrival time of the bunch. This background appears to have increased significantly over the course of the experimental campaign, reaching order of $10^{-2}\,s^{-1}\,\mu s^{-1}$ at the end of the experiment, indicating a build-up of radioactivity at the end of the beamline being seen on the MagneTOF detector. Given a typical ToF window of 5 μs, this would add a background component of 0.05 s^{-1} to all indium isotopes,

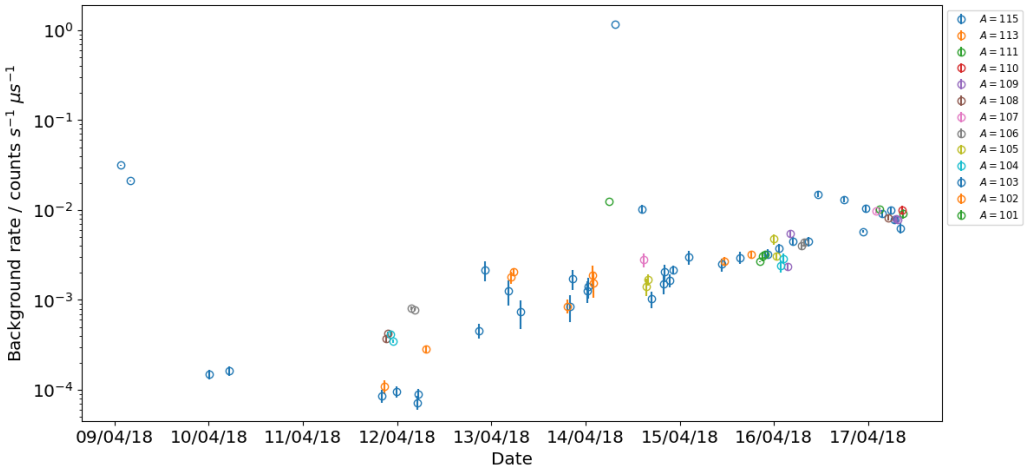

FIGURE 4.7: Background counts recorded outside of ToF gates around the ion bunches for all scans (isotopes given by the marker colour). The counts are normalised to the total scanning time in seconds and to the width of the ToF recording window in micro-seconds. The background rate scale is logarithmic. This non-bunch related background increased over the course of the experiment, most likely due to the build up of radioactive species on the neutral-beam dump at the beamline laser-exit window.

which is significant for the most exotic isotopes such as ^{101}In, where the total fitted background rate was $0.06\,\mathrm{s}^{-1}$.

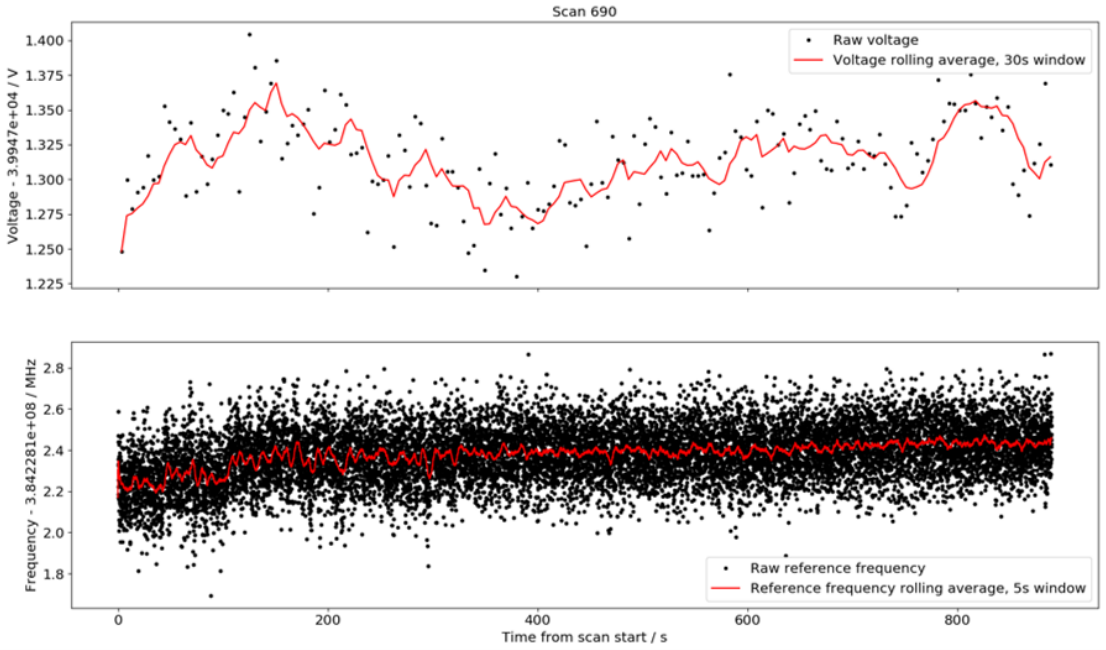

FIGURE 4.8: An example of the results of the application of rolling-average filters (red lines) to the recorded ISCOOL voltages (black points, top) and the recorded diode correction frequencies (black points, bottom). A 30 s window was used for the ISCOOL voltage and a 5 s window was used for the diode correction frequency. These are data recorded for a single scan of ^{115}In in the 246.8 nm transition.

4.2 Data analysis procedures

4.2.1 Data processing

Data values from the various .csv data sources (the laser wavenumbers, the ISCOOL voltage, the proton impacts and the digitized ion-counting signals) were first concatenated and sorted by timestamp to create a single Python pandas DataFrame object [89].

The ISCOOL voltage and diode-correction wavenumber were recorded throughout the experiment to keep track of variations in their values on time scales of the order of a few minutes, arising from temperature and humidity variations, and the voltage supply in the case of the ISCOOL voltage. As the rapid fluctuations on shorter time-scales are not considered to be representative of true variations in recording, a rolling average of 30 s on the ISCOOL voltage and 5 s on the diode-correction wavenumber were taken. Fig. 4.8 presents an example of the application of these rolling averages for voltage and frequency data from a single scan. A scanning wavenumber, a diode-correction wavenumber and an ion energy was then assigned to each ion-count event by taking the most recently recorded value (if a previous value was not available, i.e. for the first set of events, the next recorded value was taken). A value was recorded for the ISCOOL voltage on average every 5.09(1) s and for the wavenumbers every 0.03(2) s on average.

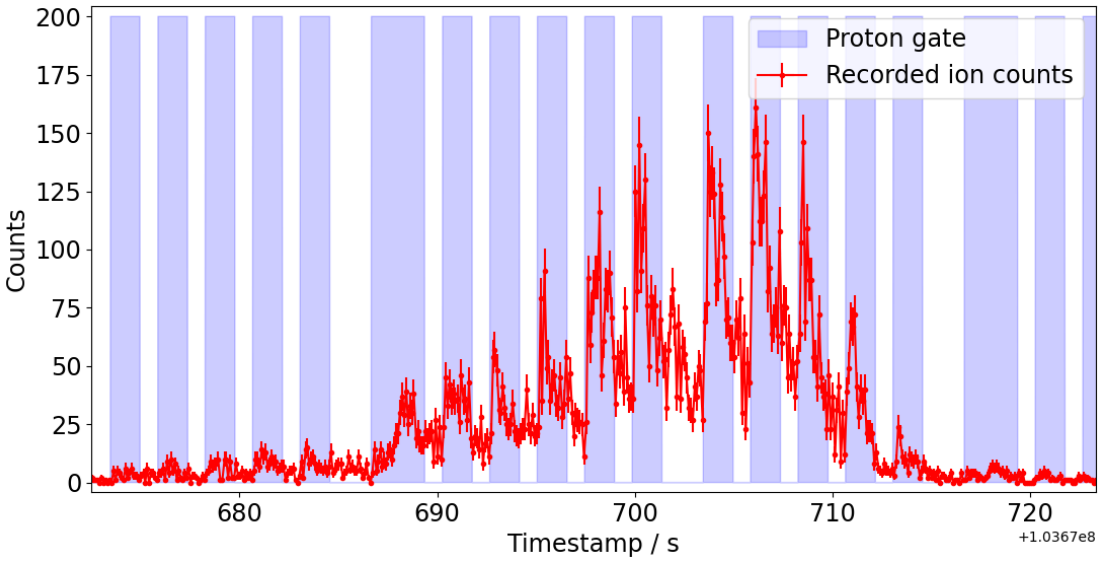

FIGURE 4.9: Recorded counts over time for a segment of a scan of the 246.0-nm transition in ^{103}In (red points), binned with a 0.1 s bin width. Data for fitting the spectra are taken from the blue shaded regions. The leading edge of each 'gate' is determined from the timestamp of the previous proton impact with some delay, each gate having a fixed width. Gates are allowed to overlap in time.

The time difference between each ion count and the previous proton impact was then calculated, minus a delay of 1 s to allow for the release of the radioactive ions from the ISOLDE target. The time position of the proton impacts was determined from the BTY.BCT.325:TOTAL_INTENSITY variable from the CERN accelerator logging service, accessed through the Python pytimber module. This time was then used to reject ion-count events which occurred outside a fixed time window after the previous proton impact. Fig. 4.9 shows the number of detected ion counts binned in time while traversing a single resonance in the 246.0-nm ionisation scheme for ^{103}In. The pulsed time structure can be seen, correlated with the leading-edge time of the proton-impact gates.

Non-ion-counting rows were then removed, leaving a DataFrame with an event Boolean (event or no event), a timestamp, a time of flight (if an event occurred, -1 otherwise), a scanning wavenumber, a correction wavenumber, an ion energy and a time since the most recent proton impact.

A drift in the correspondence between the recorded wavenumber values and the 'true' wavenumber of the laser is expected over the course of the experiment. To account for this, a correction factor of the form

$$\bar{\nu}^{\text{scan}}_{\text{true}} = \left(\alpha \frac{\bar{\nu}^{\text{diode}}_{\text{true}} - \bar{\nu}^{\text{diode}}_{\text{raw}}}{\bar{\nu}^{\text{diode}}_{\text{raw}}} + 1 \right) \bar{\nu}^{\text{scan}}_{\text{raw}} \tag{4.2}$$

was applied to the scanning wavenumber, where the calibration value for the diode wavenumber, $\bar{\nu}^{\text{diode}}_{\text{true}}$, was taken as the first recorded value in the experiment, and the α parameter was assigned for each transition to account for differences in frequency drift at different laser wavenumbers. The process of determining this correction factor, α, for the two different transitions is described in Section 4.2.4.

A data collection time for subsequent rate calculations was then assigned to each event Boolean by taking the difference in timestamp between the timestamp-sorted rows. An upper limit of 1 s was set for this collection time. The events exceeding this limit were assigned zero collection time. This prevented problems arising when data sets taken at very different times were combined into a single spectrum.

Given the event-by-event timing information, a further timing gate could then be applied to the data to remove background counts recorded outside a narrow time window around the arrival time of the ion bunch. This was done by manually selecting the bunch-arrival-time region for each scan and setting the event Boolean for counts with time of flight outside this region to false, thus removing the count but keeping the data-collection time contribution at that laser frequency. Fig. 4.10 includes an example counting histogram of the ion arrival time relative to the start trigger of the data-acquisition system, with an overlayed band indicating the selected bunch-arrival-time region. This gate was crucial in the removal of the large, frequency-independent background signal caused by the electronic noise from the Q-switch of the ionisation laser, which introduced a large spike in counts at a well-defined time preceding each bunch arrival time.

A Doppler correction of the form found in Equation 3.1 was then applied to convert from lab-frame scanning wavenumbers, $\bar{\nu}^{\text{scan}}_{\text{lab}}$, to event wavenumbers in the rest frame of the atom, $\bar{\nu}^{\text{scan}}_{\text{rest}}$, when it was interacting with the lasers. Here we write the speed relative to the speed of light (Equation 3.2) as,

$$\beta_j = \sqrt{1 - \left[\frac{m_A c^2}{V_j + m_A c^2}\right]^2}, \tag{4.3}$$

where V_j is the energy assigned to the particular event (indexed by j) from the ISCOOL voltage data and m_A is the mass of the isotope being studied with atomic weights taken from the periodictable Python module containing data from [90], ignoring isomer excitation energies.

The range of scan frequencies was then divided into equal-width regions, each being 10 MHz wide. Each event was then assigned to one of these bins (indexed by i). The event laser frequencies $\nu_{i,j}$, times $\delta t_{i,j}$, and Booleans $C_{i,j}$ for each bin were then aggregated, taking the mean laser frequency and the sum of the events and times. The binned

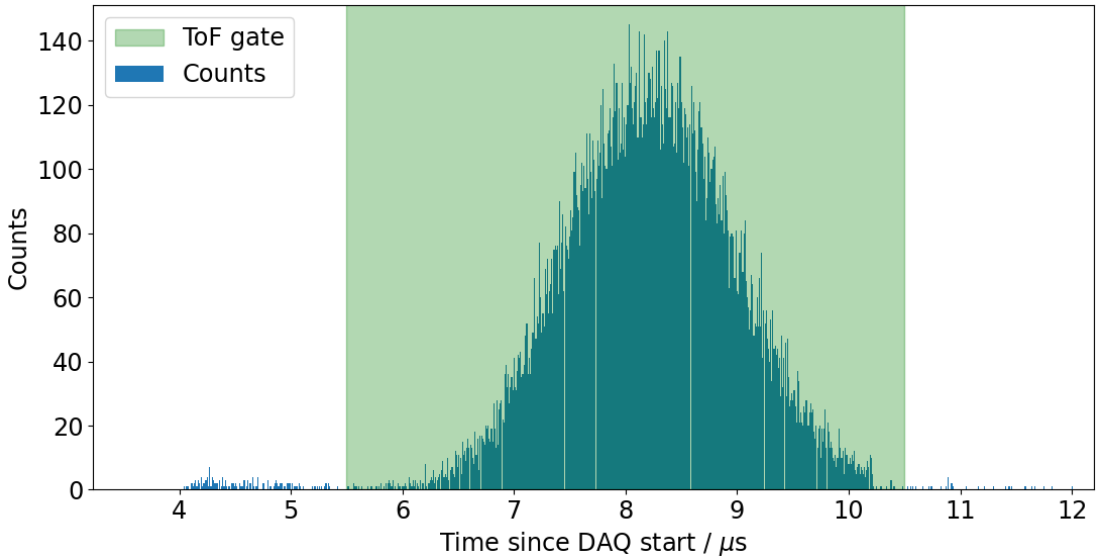

(A) An example histogram of recorded ion time of arrival, measured relative to the start trigger of the data acquisition system (experimental data as blue bars). The counts recorded outside the green band (labelled as 'ToF gate') are discarded before plotting the frequency spectrum and before fitting.

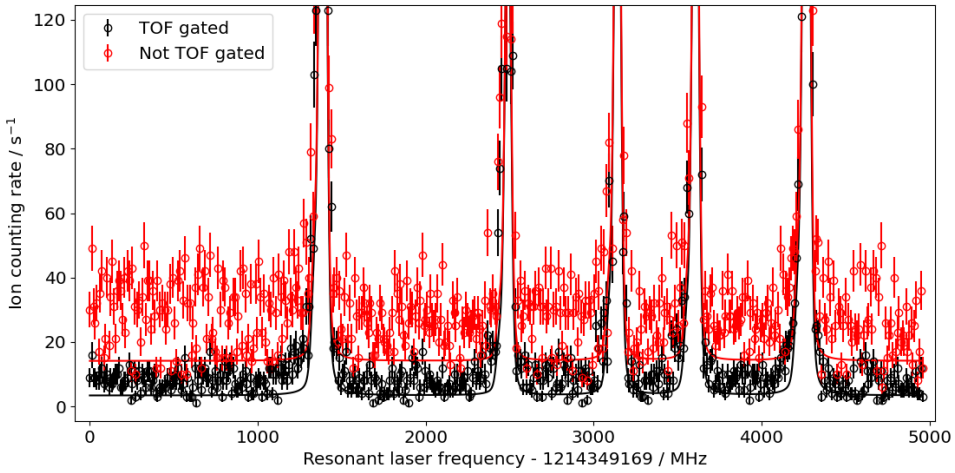

(B) Effect of the ToF gate on the spectrum through the removal of the Q-switch noise. The red points are binned data without the ion time-of-arrival gate. The black points are binned data with the gate.

FIGURE 4.10: Example data from a HFS scan of the $5s^2\ 5p\ ^2P_{1/2}$ to $5s^2\ 8s\ ^2S_{1/2}$ transition in ^{115}In.

counting rates, y_i, were defined as

$$y_i = \frac{\sum_j C_{i,j}}{\sum_j \delta t_{i,j}} \qquad \sigma\left(y_i\right) = \frac{\sqrt{\sum_j C_{i,j}}}{\sum_j \delta t_{i,j}}. \tag{4.4}$$

The uncertainty on the binned laser frequency was taken as the standard deviation of the event laser frequencies in each bin.

4.2.2 Model creation

The SATLAS data analysis package [91] was used for the creation of hyperfine structure models, fitting and the extraction of model parameters. To create the model, the centre of mass of the resonant structure was first estimated using literature values for the excitation frequency from the NIST Atomic Spectra Database [92]. Next, hyperfine parameters, A_A^k and B_A^k, for the upper and lower atomic states (indexed by k) in the studied nuclear states, were estimated based on literature or extrapolated values of the dipole and quadrupole moments from [15] (μ_A and Q_A respectively), with the relationships,

$$A_A^k = \frac{\mu_A I_{115}}{\mu_{115} I_A} A_{115}^k, \tag{4.5}$$

and,

$$B_A^k = \frac{Q_A}{Q_{115}} B_{115}^k, \tag{4.6}$$

where I_A is the assumed nuclear spin for the isotope, A. The hyperfine parameters, A_{115}^k and B_{115}^k, for ^{115}In were determined from stable-beam studies at CRIS in [27]. Given these values and the total angular momenta of the two electronic states, the hyperfine splittings between the different F states were estimated within a SATLAS HFSModel object based on the equations given in Section 2.2.1.

A Voigt resonant lineshape was used throughout this work to account for both the Lorentzian and Gaussian components of the lineshape. The Voigt profile, $V(\nu)$, is a convolution of a Gaussian and a Lorentzian profile given by,

$$V(\nu;\Gamma_G,\Gamma_L) = \int_{-\infty}^{\infty} G(\nu';\Gamma_G) L(\nu-\nu';\Gamma_L)\, d\nu', \tag{4.7}$$

which evaluates to,

$$V(\nu;\Gamma_G,\Gamma_L) = \frac{2}{\Gamma_G}\sqrt{\frac{\ln 2}{\pi}}\Re(w(z)), \tag{4.8}$$

where $w(z)$ is the Faddeeva function, Γ_L and Γ_G are the FWHMs of the Lorentzian and Gaussian components respectively, and

$$z = \frac{\sqrt{2\ln 2}(\nu + i\Gamma_L/2)}{\Gamma_G}. \tag{4.9}$$

The Gaussian component arises from inhomogeneous broadening, specifically from the Doppler-broadening effect due to the ion-bunch energy spread. The Lorentzian component comes from both the natural linewidth of the atomic states and laser power broadening [76].

The resonance peaks in this work also exhibited asymmetry, which can appear from a number of different mechanisms. In measurements of copper isotopes at CRIS, this effect was assigned to the overlap of the excitation and ionisation lasers in time [11, 12, 79]. However, here (and in all measurements subsequent to those in copper) the two laser steps were delayed with respect to one another in time, to prevent the large electric field of the ionisation laser from distorting the excitation lineshape, a technique which was shown to be effective in removing the asymmetry in copper [5, 11, 12, 79].

The main contributions are therefore understood to arise from the neutralisation process and from collisional excitation. In charge exchange, the indium atoms are neutralised into a variety of electronic states, the majority being in the ground and metastable 5p states, with a small ($\sim 1\%$) component in the 6s $^2S_{1/2}$ state and the remaining atoms distributed amongst the higher-lying states (see Fig. 4.6) [74]. Depending on the final atomic state, a differing amount of energy is transferred to the alkali atom in the neutralisation process. This means a discrete lower-energy component of the ion bunch is created, leading to a secondary resonance separated in lab-frame frequency by the Doppler effect [73].

Collisions of the neutralised atoms with residual gas particles in the interaction region can also excite the atoms [93]. These collisions also remove energy from the atoms, adding to the lower-energy ion-bunch component when these atoms decay before laser interaction.

A secondary peak for each hyperfine structure component was added to the models at a fixed negative offset in frequency to account for these effects. The frequency offset was calculated for both transitions from the energy difference between the 6s state and the lower 5p state of the transition. The intensity of the secondary peak relative to the main peak was allowed to vary during the fitting process. An example of a resonance with a corresponding secondary peak fitted to ^{115}In data is shown in Fig. 4.11.

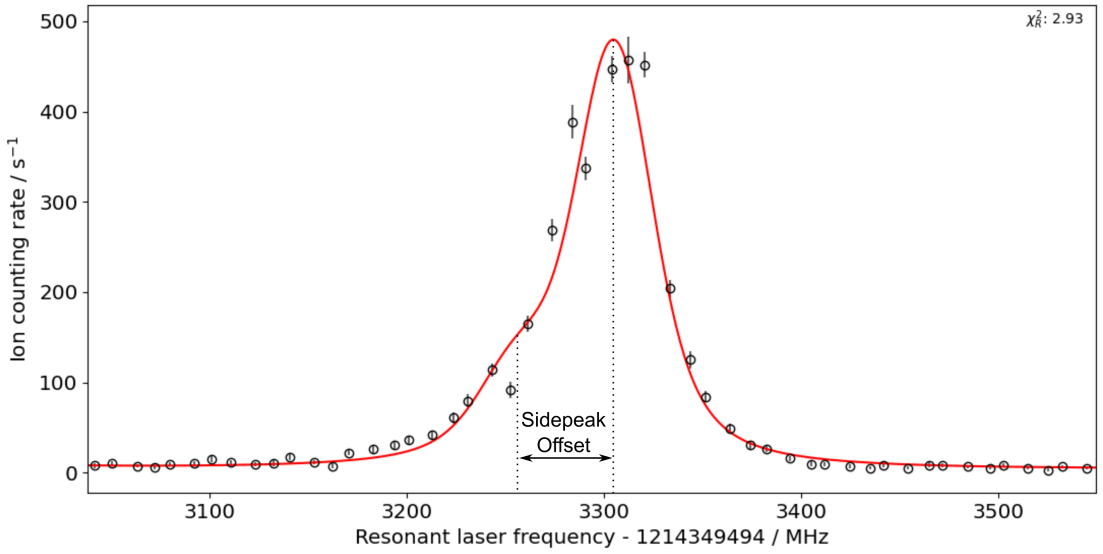

(A) 246.0 nm, ^{115}In

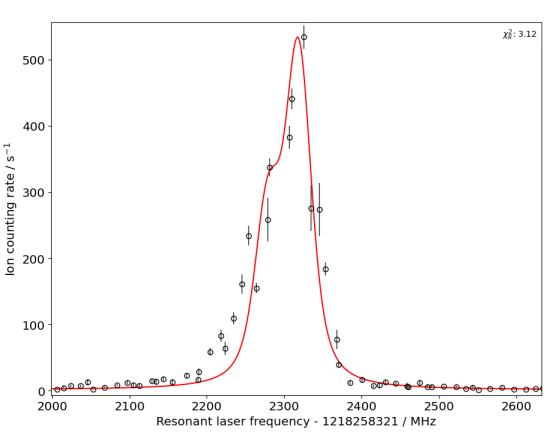

(B) 246.0 nm, ^{107}In

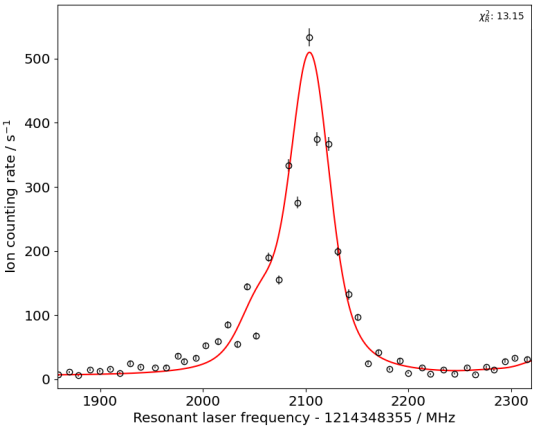

(C) 246.8 nm, ^{104}In

FIGURE 4.11: Example of parts of fitted spectra showing the secondary reduced-intensity peak, arising from the neutralisation process and from collisional excitation, offset at lower frequency relative to the main resonance. Individual figures are labelled with the associated atomic transition and isotope.

Additional excitation-decay cycles from extra collisions can also occur. The distribution of the number of collisions is given by a Poisson distribution dependent on the vacuum pressure and the length of the region where these collisions are possible. This gives rise to additional equally-spaced peaks with decreasing amplitude. These additional resonances were not considered here, however, because a single secondary peak produced the best fit of the measured spectra.

When multiple nuclear states were present in a spectrum, a SATLAS SumModel was created coupling individual models from each of the nuclear states. The individual model frequency centroids, hyperfine parameters, and peak amplitudes were left free in the fitting process as these are independent variables between the different nuclear states. However, the values for the background rate, the Gaussian and Lorentzian FWHMs,

and the secondary-peak intensity ratio were shared between the models because these values depended on the vacuum and laser conditions rather than the nuclear state being scanned.

4.2.3 Fitting the models to the data

The hyperfine structure models were fitted to the binned laser frequency vs. ion-counting rate data using a chi-square minimisation algorithm in SATLAS [91]. A Levenberg-Marquardt algorithm from the LMFIT Python package [94] within SATLAS was used. This applies a gradient method for parameter variation to minimize the cost function

$$\chi^2 = \sum_i r_i^2 = \sum_i \left(\frac{y_i - f(\nu_i)}{\sigma(y_i)} \right)^2 \tag{4.10}$$

where $f(\nu)$ is the defined model and r_i are the residuals. The reduced chi-square, $\chi^2_R = \chi^2/n$, where n is the number of degrees of freedom, can be used as a measure of the goodness-of-fit, with a value of $\chi^2_R = 1$ indicating the level of deviation between the model and the data is in accord with the data variance.

Generally, all model parameters are allowed to vary freely during the fitting. However, in scans of the 246.8-nm transition between the $5s^2\ 5p\ ^2P_{3/2}$ and $5s^2\ 9s\ ^2S_{1/2}$ levels for the odd-mass indium isotopes, the $I = 1/2$ HFS were contained within the $I = 9/2$ structure (see Fig. 4.12), meaning extraction through free fitting of both hyperfine-A values for the $I = 1/2$ state in this transition was not possible. Instead, the A_{hf} value of the upper state was constrained to fix its ratio to the A_{hf} value of the lower state. Using Equation 2.32, the ratio chosen was the weighted mean of A-ratios in ^{115}In for the 246.8-nm transition from stable-beam studies [27], studies of the neutron-rich indium isotopes [95] and values from this analysis. This value was chosen because a literature measurement of the upper-state hyperfine parameter with higher precision could not be found.

4.2.4 Wavemeter-drift compensation

As explained in Section 4.2.1, before fitting the hyperfine spectra, a correction factor (see Equation 4.2) must be applied to the recorded laser wavenumbers in order to account for temporal drifts in the relationship between the 'true' and the raw recorded values. An additional scaling parameter, α, was included in the correction factor to account for any difference in wavemeter response at different laser wavelengths. A series of measurements of ^{115}In spectra were taken over the course of the experiment, the alpha

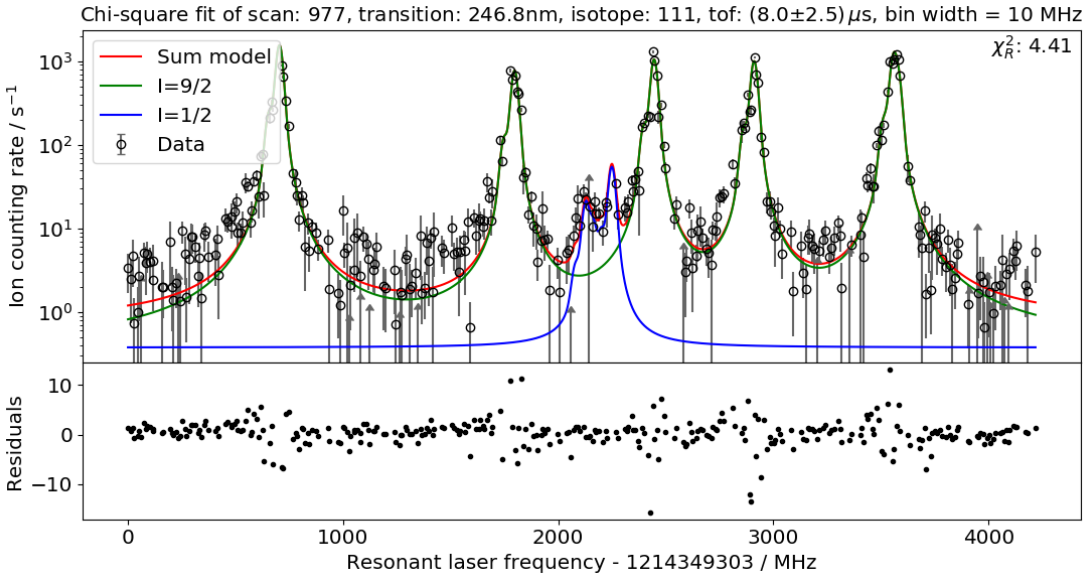

FIGURE 4.12: An example fitted spectrum of the 246.8-nm transition ($5s^2$ $5p$ $^2P_{3/2}$ to $5s^2$ $9s$ $^2S_{1/2}$) for ^{111}In. The $I^\pi = 1/2^-$ HFS (blue line) is convoluted with the $I^\pi = 9/2^+$ structure (green line). The binned data (taking a $8.0 \pm 2.5\,\mu$s ToF gate) are shown as black open circles and the sum of the two HFS models is shown as a red line, this is fitted to the data. The residuals, $r_i = (y_i - f(\nu_i))/\sigma(y_i)$ (see Equation 4.10), are shown in the lower pane as black points. The reduced chi-square (see sub-Section 4.2.3) of the fit is $\chi^2_R = 4.41$. The fitted Gaussian FWHM was $\Gamma_G = 31.0(8)$ MHz and the fitted Lorentzian FWHM was $\Gamma_L = 12.5(4)$ MHz. The total fitted FWHM was $\Gamma_{\text{tot.}} = 38.2(6)$ MHz.

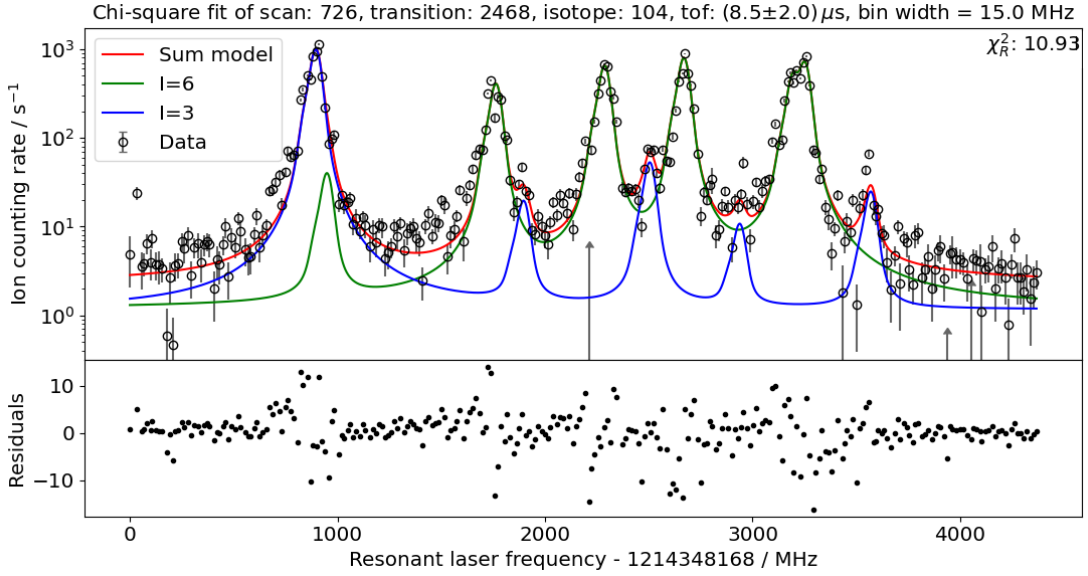

FIGURE 4.13: An example fitted spectrum of the 246.8-nm transition ($5s^2$ $5p$ $^2P_{3/2}$ to $5s^2$ $9s$ $^2S_{1/2}$) for ^{104}In. The $I^\pi = 3^+$ HFS (blue line) is convoluted with the $I^\pi = 6^+$ HFS (green line). The binned data (black points) are fitted to the sum of the two models (red line). The residuals are shown in the lower pane as black points. The reduced chi-square of the fit is $\chi^2_R = 10.93$. The fitted Gaussian FWHM was $\Gamma_G = 42.0(14)$ MHz and the fitted Lorentzian FWHM was $\Gamma_L = 24.5(8)$ MHz.

parameters for each of the two transitions studied were varied to minimise the scatter, $\sigma(\nu)$, of the fitted centroids of these scans where,

$$\sigma(\nu) = \frac{1}{\sum_{n=1}^{N} 1/\sigma_n^2} \frac{1}{N-1} \sum_{n=1}^{N} \frac{(\nu_n - \bar{\nu})^2}{\sigma_n^2}. \tag{4.11}$$

Here, N is the number of reference scans for the transition and $\{\nu_n, \sigma_n\}$ are the fitted centroids of those scans for a particular value of α. Minimal scatter was found for the 246.0-nm transition ($5s^2\ 5p\ ^2P_{1/2}$ to $5s^2\ 8s\ ^2S_{1/2}$) with $\alpha = 1$ and for the 246.8-nm transition ($5s^2\ 5p\ ^2P_{3/2}$ to $5s^2\ 9s\ ^2S_{1/2}$) at $\alpha = 1.5$. These values were used subsequently to correct all scanning data for the two transitions.

4.2.5 Peak identification in ^{101}In

After combining the data from multiple scans of each transition in ^{101}In, many resonances were observed in addition to the presumed ground-state peaks. At first it was unclear if these peaks belonged to previously unobserved isomeric nuclear states in ^{101}In, or if they arose due to an isobaric contaminant at that mass number. To distinguish between these possibilities, the proton-impact timing information was used to determine whether or not the ions contributing to a particular resonance had target-release behaviour consistent with radiogenic ions. If they were not radiogenic, they could not be ^{101}In and the corresponding resonance could be excluded.

The resonance identification was achieved by varying the time position of the proton-impact gate described in Section 4.2.1, keeping the gate width fixed at 0.2 s (see Fig. 4.14). For each proton gate, all of the resonance positions were fitted (as above in Section 4.2.3) in a combined model with shared FWHMs. Next, for each resonance, the total number of ion counts with assigned frequency within one standard deviation of the peak centroid was calculated. A flat model was then fitted to the proton-gate time vs. integrated resonance counts relationship. The probability that the data was consistent with random variation about this model (given a Poisson distribution) was then calculated.

Fig. 4.15 shows the results of this process applied to the observed peaks in the $5s^2\ 5p\ ^2P_{3/2}$ to $5s^2\ 9s\ ^2S_{1/2}$ transition. Peaks 2 to 7 show a clear increase in the number of recorded ion counts with the time after the previous proton impact, with a maximum at around 1 s for all the peaks. This corresponds well with the expected target-release profile for ^{101}In. Furthermore, their frequency positions match the predicted positions of the ^{101}In ground state with $I^\pi = 9/2^+$. The other peaks do not show the same variation, meaning these likely arose due to isobaric contamination and were excluded.

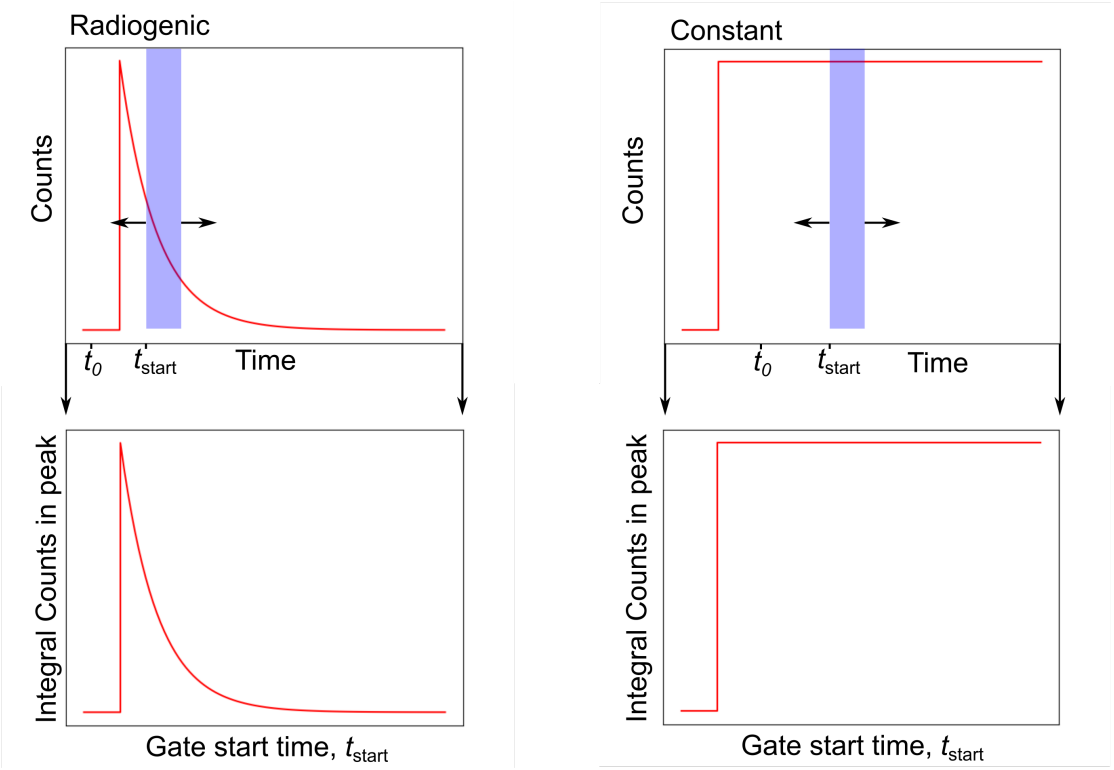

FIGURE 4.14: Schematic representation of the radiogenic-resonance identification process. If the ion-counting rate is correlated in time with the proton impact, t_0 (left), (i.e. the ions are radiogenic) the integrated counts in the resonance will vary when moving the proton impact gate start position, t_{start}. If the count rate is not correlated (right), the integral will be constant.

4.2.6 Spin determination

Considering the most recent evaluation of nuclear spins in indium [87], many states measured here have been firmly assigned using atomic beam or flop-in magnetic resonance techniques [96–99]. Other spin parity assignments come from previous collinear laser spectroscopy measurements [15, 100] and/or measurements of the angular momentum quantum number, L, from (^{3}He, d) reactions [101–103] combined with gamma and decay spectroscopy [104–106]. The ground and isomeric states for $^{115-107}$In measured here are firmly assigned, along with the ground states of ^{106,105}In.

Previous spin assignments for ^{106m}In have been inconsistent, with (p, nγ) measurements assigning $I^\pi = 3^+$ [107] while decay studies assign $I^\pi = 2^+$ [108]. Evaluators tentatively assign $I^\pi = (2)^+$ due to the strong γ feeding from the 1^+ levels [109].

For the ^{104}In ground state, previous laser spectroscopy studies assigned $I = 5, 6$ [15], while beta-decay studies of ^{104}In proposed $I = 6, 7$ [108, 110] and beta-decay studies of ^{104}Sn assigned $I = 6$ [105]. The ^{104m}In isomeric state has previously been measured with gamma spectroscopy; $I = 3$ was assigned based on the assumption of an $I = 6$ ground

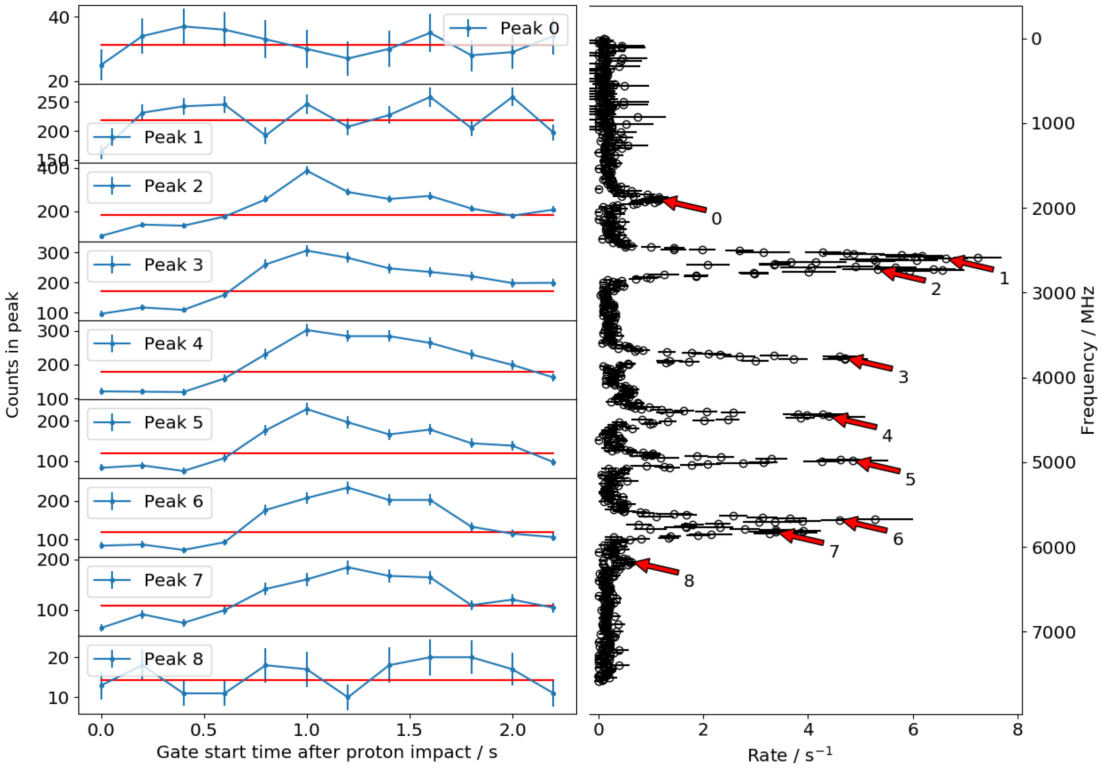

FIGURE 4.15: Combined data of $5s^2\ 5p\ ^2P_{3/2}$ to $5s^2\ 9s\ ^2S_{1/2}$ transition in ^{101}In showing variation in the sum of ion counts within one standard deviation of the fitted peak position against the start time of the 0.2 s wide gate after each proton impact. In the numbered panels on the left, the blue connected points show the data and the red lines show fitted flat models for each peak. The right pane shows the laser frequency vs. binned rate data taking all of the ions (black points), with labels indicating the peak numbers and positions. Peaks 0, 1 and 8 show no variation with proton gate time, indicating these are not from an ^{101}In state. Peaks 2-7 show variation with proton gate time; these are the ^{101}In ground state peaks.

state and the measurement of an M3 gamma [105]. The ground-state spin of ^{102}In has previously been assumed to be the same as ^{104}In. Spins in ^{103,101}In are assumed to be $I = 9/2$ by analogy to the heavier odd-even indium isotopes and from the shell model assumption of a $\pi g_{9/2}^{-1}$ ground-state configuration [87].

In these isotopes where the spin of the ground and/or isomeric state(s) are not firmly identified in literature, the fitting procedure in Section 4.2.3 was repeated using models assuming a variety of nuclear spins. The ratio of fitted A-factors of the upper and lower states could then be compared to reference A-ratio values of 0.106749(55) for the 246.0-nm transition and 0.54095(71) for the 246.8-nm transition. Assuming the validity of Equation 2.32 (i.e. in the absence of significant hyperfine-anomaly modification of the ratio), any deviation of the fit A-ratio would indicate an incorrect spin assignment.

Applying this technique to the isomeric states in ^{106,104}In, $I_m = 1$ spin can be ruled out for both states as the A-ratios in the 246.8-nm transition deviate significantly from the

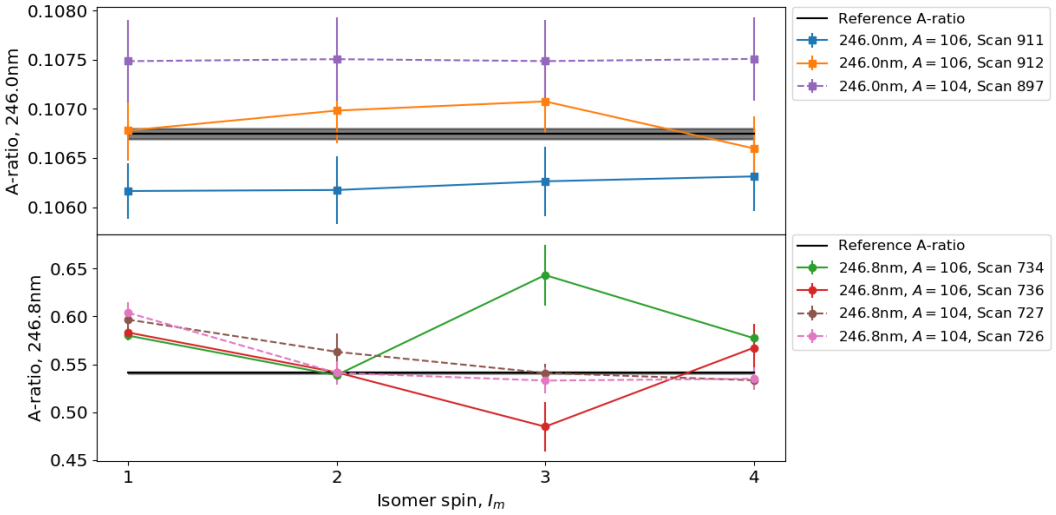

FIGURE 4.16: Fitted hyperfine A-ratio variation with isomeric state spin. Spin $I_m = 1$ can be ruled out from the 246.8-nm transition (lower pane, circles) for both ^{104m}In (dashed lines) and ^{106m}In (solid lines) because the values deviate significantly from the reference value (black bar); fits in this transition for $I_m = 3, 4$ in ^{106m}In are poor quality. Fits of the 246.0-nm transition (upper pane, squares) have no significant variation with spin.

reference, as can be seen in Fig. 4.16. However, the fit has low convergence when using $I_m = 3$ and $I_m = 4$ spins, meaning they cannot be ruled out using this method. The upper and lower atomic states in the 246.0-nm transition have the same total angular momentum, meaning the A-ratio has no variation between nuclear spin configurations.

Another method is to use this goodness-of-fit, specifically the reduced chi-square parameter, to give an indication of the most likely spin. This parameter, as a function of spin for ^{106,104}In, is shown in Fig. 4.17 for each scan. Above spin $I_m = 2$, a large increase in reduced chi-square is seen for both scans of the 246.8-nm transition in ^{106}In. These two pieces of information combined add to the weight of evidence pointing towards an $I_m = 2$ spin for the isomeric state in ^{106}In.

The techniques described above can also be applied to the nuclear ground states in ^{104,102}In. Considering Fig. 4.18 and Fig. 4.19, no significant variation is seen for any scan in either the A-ratio or reduced chi-square, meaning we cannot make conclusions about the nuclear-ground-state spins through these means.

A final possibility is to consider the deviation of the isotopic shifts using a King plot. Here we fit the scans with a particular configuration set of isomer spins, then determine the isotope shifts and combine the scan values using the methods described in Section 4.3 below. Next, we can compare the results for the two transitions according to Equation 2.29 and determine how well the spin configurations match the trend defined by the other isotopic states. Fig. 4.20 shows the result of this technique applied to the isomer

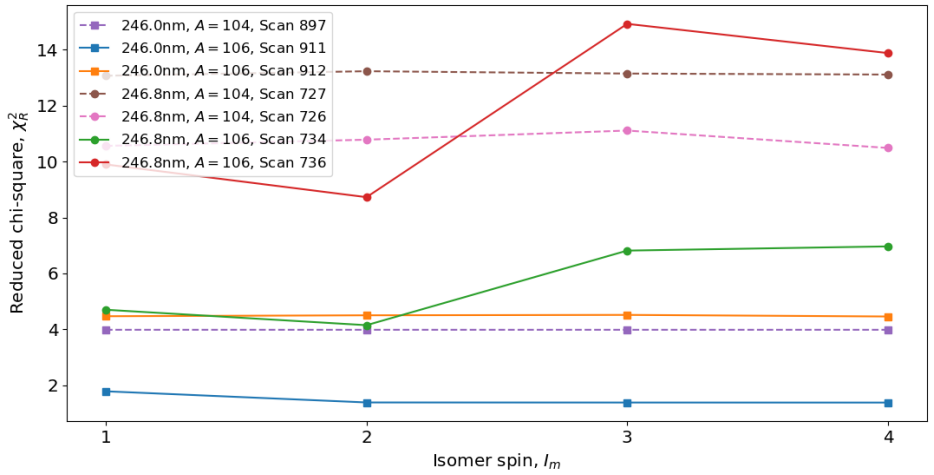

FIGURE 4.17: Reduced chi-square of ^{104,106}In scans fitted with a variety of isomeric state spins. Scans 734 (green) and 736 (red) of the 246.8-nm transition in ^{106}In, show a significant increase above spin $I_m = 2$, making spin assignments $I_m = 3, 4$ less likely. All other scans show no notable variation with spin.

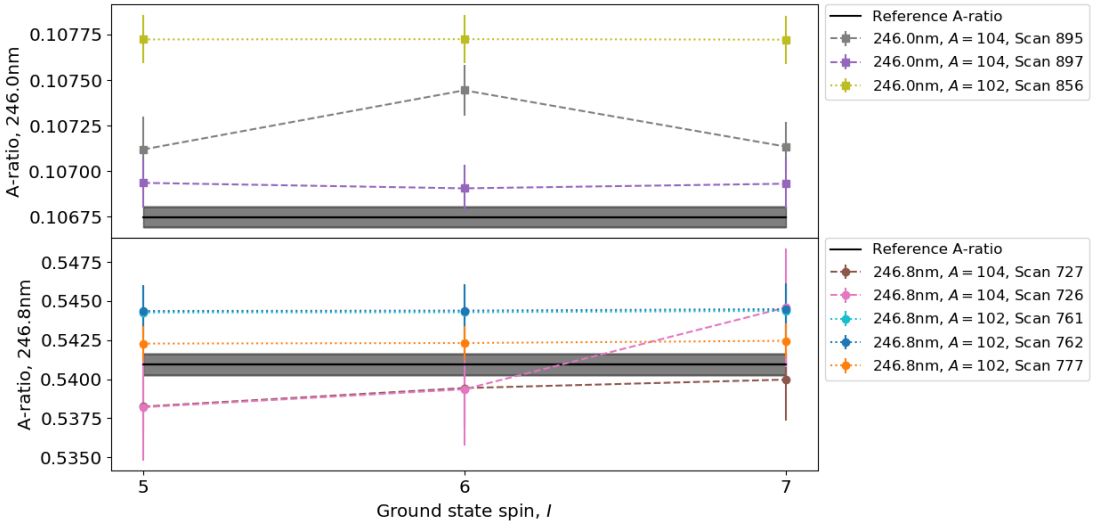

FIGURE 4.18: Fitted A-ratio variation with ground state spin. No significant variation can be seen for either ^{104}In (dashed lines) or ^{102}In (dotted lines) in either transition (upper and lower panes).

^{106m}In. The isotope shift values for $I_m \neq 2$ clearly deviate from the isotope shift trend set by the other isotopes. To quantify this deviation, we can determine the orthogonal distances of the spin-configuration modified-isotope-shift points, $\{\Delta\nu_{246.0,p}, \Delta\nu_{246.8,p}\}$, from the King plot fit line, $\Delta\nu_{246.8} = a\Delta\nu_{246.0} + b$, given by

$$d_p = \frac{|a\Delta\nu_{246.0,p} + b - \Delta\nu_{246.8,p}|}{\sqrt{1+a^2}} \tag{4.12}$$

with corresponding uncertainties coming from the fit parameters a and b, as well as

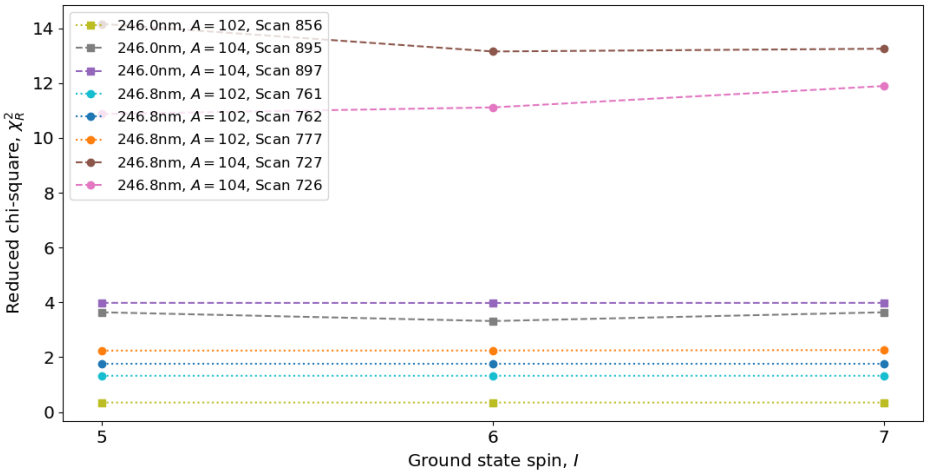

FIGURE 4.19: Reduced chi-square of ^{102,104}In scans fitted with a variety of ground state spins. No scans show a notable variation with spin.

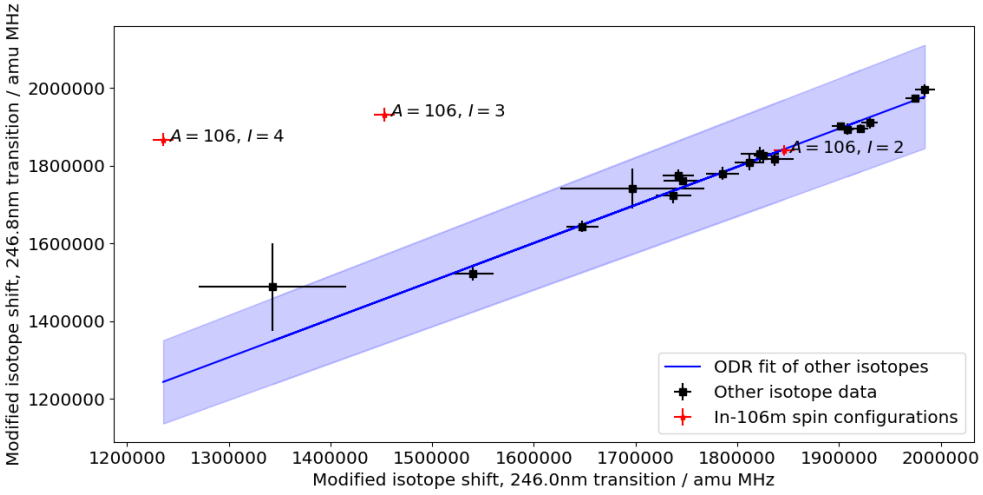

FIGURE 4.20: Variation in modified isotope shifts of the two measured transitions with spin configuration for the isomeric state in ^{106}In (red stars), plotted with modified isotope shifts for the other isotopes (black squares) plus a fit of these states (blue line with error band). Fits of ^{106m}In with spin $I_m \neq 2$ clearly deviate from the linear trend set by the other isotopes, indicating that this isomeric state has $I_m = 2$.

the modified isotope shifts. We can then determine the survival functions, $P(X > d_p/\sigma(d_p))$, of the orthogonal-distance residuals from the Standard Normal Distribution. The survival functions for each tested spin configuration is given in Table 4.3. Spins $I_m = 3, 4$ are excluded here for ^{106m}In, indicating again that this isomeric state has nuclear spin $I_m = 2$.

A	I^π	Residuals, $d_p/\sigma(d_p)$	Survival function
106m	2^+	0.0609	0.951
	3^+	5.49	3.92E-08
	4^+	7.51	5.80E-14
104m	2^+	0.0239	0.981
	3^+	0.232	0.817
	4^+	0.106	0.915
104g	5^+	0.325	0.746
	6^+	0.0292	0.977
	7^+	0.0141	0.989
102g	5^+	0.207	0.836
	6^+	0.0274	0.978
	7^+	0.200	0.841

TABLE 4.3: Orthogonal-distance residuals between modified-isotope-shift points (for a variety of spin-parity I^π and isotope/state A configurations, g and m indicating the ground and isomeric states respectively) and a baseline King plot fit, using isotope shifts from the 246.0 nm and 246.8 nm transitions. The Survival function is the probability of measuring a residual value greater than the recorded value given a Standard Normal distribution. Only $I = 3, 4$ in ^{106m}In (highlighted in red) can be excluded. The spin-parity assumed in the ENSDF evaluation [87] for each state is highlighted in blue.

4.3 Monte Carlo sampling procedures

Bayesian statistics and Monte Carlo sampling techniques were used in this work for the extraction of the atomic observables. Bayes theorem states that the posterior distribution, $P(\theta|D)$, i.e. the probability distribution of model parameter values, θ, given observed data, D, is proportional to the joint probability, $P(\theta, D)$, otherwise known as the model [111]. We can write the model as the product of the prior, $P(\theta)$, and the likelihood function, $P(D|\theta)$, meaning Bayes theorem becomes,

$$P(\theta|D) \propto P(D|\theta)P(\theta). \tag{4.13}$$

For laser spectroscopy, the observed data could be the multiple independent nuclear-moment measurements and the parameter value, θ, could be the final combined value to report. The aim of Monte Carlo sampling techniques is to collect random samples from the posterior distribution based on defined priors and likelihood functions. The distribution of these random samples should then follow the true posterior distribution giving parameter estimates and uncertainties [11].

The first step of any Bayesian method is defining the prior and likelihood distributions. The prior distribution $P(\theta)$ describes the information known about the parameter values before the data has been collected. Often very little is known about a parameter *a priori*, therefore to ensure maximum rigour in the estimation of the parameter, a non-informative prior (i.e. a flat uniform distribution) or a weakly-informative prior (for

example, a uniform distribution within a valid range) are most commonly used. The precise form of the prior must be stated to ensure the analysis can be repeated accurately.

Given a set of independent measurements, $D = \{y_n, \sigma(y_n)\}$, the likelihood function can be factorised into constituent parts,

$$P(D|\theta) = \prod_n P(y_n, \sigma(y_n)|\theta), \tag{4.14}$$

where the individual probability distributions depend on the specific relationship between parameter and data. For example, if the data are values sampled from a Normal distribution, we can estimate the mean of the distribution μ using,

$$P(D|\mu) \propto \prod_n \exp\left(-\frac{(y_n - \mu)^2}{\sigma^2(y_n)}\right). \tag{4.15}$$

There are many techniques for sampling from the posterior distribution but generally the parameter estimates follow a Markov chain where the selection probability of the next position in parameter space only depends on the last sampled position and its posterior, defined through an algorithm attempting to maximise the posterior probability. A description of a number of Markov Chain Monte Carlo (MCMC) techniques can be found in [111].

4.3.1 Reference centroid determination

To determine isotope shifts from the fitted scan centroids, we need to choose corresponding values for the centroid of the reference isotope. Typically this is done independently for each scan, taking the centroid value from the closest measurement in time of the reference-isotope spectrum. This minimizes the effect of uncorrected offsets and time drift between the absolute laser frequency and the measured laser frequency. However, if a long time passes between measurements of the reference and exotic isotopes (relative to the time scale of the laser-frequency measurement drift), this can result in an underestimate of the scan-isotope-shift uncertainty.

Instead, in this work, a Bayesian sampling method was employed to predict the reference-isotope centroid values if measured at the same time as the exotic isotopes. First, the centroid-frequency difference, $\Delta\nu_n$, and the time difference, Δt_n, between subsequent reference-isotope scans (indexed by n) were calculated. Next, the time intervals between the reference-isotope scans were sub-divided into sets of $t_\delta = 300\,\mathrm{s}$ width segments (segments indexed by l), and each segment was assigned a random frequency step $\delta_{n,l}$. These frequency steps could then be sampled from a Normal distribution to form

Gaussian random walks between the reference-isotope scan centroids. The form of the likelihood function employed was

$$P(D|\delta_0, \sigma(\delta)) \propto \prod_n \frac{1}{\sigma(\Delta\nu_n)} \exp\left(\frac{\left(\Delta\nu_n - \sum_l \delta_{n,l}\right)^2}{2\sigma^2(\Delta\nu_n)}\right) \tag{4.16}$$

where δ_0 and $\sigma^2(\delta)$ were the mean and variance of the frequency-step sampling Normal distribution and $D = \{\Delta\nu_n, \sigma(\Delta\nu_n)\}$ was the reference-isotope-centroid data set. The step-sampling distribution parameters were given weakly-informative priors,

$$P(\delta_0) = \begin{cases} 1 & -5\,\text{MHz} \leq \delta_0 \leq 5\,\text{MHz} \\ 0 & \text{otherwise} \end{cases}, \tag{4.17}$$

and

$$P(\sigma(\delta)) = \begin{cases} 1 & 0 \leq \sigma_\delta \leq 10 \cdot \max(\Delta\nu_n/\Delta t_n) t_\delta \\ 0 & \text{otherwise} \end{cases}, \tag{4.18}$$

based on the maximum-observed drift gradient.

Fig. 4.21 shows results of sampling the steps from the posterior distribution with a NUTS MCMC sampler [112] within the PYMC3 Python package [113]. 100000 samples were taken for each parameter for each transition. The black points are the fitted centroids of the reference-isotope scans plotted over time. The lines show the paths of the Gaussian random walks between these measurements. The reference centroid values used for each exotic-isotope scan are shown as red points. Their values are the mean of the frequency positions of the random walks at the closest sampling point in time to when the exotic isotopes were measured. At each of these times, a 68% highest density interval was calculated; half this interval was used as the uncertainty estimate. Given these values, isotope shifts for each nuclear state in all of the exotic-isotope scans could be calculated.

4.3.2 Combining measured values

The fitting and reference-centroid selection methods described above provided multiple independent measurements (indexed by n) of a number of parameters for particular isotopes (indexed by m) and atomic state combinations. The next step was to combine the parameter measurements ($\theta_{m,n}$ with uncertainty $\sigma(\theta_{m,n})$) into final parameter values to report, θ_m. When many measurements of a particular parameter have been taken,

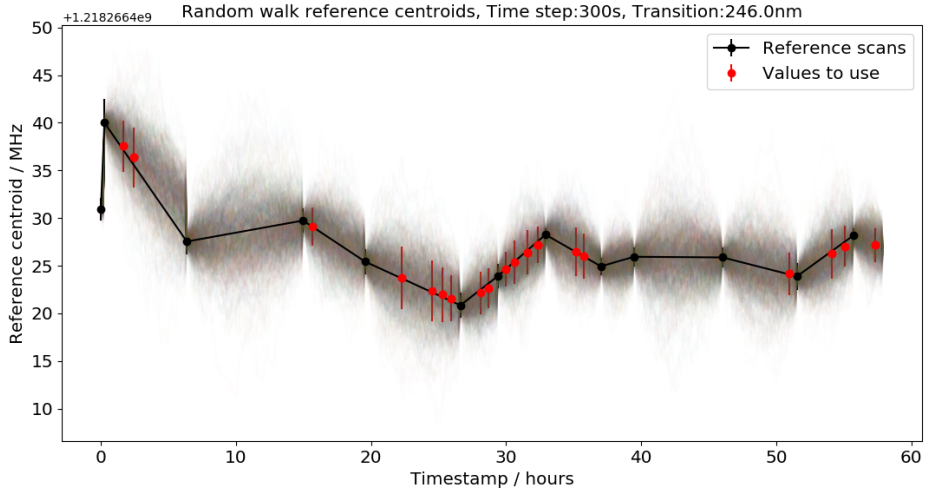

FIGURE 4.21: Variation in the ^{115}In 246.0 nm transition centroid over the course of the experiment. The black points are the fitted centroids from scans of ^{115}In. The other lines are MCMC sampled Gaussian random walks with endpoints fixed to the measured centroids. The priors on the mean and standard deviation of the steps are defined in Equation 4.17 and Equation 4.18. The red points are the mean of the random-walk positions when the exotic isotopes were measured.

and in the absence of outliers, a scatter-corrected weighted mean,

$$\theta_m = \frac{1}{\sum_n 1/\sigma^2(\theta_{m,n})} \sum_n \frac{\theta_{m,n}}{\sigma^2(\theta_{m,n})}, \tag{4.19a}$$

$$\sigma^2(\theta_m) = \frac{1}{\sum_n 1/\sigma^2(\theta_{m,n})} \frac{1}{N-1} \sum_n \frac{(\theta_{m,n} - \theta_m)^2}{\sigma^2(\theta_{n,m})}, \tag{4.19b}$$

can give a good estimate of the true value and variance, $\sigma^2(\theta_m)$, where N is the number of measurements taken. However, when only one or two measurements are available, they may not be representative of the true distribution, meaning the above equations may result in unreliable uncertainty estimates.

To estimate the true distribution, we can assume there exists some additional long-term scatter on the parameter value (with variance Σ^2). In this work, it was assumed that this scatter was constant for all isotopes but was not necessarily the same for all atomic states. Given this assumption and the assumption that the values are sampled from a Normal distribution, a likelihood function was defined (see Section 4.3)

$$P(D|\theta_m, \Sigma) \propto \prod_m \prod_n \frac{1}{\sqrt{\sigma^2(\theta_{m,n}) + \Sigma^2}} \exp\left(-\frac{(\theta_{m,n} - \theta_m)^2}{2\left(\sigma^2(\theta_{m,n}) + \Sigma^2\right)} \right). \tag{4.20}$$

A positive uniform prior was placed on the value of Σ and a flat prior was placed on the θ_m values. As above, a NUTS MCMC sampler [112] within the PYMC3 Python package [113] could then be used to sample values from the posterior distribution. The

mean of the sampled values was then taken to estimate the final parameter values. For each sampling set, a 68% highest density interval was calculated from the samples and half of this interval was used as the uncertainty estimate. This was done for the hyperfine-A parameters and isotope shifts for both states in both transitions, and for the hyperfine-B parameters in the $5s^2\ 5p\ ^2P_{3/2}$ state.

4.4 Results

For the comparison of new results to values published in literature, we can use a number of metrics to determine the level of consistency, including simply looking at the maximum difference between values. A more rigorous metric is a paired T-test, where we consider the sample mean,

$$\bar{d} = \frac{1}{N}\sum_{m=1}^{N} \frac{\theta_{\text{new}} - \theta_{\text{lit.}}}{\sqrt{\sigma^2(\theta_{\text{new}}) + \sigma^2(\theta_{\text{lit.}})}}, \tag{4.21}$$

and standard deviation, $\sigma(d)$, of the reduced differences between the measured values for a certain parameter type, θ, with N values observed. The t-statistic is given by

$$t = \frac{\bar{d}\sqrt{N}}{\sigma(d)}. \tag{4.22}$$

Using the null and alternative hypotheses for the true mean difference μ_d,

$$H_0 : \mu_d = 0; \quad H_1 : \mu_d \neq 0, \tag{4.23}$$

we can extract the probability of observing the measured set of deviations under the null hypothesis, i.e. that the deviation is caused by random variation.

4.4.1 Hyperfine parameters

Table 4.4 gives a comparison of the hyperfine parameter values determined from this work to those found in literature. As the upper states of the two transitions measured in this work are newly measured, only the ground and metastable atomic states (with configurations $5s^2\ 5p\ ^2P_{3/2}$ and $5s^2\ 5p\ ^2P_{1/2}$) are included. Literature values were also determined from laser spectroscopy.

The t-statistic (Equation 4.22) for the hyperfine-A values was 0.746, giving a probability of 0.473 that the differences are consistent with a random variation, indicating that there is no significant systematic offset between the two data sets. The differences are plotted in Fig. 4.22; all the values show a discrepancy of less than 3σ.

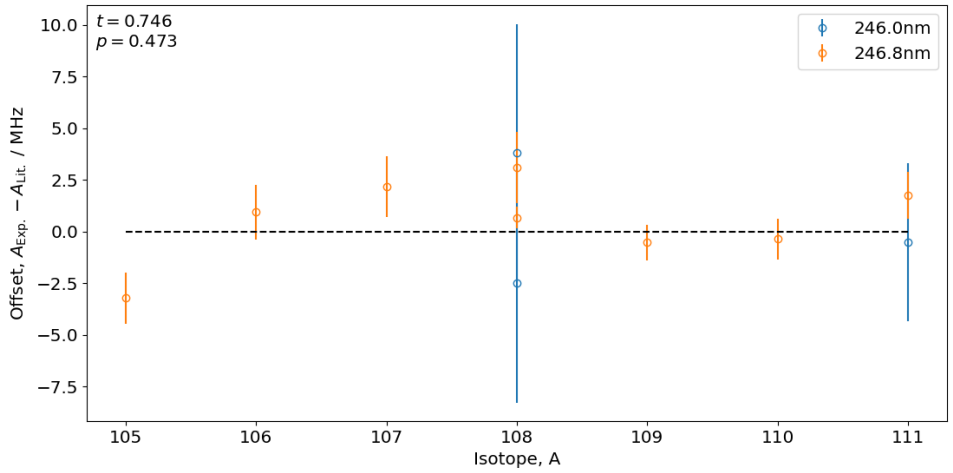

FIGURE 4.22: Difference between experimental A values from this work and literature for the lower atomic states of the two transitions measured in this work: the $5s^2\ 5p\ ^2P_{3/2}$ state (orange points labelled '246.8 nm') and the $5s^2\ 5p\ ^2P_{1/2}$ (blue points labelled '246.0 nm'). Table 4.4 includes the sources of the literature values. All the values show a discrepancy of less than 3σ.

The values for the hyperfine-B t-statistic and probability were -1.074 and 0.319 respectively, leading to a similar conclusion regarding the consistency. The largest discrepancy is in the $I^\pi = 7^+$ ground state in ^{108}In, where a 4σ difference between the literature value in [100] and the value measured in this work was observed. All the other values show a discrepancy of less than 2σ.

4.4.2 Magnetic dipole moments

Nuclear magnetic dipole moments in this work were extracted from the final hyperfine-A parameters according to Equation 2.30 using the $I^\pi = 9/2^+$ state in ^{115}In as a reference. The reference dipole moment was $\mu_{115} = +5.5408(2)\mu_N$, derived from magnetic resonance measurements of liquid ^{115}In in Flynn et al. [28]. The hyperfine parameters determined for ^{115}In in this work were used as the reference values. This ensured that any systematic multiplicative offset in the final hyperfine parameters would cancel in the calculation of dipole moments. The final magnetic dipole and electric quadrupole moments are both given in Table 4.5.

4.4.3 Electric quadrupole moments

A precise reference measurement for the nuclear electric quadrupole moments of the indium isotopes unfortunately does not exist in literature. Historically, an estimated

		Hyperfine parameters / MHz					
		$5s^2\ 5p\ ^2P_{3/2}$				$5s^2\ 5p\ ^2P_{1/2}$	
A	I^π	A_{Exp}	A_{Lit}	B_{Exp}	B_{Lit}	A_{Exp}	A_{Lit}
101g	$(9/2^+)$	+256.87(48)		+291.9(69)		+2412.9(58)	
102g	(6^+)	+149.33(22)		+282.1(35)		+1406.9(58)	
103m	$(1/2^-)$	-44.4(38)				-419.8(72)	
103g	$(9/2^+)$	+251.48(27)		+380.6(42)		+2372.3(33)	
104m	(3^+)	+324.4(12)		+262.8(88)		+3036.7(42)	
104g	(5^+)		+174.2(10)[b]		+362(58)[b]		
104g	(6^+)	+149.82(32)		+414.3(50)		+1417.5(41)	
105m	$1/2^-$	-61.0(79)				-491(10)	
105g	$9/2^+$	+247.38(32)	+250.6(12)[b]	+444.4(45)	+460(28)[b]	+2333.7(41)	
106m	$(2)^+$	+480.67(67)		+236.2(47)		+4537.9(42)	
106g	7^+	+137.73(28)	+136.8(13)[b]	+505.7(43)	+540(34)[b]	+1301.4(41)	
107m	$1/2^-$	-67.2(65)				-541.1(94)	
107g	$9/2^+$	+245.26(41)	+243.1(14)[a]	+444.2(66)	+448(29)[a]	+2303.6(58)	
108m	2^+	+487.28(65)	+484.2(16)[c]	+272.4(49)	+259(8)[c]	+4579.8(59)	+4576.0(22)[b]
108g	7^+	+128.27(36)	+127.6(4)[c]	+526.9(63)	+558(4)[c]	+1206.5(58)	+1209.0(5)[b]
109m1	$1/2^-$	-61.7(24)				-623.4(51)	
109g	$9/2^+$	+241.16(36)	+241.7(8)[a]	+483.7(49)	+467(15)[a]	+2278.7(41)	
109m2	$19/2^+$					+945.7(41)	
110m	2^+	+426.5(12)		+180.4(73)			
110g	7^+	+132.32(41)	+132.7(9)[a]	+540.3(66)	+555(12)[a]		
111m	$1/2^-$	-60.2(47)				-685.3(47)	
111g	$9/2^+$	+241.04(51)	+239.3(10)[a]	+436.3(63)	+446(12)[a]	+2268.4(33)	+2268.9(19)[b]
112g	4^+		+259.6(4)[b]		+396(6)[b]		+2457.2(30)[b]
113m	$1/2^-$	-72.1(62)				-781.6(81)	
113g	$9/2^+$	+241.56(26)		+445.0(38)		+2276.9(58)	
114g	5^+		+183.5(4)[b]		+410(6)[b]		+1729.0(2.0)[b]
115g	$9/2^+$	+242.069(97)		+451.3(14)		+2282.0(15)	

TABLE 4.4: Hyperfine parameters for the $5s^2\ 5p\ ^2P_{3/2}$ and $5s^2\ 5p\ ^2P_{1/2}$ states, from measurements of the 246.8 nm and 246.0 nm transitions respectively, compared to literature values. Values marked [a] are from [114], those marked [b] are quoted in [15], and those marked [c] are from [100]. Ground states are labelled with 'g', while isomeric states are labelled with 'm'. The ^{104}In ground state was assigned spin $I^\pi = 5^+$ in [b] but spin $I^\pi = 6^+$ in this work.

value for ^{115}In of $Q_{115} = +0.810$ has been used [15, 114]. This is deduced from a base value determined by Koster [115], with a Sternheimer correction factor (extrapolated from gallium and aluminium) of $C = 0.87$ applied [114, 116]. This reference value was previously used in a method of ratios (Equation 2.31) similar to the determination of dipole moments above.

Instead, here a recent relativistic atomic coupled-cluster calculation [27] of the electric field gradient of the $5s^2\ 5p\ ^2P_{3/2}$ state, $\partial^2V/\partial z^2 = (+575.6 \pm 4.0)$ b, is used inside Equation 2.16 to determine the quadrupole moments from the hyperfine-B values. The calculations also determined the ratio of the hyperfine-A parameter to the gyromagnetic

Mass	I^π	Q_s	Magnetic moments, μ				
		5p $^2P_{3/2}$	5p $^2P_{1/2}$	8s $^2S_{1/2}$	5p $^2P_{3/2}$	9s $^2S_{1/2}$	Mean
101g	$9/2^+$	0.507(12)	5.859(15)	5.837(25)	5.880(11)	5.859(33)	5.8674(82)
102g	6^+	0.4900(70)	4.555(19)	4.595(16)	4.5575(69)	4.585(18)	4.5648(83)
103m	$1/2^-$		-0.1133(20)	-0.135(12)	-0.1128(96)		-0.1138(24)
103g	$9/2^+$	0.6612(86)	5.7601(90)	5.7600(78)	5.7563(67)	5.783(17)	5.7599(43)
104m	3^+	0.457(16)	4.9156(76)	4.961(15)	4.951(18)	4.924(77)	4.928(11)
104g	6^+	0.720(10)	4.589(14)	4.607(12)	4.5723(100)	4.566(26)	4.5862(88)
105m	$1/2^-$		-0.1324(28)	-0.13(22)	-0.155(20)		-0.1327(27)
105g	$9/2^+$	0.7721(95)	5.667(11)	5.6750(93)	5.6624(77)	5.660(19)	5.6668(50)
106m	2^+	0.4104(86)	4.8970(56)	4.880(12)	4.8899(71)	4.889(18)	4.8924(40)
106g	7^-	0.8786(97)	4.916(16)	4.918(13)	4.904(10)	4.943(25)	4.9127(69)
107m	$1/2^-$		-0.146(25)	-0.181(16)	-0.171(16)		-0.1474(46)
107g	$9/2^+$	0.772(13)	5.593(14)	5.599(13)	5.6138(96)	5.649(24)	5.6082(81)
108m	2^+	0.4732(91)	4.9423(71)	4.865(12)	4.9571(69)	4.911(21)	4.936(18)
108g	7^-	0.915(13)	4.557(22)	4.582(19)	4.567(13)	4.666(29)	4.579(18)
109m1	$1/2^-$		-0.1682(14)	-0.1475(85)	-0.1569(62)		-0.1672(28)
109g	$9/2^+$	0.840(10)	5.533(11)	5.5279(88)	5.5200(84)	5.557(19)	5.5283(55)
109m2	$19/2^+$		4.848(21)	4.817(22)			4.833(15)
110m	2^+	0.313(13)			4.339(12)	4.286(52)	4.336(12)
110g	7^-	0.939(13)			4.712(15)	4.716(44)	4.712(14)
111m	$1/2^-$		-0.1849(13)	-0.2046(79)	-0.153(12)		-0.185(33)
111g	$9/2^+$	0.758(12)	5.5078(89)	5.5226(80)	5.517(12)	5.494(25)	5.5153(52)
113m	$1/2^-$		-0.2109(22)	-0.228(13)	-0.183(16)		-0.2108(32)
113g	$9/2^+$	0.7732(86)	5.528(14)	5.533(13)	5.5292(63)	5.530(15)	5.5298(50)
115g	$9/2^+$	0.7841(60)					

TABLE 4.5: Electric quadrupole, Q_s, and magnetic dipole, μ, moments determined through this work. The magnetic moment values determined from each of the measured atomic states are shown individually, alongside a weighted means of the values in the final column labelled 'Mean'. Ground states are labelled with 'g', while isomeric states are labelled with 'm'.

ratio, allowing for the extraction of the magnetic moments of ^{115}In and ^{113}In when combined with the measured hyperfine-A values in [27]. The values were found to be consistent with those measured using NMR in [28], giving confidence in the calculations and therefore the value for the electric field gradient.

The $5s^2$ 5p $^2P_{3/2}$ state was the only atomic state probed with $J > 1/2$, so was the only state from which determination of the quadrupole moments was possible.

4.4.4 Isotope shifts

Table 4.6 presents the final isotope shifts and uncertainties determined from this work, relative to the reference isotope, ^{115}In. The only available measurements of the isotope shifts of the two reported transitions is from a previous investigation by the CRIS collaboration. These measurements looked at the stable indium isotopes with

		Isotope shift, $\delta\nu^{115,A}$ / MHz		Change in m-s charge radius, $\delta\langle r^2\rangle^{115,A}$ / fm^2	
A	I^π	246.0 nm	246.8 nm	246.0 nm	246.8 nm
101g	$(9/2^+)$	-2392(12)	-2406(17)	-1.5819(81)[663]	-1.526(12)[64]
102g	(6^+)	-2189(10)	-2187.3(73)	-1.4476(70)[610]	-1.3864(49)[588]
103g	$(9/2^+)$	-1933.8(62)	-1919(15)	-1.2784(41)[558]	-1.2129(99)[538]
103m	$(1/2^-)$	-1955.8(83)	-1936(15)	-1.2932(56)[558]	-1.225(10)[54]
104g	(6^+)	-1749.3(75)	-1749.5(90)	-1.1564(50)[506]	-1.1059(61)[488]
104m	(3^+)	-1767.0(77)	-1744.4(96)	-1.1683(52)[506]	-1.1025(65)[488]
105g	$9/2^+$	-1512.4(75)	-1513(13)	-0.9992(50)[456]	-0.9538(86)[439]
105m	$1/2^-$	-1502(12)	-1499(17)	-0.992(81)[456]	-0.944(12)[44]
106g	7^+	-1376.8(75)	-1376.2(98)	-0.9099(50)[406]	-0.8687(67)[392]
106m	$(2)^+$	-1362.8(76)	-1359.3(99)	-0.9005(51)[406]	-0.8572(67)[392]
107g	$9/2^+$	-1162(11)	-1158(11)	-0.7674(71)[358]	-0.7286(77)[345]
107m	$1/2^-$	-1130(11)	-1121(13)	-0.7462(75)[358]	-0.7032(85)[345]
108g	7^+	-1036(10)	-1025(10)	-0.6845(70)[310]	-0.6459(71)[299]
108m	2^+	-1028(10)	-1032(10)	-0.679(70)[310]	-0.6507(71)[299]
109g	$9/2^+$	-834.8(74)	-851.0(68)	-0.5511(50)[263]	-0.5351(46)[254]
109m	$1/2^-$	-789.6(76)	-787.6(70)	-0.5208(51)[263]	-0.4921(47)[254]
110g	7^+		-737.8(34)		-0.4657(23)[210]
110m	2^+		-741.4(38)		-0.4682(26)[210]
111g	$9/2^+$	-548.1(61)	-552.7(33)	-0.3619(41)[173]	-0.3474(23)[166]
111m	$1/2^-$	-483.3(64)	-478.0(56)	-0.3184(43)[172]	-0.2966(38)[166]
113g	$9/2^+$	-262(11)	-268.5(78)	-0.1726(73)[85]	-0.1686(53)[82]
113m	$1/2^-$	-207(11)	-229(17)	-0.136(75)[85]	-0.142(12)[8]

TABLE 4.6: Isotope shifts and changes in mean-square charge radii for the 246.0 nm transition between the $5s^2\ 5p\ ^2P_{1/2}$ and $5s^2\ 8s\ ^2S_{1/2}$ states, and for the 246.8 nm transition between the $5s^2\ 5p\ ^2P_{3/2}$ and $5s^2\ 9s\ ^2S_{1/2}$ states. The charge radii are calculated using theoretical field- and mass-shift factors from Sahoo et al. [25]. Statistical uncertainties are given in rounded brackets and systematic uncertainties for the radii, from the theoretical field- and mass-shift factors, are given in square brackets. Ground states are labelled with 'g', while isomeric states are labelled with 'm'.

the CRIS ablation ion source [27]; values of $\delta\nu^{115,113}(246.0\,\text{nm}) = -268(2)(5)\,\text{MHz}$ and $\delta\nu^{115,113}(246.8\,\text{nm}) = -270(2)(6)\,\text{MHz}$ were reported for the ground-state isotope shift ($I^\pi = 9/2^+$) of ^{113}In (the two uncertainties correspond to the statistical and systematic errors). Both of these values are within 1σ of the values reported here, giving confidence in the analysis.

4.4.5 Changes in mean-square charge radii

To convert measurements of isotope shifts to changes in mean-square charge radii, we require values for the atomic field- and mass-shift factors (F and M in Equation 2.28). These parameters can be extracted using a King plot method in elemental cases where independent measurements of the absolute charge radii exist in more than three isotopes [34]. In odd-proton elements, however, a maximum of two stable isotopes exists

Transition	Dirac-Fock [15]		Analytic response [25]	
	F / MHz fm^{-2}	M / MHz u	F / MHz fm^{-2}	M / MHz u
5p ^{2}P$_{3/2}$ $\rightarrow$ 9s ^{2}S$_{1/2}$			1473.1(55)	$1.31(78) \times 10^5$
5p ^{2}P$_{1/2}$ $\rightarrow$ 8s ^{2}S$_{1/2}$			1491.2(65)	$2.7(82) \times 10^4$
5p ^{2}P$_{1/2}$ $\rightarrow$ 6s ^{2}S$_{1/2}$	2070(10)	$-4.0(80) \times 10^4$	1818.1(61)	$-2.98(86) \times 10^5$
5p ^{2}P$_{3/2}$ $\rightarrow$ 6s ^{2}S$_{1/2}$	2078(78)	$-6.2(73) \times 10^4$	1825.2(56)	$-2.32(82) \times 10^5$

TABLE 4.7: F and M values in Equation 2.28 for various transitions from the Dirac-Fock calculations used in Eberz et al. [15] (left) and from the analytic-response calculations of Sahoo et al. [25] used in this work (right).

and therefore few cases have a sufficient number of absolute charge-radii measurements. In elements, such as indium, where these measurements do not exist, we must rely on atomic-theory calculations to determine F and M. In this work, recently published relativistic coupled-cluster calculations by Sahoo et al. using the analytic-response approach were utilized [25]. The latest values used in this work are presented in Table 4.7, alongside Dirac-Fock values used in Eberz et al. [15]. Coupled-cluster calculations are widely considered to be the most accurate techniques for treating electron-correlation effects [117]. The advantage of the analytic-response approach over more commonly used techniques is that uncertainties can be controlled [25].

Fig. 4.23 shows a comparison of changes in mean-square charge radii from this work and from Eberz et al. [15]. Eberz used a transition field-shift value of $F = 2070(10)\,\text{MHz fm}^{-2}$ for the 410 nm transition between the 5s^2 5p ^{2}P$_{1/2}$ and 5s^2 6s ^{2}S$_{1/2}$ states. This was derived from a relativistic Dirac-Fock calculation. The SMS to NMS ratio was calibrated relative to the neighbouring tin and cadmium elements. A systematic offset is seen in Fig. 4.23 between the reported Eberz values and the newly measured values due to the difference in these field and mass shifts. To account for this, charge-radii values were recalculated based on the isotope shifts measured in the Eberz paper [15] with up-to-date analytic-response calculations of the field and mass shift factors from Sahoo et al. for the two measured transitions [25]. These changes in mean-square charge radii agree with the values determined from this work when using the same atomic calculations, within the systematic uncertainties associated with the theory. This provides increased confidence in the values and uncertainties of the atomic parameters determined by Sahoo et al. [25].

4.4.6 King plot analysis

King plots were not used in this work to extract changes in mean-square charge radii because reliable values for reference field and mass shift factors, or muonic-atom radii data, do not exist. However, King plots can be used for an additional comparison of

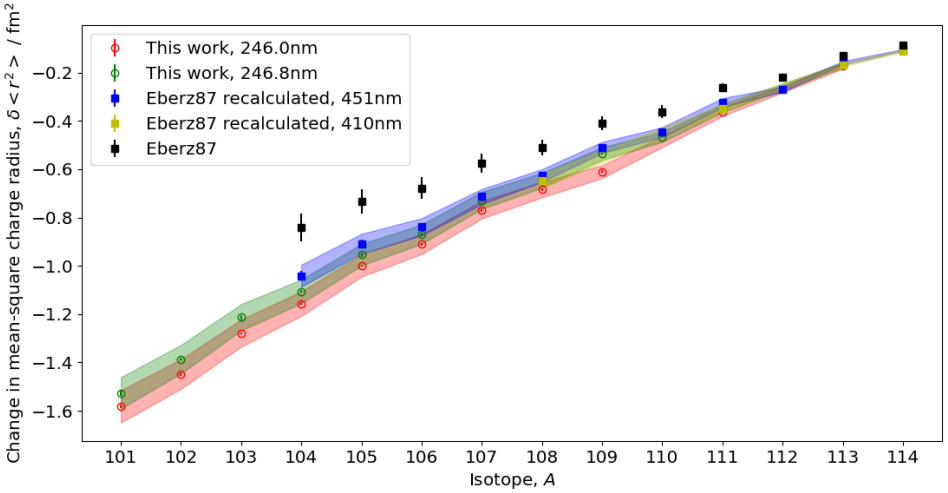

FIGURE 4.23: A comparison of changes in mean-square charge radii for indium ground states from this work and literature. The black squares are the charge radii values reported by Eberz et al. [15]. The blue and yellow squares use the isotope shifts reported in [15] together with more recent theoretical calculations [25] of the field and mass shift factors to re-calculate the radii for the two measured atomic transitions. The green and red circles are the values determined from this analysis using the F and M from the same calculations. All the points have error bars showing the statistical uncertainties from the measurement of the isotope shift. The error bands show the combined statistical and systematic uncertainties, including the theoretical uncertainties.

the results of this work to literature isotope shifts and for validation of the theoretical analytic-response calculations of field shifts. Fig. 4.24 shows four King plots with a comparison of the modified isotope shifts for the two transitions measured in this work to the modified isotope shifts for the transitions measured by Eberz et al. [15]: the 5p $^2P_{1/2} \rightarrow$ 6s $^2S_{1/2}$ transition at 410 nm and the 5p $^2P_{3/2} \rightarrow$ 6s $^2S_{1/2}$ transition at 451 nm. The King plots are fitted with a linear model, according to Equation 2.29, (red line) with Orthogonal-Distance Regression (ODR) [118]. However, the fits are significantly under constrained (shown by the low reduced-chi-square values) due to the size of the uncertainties on the modified isotope shifts and the low number of overlapping measured values, meaning consistency is tentative.

We can also compare the two transitions measured in this work to each other, as shown in Fig. 4.25. Here the relationship is stronger, with a larger reduced chi-square of the ODR fit of $\chi^2_r = 0.610$, meaning we can be more confident about the consistency of these two sets of isotope shifts.

Equation 2.29 shows that the gradients of the fitted linear models for the King plots give values for the ratio of the two field-shift factors of the two plotted transitions, F_i/F_j, where F_i is for the y-axis transition and F_j is for the x-axis transition (labelled 'King'). These values can then be compared to the equivalent analytic-response coupled-cluster

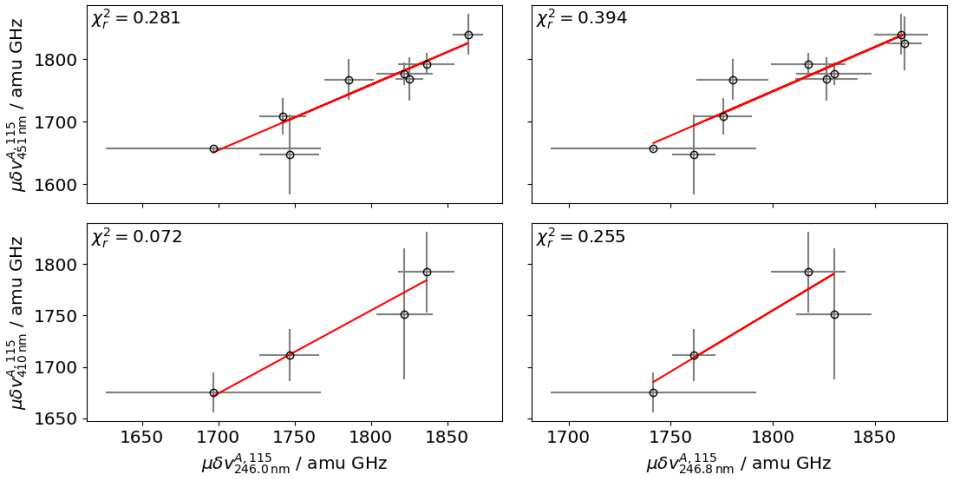

FIGURE 4.24: King plots comparing the isotope shifts measured in this work to those found in Eberz et al. [15], with data shown as black points. Axes are shared across rows and down columns. Each plot is fitted with a linear model (red lines), with the reduced chi-square of the fit shown in the top left of each window. Left x-axis: 5p $^2P_{1/2} \rightarrow$ 8s $^2S_{1/2}$, Right x-axis: 5p $^2P_{3/2} \rightarrow$ 9s $^2S_{1/2}$, Lower y-axis: 5p $^2P_{1/2} \rightarrow$ 6s $^2S_{1/2}$, Upper y-axis: 5p $^2P_{3/2} \rightarrow$ 6s $^2S_{1/2}$.

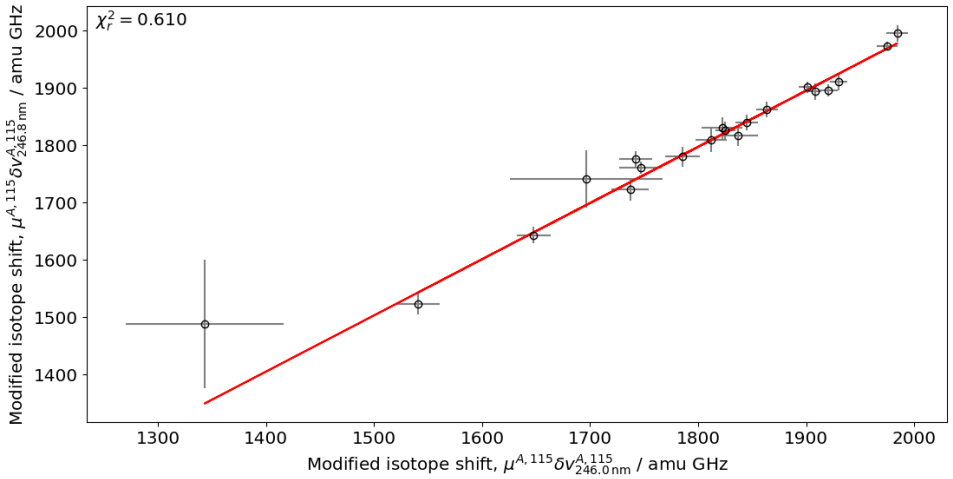

FIGURE 4.25: King plot comparing the modified isotopes shifts in the two measured transitions in this work: the 246.0 nm transition between the $5s^2$ 5p $^2P_{1/2}$ and $5s^2$ 8s $^2S_{1/2}$ states on the horizontal axis, and the 246.8 nm transition between the $5s^2$ 5p $^2P_{3/2}$ and $5s^2$ 9s $^2S_{1/2}$ states on the vertical axis. All isotope-shift data are from this work.

theory values of Sahoo et al. [25]. All values appear consistent within $\sim 1\,\sigma$, except for the Eberz et al. [15] 5p ^{2}P$_{1/2}$ $\rightarrow$6s ^{2}S$_{1/2}$ comparison to the 5p ^{2}P$_{1/2}$ $\rightarrow$8s ^{2}S$_{1/2}$ from this work, where the deviation is $3.4\,\sigma$. However, with a reduced chi-square of $\chi^2_r = 0.072$, the error on this fit is likely underestimated. The comparison of the two measured transitions in this work gives the most precise value and provides the most confidence in the analytic response calculations.

F_i/F_j	5p ^{2}P$_{1/2}$ $\rightarrow$8s ^{2}S$_{1/2}$		5p ^{2}P$_{3/2}$ $\rightarrow$9s ^{2}S$_{1/2}$	
	King	AR	King	AR
5p ^{2}P$_{3/2}$ $\rightarrow$9s ^{2}S$_{1/2}$	0.980(32)	0.9879(57)		
5p ^{2}P$_{1/2}$ $\rightarrow$6s ^{2}S$_{1/2}$ †	0.81(12)	1.2192(67)	1.19(34)	1.2342(62)
5p ^{2}P$_{3/2}$ $\rightarrow$6s ^{2}S$_{1/2}$ †	1.04(16)	1.2240(65)	1.41(24)	1.2390(60)

TABLE 4.8: Ratios of the field-shift factors, F_i/F_j, from King plots presented above (columns labelled 'King') compared to values from analytic-response calculations in Sahoo et al. [25] (columns labelled 'AR'). The x-axis transition for F_j is given by the column label and the y-axis transition for F_i is given by the row label. The transitions labelled † use isotope shift values from Eberz et al. [15] in the King plot.

4.4.7 Isomer shift analysis

As an alternative to King plots, we can also consider the measured isomer shifts as a test of theoretical field-shift factors. Similar to isotope shifts, isomer shifts are changes in centroid frequency between nuclear states of the same isotope. Between the two nuclear states, the inverse of the mass-modification factor, $(A' - A)/(A'A)$, found in the definition of the isotope shift (Equation 2.28) is small (of the order of $10^{-7}\,\mathrm{u}^{-1}$ for a 1 MeV isomer) due to the similar mass of ground state and isomer. This means the mass-shift contribution to isomer shifts is small relative to the field-shift contribution, being of the order of 0.01 MHz for a typical mass-shift constant, $M = 1 \times 10^5\,\mathrm{MHz\,u}$, in the 1 MeV isomer case. Therefore, taking the ratio of two isomer shifts in two different atomic transitions (for the same nuclear states) removes the dependence on the change in mean-square charge radius, giving

$$\frac{\delta\nu_i}{\delta\nu_j} \approx \frac{F_i}{F_j}. \tag{4.24}$$

Fig. 4.26 shows the isomer-shift ratios of the two transitions measured in this work compared to the ratio of theoretical field shifts for those two transitions from the analytic-response calculations of Sahoo et al. [25]. The isomer-shift ratios have significantly larger uncertainties from the contributions of the individual isotope shifts, meaning the mean value is dominated by the isotopes closer to stability. The mean is consistent with the theoretical ratio, as are the individual isomer shift ratios. This provides more confidence in the analytic-response calculations of the field shifts by Sahoo et al. [25].

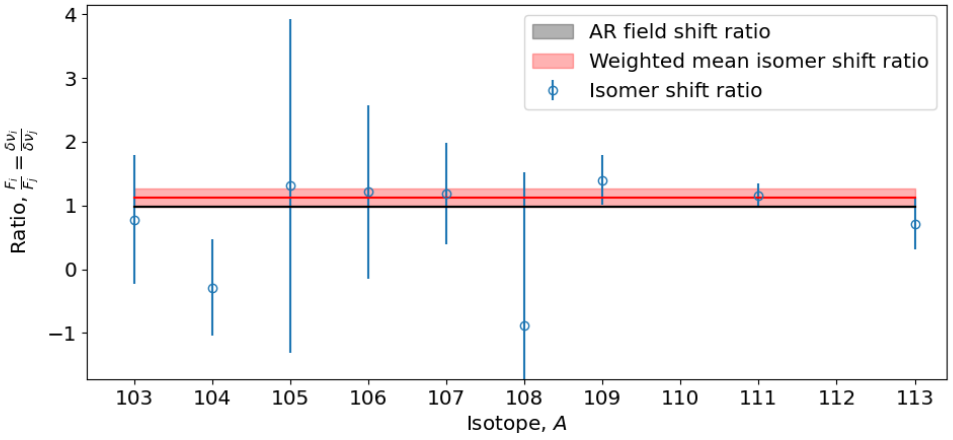

FIGURE 4.26: Ratios of isomer shifts in the two measured transitions of this work (blue points) compared to the ratio of field shifts from the analytic-response calculations of Sahoo et al. [25] (black bar). The weighted mean of the isomer shift ratios is also shown (red bar); the mean is dominated by the $A = 111$ ratio. The theoretical field-shift ratio is consistent with this mean and with each individual measurement ratio within 2σ.

Chapter 5

Evolution of nuclear observables in indium

Recent advances in a variety of experimental and theoretical techniques have led to renewed interest in the neutron-deficient tin region of the nuclear chart [6, 119–124]. Measurements of the strengths of E2 transitions ($B(E2)$) between the ground $I^\pi = 0^+$ states and first-excited $I^\pi = 2^+$ states in the even-even tin isotopes in particular have raised questions about the nature of the supposedly doubly-magic ^{100}Sn, due to the possibility of an increased level of quadrupole deformation in isotopes approaching the neutron shell closure at $Z = 50$ (see Fig. 5.11). These E2 transition strengths can be written as,

$$B(E2; 0_1^+ \leftarrow 2_1^+) = \left\langle 2_1^+ \left|\left|\hat{Q}\right|\right| 0_1^+ \right\rangle^2, \tag{5.1}$$

where $\hat{Q}$ is the quadrupole operator defined in Equation 2.6 [125]. Many nuclear models in the region rely on the supposed stability of the ^{100}Sn core when building the valence space, for example in the $\pi g_{9/2}$ states in indium where single-particle behaviour has been the foundation of shell-model and density-functional-theory (DFT) predictions of nuclear properties [126]. This chapter discusses the impact of the measurements presented in this thesis on understanding of the evolution of nuclear structure towards ^{100}Sn through comparisons to predictions of the droplet model, shell model and DFT.

5.1 Theoretical models

5.1.1 Droplet model

Historically, the first attempt to describe nuclei treated them as an incompressible fluid with a uniform density and well-defined surface. This is the liquid-drop model, which

gave rise to the semi-empirical mass formula for the reproduction of nuclear binding energies through a series of phenomenological terms [73],

$$BE(A,Z) = a_v A - a_s A^{2/3} - a_c Z(Z-1)A^{-1/3} - a_{\text{sym.}}\frac{(A-2Z)^2}{A} + \delta(A,Z), \quad (5.2)$$

where a_v is the nuclear volume coefficient, a_s is the surface coefficient, a_c is the Coulomb force coefficient, $a_{\text{sym.}}$ incorporates the mass-asymmetry effect and $\delta(A,Z)$ is the pairing term.

Additional terms were added to the liquid droplet model to form the more modern droplet model and finite-range droplet model [127]. Droplet-model mean-square charge radius values, $\langle r^2 \rangle$, can then be determined from,

$$\langle r^2 \rangle = \langle r^2 \rangle_u + \langle r^2 \rangle_r + \langle r^2 \rangle_d , \quad (5.3)$$

where $\langle r^2 \rangle_u$ is the uniform distribution contribution, with a certain shape, $\langle r^2 \rangle_r$ comes from the redistribution from the proton Coulomb repulsion, also with a certain shape, and $\langle r^2 \rangle_d = 3b^2$ is the nuclear diffuseness term, taken as a constant for all nuclei [127]. $\langle r^2 \rangle_u$ and $\langle r^2 \rangle_r$ contain expansions in terms of the deformation parameters, β_i (see Section 5.4.1), and are proportional to the square of the sharp proton distribution, R_z^2, where,

$$R_z = r_0 A^{1/3}(1+\bar{\epsilon}) - \frac{N}{A}t, \quad (5.4)$$

and $r_0 = (3/(4\pi\rho_\infty))^{1/3}$ is the nuclear radius constant. The neutron-skin thickness, t, and the correction factor, $\bar{\epsilon}$, contain the parameters listed in Table 5.1. The phenomenological coefficients are tuned to fit experimental values for nuclear charge radii, binding energies (from measurements of nuclear masses) and other nuclear parameters such as nuclear excitation energies or spectroscopic factors [128].

5.1.2 Shell model

The droplet model has been successful at describing the macroscopic variation in nuclear size and binding energy across the nuclear chart. However, it has been unable to account for the variation in structure close to proton and neutron magic numbers. The shell model approaches the problem through the nuclear many-body Hamiltonian, Equation 2.2, assuming as a first approximation that the nucleus is a system of independent nucleons each moving in an average field, i.e. that $H \approx H_0$ [13, 24]. Mayer found that a simple harmonic oscillator mean field with additional spin-orbit terms reproduced the observed magic-number energy gaps ($N, Z = 2, 8, 28, 50$ and beyond) [1–3]. This

potential can be written as,

$$U(r) = \frac{1}{2}m\omega^2 r^2 + C\vec{l}\cdot\vec{s} + Dl^2, \tag{5.5}$$

and gave rise to the angular-momentum representation of single-nucleon states. $H_{\text{res.}}$ can then be treated as a small perturbation in more precise calculations, often now required to reproduce experimental values with sufficient accuracy [73].

5.1.3 Density functional theory

Nuclear theories attempting to describe bulk nuclear properties through mean fields have generally been very successful throughout the entire nuclear chart [4, 5]. Historically, two of the most widespread approaches were the Hartree-Fock method with Skyrme forces [129] and the theory of finite fermi systems (TFFS) approach from Migdal [130]. In the Hartree-Fock approximation, the many-body wavefunction of the nucleus is replaced with a Slater determinant containing single-particle wavefunctions derived from the nuclear mean field. Skyrme forces provide an approximation of the mean field derived from a nuclear-density-dependent phenomenological approach [131].

Fayans et al. combined the two approaches into a self-consistent TFFS or energy-density functional (EDF) for the prediction of ground-state nuclear properties [132,133]. Saperstein et al. later expanded on the Fayans formalism to include additional phonon coupling corrections to the EDFs decribed in the next section [134–137].

5.1.4 Phonon-coupling corrections to the theory of finite fermi systems

In a theory of finite fermi systems (TFFS) formalism, the magnetic moment for a single quasi-particle state (i.e. a single proton or neutron combined with additional core effects not explicitly included in the calculations), λ, is derived from the diagonal matrix element,

$$\mu_\lambda = \langle\lambda|V(M1;\omega=0)|\lambda\rangle\,, \tag{5.6}$$

where $V(M1;\omega = 0)$ is the static effective field [135]. The effective field obeys an equation of the form,

$$V(M1;\omega) = V_0(M1) + FA(\omega)V(M1;\omega), \tag{5.7}$$

where $V_0(M1) = e_q\hat{\mu}$ and $\hat{\mu}$ is the magnetic moment operator, e_q is the effective quasi-particle charge, F is a Landau-Migdal (LM) coupling parameter [138] for the particle-core interaction and $A(\omega)$ is the particle-hole propagator [134]. The LM coupling parameter, F, contains a central force term plus meson-exchange terms. The calculations are performed in a self-consistent basis through a Fayans energy-density functional [133].

Quadrupole moments in the TFFS formalism are determined in a similar way, through the diagonal matrix element for a single quasi-particle state [136, 139],

$$Q_\lambda = \langle\lambda|V(E2;\omega=0)|\lambda\rangle \tag{5.8}$$

where the effective field, $\hat{V}(E2;\omega)$, follows an equation similar to Equation 5.7, but the terms are now matrices. The field for the quadrupole moment follows the E2-operator (Equation 2.6) expressed in terms of the spherical tensor component Y_{20} [16, 136],

$$\hat{V}_0(\mathbf{r}) \propto \begin{pmatrix} e_q\sqrt{\frac{16\pi}{5}}r^2Y_{20}(\mathbf{n}) \\ 0 \\ 0 \end{pmatrix}. \tag{5.9}$$

Phonon-coupling (PC) corrections to magnetic moments are introduced as a perturbation to the TFFS matrix element, $V_{\lambda'\lambda} = (\phi_{\lambda'}, V(M1)\phi_\lambda)$, up to second order in the phonon-creation vertex strength, g_L^2, which takes the form [135],

$$\begin{aligned}\delta^{(2)}V_{\lambda'\lambda} = (\delta^{(2)}\phi_{\lambda'}, V\phi_\lambda)) + (\phi_{\lambda'}, V\delta^{(2)}\phi_\lambda) + (\delta^{(1)}\phi_{\lambda'}, V\delta^{(1)}\phi_\lambda) + (\phi_{\lambda'}, \delta^{(2)}V\phi_\lambda) \\ + (\delta^{(1)}\phi_{\lambda'}, \delta^{(1)}V\phi_\lambda) + (\phi_{\lambda'}, \delta^{(1)}V\delta^{(1)}\phi_\lambda).\end{aligned} \tag{5.10}$$

The last two terms can be included in the TFFS. The first two terms lead to the 'end correction' from second-order variations in the single-particle wavefunctions, $\delta V^{\text{end}}_{\lambda'\lambda}$ [134]. The central two terms lead to 'triangle' diagrams (GDD) for the phonon interaction with the effective field, $\delta V^{\text{GDD}}_{1,2}$, and phonon exchange, $\delta V^{\text{GGD}}_{\lambda'\lambda}$. The final correction takes the form,

$$\delta V = \delta V^{\text{end}}_{\lambda'\lambda} + \delta V^{\text{GGD}}_{\lambda'\lambda} + \delta V^{\text{GDD}}_1 + \left[\delta V^{\text{GDD}}_2 + \delta V_{\text{non-pole}}\right], \tag{5.11}$$

where $\delta V_{\text{non-pole}}$ contains all non-pole PC corrections. The two parts, δV^{GDD}_1 and δV^{GDD}_2, are two independent integrals in the direct M1-phonon interaction calculation. δV^{GDD}_1 grows regularly with ω while δV^{GDD}_2 has $1/\omega$ behaviour [136]. Three of the possible Feynman diagrams for the three interaction types are shown in Fig. 5.1. The magnitude of the first two terms are generally significantly larger than the GDD terms, but they have opposite signs and largely cancel each other [134].

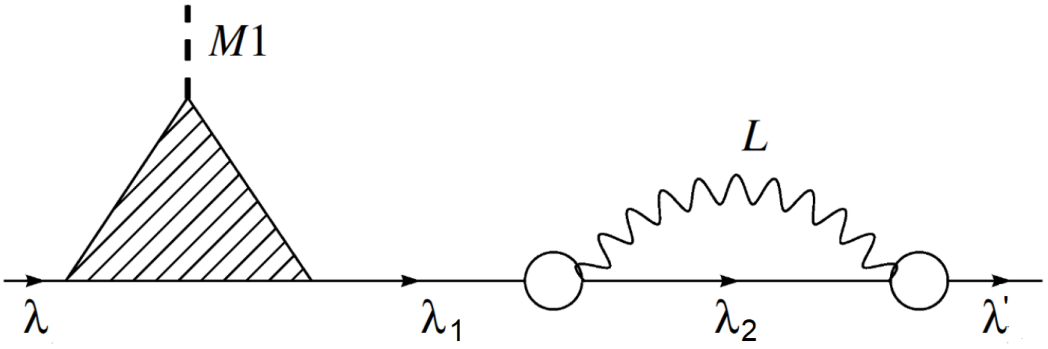

(A) $\delta V^{\text{end}}_{\lambda'\lambda}$

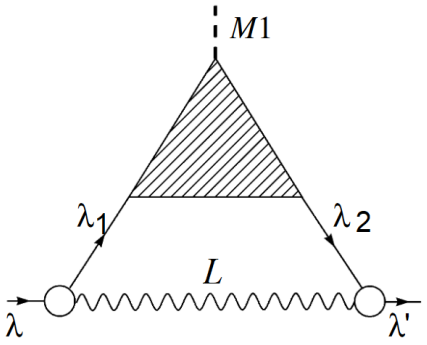

(B) $\delta V^{\text{GGD}}_{\lambda'\lambda}$

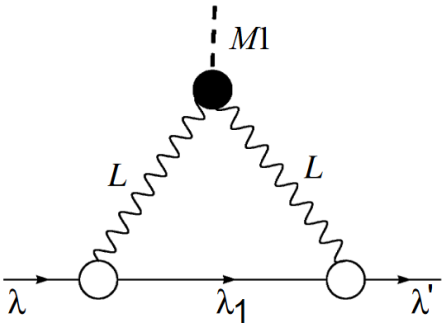

(C) $\delta V^{\text{GDD}}_{1,2}$

FIGURE 5.1: A subset of possible diagrams for phonon-coupling corrections to the magnetic moment of a single quasiparticle state to second order in the phonon creation amplitude, g_L (open circle vertices). The captions are the terms in Equation 5.11 to which the diagrams contribute. λ and λ' are the incoming and outgoing quasiparticles respectively. The wavy lines labelled L are the phonons. Figures adapted from [135].

The PC corrections to the quadrupole moments are introduced in the same way as for the magnetic moments as a second-order perturbation in g_L to $V_{\lambda'\lambda} = (\phi_{\lambda'}, V(E2)\phi_\lambda)$ [136]. This gives the same set of Feynman diagrams found in Fig. 5.1 with the M1 interaction replaced with E2. The final correction takes the same form as for the magnetic moments, found in Equation 5.11.

5.2 Magnetic moments in the odd proton- even neutron states

A number of different nuclear configurations are of interest in the neutron-deficient indium isotopes. The first that will be discussed in this chapter, and perhaps the simplest, is the ground states of the odd proton- even neutron isotopes. Historically, these have been considered to be one of the most clear manifestations of single-particle behaviour

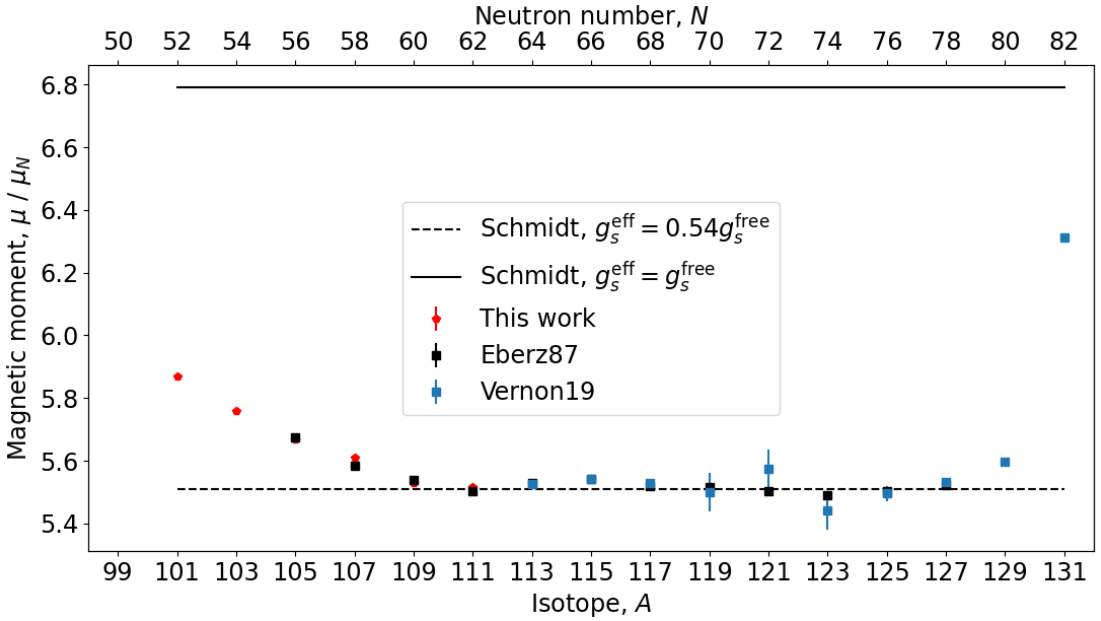

FIGURE 5.2: Comparison of the newly measured $I^\pi = 9/2^+$ magnetic dipole moments (red pentagons) to the literature values from Eberz et al. [15] (black squares) and previous CRIS measurements in the PhD thesis of A. R. Vernon [24] (blue squares). Schmidt values with two different quenching factors on g_s^π are compared to the data. The dashed black line has $g_s^\pi(\text{eff.}) = 0.54 g_s^\pi$ and the solid back line is the pure single particle $g_s^\pi(\text{eff.}) = g_s^\pi$. A more gradual increase in magnetic moment is observed for the neutron-deficient isotopes when compared to the sudden increase seen at $N = 82$.

in the nuclear chart [13]. The paired neutrons and single-proton hole in the $\pi\, 1g_{9/2}$ shell give rise to $I^\pi = 9/2^+$ ground-state configurations across the isotopic chain.

Given $\pi\, 1g_{9/2}$ is a $j = l + 1/2$ state, Equation 2.4 gives a naïve estimation of $\mu = +6.793\,\mu_N$ for the magnetic dipole moment in a pure single-particle picture, where there is zero contribution from the core and the free proton value of $g_s^\pi = +5.586$ is used. We can include the quenching effect of the surrounding medium on the proton moment by using an 'effective' g_s^π value, $g_s^\pi(\text{eff.})$ [16], accounting for the effects of nucleons not explicitly included in the model space [13]. Fig. 5.2 compares this single-particle 'Schmidt' value with $g_s^\pi(\text{eff.}) = g_s^\pi$ and $g_s^\pi(\text{eff.}) = 0.54 g_s^\pi$ to the literature dipole moments measured in [15] and to the values measured in this work. In the range $A = 111 - 129$, the single-particle picture holds up relatively well, with a constant moment following the quenched Schmidt moment. However, outside this range the dipole moments start to increase, gradually trending towards the pure single-particle value in the lighter isotopes and rapidly increasing at $N = 82$ [13].

Introducing collective contributions can start to explain this behaviour. Saperstein et al. in [134], for example, use a DF3 Fayans energy-density functional in a collective model to successfully predict the gradual increase in magnetic moment in the neutron-deficient isotopes below $N = 62$, as shown in Fig. 5.3. However, the calculations

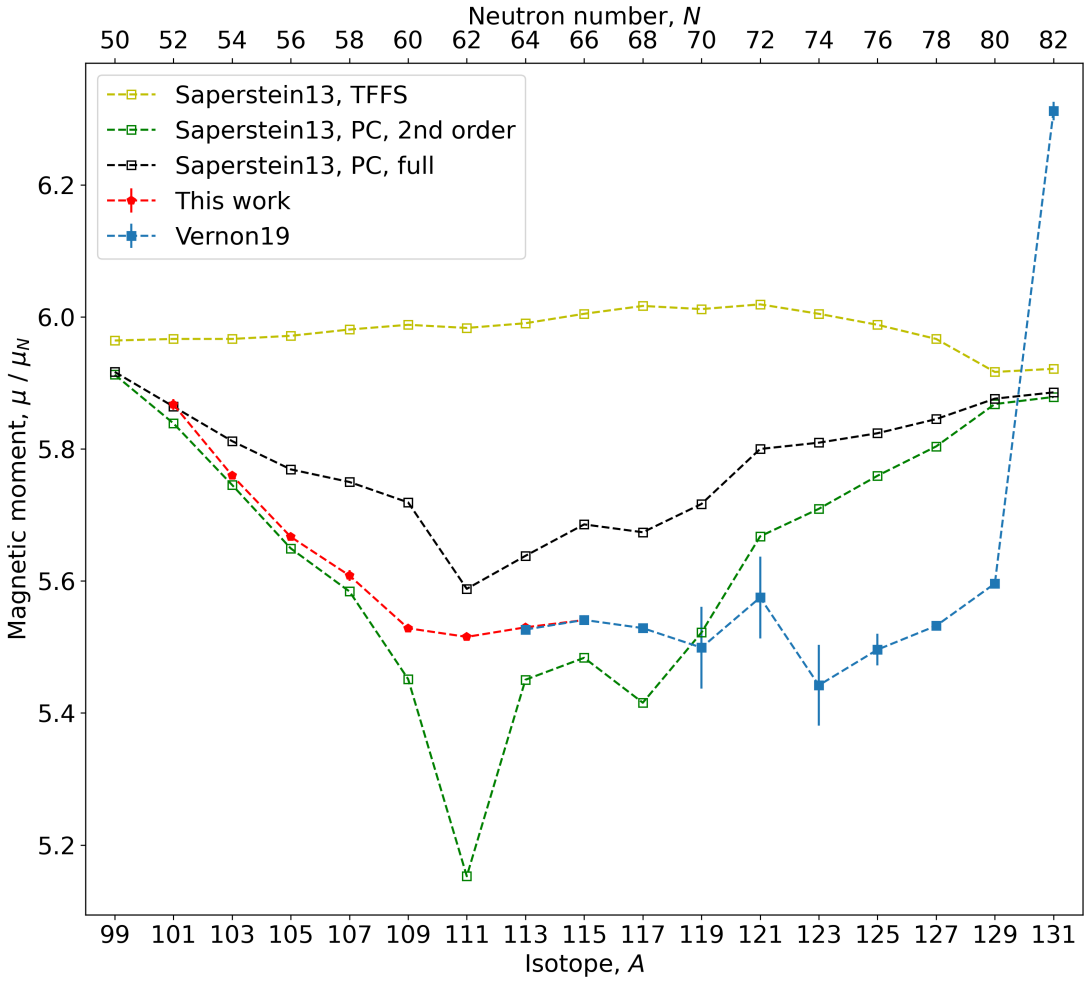

FIGURE 5.3: Comparison of the magnetic moments of the $I^\pi = 9/2^+$ states measured in this work (red pentagons) to the theoretical values determined by Saperstein et al. in [134] and the CRIS measurements reported in A. R. Vernon's thesis (blue squares) [24]. The yellow squares are the underlying theory of finite fermi systems values, the green squares include additional phonon-coupling corrections limited to second-order variations in the phonon-field matrix element, the black points include higher order corrections under additional assumptions detailed in the main text.

also predict a gradual increase from $N = 62$ to $N = 82$ which is not reproduced by experiment [24]. The figure also compares different stages in the development of the calculations, the difference between the yellow theory-of-finite-fermi-systems (TFFS) points and the phonon-coupling (PC) values showing the crucial impact of including the phonon-coupling corrections in the calculations.

The two sets of PC points differ in the introduction of an additional ansatz. Saperstein et al. [135] notes that when the external M1 field is $V_0 = \mathbf{j}$, through the conservation of angular momentum the total PC correction (Equation 5.11) should be zero. It can be analytically or numerically shown that the first four terms of the equation are independently zero, meaning the last two terms (in square brackets) cancel in this case. The

authors suppose that this cancellation is true for every M1 field, meaning the last two terms can be neglected in the general case. Here the experimental results show worse agreement with the black squares in Fig. 5.3, which use this additional ansatz, over the green squares which include all the terms in Equation 5.11.

The odd proton- even neutron isotopes also all have low-lying isomeric states with an $I^{\pi} = 1/2^{-}$ configuration. These appear in the shell-model picture when the single-proton hole moves down to the closely-spaced $\pi\, 2p_{1/2}$ orbital. Assuming single-particle behaviour, a constant magnetic moment would also be expected for these isomeric states. However, as Fig. 5.4 shows, this is not the case. Instead, a linearly decreasing trend in magnetic moment with neutron number is observed up to $N = 76$, before a rapid increase occurs to the $N = 82$ neutron shell closure. A continuation of the previously observed linear trend was measured towards the lighter isotopes in this work.

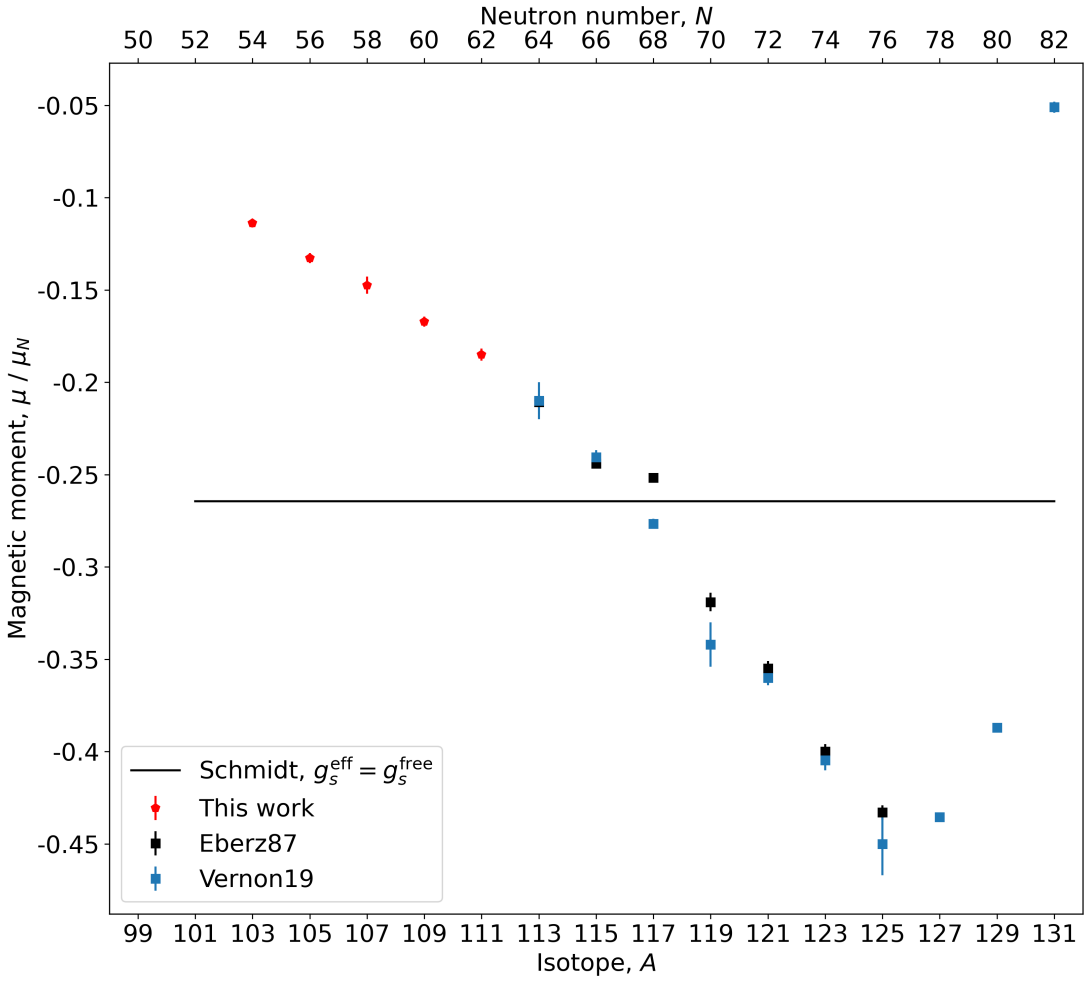

FIGURE 5.4: Comparison of the newly measured $I^{\pi} = 1/2^{-}$ magnetic dipole moments (red pentagons) to the literature values from Eberz et al. [15] (black squares) and previous CRIS measurements in the PhD thesis of A. R. Vernon [24] (blue squares). The pure single particle Schmidt value is shown as a black line.

5.3 Moments of the odd proton- odd neutron states

5.3.1 Magnetic moments

The additivity rule can be used to estimate the magnetic moment of odd proton- odd neutron states, assuming the state is 'composed' in a simple shell-model picture from a single-proton and a single-neutron hole or particle surrounding an inert core. For a state with nuclear spin I, the Clebsch-Gordon coefficients give a magnetic moment [16],

$$\mu(I) = \frac{I}{2}\left[\frac{\mu(I_\pi)}{I_\pi} + \frac{\mu(I_\nu)}{I_\nu} + (\frac{\mu(I_\pi)}{I_\pi} - \frac{\mu(I_\nu)}{I_\nu})\frac{I_\pi(I_\pi+1) - I_\nu(I_\nu+1)}{I(I+1)}\right] \tag{5.12}$$

where I_π and I_ν are the spins and $\mu(I_\pi)$ and $\mu(I_\nu)$ are the magnetic moments of the single-proton state and the single-neutron state respectively.

In the case of the even-mass indium isotopes with an odd number of protons and an odd number of neutrons, the cadmium and tin isotopes with paired protons and a single-unpaired neutron can be used as single-neutron states for $\mu(I_\nu)$. The ground state of ^{101}In is chosen for the single-proton state, being the lightest isotope measured here under the assumption that states closer to ^{100}Sn will have decreased collectivity relative to those in the mid-shell. Using the same logic, the lightest and heaviest tin and cadmium isotopes measured in literature, specifically ^{101}Cd [140] and ^{131}Sn [141], are chosen as single-neutron moments. The ground-state magnetic moment of ^{111}Sn from Eberz et al. [142] is also included to identify contributions of the $\nu 1g_{7/2}$ orbital. However, being far from either shell closure, this is likely also a collective state.

Fig. 5.5 shows a relatively good agreement is reached for the g-factors of the ground states of the neutron-deficient isotopes using a $\pi 1g_{9/2}^{-1} \otimes \nu 2d_{5/2}$ configuration, coupling the ^{101}Cd $I^\pi = 5/2^+$ to the ^{101}In $I^\pi = 9/2^+$. Calculations using the ^{131}Sn $I^\pi = 3/2^+$ and the ^{111}Sn $I^\pi = 7/2^+$ overestimate the g-factors. Nuclear g-factors are used here to allow for comparison between the various spin states.

The picture is less clear in the isomeric states, where a larger deviation is seen in the $I^\pi = 2^+$ states in particular. These may contain an increased admixture of other orbitals, potentially the $\nu 1g_{7/2}$ or $\nu 2d_{3/2}$. An increase in admixture with neutron number was predicted for the neighbouring Cd isotones [140]. An increasing contribution of the $1g_{7/2}$ orbital between $N = 59$ and $N = 61$ is also consistent with the assigned change in ground-state configuration of the tin isotopes, with $I^\pi(^{109}\mathrm{Sn}_{59}) = (5/2^+)$ and $I^\pi(^{111}\mathrm{Sn}_{61}) = 7/2^+$ (see Fig. 5.6) [143].

The excitation energies of states in the neighbouring isotones can also add to the discussion of possible admixtures in the odd-odd indium states. Fig. 5.6 shows a variety

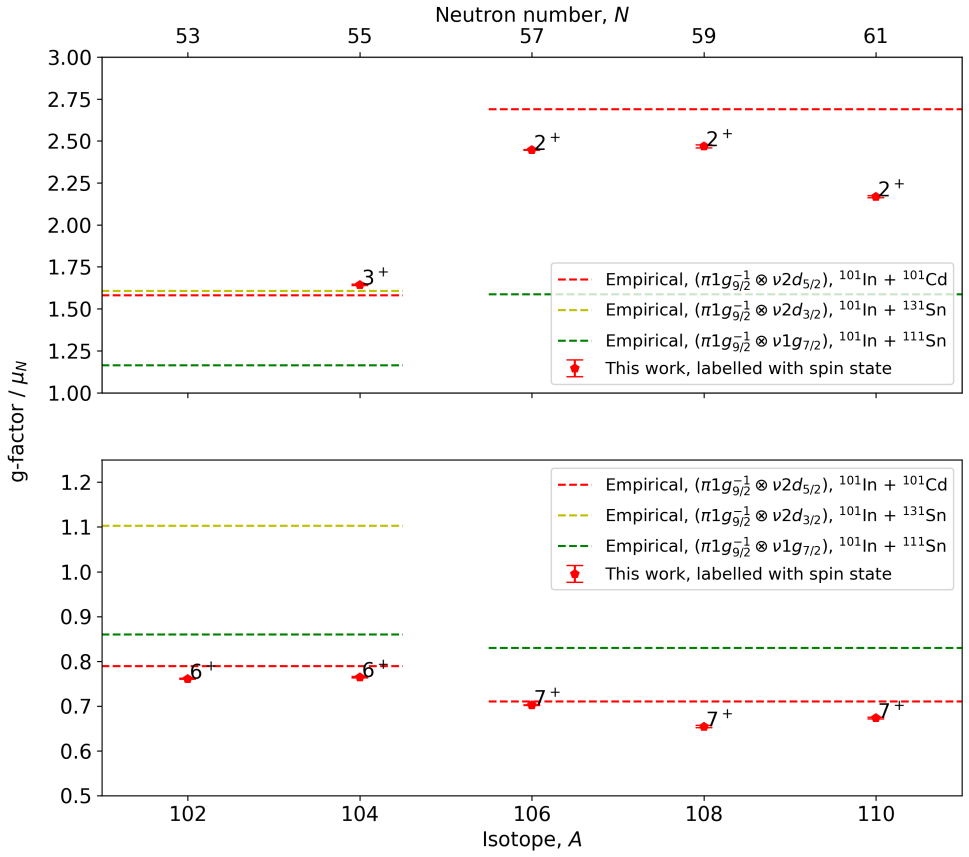

FIGURE 5.5: Ground (lower) and isomeric (upper) state g-factors of odd proton- odd neutron indium isotopes measured in this work (red pentagons) compared to empirical values (dashed lines) derived from the additivity rule (Equation 5.12). The red line combines the ^{101}In magnetic moment from this work ($I^\pi = 9/2^+$) as a proton moment, $\mu(I_\pi)$, with a ^{101}Cd measurement from [140] ($I^\pi = 5/2^+$) for the neutron moment, $\mu(I_\nu)$. The yellow line uses the ^{131}Sn value from [141] ($I^\pi = 3/2^+$) for $\mu(I_\nu)$, while the green line uses the ^{111}Sn value from [142] ($I^\pi = 7/2^+$) for the neutron moment. The values from this work are labelled with the assigned configuration of the indium state; these spin values were used for the total nuclear spin in the empirical calculations.

of these excitation energies in the even proton- odd neutron isotopes of tin and cadmium collated from [87]. For both elements, the ground states of the low-mass isotopes have assigned $I^\pi = 5/2^+$ from a relatively pure $\nu 2d_{5/2}$ configuration. The first excited $7/2^+$ state decreases in energy with increasing neutron number in both cases, reaching a minimum around $N = 57 - 61$, matching the increased $\nu 1g_{7/2}$ contribution to the indium isomeric admixture. In the mid-shell, $N = 59 - 73$, a variety of low-lying states exist with various configurations, indicating a more complex admixture. The ground state becomes $1/2^+$ for both elements at $N = 63 - 69$ from the dominant $\nu 3s_{1/2}$ orbital, before the $\nu 2d_{3/2}$ and $\nu 1h_{11/2}$ start to dominate in the heavier isotopes. The evolution of the $\nu 3s_{1/2}$ orbital in tin and cadmium is replicated in the excitation energies of the

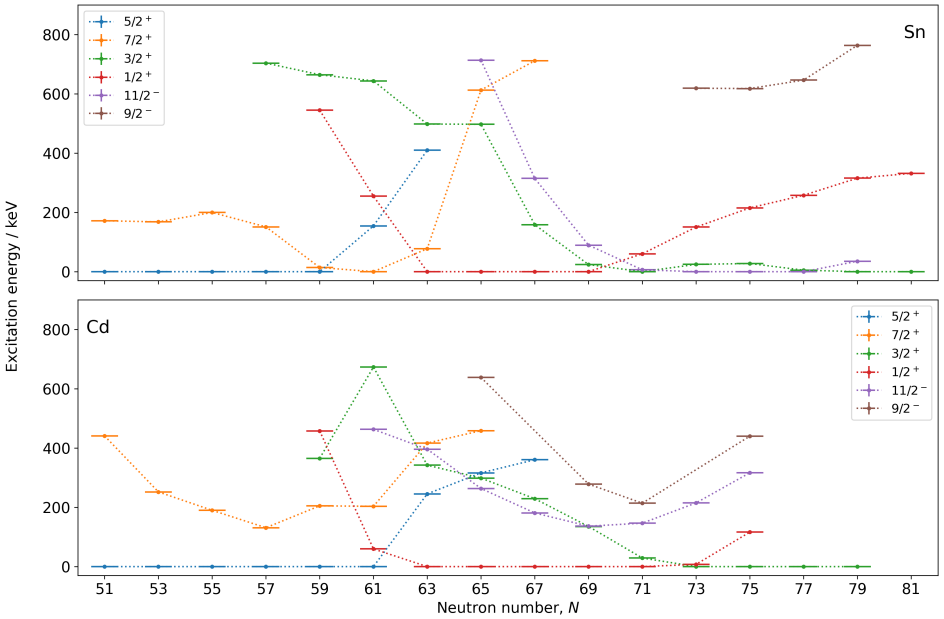

FIGURE 5.6: Excitation energies of states in Sn (upper) and Cd (lower) with odd neutron number from the most recent ENSDF evaluation [87]. The lowest-energy state with a particular spin-parity configuration (indicated in the legends) is included up to 770 keV, with the ground state for each isotope indicated by the point at zero excitation energy. The x-axis and the colours assigned to each spin-parity configuration are shared between the two sets of axes.

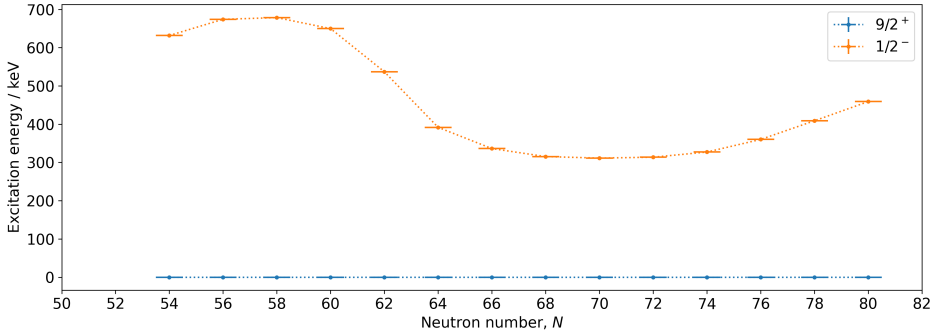

FIGURE 5.7: Excitation energies of the $I^\pi = 1/2^-$ states in indium from the most recent ENSDF evaluation [87] (orange points) with $I^\pi = 9/2^+$ ground states across the isotopic chain.

$I^\pi = 1/2^-$ states in indium, shown in Fig. 5.7.

Using CRIS measurements of the neutron-rich indium magnetic moments between ^{114}In and ^{131}In [24], we can also consider various configurations in these heavier isotopes. Measurements of the tin isotopes from [141] are considered for single-neutron states.

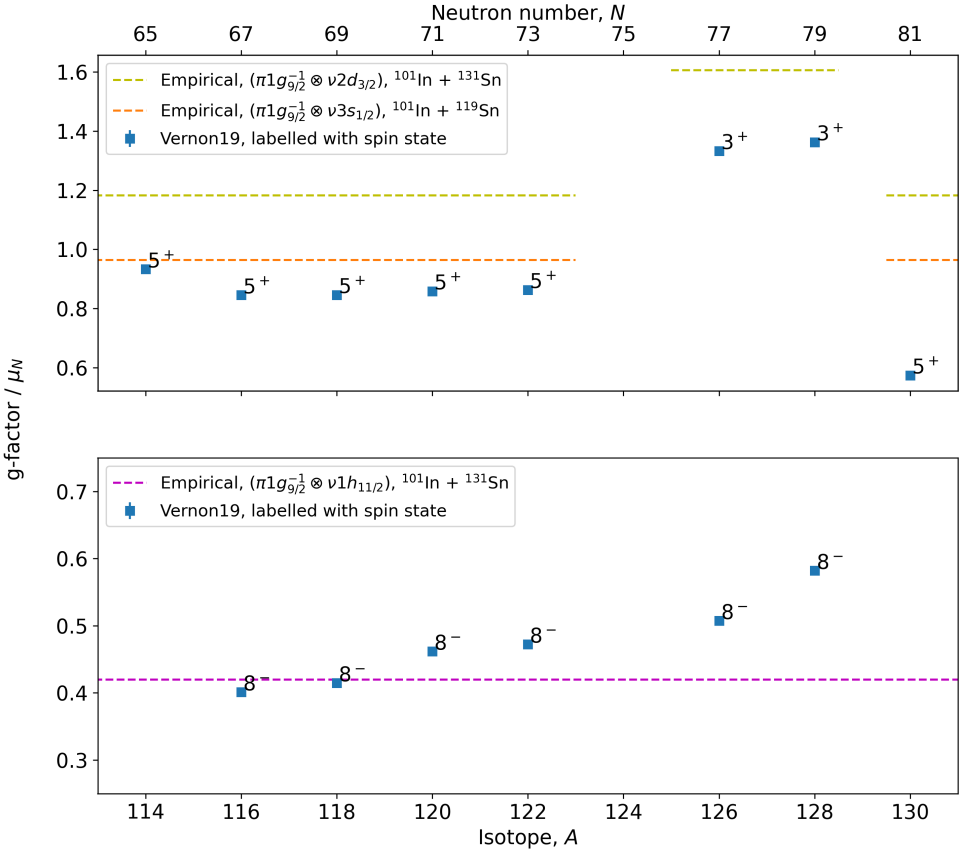

FIGURE 5.8: Ground (lower) and isomeric (upper) state g-factors of odd proton- odd neutron indium isotopes from CRIS measurements of the neutron rich indium isotopes in [24] (blue squares) compared to empirical values (dashed lines). The purple line combines the ^{101}In $I^\pi = 9/2^+$ moment from this work for the proton $\mu(I_\pi)$ with the ^{131}Sn $I^\pi = 11/2^+$ moment from [141] for the neutron $\mu(I_\nu)$. The yellow line uses the ^{131}Sn $I^\pi = 3/2^+$ for $\mu(I_\nu)$ and the orange line uses the ^{119}Sn $I^\pi = 1/2^+$ for the neutron moment, both also from [141]. The values are labelled with the assigned configuration of the indium state which was used in the empirical calculations.

The ground-state magnetic moment of ^{101}In from this work is used again as the single-proton value. Fig. 5.8 shows the result of the additivity-rule calculations. Here the $I^\pi = 5^+$ states follow the $\nu 3s_{1/2}$ configuration values relatively well for $N = 65 - 69$, while the $\nu d_{3/2}$ value overestimates the 5^+ g-factors. The $I^\pi = 8^-$ states gradual diverge from the $\nu h_{11/2}$ values with increasing neutron number. The g-factors of the $I^\pi = 3^+$ states in $N = 77, 79$ are not well reproduced by any of the empirical calculations, the closest being the $\nu d_{3/2}$ calculations which overestimate the values. The g-factor of the 5^+ state in $^{130}\text{In}_{81}$ decreases significantly relative to the 5^+ states in the lighter isotopes.

5.3.2 Quadrupole moments

An additivity rule also exists for coupling single-particle proton and neutron quadrupole moments for odd-odd nuclei [13]. Here, for a state with nuclear spin I,

$$Q(I) = \begin{pmatrix} I & 2 & I \\ -I & 0 & I \end{pmatrix} (-1)^{I_\pi + I_\nu + I}(2I+1) \times \left[\frac{\begin{Bmatrix} I_\pi & I & I_\nu \\ I & I_\pi & 2 \end{Bmatrix}}{\begin{pmatrix} I_\pi & 2 & I_\pi \\ -I_\pi & 0 & I_\pi \end{pmatrix}} Q(I_\pi) + \frac{\begin{Bmatrix} I_\nu & I & I_\pi \\ I & I_\nu & 2 \end{Bmatrix}}{\begin{pmatrix} I_\nu & 2 & I_\nu \\ -I_\nu & 0 & I_\nu \end{pmatrix}} Q(I_\nu) \right], \tag{5.13}$$

where $Q(I_\pi)$ and $Q(I_\nu)$ are the quadrupole moments of the single-proton and single-neutron states respectively and the {} and () matrices represent the Wigner-6j and Wigner-3j symbols respectively.

To determine empirical moments for the even-mass indium isotopes, isotopes in the neighbouring elements are again used for the single-neutron states, specifically the quadrupole moments of ^{101}Cd and ^{131}Sn measured by Yordanov et al. [140, 141]. These were combined here with the quadrupole moment of the $9/2^+$ state in ^{101}In measured in this work for the proton moment, $Q(I_\pi) = 0.507(12)$ b. Fig. 5.9 shows the comparison of the measured quadrupole moments of the even-mass states to the resultant empirical moments. Collective effects are larger in the quadrupole moments [124], as can be seen for example in the calculations by Heyde in the odd-even indium $I^\pi = 9/2^+$ states (Fig. 2.1 vs. Fig. 5.10), meaning the agreement is less good here than in the dipole moments. The quadrupole moments of the ground states appear to approach the $\nu 2d_{5/2}$ value, decreasing with neutron number towards $N = 50$.

5.4 Collectivity from ground state properties

We can also probe the evolution of single-particle behaviour by considering the quadrupole moments of the odd proton- even neutron $I^\pi = 9/2^+$ ground states. A relatively constant behaviour is also observed in these moments around the mid-shell, with values of $Q_s \approx 0.8$ b reported [15, 114]. However, here Heyde predicted a significant contribution of collectivity, approximately 60% of the overall theoretical values [126], observing the decreasing particle-core coupling strength approaching the two shell closures. Fig. 5.10 clearly shows this effect, with decreasing quadrupole moments in isotopes with $N > 70$ and $N < 56$, in the literature values from [15] and [24] and in the values determined

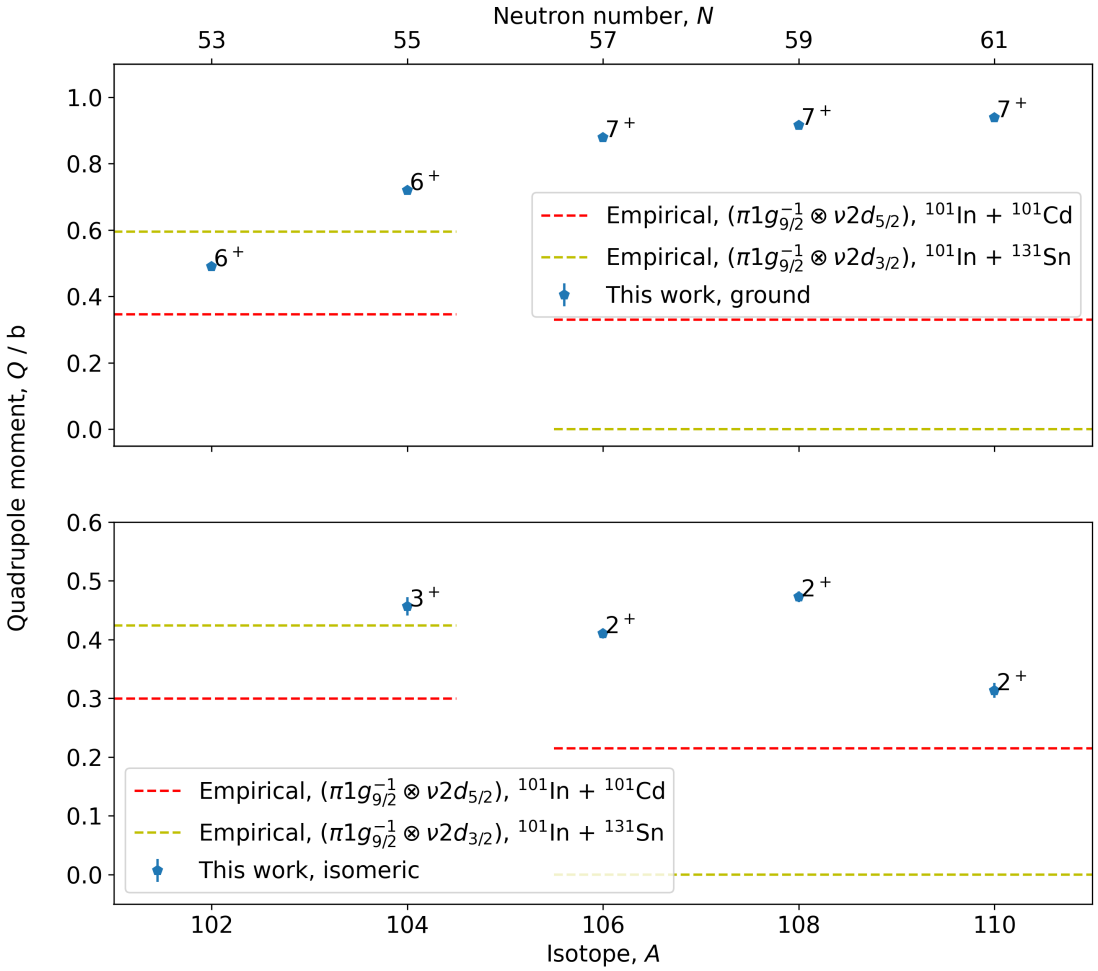

FIGURE 5.9: Quadrupole moments of odd proton- odd neutron indium isotope ground states (upper) and isomeric states (lower) measured in this work compared to empirical values (dashed lines) derived from the additivity rule (Equation 5.13). The red line combines the quadrupole moment of ^{101}In $I^{\pi} = 9/2^{+}$ measured in this work as the proton moment, $Q(I_{\pi})$, with the ^{101}Cd $I^{\pi} = 5/2^{+}$ value from [140] for the neutron moment, $Q(I_{\nu})$. The yellow line replace the neutron moment with the ^{131}Sn $I^{\pi} = 3/2^{+}$ value from [141]. The values from this work are labelled with the assigned configuration of the indium state.

from this work respectively. The figure also includes the particle-core coupling calculations by Heyde et al. [144] extracted from [126], with the single-particle and collective contributions individually labelled. The measured quadrupole moment approaches the level of the theoretical single-particle quadrupole moment at the $N = 82$ shell closure. Equal values are observed at $N = 52$ and $N = 80$, suggesting a similar strength of the two shell closures.

The effect of decreasing collectivity approaching the two doubly-magic nuclei is also clear in the $0_1^+ \rightarrow 2_1^+$ $E2$ transition strengths, $B(E2)$, of the even-mass tin isotopes which are shown in Fig. 5.11. A correlation is evident between the reported quadrupole moments and literature $B(E2)$ values collated from a variety of sources [121, 145–158]. The two

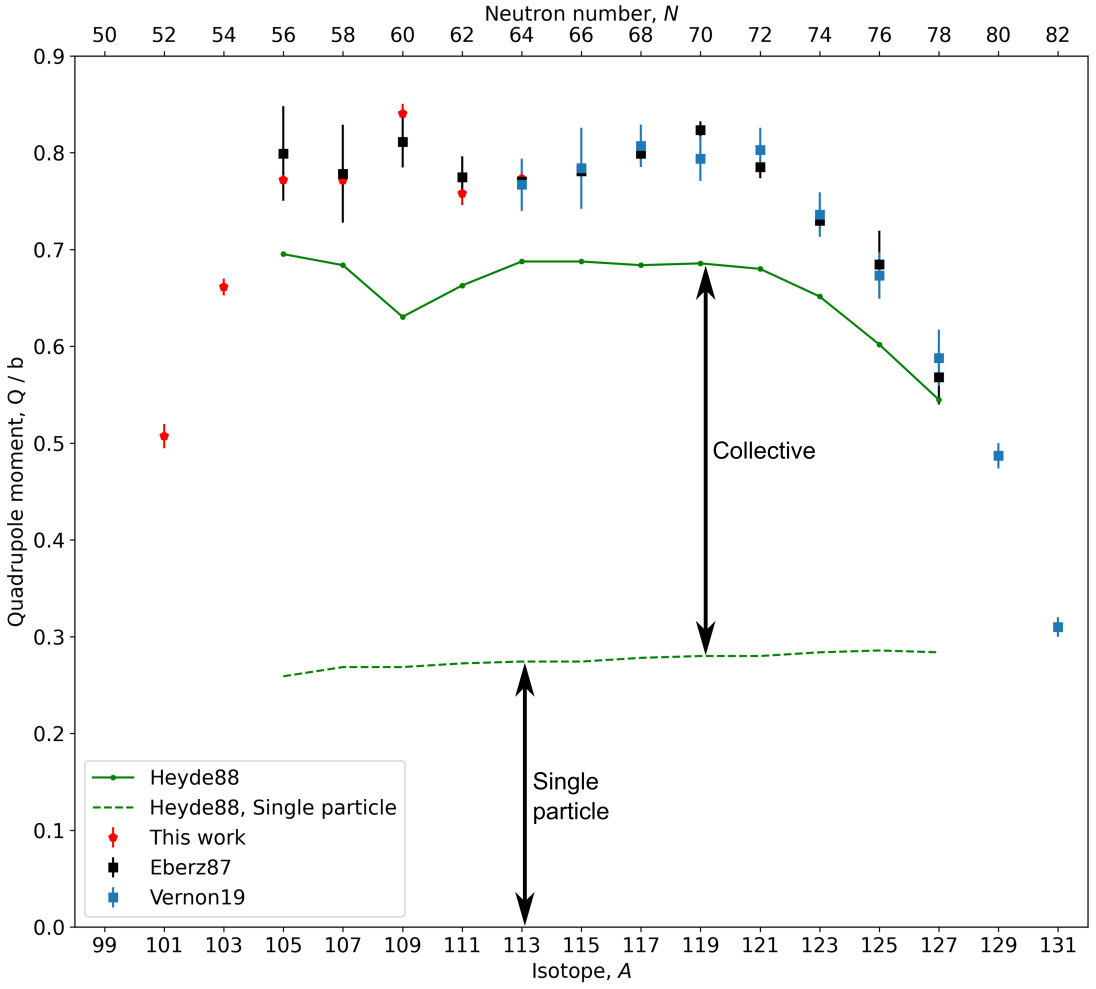

FIGURE 5.10: Comparison of the measured quadrupoles of the $I^{\pi} = 9/2^{+}$ states in this work (red pentagons) to literature values from Eberz et al. [15] (black squares) and from previous CRIS measurements in the thesis of A. R. Vernon [24] (blue squares). The quality of spectroscopic data has improved between the measurements in Vernon and this work leading to the reduction in the size of the error bars. Multiple isomeric states were also observed in some of the neutron-rich isotopes. Particle-core coupling shell model calculations by Heyde et al. [144] are also included (green). These are separated into the single particle (dashed line) and collective contributions extracted from [126], with the total values shown as a solid green line.

sets of measurements, the $B(E2)$ values and the quadrupole moments, both indicate that the two doubly-magic nuclei at $N = 50$ and $N = 82$ follow the expected behaviour of good shell closures.

The correlation between the quadrupole moments and the $B(E2)$ values was quantified using a linear orthogonal-distance-regression fit, presented in Fig. 5.12. The ratio of the $B(E2)$ values to the excitation energies of the 2^{+} states, E_{ex}^{2+}, is used as the independent x-axis variable to remove the leading-order contribution of the excitation energy on the transition strength.

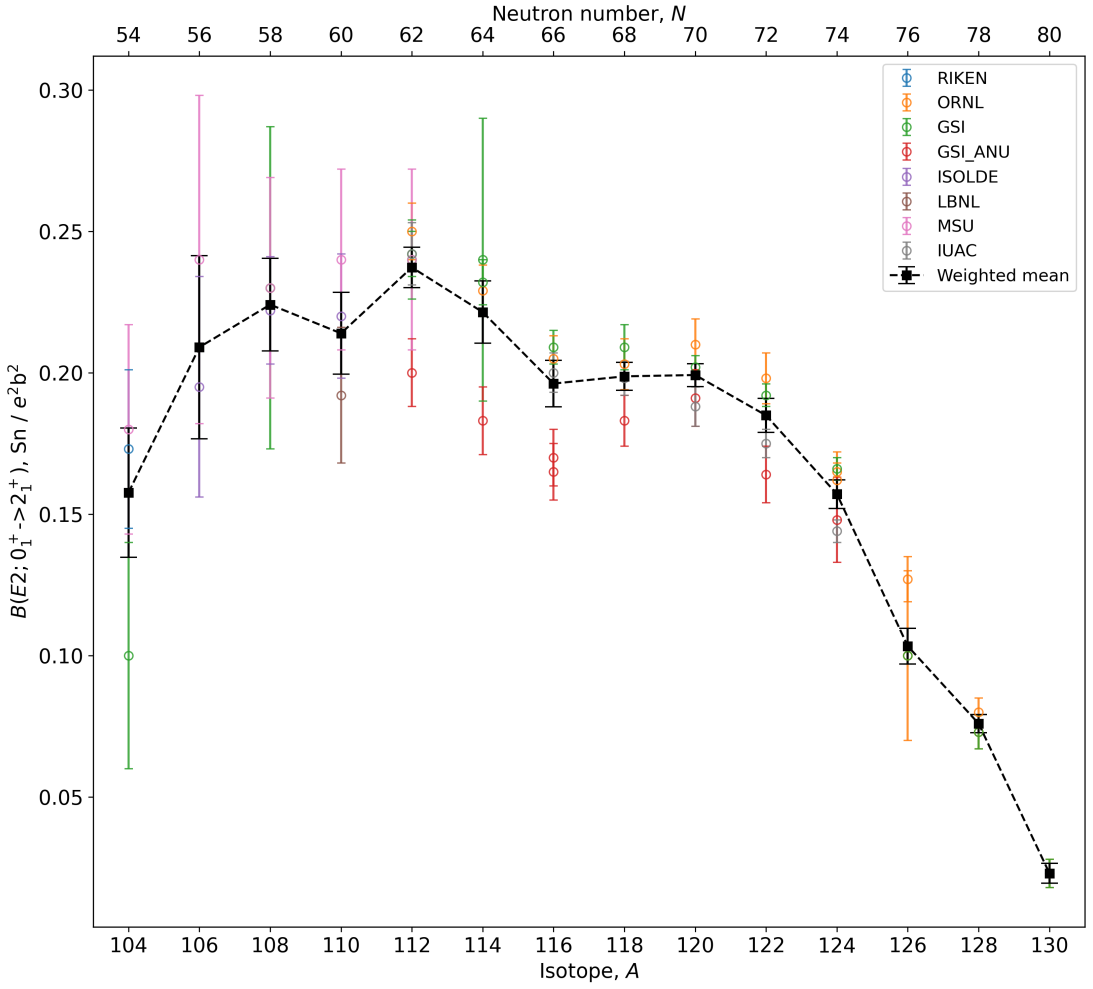

FIGURE 5.11: Measured $E2$ transition strengths in the even-even tin isotopes, $B(E2)$, from a variety of sources [121, 145–158] plotted against neutron number. The institute where the individual sets of measurements were performed is indicated in the legend. The black squares are the weighted means of the measurements for each isotope.

It has been suggested that the 'dip' in the previously measured quadrupole moments around $N = 64$ (see Fig. 5.10) could be indicative of a sub-shell closure at this neutron number [126]. However, the new measurements from this work and [24] make this dip less clear. It is unclear whether this dip exists in the $B(E2)$ strengths in the tin isotopes, due to the relatively large spread of measured values and the size of the error bars. The weighted mean of the $B(E2)$s in Fig. 5.11 must be considered with caution because systematic offsets are possible between $B(E2)$ values from measurements of state lifetimes and from Coulomb excitation. This is due to possible 'feeding' of the upper state leading to an overestimation of the state lifetime and therefore an underestimation of $B(E2)$ from lifetime measurements. In addition, $B(E2)$ values include effects from the excited 2^+ states as well as the ground states, so it is unclear which state the deformation comes from.

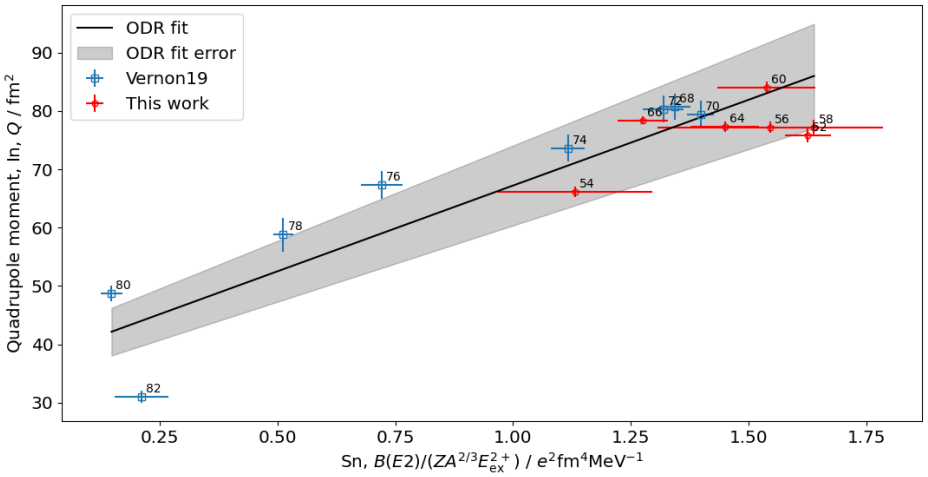

FIGURE 5.12: A plot of the ratio $B(E2)/(ZA^{2/3}E_{\mathrm{ex}}^{2+})$ determined from literature values [121, 145–158] vs the quadrupole moments of the corresponding isotonic $I^{\pi} = 9/2^{+}$ states from this work (red pentagons) and CRIS measurements in A. R. Vernon's PhD thesis (blue squares) [24]. The points are labelled with the neutron number. The black line corresponds to a linear orthogonal-distance-regression fit.

The quadrupole moments of the $I^{\pi} = 9/2^{+}$ states were also determined by Saperstein et al. using DF3-a Fayans energy-density functional calculations similar to those used to determine the magnetic moments [136,137]. Fig. 5.13 shows a comparison of these values to the experimental values determined from this work and from CRIS measurements in [24]. Here we again see the important contribution of the phonon-coupling corrections and the best agreement in the green squares where the corrections include all terms in Equation 5.11 and are limited to second order in the phonon-coupling constant, g_L.

5.4.1 Deformation parameters

Quadrupole nuclear deformation can appear in two forms: static deformation, where the nuclear shape remains constant with time, and dynamic deformation, containing the variation in the nuclear shape with time. The two can be combined to form a total deformation via,

$$\left(\beta_2^{\mathrm{total}}\right)^2 = \left(\beta_2^{\mathrm{static}}\right)^2 + \left(\beta_2^{\mathrm{dynamic}}\right)^2, \tag{5.14}$$

where β_2 denotes the components of the quadrupole deformation.

In a simple hydrodynamical model of the nucleus [16, 17], the intrinsic quadrupole moment, Q_0, appears due to the static part of the deformation and can be written as,

$$Q_0 = \frac{3}{\sqrt{5\pi}} eZR^2\beta_2^{\mathrm{static}}\left[1 + \frac{2}{7}\sqrt{\frac{5}{\pi}}\beta_2^{\mathrm{static}} + \pi^2\left(\frac{a}{R}\right)^2\right], \tag{5.15}$$

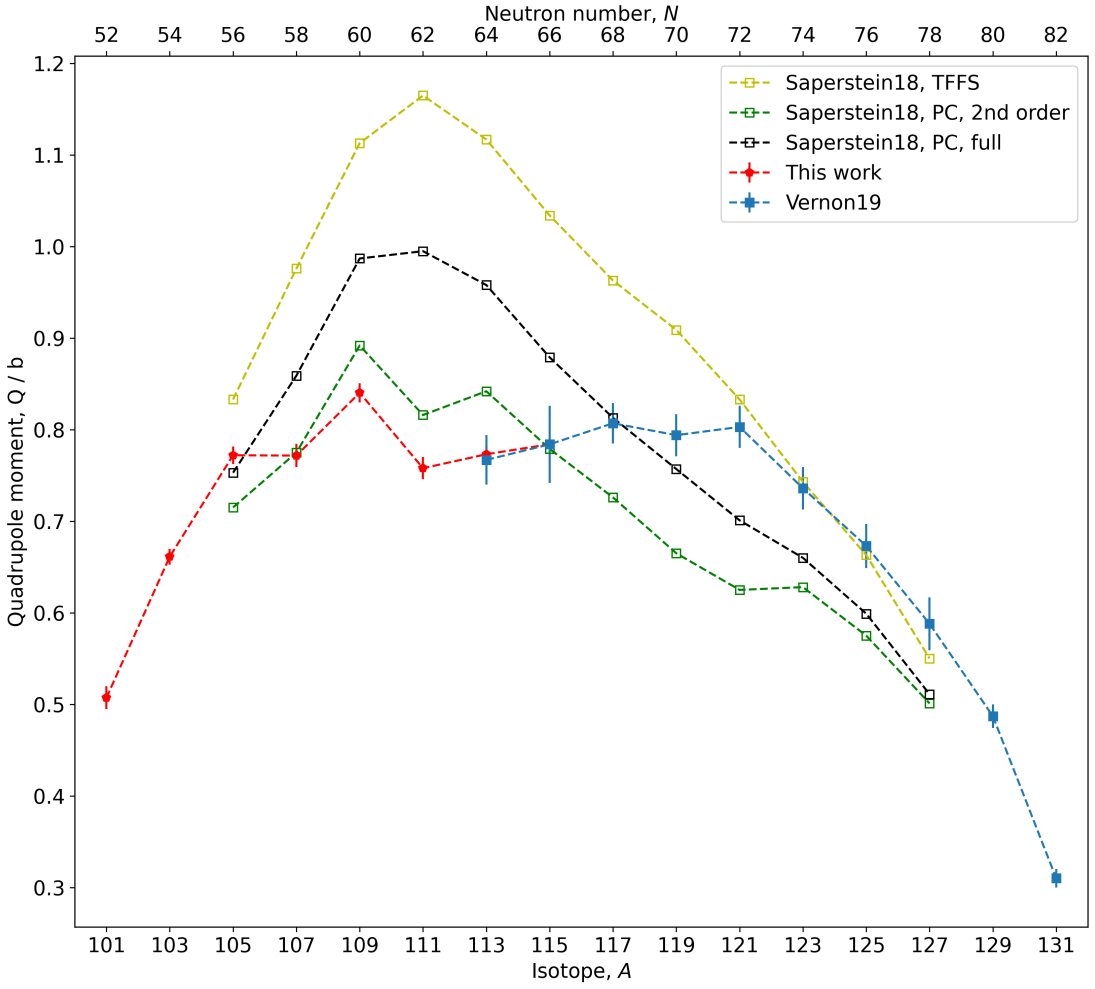

FIGURE 5.13: Comparison of the quadrupole moments of the $I^\pi = 9/2^+$ states measured in this work (red pentagons) and in A. R. Vernon's thesis (blue squares) [24] to the theoretical values determined by Saperstein et al. in [137]. The yellow squares are the underlying theory of finite fermi systems values, the green squares include additional phonon-coupling corrections limited to second-order variations in the phonon-field coupling constant, the black points include higher order corrections under additional assumptions.

where $R = 1.18A^{1/3}$ fm and a is the surface correction. The surface correction is typically small [16] so it is neglected here. Solving for β_2^{static}, this equation can be used to determine the static deformation parameter from measured spectroscopic quadrupole moments,

$$\beta_2^{\text{static}} = \frac{7}{4}\sqrt{\frac{\pi}{5}}\left[\sqrt{1+\frac{40}{21}\frac{Q_0}{eZR^2}}-1\right], \tag{5.16}$$

when combined with the strong-coupling projection, Equation 2.9, to convert to intrinsic quadrupoles. The sign of the static quadrupole deformation can be inferred from the sign of the measured spectroscopic quadrupole moment.

Fig. 5.14 shows a comparison of the results of these calculation applied to measurements

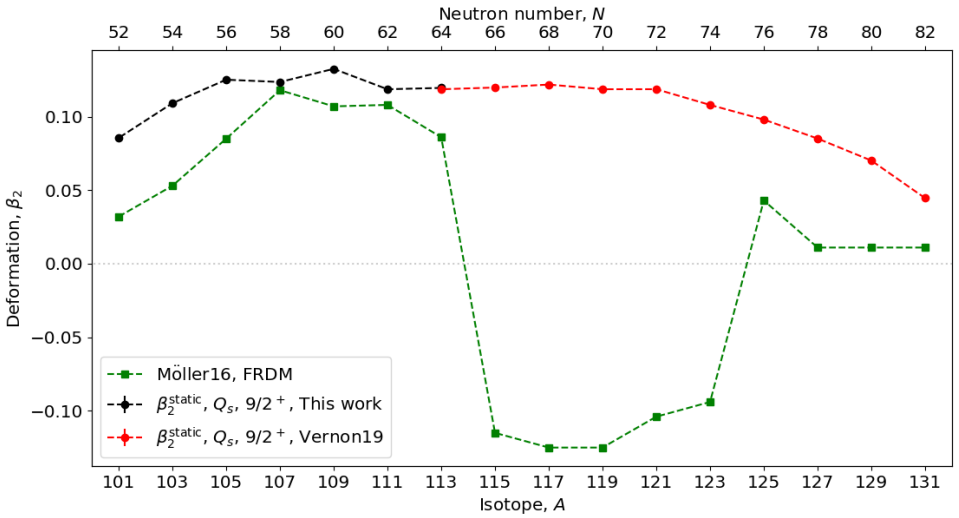

FIGURE 5.14: Static deformation parameters, β_2^{static}, determined from the quadrupole moments, Q_s, of the **odd proton- even neutron** $I^\pi = 9/2^+$ states measured in this work (black points) and in A. R. Vernon's thesis [24] (red points). Error bars are smaller than the points. These are compared to finite-range droplet model β_2^{total} values from [159] (green squares).

of the $I^\pi = 9/2^+$ states in the odd proton- even neutron indium isotopes. The static deformation values, β_2^{static}, determined from spectroscopic quadrupole moments through Equation 2.9 and Equation 5.16, are compared to the absolute β_2 values from finite-range droplet model (FRDM) calculations by Möller et al. in [159]. These FRDM calculations are a more recent formulation of the droplet model discussed in Section 5.1.1 and Section 5.4.2, containing additional terms and updated model parameters. The calculations return values of the same order as the static deformations in the mid-shell isotopes $58 \leq N \leq 70$, but predict a change in sign of the deformation which is not observed in the experimental quadrupole moments. The calculations also underestimate the deformation towards the two shell closures, so overall they predict a small dynamic deformation contribution. Fig. 5.15 shows the results of the same calculations applied to the odd proton- odd neutron ground states. The differential evolution in the $N = 53-61$ and $N = 67-73$ segments of the isotopic chain are relatively well reproduced by Möller et al. [159]. However, the magnitude of the predicted deformation is larger than the static deformation values for $N = 67 - 73$ and the sign is incorrectly predicted.

5.4.2 Nuclear charge radii

Another possible approach to consider evolution of deformation is to compare changes in mean-square charge radii directly to isodeformation lines, where certain values for the deformation parameters, $\beta_\lambda^{\text{total}}$, are assumed and the corresponding nuclear charge radii are calculated from the droplet model through Equation 5.3 and Equation 5.4.

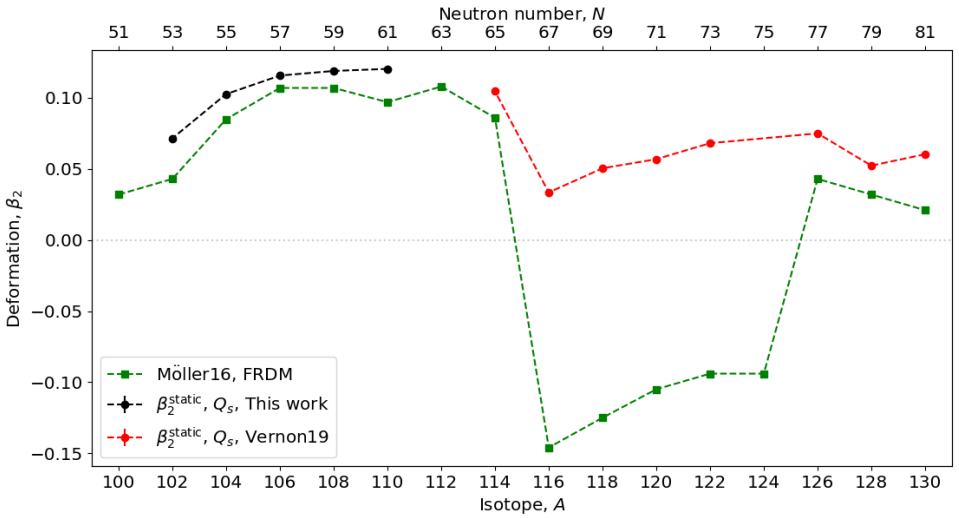

FIGURE 5.15: Static deformation parameters, β_2^{static}, determined from the spectroscopic quadrupole moments, Q_s, of the ground states of the **odd proton- odd neutron** isotopes measured in this work (black points) and in A. R. Vernon's thesis [24] (red points). Error bars are smaller than the points. These are compared to finite-range droplet model β_2^{total} values from [159] (green squares).

These calculations were performed here using the parameter values listed in Table 5.1, combined with a variety of total quadrupole deformation values. Higher-order deformation parameters (β_4, β_6 etc.) were taken as zero. The exact form of the equations is found in [127].

The experimental change in mean-square charge radius of ^{101}In was used to offset the droplet-model $\langle r^2 \rangle$ values, using the static deformation of ^{101}In (from Equation 5.16) in $\beta_2^{\text{total}}(^{101}\text{In}) = \beta_2^{\text{static}}(^{101}\text{In}) = 0.085514(4)$, to allow for a comparison to the $\delta\langle r^2 \rangle$ determined through this work. This comparison is shown in Fig. 5.16, where the changes in mean-square charge radii from CRIS work in [24] have also been plotted. A single point for each measured nuclear state is plotted, taking a weighted mean of the two evaluated radii where measurements were performed in both atomic transitions in this work and in [24].

Parameter	Value	Source	Description
ρ_∞	$0.159\,\text{fm}^{-3}$	[160]	Saturation density of symmetric infinite nuclear matter
b	0.99 fm	[127]	Nuclear diffuseness
a_2	18 MeV	[160]	Surface energy coefficient
J	29.5 MeV	[160]	Symmetry energy coefficient
Q	45 MeV	[160]	Effective surface stillness
K	240 MeV	[127]	Compressibility coefficient
L	-5 MeV	[160]	Density symmetry coefficient

TABLE 5.1: Parameter values used in the determination of isodeformation lines for Fig. 5.16. The source of the values and a short description of their meaning are also listed.

The variation in the total quadrupole deformation follows the expected parabolic trend across the indium isotopic chain, reaching a maximum of $\beta_2^{\text{total}} \approx 0.25$ around the mid-shell ($N = 62 - 68$) and decreasing to $N = 82$ and $N = 101$. $^{131}\text{In}_{82}$ takes the expected small prolate quadrupole deformation (from the proton hole in the doubly-closed shell) in this calculation. This would likely increase if the isodeformation lines were offset with the static deformation at the neutron-closed shell, ^{99}In, instead of ^{101}In, assuming the decreasing deformation with decreasing neutron number continues for $50 \leq N < 52$. The predicted non-spherical shape at the $N = 82$ shell closure would also vary with the droplet-model parametrisation (Table 5.1) leading to variation in the gradients of the isodeformation lines.

The differences in deformation between ground and isomeric states are small relative to the overall variation between isotopes, indicating no significant changes in shape are observed between the nuclear states of each isotope measured here.

Even given the arbitrary offset of the isodeformation lines, when Fig. 5.16 is compared to the static quadrupole deformation parameters shown in Fig. 5.14 and Fig. 5.15, it is also clear that the dynamic deformation makes up a significant proportion of the total around the mid-shell and that the calculations of Möller et al. in [159] underestimate the magnitude of the total quadrupole deformation in these isotopes in particular.

5.4.3 Odd-Even staggering

Another parameter which can be used to study smaller-scale effects in nuclear charge radii is the so called odd-even staggering (OES) parameter, or triple-difference radius, defined in [5] for example,

$$\Delta_r^{(3)} \equiv \frac{1}{2}(\delta \left\langle r^2 \right\rangle_{A+1} - 2\delta \left\langle r^2 \right\rangle_A + \delta \left\langle r^2 \right\rangle_{A-1}), \tag{5.17}$$

where $\delta \left\langle r^2 \right\rangle_A$ is the change in mean-square charge radius for an isotope with mass number A relative to a reference isotope. Fig. 5.17 shows this parameter evaluated from the individual radii changes determined from the 246.8-nm transition isotope shifts measured in this work compared to similar values in the neighbouring tin and cadmium isotones. A similar magnitude of odd-even staggering is observed for Cd and In in $N = 53 - 61$, and for Sn and In in $N = 59 - 61$. Charge radii values for the neutron-rich indium isotopes from CRIS measurements in [24] are also included, also determined from isotope shift measurements of the 246.8 nm transition. Here again a good agreement is found between the OES values of In, Sn and Cd in the range $N = 65 - 70$.

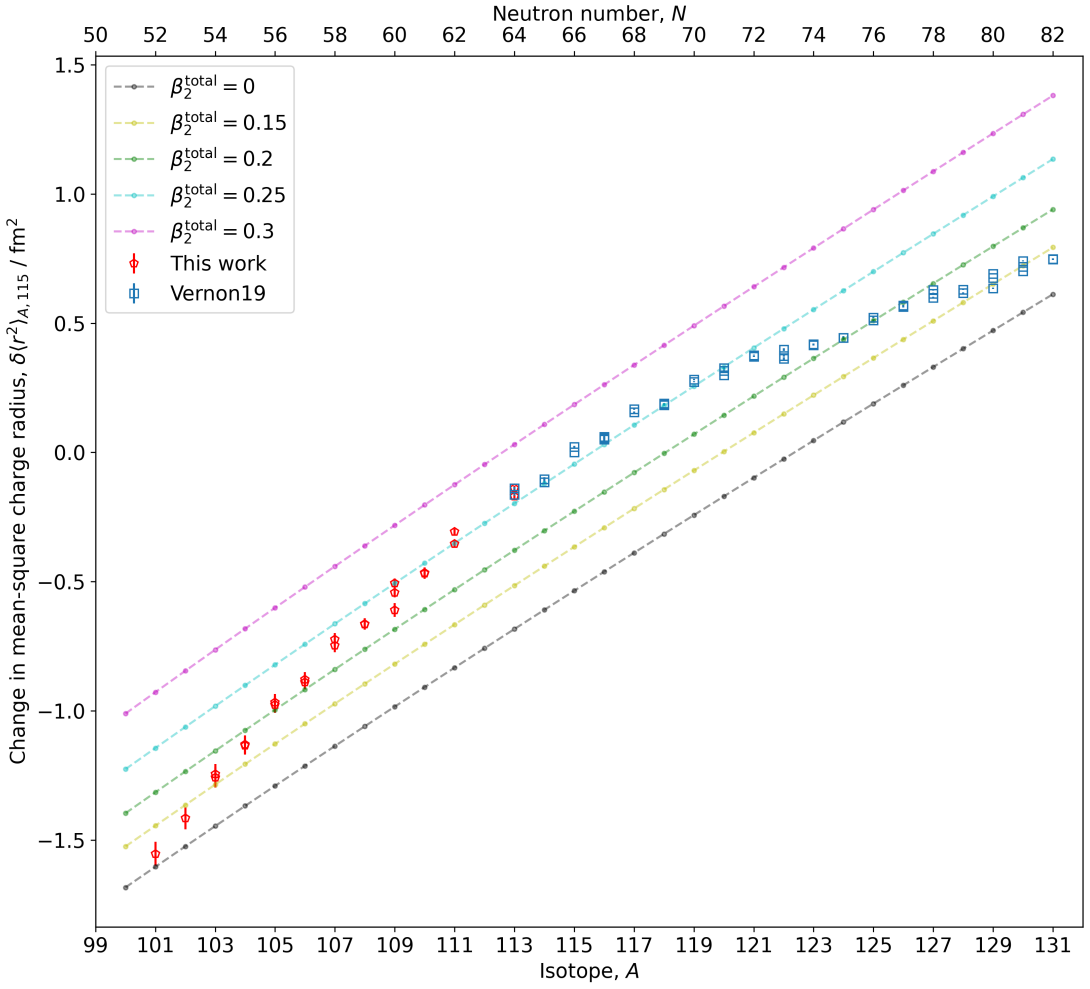

FIGURE 5.16: Changes in mean-square charge radii for the various nuclear states measured in this work (red pentagons) and in CRIS measurements reported in A. R. Vernon's thesis [24] (blue squares) in the range $^{101-131}$In. These are compared to isodeformation lines (dashed lines) where charge radii are calculated from the droplet model assuming certain values for the quadrupole deformation parameter, β_2^{total}, and taking model parameters from [127] and [160] (see Table 5.1). The β_2^{total} value used for each line is indicated in the legend. The droplet-model charge radii values are offset using the estimation $\beta_2^{\text{total}}(^{101}\text{In}) = \beta_2^{\text{static}}(^{101}\text{In}) = 0.085514(4)$ where β_2^{static} is from Equation 5.16.

The OES magnitude decreases for $N = 71 - 74$ for indium. A similar decrease in OES magnitude was recently observed in the $Z = 29$ copper isotopes (one proton outside the $Z = 28$ shell closure) approaching the $N = 50$ shell closure, shown in Fig. 5.18; the effect could not be reproduced by Fayans EDF calculations in copper [5]. It would be interesting to see whether this effect is observed in future results from the neutron-rich $Z = 51$ antimony isotopes also.

Unfortunately, no measurement of ^{112}In was taken in either this work or in [24] meaning a comparison to Cd and Sn in $^{111-113}$In, where the Cd and Sn OES deviate from each other significantly, is not possible. Values from Eberz et al. [15] are included in the

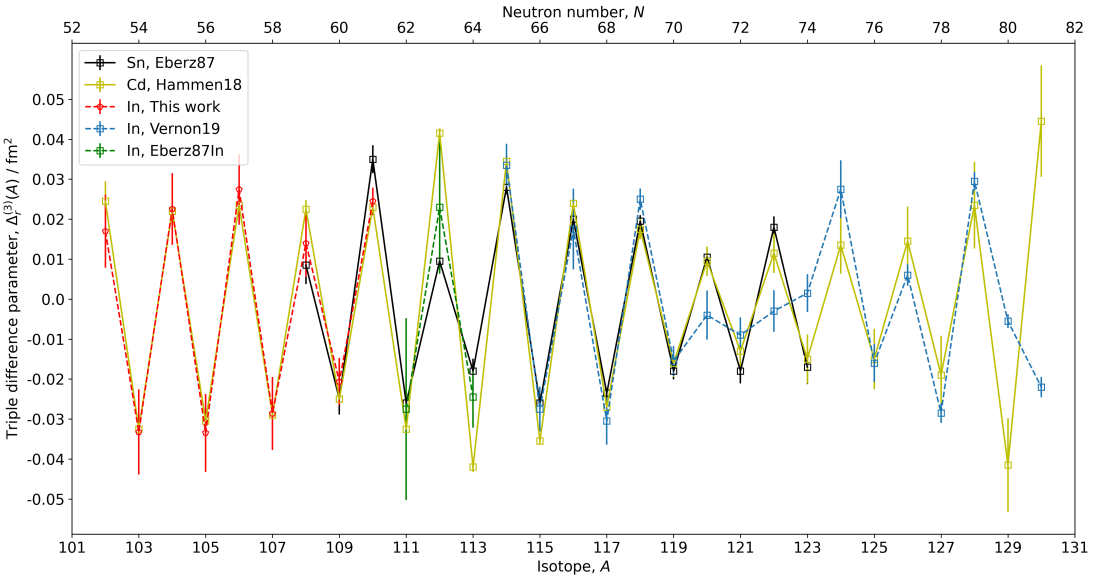

FIGURE 5.17: Triple-difference parameter in the indium nuclear ground states from this work for the 5p $^2P_{3/2}$ to 9s $^2S_{1/2}$ transition (blue pentagons) compared to isotonic literature cadmium (yellow squares) and tin (black squares) values from Hammen et al. [120] and Eberz et al. [142] respectively. Indium values for the neutron-rich isotopes (red pentagons) are also included from A. R. Vernon's thesis [24], in addition to values for $^{111-113}$In from Eberz et al. [15] (green squares).

figure for these isotopes and appear to fall between the Sn and Cd values. However, the uncertainties are large relative to the differences meaning it is difficult to form strong conclusions about the variations between isotones.

5.5 Results summary

The new results presented in this thesis have various impacts on the understanding of the nuclear structure of the indium isotopes. New measurements of ground-state magnetic moments for ^{101,102,103}In indicate a continuation of the previously observed upward trend away from the quenched Schmidt value. New measurements of isomeric-state magnetic moments were also recorded for most of the neutron-deficient isotopes, showing currently unexplained behaviours. New ground-state quadrupole moment and charge radii measurements were also recorded in $^{101-103}$In, confirming the strength of the $N, Z = 50$ double shell closure.

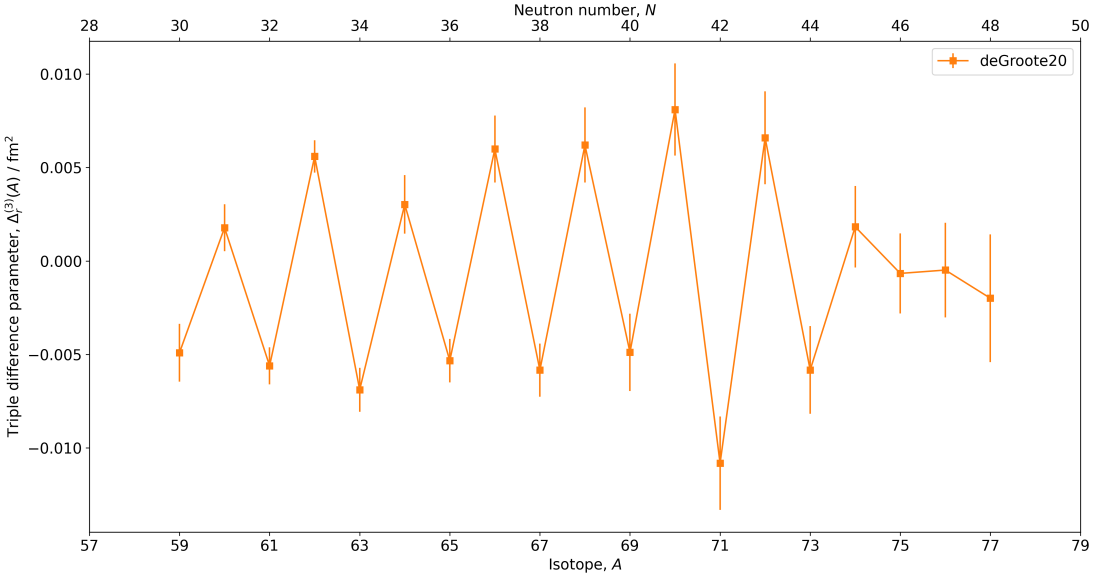

FIGURE 5.18: Triple-difference parameter in the copper nuclear ground states from CRIS measurements in de Groote et al. [5]. A similar reduction to indium in OES is observed for $N = 44 - 48$ approaching the $N = 50$ shell closure.

Chapter 6

Advances in sensitivity

6.1 Current limitations of the CRIS technique

The most-interesting future isotopic cases for the CRIS experiment, such as the isotopes in the ^{100}Sn region, often reside towards the limits of stability in the chart of nuclides. This means that they are produced at ISOLDE at very low rates, typically a few particles per second. Given the maximum mass-resolving power of the ISOLDE HRS is $m/\Delta m = 6000$ [63], isobars closer to stability (and therefore produced at many orders of magnitude higher rate) still contribute to the final ion beam and are in fact often the dominant contribution. The experimental challenges created by the low-production rates of the ions of interest and the significant isobaric components combined present the current experimental limits of the CRIS technique. To improve the reach and therefore the experimental impact of CRIS, new methods must be devised to increase the sensitivity and background suppression of CRIS. In this chapter, two possible development avenues will be described. Firstly, the development of an independent radio-frequency-quadrupole (RFQ) cooler buncher to complement or replace the function of ISCOOL (see Section 3.2.3) at CRIS. Secondly, the implementation of a field-ionisation setup as a replacement for non-resonant laser ionisation of resonantly excited atoms in the CRIS beamline, alongside an outline of the results of applying this technique to spectroscopy of the stable indium isotopes, working towards an extension of the nuclear structure results of this thesis.

6.2 A Cooler buncher for CRIS

6.2.1 Motivation

The ion-bunching technique described in Section 3.2.3 is essential to the sensitivity of the CRIS technique. Currently, ions are held in the ISOLDE ISCOOL ion trap before being periodically released at a repetition rate matching the duty cycle of the CRIS lasers. The release is timed so that the bunch is in the CRIS laser-atom interaction region when the series of laser pulses fire. This combination of precise timing and bunching maximises the number of ions which interact with the laser light, thus maximising efficiency. ISCOOL also contains helium gas at up to approximately 0.1 mbar pressure [7], which reduces the width of the distribution of ion energies during the trapping phase, leading to a reduction in the measured Doppler lineshape broadening when performing laser spectroscopy.

However, ISCOOL is a shared device, located on the HRS vacuum line and used by various experimental beamlines at ISOLDE. This means that preparation work, in conditions that match those found when running time-limited experiments on exotic isotopes, is currently not possible to perform in parallel with the running of other experiments at ISOLDE. In practice this means a large segment of time must be set aside at the start of CRIS experiments for setting up ISOLDE-dependent parts of the apparatus, primarily the ion-beam transport through the CRIS beamline and the spatial and temporal overlap of the ion beam and laser paths. The time-pressured nature of this work inevitably means that it will be sub-optimal, possibly leading to lower ion-transport efficiency and lower laser excitation and ionisation efficiencies.

Secondly, as exemplified in Chapter 4, periodic measurements of a single, usually stable, reference isotope are required in CRIS experiments to monitor long-term variations in laser-frequency measurement, to ensure accurate extraction of isotope shifts and hyperfine parameters from the measured spectra. Each time one of these reference measurements is required, typically every 2 to 8 hours, the magnetic field of the HRS mass-selecting magnets is changed from that optimised for the exotic isotope to the field required for transport of the reference isotope. This is a time consuming process, with each field change taking of the order of 7 minutes.

Using the example of the neutron-deficient indium experiment described in Chapter 4 and Chapter 5, assuming 7 minutes per mass change and using the scanning timestamp information, the fractional time spent performing each of these tasks was calculated. Fig. 6.1 shows the result, only 28% of the experiment was spent scanning hyperfine structure, including reference measurements, while 5% was spent changing the HRS magnetic field. The remaining time was spent in setup and optimisation, or was lost

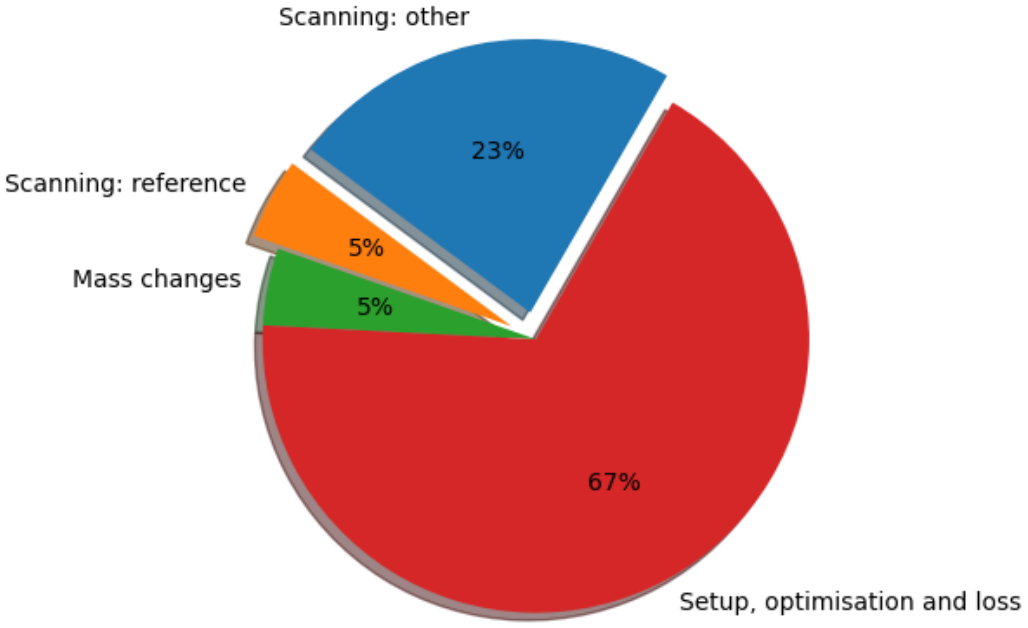

FIGURE 6.1: The fractional time performing various tasks during the neutron-deficient indium experiment on the 9th to the 16th April 2018 (see Chapter 4). The majority of the time was spent in setup, optimisation and fixing problems when they arose. 28 % of the time was spent scanning hyperfine structure, with 5 % on the reference isotope, ^{115}In. The remaining time was spent switching between HRS masses.

when equipment failed. The setup time was primarily dedicated to optimising the ion beam transport through the HRS separator magnets, ISCOOL and the CRIS beamline. Other contributions were from testing and faulty operation of the ISOLDE tape station (for the measurement of the decay of radioactive products) and optimisation of the RILIS lasers (see Section 4.1.1). Time was lost during the experiment due to a failure of the charge exchange cell (CEC) heating coil, issues with the ionisation laser and the pump laser for the M-squared SolsTiS seed laser, multiple failures of the 40 kV high tension on the HRS target, and losses of incident proton beam from the PSB due to accelerator magnet failures.

Clearly, both mass changes and setup/optimisation result in the loss of a significant amount of experimental time which could otherwise be used for the measurement of the most exotic isotopes with the lowest production rates. In these isotopes, extra measurement time would increase the precision of extracted nuclear observables and could potentially result in additional nuclear states being identified.

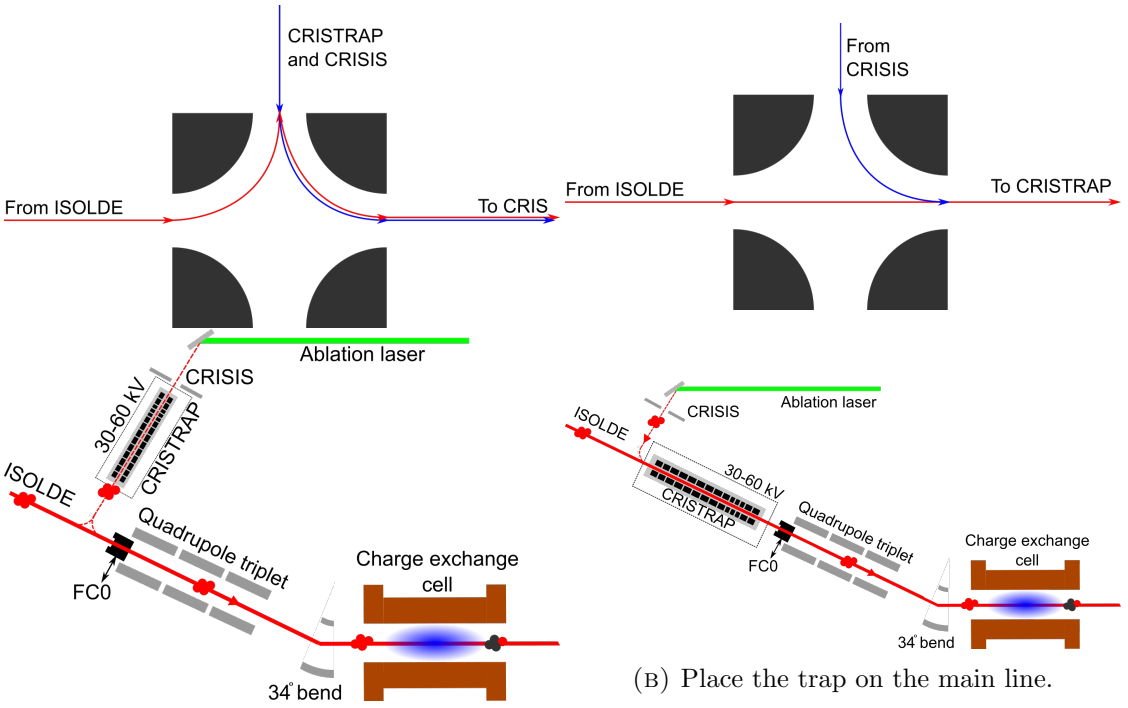

(A) Place the trap on the CRISIS line.

(B) Place the trap on the main line.

FIGURE 6.2: Two potential locations for a CRIS ion trap so that both the ISOLDE and CRISIS beams can be trapped, bunched and cooled. The use of an electrostatic switchyard is also shown for both cases (top). If the trap is on the CRISIS line (A), the ISOLDE beam enters and exits the trap on the same side. The CRISIS beam would enter on the opposite side. The ISOLDE beam can bypass the trap in this case. If the trap is on the main line (B), both beams pass through the trap and the trap cannot be bypassed.

A possible addition to the CRIS experiment currently being considered [161,162], which could potentially reduces these losses, is the installation of an independent ion trap cooler-buncher between the CRIS ablation ion source (CRISIS) and the charge exchange cell. Two possible locations for the trap are shown in Fig. 6.2. This trap would have the same function as ISCOOL during ISOLDE beam experiments: cooling the ion beam with a helium buffer gas, trapping and periodically releasing ion bunches for spectroscopy.

An independent ion trap would come with a number of advantages. Firstly, as the beam properties of the bunches leaving the trap are independent of the ion beam entering, the new cooler would decouple the CRIS beamline from the rest of ISOLDE. This would mean ions would have the same beam properties when leaving the trap, independent of whether they were created in one of the ISOLDE ion sources or in the CRIS ion source. This would allow for continuous optimisation of ion-beam transport efficiency, laser-atom overlap and ion-beam quality using the CRISIS, in the knowledge that the improvements made would transfer to ISOLDE beams. Performing this optimisation

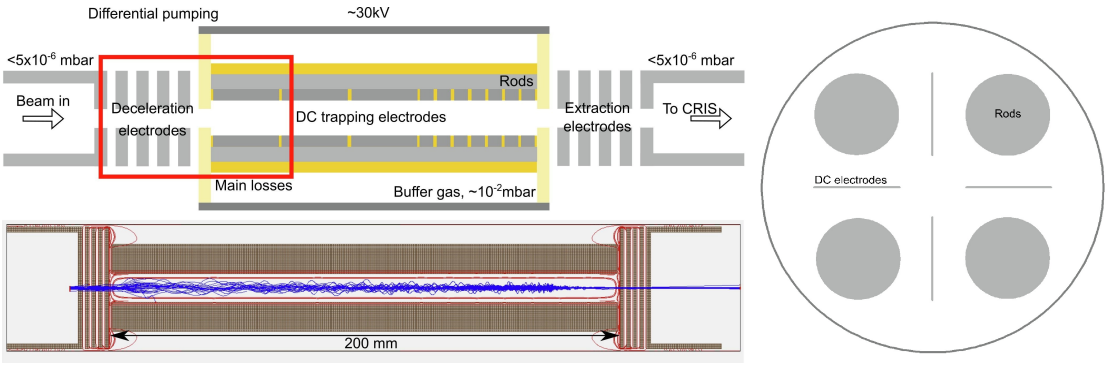

FIGURE 6.3: Possible design for the CRIS ion trap cooler buncher. Upper - Schematic representation showing the direction of ion travel, the deceleration and extraction electrodes, and the central trapping region. DC voltages would be applied to the PCB segments to trap longitudinally. 70% of the losses occurred in the red box in the simulation. Right - Cross section showing the rods and PCBs. RF voltages would be applied to the rods to trap radially. Lower - SIMION simulation showing ion trajectories for an $A = 70$ beam (blue) and equipotential contours (red). The central trapping region was 200 mm in length.

using the CRISIS and a CRIS ion trap would also significantly reduce the setup times required at the start of ISOLDE beam experiments.

Secondly, with an electrostatic switchyard, simple and fast switching between an ISOLDE beam and a CRISIS beam would be possible. This would mean the necessary periodic reference measurements of a stable isotope could be performed using a beam from the CRISIS, reducing the need for slow HRS mass switching and providing significantly more time for the measurement of the most exotic isotopes.

6.2.2 Design

Due to tight spatial constraints in the ion-source region of the CRIS beamline, a compact cooler-buncher design was envisaged. In the first prototype design described here (and shown in Fig. 6.3), a set of four 200 mm long cylindrical rods are used to create the quadrupole radial trapping field (see Section 3.2.3) through the application of an AC voltage. The inner radius of the rods is 5.3 mm, so to maintain a trapping parameter of $q = 0.5$ (Equation 3.8) with sufficient pseudo-potential depth, AC frequencies in the MHz range will be required. To produce these frequencies at the required voltage amplitude, two options are available: a resonant LCR circuit at fixed frequency or a H-bridge arrangement of MOSFET transistors driven by a low-voltage square wave, switching between two opposite-polarity high-voltage terminals.

To avoid segmenting the rods, the longitudinal trapping field will be applied using four printed circuit boards (PCBs) inserted between them, with copper pads arranged along the length and DC voltages applied to create the static electric potential well. This

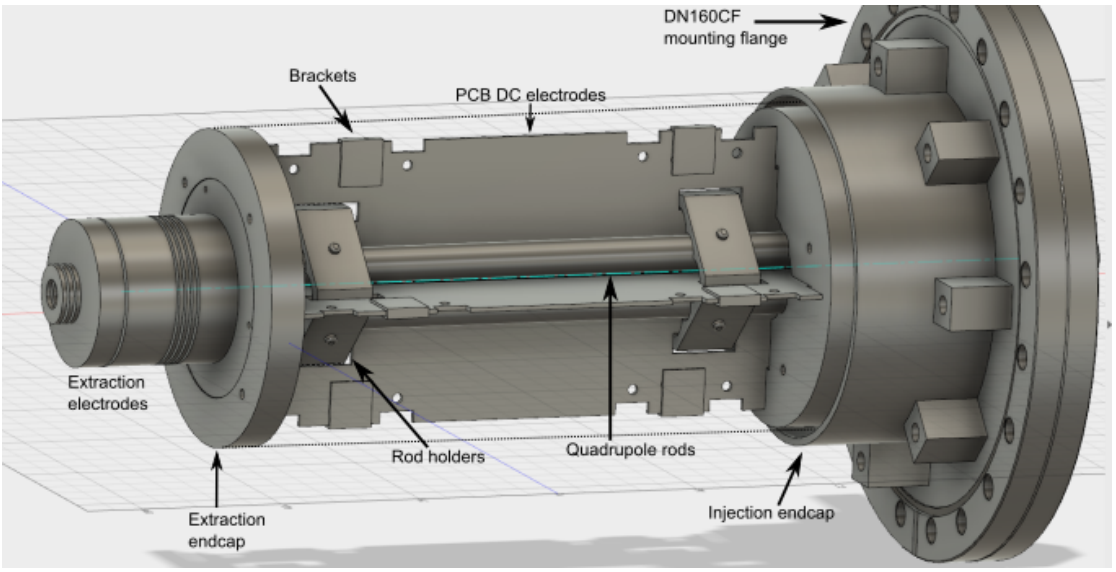

FIGURE 6.4: CAD drawing of the initial trap prototype. The injection endcap is a 3D printed piece onto which the quadrupole rods for RF and the PCBs for DC are mounted. The ion beam would enter through the bored mounting flange and exit through the extraction electrodes. The cylindrical region between the extraction and injection endcaps (dashed lines) is enclosed by a steel tube (not shown) to maintain buffer-gas pressure up to 0.1 mbar in the central trap region.

ensures the precise alignment of the rods along the full length of the trap. Initially, the individual segments will be connected to separate voltage supplies during optimisation. However, when an optimal arrangement of DC voltages is found, surface-mounted resistors could be installed in a series of voltage dividers, reducing the number of DC voltage supplies required.

The DC and AC voltages are applied on top of a platform floating voltage of at least 5 kV which is applied to all electrodes in the central trapping region. This decelerates the incoming keV energy ions so they can be captured by the buffer gas and trapping electrodes.

To perform buffer gas cooling of the trapped ions, the inner trap section will be connected to a helium gas feed to maintain an internal pressure of up to 0.1 mbar (determined from simulation). Flow rate calculations have indicated that the regions before and after the trap can be maintained at pressures below 1×10^{-5} mbar with this internal pressure, provided large $1000\,\mathrm{L\,s^{-1}}$ turbo pumps are used in these regions and input apertures of 1-3 mm diameter are used for the input and exit of ions.

For prototyping, the trap was mounted on 3D printed endcap pieces, printed from polylactic-acid (PLA) polymer. Vacuum tests in this work have demonstrated the vacuum compatibility of PLA, reaching pressures below 1×10^{-8} mbar [161, 162], meaning contamination of the helium buffer gas should not be significant. In these tests a vacuum

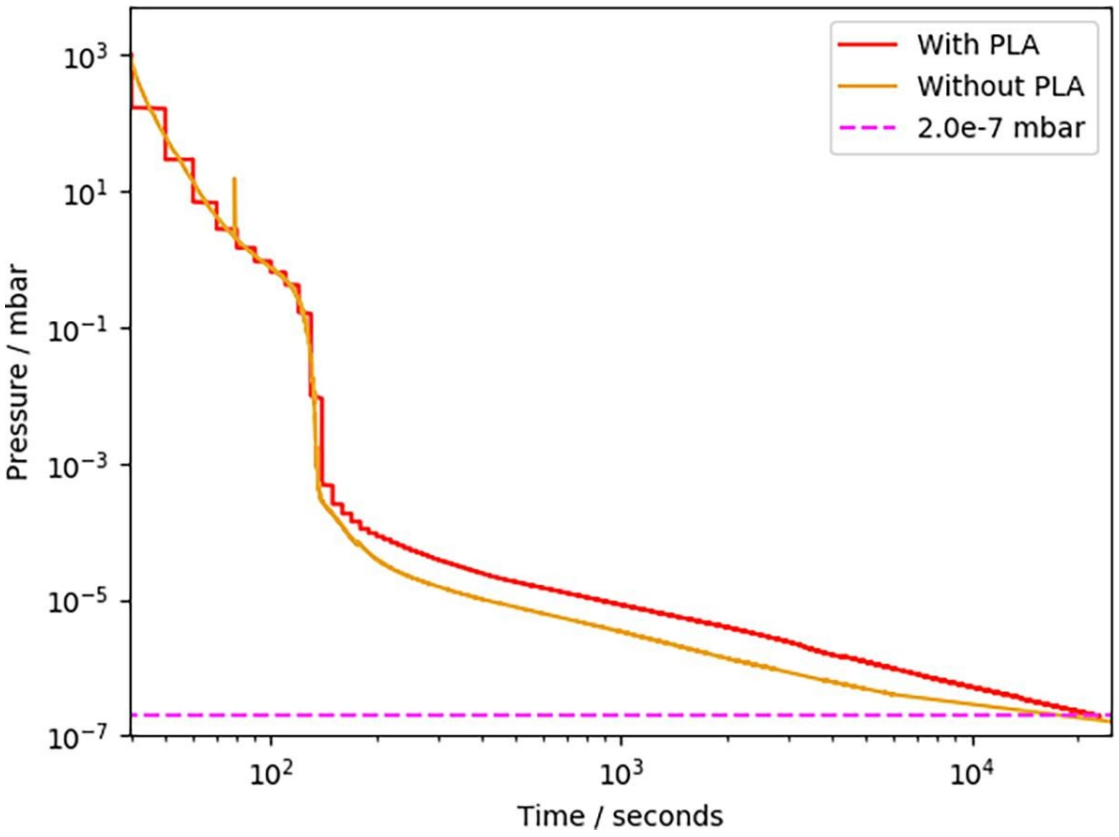

FIGURE 6.5: Pump down plot of pressure vs time for a vacuum chamber with and without a 20 mm side-length printed piece of polylactic-acid polymer. No significant change in pump-down time is seen.

chamber was pumped down with and without a 20 mm side-length piece of printed PLA. The pressure-plot result of the tests is shown in Fig. 6.5.

The polymer mounting pieces also act as the electrical insulators between the central, high-voltage section of the trap and the outer grounded mounting pieces. The dielectric breakdown strength of PLA at room temperature has been shown to be 6.2 MV cm^{-1} [163]; the minimum separation between the electrically-isolated sections is 5 mm in this design so electrical breakdown should not occur.

6.2.3 Simulation

The trap design was tested and optimised using the SIMION ion-tracing software package [164]. SIMION uses a method of successive over-relaxation to calculate 3D electric field contours and the resultant ion trajectories for given electrode voltages and ion initial conditions. In these simulations, a 30-keV ion beam at atomic mass $A = 12$ and $A = 70$ were input at a focus, with a 20 π mm mrad transverse emittance and a Gaussian transverse spacial profile with 0.5 mm standard deviation [161]. To decelerate the ions into the trap, a series of 1-mm separated planar electrodes were used in the model to

approximate a longitudinal potential structure of the form,

$$V(z) = V_0(1 - e^{-az}), \tag{6.1}$$

where V_0 is the platform voltage, set to produce a 100 eV ion energy at the start of the central trapping and cooling region, and a is a tuning parameter. This exponential deceleration structure can be shown [165] to produce a transverse focussing effect, with a first focal point at,

$$z_1 = \frac{4\pi}{a\sqrt{3}}. \tag{6.2}$$

The a parameter was varied in the range $(0.1 \leq a \leq 1.0)\,\mathrm{mm}^{-1}$ and the simulated ion-transmission efficiency into the central trapping region was recorded. Maximal injection efficiency was found with a value of $a = 0.4\,\mathrm{mm}^{-1}$.

The successfully injected simulated ions were guided down a longitudinal potential ramp into a static potential well, while being trapped radially with square-wave AC. The collisional cooling was simulated using the HS1 hard-sphere collisional model [166], with the collisional probability defined by the helium atomic radius and the internal pressure.

The simulated ions were held in the trap for 2 ms, before the output side of the longitudinal potential well was instantaneously lowered to create another potential ramp, allowing the ions to exit. An electrode structure identical to the input deceleration arrangement was included (reflected in the transverse plane) to re-accelerate the ions back to 30 keV. The recorded total transport efficiency through the trap, the 95 % input acceptance and the final transverse emittance are given in Table 6.1, also reported in [161].

Mass, A	Pressure / mbar	Transmission probability / %	Acceptance / π mm mrad	Output emittance / π mm mrad
12	0.012	11	10	16
70	0.034	54	20	1.5

TABLE 6.1: Simulated RFQ trapping parameters with total ion-transmission probabilities, the input-beam acceptance and output-beam emittance after reacceleration at optimised buffer gas pressures, as reported in [161]. A 30 keV focussed input beam with 20 π mm mrad transverse emittance and a Gaussian radial profile with 0.5 mm standard deviation was used. The ions were released after 2 ms trapping time.

Overall, the simulations and design studies indicated that a compact trap design was plausible, and further development of the design and implementation of this addition to the CRIS beamline was worth pursuing. Following this work, the design was implemented and preliminary ion-guide testing was performed [162]. Currently an even more compact design using PCBs as flat radial-trapping electrodes is under development in Manchester.

6.3 Field ionisation development

6.3.1 Motivation

Two factors must be considered when attempting to increase the sensitivity of the CRIS technique: increasing the ratio of the number of recorded resonantly-ionised ions to the yield of ions from the ISOLDE ion source, i.e. increasing efficiency, and reducing the number of non-resonant background counts. As discussed in Section 4.1.4, the primary loss in efficiency in the neutron-deficient indium experiment in particular was in the neutralisation of the ion beam into the probed atomic state. Unfortunately, this is difficult to improve upon because the population of the atomic states in charge exchange is a probabilistic process, dependent on the temperature and density of the alkali vapour which have been optimised [74].

Therefore, to improve sensitivity for the measurement of the most exotic indium isotopes, we must instead consider reducing the main sources of background. Again as discussed in Section 4.1.4, one of the main background sources in the indium experiment was the ionisation of atom-beam components through collisions with residual gas in the interaction region between the electrostatic deflection plates after the charge exchange cell and before the deflectors guiding ions to the charged-particle detector. To reduce this effect, we can consider either reducing the pressure in the region or reducing the volume where the ionisation is allowed to occur, thereby reducing the probability of interaction between a gas particle and an ion. For this reason, the pressure has been a main focus in the design of the interaction region since its inception. However, further reduction below the current $\approx 1 \times 10^{-10}$ mbar level would be expensive and challenging.

With the aim of reducing the volume of ionisation, an addition to the CRIS experiment that has been tested and is currently undergoing further development is the installation of a field-ionisation unit. This is located inside the interaction region and replaces the function of the final ionisation laser. In a field-ionisation scheme, resonant excitation lasers are used to excite the neutralised atoms into a Rydberg state before they enter the field-ionisation unit. Next, a series of electrostatic deflectors separate ions created before the unit from the neutral atoms. Following this, a high-field region, created by a set of alternating-potential grids, ionises the resonantly excited atoms. In future, the high-field region will be held at an electric potential offset relative to the surrounding grounded vacuum chambers, meaning the ions created inside are accelerated to an energy different to that of ions created before or after the field-ionisation unit. This will allow for further separation in time and, through electrostatic deflection, space of background ions created outside the unit.

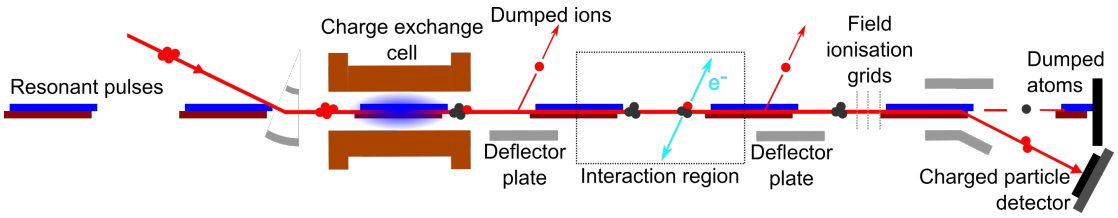

FIGURE 6.6: Schematic diagram of a field-ionisation experiment at CRIS. Neutralised atoms are resonantly excited into a Rydberg state close to the ionisation potential. Collisionally-ionised and laser-ionised ions are then removed. Following this, the excited Rydberg atoms are ionised in a region of high electric field and are deflected into the charged-particle detector.

In summation, only ions created within the field-ionisation unit will be detected by the charged particle detector, reducing the length of the ionisation region from the full 1.5 m (between the CEC deflectors and the final electrostatic bend) to the size of the field-ionisation unit, of the order of 3 cm. This reduces the collisional ionisation background approximately proportionally, i.e. by a factor of 100. This may be increased in future by further reducing the longitudinal length of the high-field region.

Using field ionisation also removes all laser-related background effects. This may become significant for indium or other atomic cases, as previously the non-resonant ionisation of beam components due to the high-photon density of the final ionisation laser has been a significant source of background [167]. These beam components may be isobaric contaminants neutralised into high-lying atomic states [74], atoms excited into higher-lying states through gas collisions [168], or atoms ionised through lower cross-section processes such as multi-photon ionisation from lower-lying states (the dominant background contribution at $A = 100$ in the neutron-deficient indium experiment, see Section 4.1.4). All of these background contributions are removed when utilising field ionisation because any ions created in the laser-interaction region are removed before the bunch enters the field-ionisation region.

6.3.2 Measurements

Spectroscopy was performed on the Rydberg states of the stable indium isotopes at CRIS using field-ionisation in 2019 [167]. The bunches of indium ions were created in the CRIS ion source using laser ablation (see Section 3.3.6). The ablation laser used was the 532-nm Litron LPY 601 50-100 PIV Nd:YAG laser located in the CRIS laser cabin (see Section 3.3.2), pulsed at 100 Hz repetition rate. The indium ions were accelerated to 25 keV before they were neutralised in the charge exchange cell (CEC) using a sodium vapour. The CEC was held at 300 °C to maximise the efficiency of neutralisation. The total efficiency of neutralisation was measured as 60(10)%, which must be multiplied

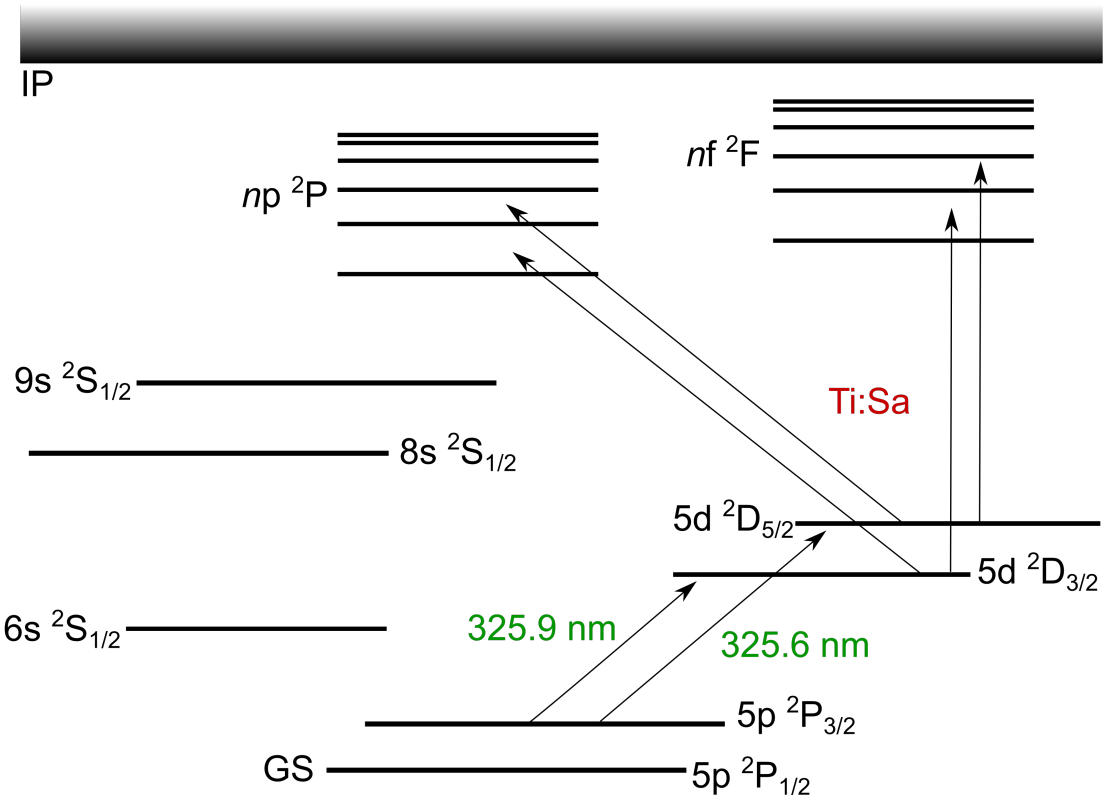

FIGURE 6.7: Schematic of the indium level scheme (not to scale). Atoms were excited from the 5p $^2P_{3/2}$ metastable level to either the 5d $^2D_{3/2}$ or 5d $^2D_{5/2}$ level using 325 nm frequency-doubled PDL light. The injection seeded laser was subsequently used to excite to a Rydberg state in the np or nf series from which the atoms could be field ionised. The ground state is labelled 'GS' and the ionisation potential is labelled 'IP'.

by the 64% predicted from simulation as being in the probed $5s^2$ 5p $^2P_{3/2}$ metastable state [74].

The neutralised atoms were then excited to either the $5s^2$ 5d $^2D_{3/2}$ or $5s^2$ 5d $^2D_{5/2}$ state using the Spectron Spectrolase 4000 pulsed dye laser (PDL) in the CRIS laser cabin, with DCM dye in ethanol solution. The dye laser was pumped at 100 Hz and 532 nm by the second output of the Litron LPY unit used for ablation. The PDL produced fundamental light at 650 nm which was then frequency doubled, using a BBO crystal at the correct phase matching angle, to reach the required wavelength, 325 nm [167]. A second laser was used to excite from this intermediate state to a Rydberg state in the $5s^2$ nf ^2F or $5s^2$ np ^2P series. This second laser was the fundamental light from the injection-seeded laser system described in Section 3.3.2, using the Sirah Matisse Ti:Sa CW laser system as a seed.

Once excited to the Rydberg state, the atom bunches entered the field-ionisation unit where they were ionised by an electric field gradient of 7.5 kV cm^{-1}. Three grids of parallel wires, spaced 4 mm apart, were used to create the field, with outer grids grounded and the central grid held at high potential. The grids were comprised of 10 μm thick

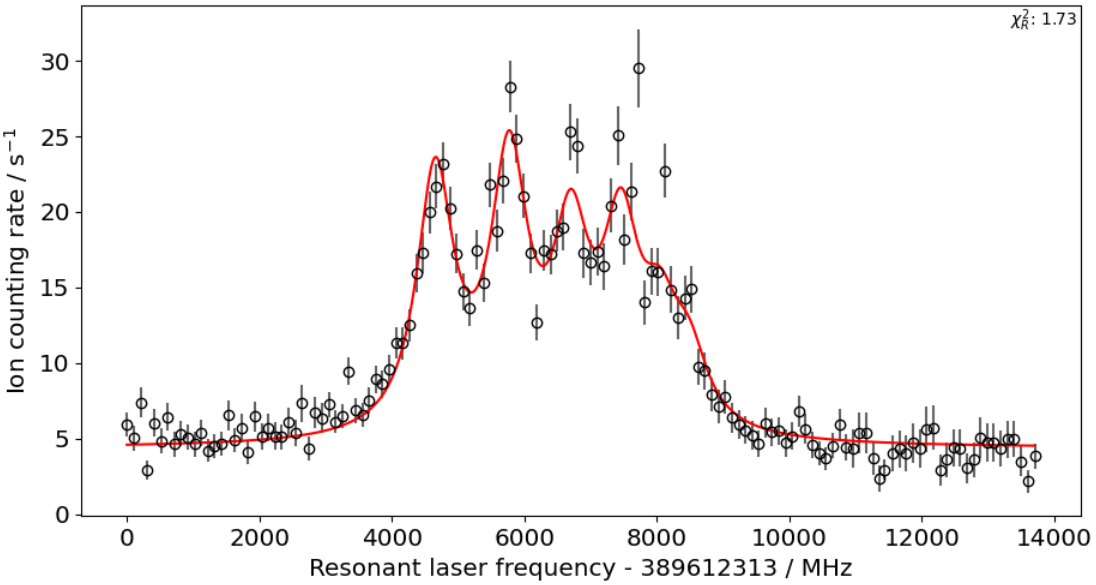

(A) Scan of the 5d $^2D_{5/2}$ to 12f $^2F_{5/2,7/2}$ transition. The linewidth is here dominated by the Lorentzian contribution with $\Gamma_l = 675(30)$ MHz and $\Gamma_g = 8(16)$ MHz.

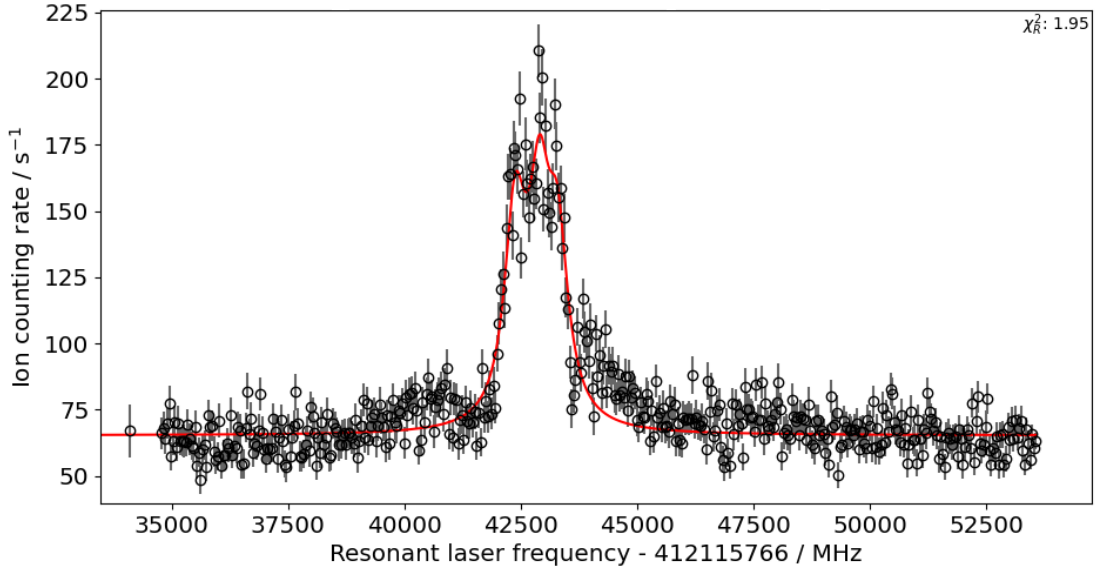

(B) Scan of the 5d $^2D_{3/2}$ to 53f $^2F_{5/2,7/2}$ transition. The linewidth is $\Gamma_l = 536(35)$ MHz and $\Gamma_g = 9(47)$ MHz.

FIGURE 6.8: Example spectra from this work studying the Rydberg states of the stable-indium isotopes through field ionisation. The resonant laser frequency on the x-axes is the frequency of the injection-seeded laser used for the second-step excitation to the Rydberg state. Data are shown as black points and the hyperfine-structure fits are shown as red lines.

parallel wires, separated by 1 mm. Non-resonantly excited ions were removed in several stages between the CEC and the field-ionisation unit with electrostatic deflectors. After a further 30 cm, the remaining ions were electrostatically deflected through 20° onto the ETP MagneToF charged-particle detector.

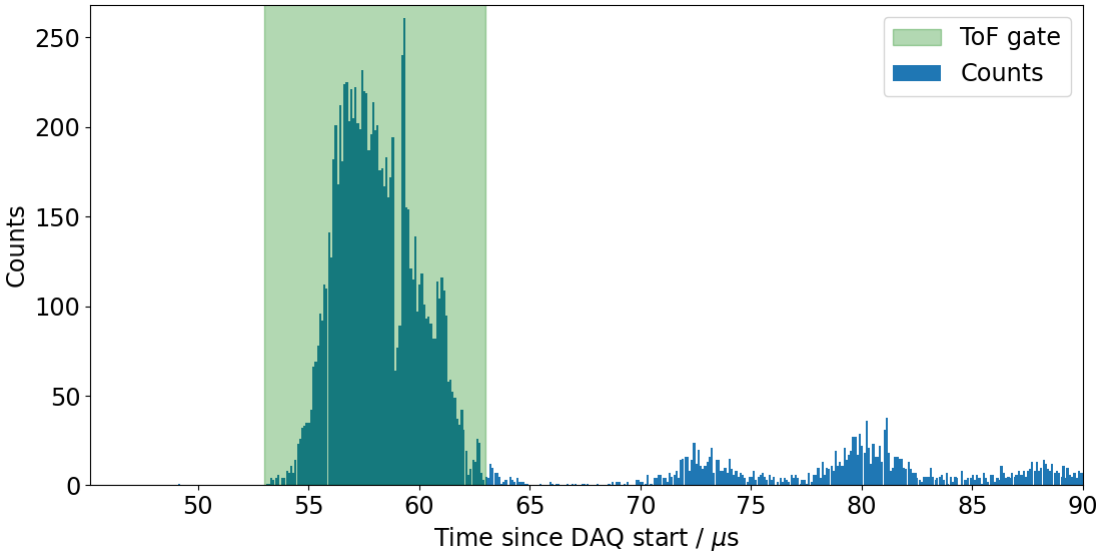

FIGURE 6.9: Histogram of the measured ion-time-of-flight values for the 5d $^2D_{5/2}$ to 12f $^2F_{5/2,7/2}$ scan shown in Fig. 6.8(A). Ion counts are shown as blue bars. The timing gate is shown as a green band.

Laser wavenumbers (including that of the locked Toptica diode laser) and digitized ion-counting signals were collected as described in Section 4.2.1. However, the platform voltage of the independent CRIS ion source, generated by a Heinzinger PNChp 30000-5 power supply, was not continuously recorded here, leading to a systematic uncertainty in the ion beam energy of 10 eV [167].

6.3.3 Data analysis

Rydberg states in the $5s^2$ nf and $5s^2$ np series were measured in this work with principal quantum numbers in the range $n = 12 - 72$. To perform the analysis, the laser wavenumber of the second excitation step and ion-counting signal values for each scan were first concatenated and sorted by timestamp. Next, wavenumbers were assigned to each ion-count event, taking the most-recently recorded value. The drift in the recorded wavenumber values was then accounted for using Equation 4.2 and the recorded diode laser frequencies. A data collection time was then assigned to each ion-count event using the difference in timestamp between dataset rows.

Due to the pulsed-time structure of the ion-ablation process, the event-by-event timing information could be used to apply a timing gate to remove ion counts outside a window around the arrival time of the ion bunches, reducing the ion-counting background. The scanning frequencies, ion counts and data-collection times were then aggregated, dividing the scanning region into 10 MHz width bins, taking the mean of laser frequencies in each bin and assigning count rates according to Equation 4.4.

Hyperfine structure models for each transition were generated using the SATLAS data analysis package [91] using a similar technique to Section 4.2.2 (see Fig. 6.8). Approximate excitation energies of the Rydberg states were used to estimate the centres of mass of the resonant structures when combined with the excitation energy of the intermediate $5s^2\ 5d\ ^2D_{3/2}$ or $5s^2\ 5d\ ^2D_{5/2}$ state from the NIST specral-lines database [92]. These excitation energies were estimated using the Rydberg-Ritz formula,

$$E_n = E_{\mathrm{IP}} - \frac{R_{\mathrm{In}-115}}{(n-\delta_n)^2}, \tag{6.3}$$

where δ_n are the quantum defects of the levels, E_n are the level energies, E_{IP} is the energy of the ionisation potential, n is the principal quantum number, and $R_{\mathrm{In}-115} = (\mu_e/M_{\mathrm{In}-115})R = 109736.79\,\mathrm{cm}^{-1}$ is the Rydberg constant for ^{115}In [169], where $M_{\mathrm{In}-115}$ is the atomic mass and

$$\mu_e = \frac{m_e M_{\mathrm{In}-115}}{m_e + M_{\mathrm{In}-115}} \tag{6.4}$$

is the reduced electron mass. δ_n are taken as zero for the initial approximation and the ionisation potential was estimated using the evaluated value in [92], $E_{\mathrm{IP}} = 46670.106\,\mathrm{cm}^{-1}$.

A Voigt resonant lineshape (see Section 4.2.2) was used to account for the lineshape broadening of the resonant structures. The models were fitted to the data using a Levenberg-Marquart algorithm in LMFIT [94], minimising the chi-square as in Section 4.2.3. The hyperfine-A and B factors for the upper Rydberg states are expected to be small relative to the recorded linewidths. These factors were therefore fixed at zero. For lower-quality scans, the ratios of peak rates within the HFS were partially fixed to the ratios defined by Racah calculations. Otherwise, model parameters including the FWHM components, the centres of mass and the lower-state hyperfine parameters were allowed to vary freely in fitting.

The complete data aggregation, correction and fitting process used the same custom Python modules developed for the analysis in Chapter 4 based on the SATLAS data analysis package [91], adapted to work with CRIS-ion-source experimental data. More details on steps of the analysis procedure can be found in Chapter 4.

Periodic scans of the transitions to the $5s^2$ 21f and $5s^2$ 21p states were performed. These were used in the calculation of the absolute level energies to account for variations in the ion-beam energy and recorded wavenumber. For each scan, the nearest scan (in time) of the corresponding $n = 21$ state was used as a reference. First, the difference in fitted centroid frequency between the reference and transition of interest was calculated. Next, an absolute level energy of the $n = 21$ state was added to this difference to determine the level energy of the Rydberg state of interest. Finally, a weighted mean (Equation 4.19)

of values from scans to a given state was used to provide a final value for the excitation energy.

The absolute energy levels of the $5s^2$ 21f and $5s^2$ 21p states were determined through a weighted mean of scan transition energies to each state, combined with literature measurements of the $5s^2$ 5d $^2D_{3/2}$ and $5s^2$ 5d $^2D_{5/2}$ states from George et al. [170], $E(5s^2\ 5d\ ^2D_{3/2}) = 32892.230(5)\,\mathrm{cm}^{-1}$ and $E(5s^2\ 5d\ ^2D_{5/2}) = 32915.539(5)\,\mathrm{cm}^{-1}$. The variation in ion-beam energy and wavemeter readout were included as systematic uncertainties in the final level energies.

6.3.4 Determination of the ionisation potential of ^{115}In

Once the level energies had been determined, they could be used to evaluate the quantum defect parameters, δ_n, and the energy of the ionisation potential, E_{IP}, using Equation 6.3. According to a quantum-mechanical calculation performed by Hartree [171], the quantum defect parameters can be written as an expansion in inverse-even powers of $(n-\delta_0)$, where δ_0 is a quantum defect shared between levels of the same series [169,172],

$$\delta_n = a_0 + \frac{a_1}{(n-\delta_0)^2} + \frac{a_2}{(n-\delta_0)^4} + \frac{a_3}{(n-\delta_0)^6} + \mathcal{O}\left((n-\delta_0)^{-8}\right) \tag{6.5}$$

where $a_{0,1,2,3,\ldots}$ are constants fitted to level energies. This calculation assumes a spherical potential, containing a coulomb Hamiltonian and a short-range correction potential, and is non-perturbative [169]. Higher-order terms in Equation 6.5 and any non-central corrections (leading to odd-power terms in a perturbative expansion) are not considered here.

The first step in the IP determination was to perform the fitting of the $a_{0,1,2,3}$ and δ_0 parameters. This was done by fitting Equation 6.3 and Equation 6.5 to five energy levels of the studied series with the lowest energies from [170], using a previous measurement of the ionisation potential in [173], $E_{\mathrm{IP}} = 46670.106(6)\,\mathrm{cm}^{-1}$.

The resultant fit parameters could then be used to determine δ_n values for all the measured states in this work using Equation 6.5. Using $(n-\delta_n)$ as the independent variable, the level energies measured in this work could then be fitted using Equation 6.3, with E_{IP} as a single fit parameter. Fig. 6.10 shows the result of this fitting process applied to the level energies of the $5s^2$ nf series determined through this work, with the Rydberg-Ritz excitation energy fit in the upper pane and the residuals of this fit in the lower pane. The value of the IP determined through this fit was $E_{\mathrm{IP}} = 46670.98(16)\,\mathrm{cm}^{-1}$.

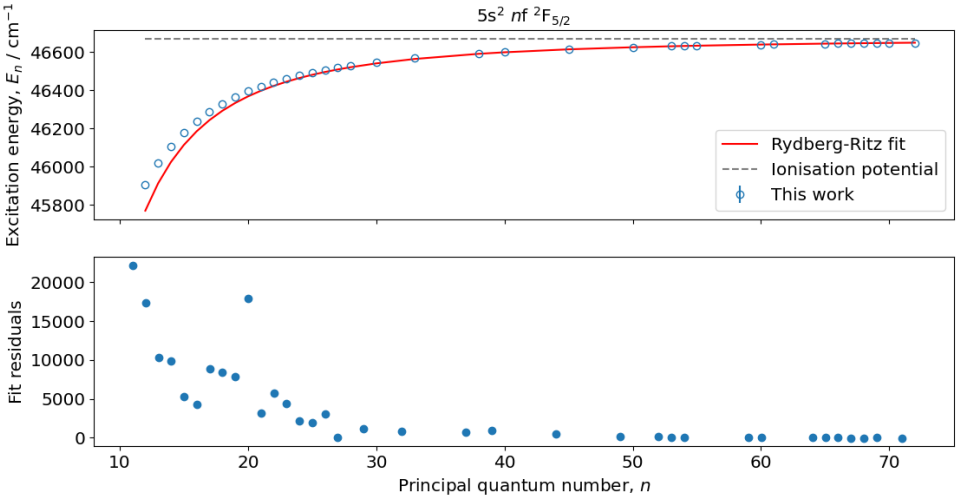

FIGURE 6.10: Fit of the calculated excitation energies of states in the $5s^2\ nf\ ^2F_{5/2}$ series (blue points, upper) with the Rydberg-Ritz model of Equation 6.3 (red line, upper). The fitted ionisation potential (IP) is also shown as a grey dashed line in the upper pane. The lower pane shows the reduced residuals of this fit.

In addition to the determination of the ionisation potential of ^{115}In and multiple Rydberg state level energies, this work also validated the use of the field-ionisation apparatus at CRIS, which can now be applied to other stable or exotic isotopic cases.

Chapter 7

Summary

Collinear laser spectroscopy measurements of the neutron-deficient indium isotopes have been performed at the Collinear Resonance Ionisation Spectroscopy (CRIS) experiment at the ISOLDE facility at CERN in Geneva, Switzerland. CRIS is at the forefront of the laser spectroscopy field; its successful combination of high experimental sensitivity with sufficient precision means nuclear-ground-state properties in a wide variety of exotic nuclear cases can and have been measured [4, 5, 25, 62, 174, 175]. These measurements are crucial in the development of nuclear theories derived from basic principles.

The primary focus of this thesis has been the measurement, analysis and interpretation of the behaviour of the neutron-deficient indium isotopes. The layout of aspects of the ISOLDE facility relevant to CRIS experiments including the targets, HRS separator and ISCOOL, were detailed in Chapter 3. Specific details of the CRIS experiment common to all element studies were also discussed in this chapter, including aspects of the vacuum beamline, the neutralisation system and the laser systems present at the time of writing.

The following chapter, Chapter 4, discussed the experimental details specific to the neutron-deficient-indium experimental campaign carried out in April 2018, including the laser configuration and the configuration of ISOLDE. This chapter also detailed the whole data-analysis process, following the data from the initial extraction, processing and gating, through to the model fitting and parameter extraction. Spurious non-radiogenic resonances in ^{101}In were identified and accounted for in model fitting, allowing for the extraction of ground state properties. The isomeric state in ^{106}In was given a firm spin determination of $I^{\pi} = 2^{+}$ based on King plot, hyperfine-A ratio and reduced chi-square analysis. Finally, Monte-Carlo sampling procedures were used for the determination of reference-centroid values for measurement isotope shifts (a new technique) and for the determination of final parameter values.

The initial impact of these new results, through comparison to calculations of the shell model, droplet model and density functional theory (DFT), was discussed in Chapter 5. The chapter started with brief introductions to each of these model frameworks, more thorough outlines can be found in some of the referenced literature. The discussion was then divided into three main sections: single-particle behaviour in the magnetic moments of the odd-mass indium isotopes with paired neutrons, additivity in the even-mass isotopes, and deformation in the quadrupole moments and mean-square charge radii.

The single-particle nature of the mid-shell $I^\pi = 9/2^+$ states is brought further into question by these results, which include new measurements of the ground-state magnetic moments of ^{101,103}In. A continuation of the upward linear trend with decreasing neutron number is observed, moving away from the constant quenched moment of the mid-shell towards the pure single-particle Schmidt value approaching the neutron shell closure at $N = 50$. DFT calculations by Saperstein et al. [134] successfully predicted this gradual increase in the moment in the neutron-deficient isotopes (when phonon-coupling (PC) corrections were included) but failed to predict the rapid increase observed at $N = 82$. The mechanism underlying the strikingly linear decrease in the magnetic moments of the $I^\pi = 1/2^-$ states with N remains unclear; a continuation of this trend was observed in $^{103-111}$In, where the magnetic moments were measured for the first time in this work.

Additivity rules for dipole and quadrupole moments were used to investigate the configuration of the odd proton- odd neutron states. The g-factors of the $^{102-110}$In ground states indicate that they follow a $(\pi 1g_{9/2}^{-1} \otimes \nu 2d_{5/2})$ configuration. However, the conclusions that can be drawn with comparisons to the isomeric states and the quadrupole moments are less clear. The neutron-rich 5^+ and 8^+ states follow $(\pi 1g_{9/2}^{-1} \otimes \nu 3s_{1/2})$ and $(\pi 1g_{9/2}^{-1} \otimes \nu 1h_{11/2})$ configurations respectively for $^{114-122}$In.

In contrast to the magnetic moments, the large collective contribution to the quadrupole moments of the $9/2^+$ states was predicted by Heyde et al. [144] in shell-model calculations. The decreasing collectivity and deformation approaching the two neutron shell closures is apparent when combined with tin $B(E2)$ measurements, with the new measurements of ^{101,103}In here indicating a similar effect on the quadrupole moments at the two ends of the isotopic chain. The DFT calculations with PC corrections by Saperstein et al. [137] also perform relatively well in the prediction of these quadrupoles. Quadrupole deformation parameters were also determined from quadrupole moments and charge radii. Finite-range droplet model calculations by Möller et al. [159] predict the general trends in static deformation, but underestimate the dynamic-deformation contribution.

Future measurements will more directly probe the behaviour of indium through measurements of ^{100}In and ^{99}In. Some of the planned developments to the CRIS experiment, motivated by the possibility of the measurement of lower-production-rate isotopes such as these, were described in Chapter 6. Firstly, an initial design for a compact radio-frequency quadrupole ion trap for CRIS has been created and validated through simulation. The trap would liberate significant amounts of experimental time for the measurement of the most exotic isotopes and would allow for continuous optimisation of ion-beam transport. Secondly, a field-ionisation apparatus has been implemented and validated through measurements of the Rydberg series of stable ^{115}In. The apparatus removes all laser-related background contributions, which are currently the dominant source in the most-exotic isotopes, and also significantly reduces the ionisation volume and therefore the rate of collisional ionisation. In combination, these improvements will increase the sensitivity of the CRIS experiment by more than three orders of magnitude, making future CRIS measurements of ^{100}In and ^{99}In feasible.

Bibliography

[1] M. G. Mayer, Phys. Rev. **75**, 1969 (1949), [https://link.aps.org/doi/10.1103/PhysRev.75.1969].

[2] O. Haxel, J. H. D. Jensen and H. E. Suess, Phys. Rev. **75**, 1766 (1949), [https://link.aps.org/doi/10.1103/PhysRev.75.1766.2].

[3] D. R. Inglis, Phys. Rev. **50**, 783 (1936), [https://link.aps.org/doi/10.1103/PhysRev.50.783].

[4] Á. Koszorús *et al.*, Nature Physics (2021), [https://doi.org/10.1038/s41567-020-01136-5].

[5] R. P. de Groote *et al.*, Nature Physics **16**, 620 (2020), [https://doi.org/10.1038/s41567-020-0868-y].

[6] T. D. Morris *et al.*, Phys. Rev. Lett. **120**, 152503 (2018), [https://link.aps.org/doi/10.1103/PhysRevLett.120.152503].

[7] I. Podadera-Aliseda and M. Lindroos, *New developments on preparation of cooled and bunched Radioactive Ion beams at ISOL facilities: the ISCOOL project and the rotating wall cooling*, PhD thesis, Universitat Politecnica de Catalunya, 2006, http://cds.cern.ch/record/975263, Presented on 07 Jul 2006.

[8] A. Nieminen *et al.*, Nuclear Instruments and Methods in Physics Research Section A: Accelerators, Spectrometers, Detectors and Associated Equipment **469**, 244 (2001), [https://doi.org/10.1016/S0168-9002(00)00750-6].

[9] K. T. Flanagan *et al.*, Phys. Rev. Lett. **111**, 212501 (2013), [https://link.aps.org/doi/10.1103/PhysRevLett.111.212501].

[10] T. Cocolios *et al.*, Nuclear Instruments and Methods in Physics Research Section B: Beam Interactions with Materials and Atoms **317**, 565 (2013), [https://doi.org/10.1016/j.nimb.2013.05.088], XVIth International Conference on ElectroMagnetic Isotope Separators and Techniques Related to their Applications, December 27, 2012 at Matsue, Japan.

[11] R. P. de Groote, *High resolution collinear resonance ionization spectroscopy of neutron-rich ^{76,77,78}Cu isotopes*, PhD thesis, 2017, https://cds.cern.ch/record/2285661, Presented 18 Sep 2017.

[12] R. P. de Groote *et al.*, Phys. Rev. C **96**, 041302 (2017), [https://link.aps.org/doi/10.1103/PhysRevC.96.041302].

[13] K. L. G. Heyde, *The Nuclear Shell Model*Springer Series in Nuclear and Particle Physics, 2 ed. (Springer-Verlag New York Berlin Heidelberg, 1994).

[14] K. Heyde, M. Waroquier and R. A. Meyer, Phys. Rev. C **17**, 1219 (1978), [https://link.aps.org/doi/10.1103/PhysRevC.17.1219].

[15] J. Eberz *et al.*, Nuclear Physics A **464**, 9 (1987), [https://doi.org/10.1016/0375-9474(87)90419-2].

[16] G. Neyens, Reports on Progress in Physics **66**, 633 (2003), [https://doi.org/10.1088/0034-4885/66/4/205].

[17] H. Sagawa and A. Arima, Physics Letters B **202**, 15 (1988), [https://doi.org/10.1016/0370-2693(88)90845-3].

[18] E. Tiesinga, P. J. Mohr, D. B. Newell and B. N. Taylor, The 2018 CODATA Recommended Values of the Fundamental Physical Constants, 2020, Web version 8.1. Database developed by J. Baker, M. Douma, and S. Kotochigova. Available at http://physics.nist.gov/constants.

[19] J. Persson, Atomic Data and Nuclear Data Tables **99**, 62 (2013), [https://doi.org/10.1016/j.adt.2012.04.002].

[20] V. A. Korol and M. G. Kozlov, Phys. Rev. A **76**, 022103 (2007), [https://link.aps.org/doi/10.1103/PhysRevA.76.022103].

[21] B. K. Sahoo, Journal of Physics B: Atomic, Molecular and Optical Physics **43**, 231001 (2010), [https://doi.org/10.1088/0953-4075/43/23/231001].

[22] C. J. Foot, *Atomic physics*Oxford master series in physics. Atomic, optical and laser physics ; 7 (Oxford University Press, Oxford, 2005).

[23] B. Cheal, T. E. Cocolios and S. Fritzsche, Phys. Rev. A **86**, 042501 (2012), [https://link.aps.org/doi/10.1103/PhysRevA.86.042501].

[24] A. R. Vernon, *Evolution of the indium proton-hole states up to $N = 82$ studied with laser spectroscopy*, PhD thesis, The University of Manchester, 2019, https://cds.cern.ch/record/2723917, Presented February 2019.

[25] B. K. Sahoo *et al.*, New Journal of Physics **22**, 012001 (2020), [https://doi.org/10.1088/1367-2630/ab66dd].

[26] C. Piller *et al.*, Phys. Rev. C **42**, 182 (1990), [https://link.aps.org/doi/10.1103/PhysRevC.42.182].

[27] R. F. Garcia Ruiz *et al.*, Phys. Rev. X **8**, 041005 (2018), [https://link.aps.org/doi/10.1103/PhysRevX.8.041005].

[28] C. P. Flynn and E. F. W. Seymour, Proceedings of the Physical Society **76**, 301 (1960), [https://doi.org/10.1088/0370-1328/76/2/415].

[29] W. G. Proctor, Phys. Rev. **79**, 35 (1950), [https://link.aps.org/doi/10.1103/PhysRev.79.35].

[30] W. Sahm and A. Schwenk, Zeitschrift fr Naturforschung A **29**, 1754 (1974), [https://doi.org/10.1515/zna-1974-1208].

[31] M. De Rydt *et al.*, Nuclear Instruments and Methods in Physics Research Section A: Accelerators, Spectrometers, Detectors and Associated Equipment **612**, 112 (2009), [https://doi.org/10.1016/j.nima.2009.09.125].

[32] M. De Rydt *et al.*, Physics Letters B **678**, 344 (2009), [https://doi.org/10.1016/j.physletb.2009.06.043].

[33] R. F. Garcia Ruiz *et al.*, Nature Physics **12**, 594 (2016), [https://doi.org/10.1038/nphys3645].

[34] C. Gorges *et al.*, Phys. Rev. Lett. **122**, 192502 (2019), [https://link.aps.org/doi/10.1103/PhysRevLett.122.192502].

[35] B. A. Marsh *et al.*, Nature Physics **14**, 1163 (2018), [https://doi.org/10.1038/s41567-018-0292-8].

[36] A. Voss *et al.*, Phys. Rev. C **91**, 044307 (2015), [https://link.aps.org/doi/10.1103/PhysRevC.91.044307].

[37] T. J. Procter *et al.*, The European Physical Journal A **51**, 23 (2015), [https://doi.org/10.1140/epja/i2015-15023-2].

[38] D. T. Yordanov *et al.*, Journal of Physics G: Nuclear and Particle Physics **44**, 075104 (2017), [https://doi.org/10.1088/1361-6471/aa718b].

[39] B. Cheal and K. T. Flanagan, Journal of Physics G: Nuclear and Particle Physics **37**, 113101 (2010), [https://doi.org/10.1088/0954-3899/37/11/113101].

[40] R. Ferrer *et al.*, Nature Communications **8**, 14520 (2017), [https://doi.org/10.1038/ncomms14520].

[41] W. Nörtershäuser, Hyperfine Interactions **198**, 73 (2010), [https://doi.org/10.1007/s10751-010-0230-3].

[42] K. Minamisono *et al.*, Nuclear Instruments and Methods in Physics Research Section A: Accelerators, Spectrometers, Detectors and Associated Equipment **709**, 85 (2013), [https://doi.org/10.1016/j.nima.2013.01.038].

[43] R. de Groote *et al.*, Nuclear Instruments and Methods in Physics Research Section B: Beam Interactions with Materials and Atoms **463**, 437 (2020), [https://doi.org/10.1016/j.nimb.2019.04.028].

[44] K. Kreim, *Collinear Laser Spectroscopy of Potassium: Nuclear Charge Radii beyond N = 28*, PhD thesis, Max Planck Institute for Nuclear Physics, University of Heidelberg, 2013, http://cds.cern.ch/record/2243051, Presented July 2013.

[45] E. Mané *et al.*, The European Physical Journal A **42**, 503 (2009), [https://doi.org/10.1140/epja/i2009-10828-0].

[46] P. Vingerhoets *et al.*, Phys. Rev. C **82**, 064311 (2010), [https://link.aps.org/doi/10.1103/PhysRevC.82.064311].

[47] T. Day Goodacre *et al.*, Spectrochimica Acta Part B: Atomic Spectroscopy **129**, 58 (2017), [https://doi.org/10.1016/j.sab.2017.01.001].

[48] ETP, MagneTOF: A New Class of Robust Sub-nanosecond TOF Detectors with Exceptional Dynamic Range, 2013, URL: https://www.etp-ms.com/faqs/literature.

[49] R. D. Harding *et al.*, Phys. Rev. C **102**, 024312 (2020), [https://link.aps.org/doi/10.1103/PhysRevC.102.024312].

[50] R. D. Harding, *Laser-assisted spectroscopy of Au and Na isotopes at ISOLDE*, PhD thesis, University of York, 2019, http://etheses.whiterose.ac.uk/26900/.

[51] S. Knauer *et al.*, International Journal of Mass Spectrometry **423**, 46 (2017), [https://doi.org/10.1016/j.ijms.2017.10.007].

[52] C. Jesch *et al.*, Hyperfine Interactions **235**, 97 (2015), [https://doi.org/10.1007/s10751-015-1184-2].

[53] M. Seliverstov *et al.*, Physics Letters B **719**, 362 (2013), [https://doi.org/10.1016/j.physletb.2013.01.043].

[54] U. Köster, V. Fedoseyev and V. Mishin, Spectrochimica Acta Part B: Atomic Spectroscopy **58**, 1047 (2003), [https://doi.org/10.1016/S0584-8547(03)00075-2], LAP-2002 International Conference on Laser Probing.

[55] K. Chrysalidis *et al.*, Nuclear Instruments and Methods in Physics Research Section B: Beam Interactions with Materials and Atoms **463**, 476 (2020), [https://doi.org/10.1016/j.nimb.2019.04.020].

[56] S. Raeder *et al.*, Nuclear Instruments and Methods in Physics Research Section B: Beam Interactions with Materials and Atoms **376**, 382 (2016), [https://doi.org/10.1016/j.nimb.2015.12.014], Proceedings of the XVIIth International Conference on Electromagnetic Isotope Separators and Related Topics (EMIS2015), Grand Rapids, MI, U.S.A., 11-15 May 2015.

[57] Y. Kudryavtsev, R. Ferrer, M. Huyse, P. Van den Bergh and P. Van Duppen, Nuclear Instruments and Methods in Physics Research Section B: Beam Interactions with Materials and Atoms **297**, 7 (2013), [https://doi.org/10.1016/j.nimb.2012.12.008].

[58] M. Block, M. Laatiaoui and S. Raeder, Progress in Particle and Nuclear Physics **116**, 103834 (2021), [https://doi.org/10.1016/j.ppnp.2020.103834].

[59] C. J. Cooper *et al.*, Europhysics Letters (EPL) **28**, 397 (1994), [https://doi.org/10.1209/0295-5075/28/6/004].

[60] L.-B. Wang *et al.*, Phys. Rev. Lett. **93**, 142501 (2004), [https://link.aps.org/doi/10.1103/PhysRevLett.93.142501].

[61] Y. A. Kudriavtsev and V. S. Letokhov, Applied Physics B **29**, 219 (1982), [https://doi.org/10.1007/BF00688671].

[62] K. M. Lynch *et al.*, Phys. Rev. X **4**, 011055 (2014), [https://link.aps.org/doi/10.1103/PhysRevX.4.011055].

[63] R. Catherall *et al.*, Journal of Physics G: Nuclear and Particle Physics **44**, 094002 (2017), [https://doi.org/10.1088/1361-6471/aa7eba].

[64] K. Hanke, International Journal of Modern Physics A **28**, 1330019 (2013), [https://doi.org/10.1142/S0217751X13300196].

[65] A. Gottberg, Nuclear Instruments and Methods in Physics Research Section B: Beam Interactions with Materials and Atoms **376**, 8 (2016), [https://doi.org/10.1016/j.nimb.2016.01.020], Proceedings of the XVIIth International Conference on Electromagnetic Isotope Separators and Related Topics (EMIS2015), Grand Rapids, MI, U.S.A., 11-15 May 2015.

[66] M. J. G. Borge and B. Jonson, Journal of Physics G: Nuclear and Particle Physics **44**, 044011 (2017), [https://doi.org/10.1088/1361-6471/aa5f03].

[67] P. Van Duppen, *Isotope Separation On Line and Post Acceleration* (Springer Berlin Heidelberg, Berlin, Heidelberg, 2006), pp. 37–77, https://doi.org/10.1007/3-540-33787-3_2.

[68] V. Mishin *et al.*, Nuclear Instruments and Methods in Physics Research Section B: Beam Interactions with Materials and Atoms **73**, 550 (1993), [https://doi.org/10.1016/0168-583X(93)95839-W].

[69] T. Day Goodacre *et al.*, Nuclear Instruments and Methods in Physics Research Section B: Beam Interactions with Materials and Atoms **376**, 39 (2016), [https://doi.org/10.1016/j.nimb.2016.03.005], Proceedings of the XVIIth International Conference on Electromagnetic Isotope Separators and Related Topics (EMIS2015), Grand Rapids, MI, U.S.A., 11-15 May 2015.

[70] S. Rothe *et al.*, Nuclear Instruments and Methods in Physics Research Section B: Beam Interactions with Materials and Atoms **376**, 91 (2016), [https://doi.org/10.1016/j.nimb.2016.02.024], Proceedings of the XVIIth International Conference on Electromagnetic Isotope Separators and Related Topics (EMIS2015), Grand Rapids, MI, U.S.A., 11-15 May 2015.

[71] D. Fink *et al.*, Nuclear Instruments and Methods in Physics Research Section B: Beam Interactions with Materials and Atoms **317**, 417 (2013), [https://doi.org/10.1016/j.nimb.2013.06.039], XVIth International Conference on ElectroMagnetic Isotope Separators and Techniques Related to their Applications, December 27, 2012 at Matsue, Japan.

[72] D. W. Jordan, *Nonlinear ordinary differential equations an introduction for scientists and engineers*Oxford Texts in Applied and Engineering Mathematics, 4th ed. ed. (Oxford University Press, Oxford, 2007), chap. 9, pp. 305–324.

[73] C. L. Binnersley, *Investigating the properties of multi-quasiparticle isomers in neutron-rich indium isotopes using laser spectroscopy*, PhD thesis, The University of Manchester, 2019, https://www.escholar.manchester.ac.uk/jrul/item/?pid=uk-ac-man-scw:319873, Presented in February 2019.

[74] A. R. Vernon *et al.*, Spectrochimica Acta Part B: Atomic Spectroscopy **153**, 61 (2019), [https://doi.org/10.1016/j.sab.2019.02.001].

[75] Sirah, Matisse user's guide, 2009, https://www.spectra-physics.com/mam/celum/celum_assets/sp/resources/Matisse_Users_Guide_Rev_18.pdf.

[76] S. Hooker and C. Webb, *Laser Physics* (Oxford University Press, 2010).

[77] M Squared, SolsTiS Datasheet: Ultra narrow linewidth CW Ti:sapphire laser, 2019, https://www.m2lasers.com/solstis-details.html?file=SolsTiS-datasheet.pdf.

[78] S. G. Wilkins, *Collinear resonance ionization spectroscopy of exotic francium and radium isotopes*, PhD thesis, The University of Manchester, 2017, http://cds.cern.ch/record/2308239, Presented 26 Jan 2018.

[79] R. P. de Groote *et al.*, Phys. Rev. Lett. **115**, 132501 (2015), [https://link.aps.org/doi/10.1103/PhysRevLett.115.132501].

[80] A. Koszorús *et al.*, Phys. Rev. C **100**, 034304 (2019), [https://link.aps.org/doi/10.1103/PhysRevC.100.034304].

[81] V. Sonnenschein *et al.*, Laser Physics **27**, 085701 (2017), [https://doi.org/10.1088/1555-6611/aa7834].

[82] T. Kessler, H. Tomita, C. Mattolat, S. Raeder and K. Wendt, Laser Physics **18**, 842 (2008), [https://doi.org/10.1134/S1054660X08070074].

[83] C. Mattolat *et al.*, AIP Conference Proceedings **1104**, 114 (2009), [https://aip.scitation.org/doi/pdf/10.1063/1.3115586].

[84] HighFinesse, *WS6-200 Series*, 2019, Accessed May 2020, URL: https://www.highfinesse.com/en/wavelengthmeter/wavelengthmeter-further-information/technical-information-wavelengthmeter-ws6-200-series.pdf.

[85] C. M. Ricketts, Summer student project report - A versatile ion source for improving the sensitivity and resolution of the CRIS beamline at ISOLDE. CRIS - Collinear resonance ionisation spectroscopy, Online, 2016, https://cds.cern.ch/record/2214595.

[86] U. Köster, The European Physical Journal A **15**, 255 (2002), [https://doi.org/10.1140/epja/i2001-10264-2].

[87] From ENSDF Database as of March 12, 2020. Version available at http://www.nndc.bnl.gov/ensarchivals/.

[88] T. G. Eck and P. Kusch, Phys. Rev. **106**, 958 (1957), [https://link.aps.org/doi/10.1103/PhysRev.106.958].

[89] J. Reback *et al.*, pandas-dev/pandas: Pandas 1.0.3, 2020, https://doi.org/10.5281/zenodo.3715232.

[90] J. S. Coursey, R. A. Dragoset and D. J. Schwab, Atomic weights and isotopic compositions, 1999, http://physics.nist.gov/Comp.

[91] W. Gins *et al.*, Computer Physics Communications **222**, 286 (2018), [https://doi.org/10.1016/j.cpc.2017.09.012].

[92] A. Kramida, Yu. Ralchenko, J. Reader and and NIST ASD Team, NIST Atomic Spectra Database (ver. 5.7.1), [Online]. Available: https://physics.nist.gov/asd [2020, January 31]. National Institute of Standards and Technology, Gaithersburg, MD., 2019.

[93] N. Bendali, H. T. Duong, P. Juncar, J. M. S. Jalm and J. L. Vialle, Journal of Physics B: Atomic and Molecular Physics **19**, 233 (1986), [https://doi.org/10.1088/0022-3700/19/2/012].

[94] M. Newville, T. Stensitzki, D. B. Allen and A. Ingargiola, LMFIT: Non-Linear Least-Square Minimization and Curve-Fitting for Python, 2014, https://doi.org/10.5281/zenodo.11813.

[95] A. R. Vernon, Private communications, 2019.

[96] L. L. Marino, W. B. Ewbank, W. A. Nierenberg, H. A. Shugart and H. B. Silsbee, Phys. Rev. **111**, 286 (1958), [https://link.aps.org/doi/10.1103/PhysRev.111.286].

[97] D. Vandeplassche, E. van Walle, J. Wouters, N. Severijns and L. Vanneste, Phys. Rev. Lett. **57**, 2641 (1986), [https://link.aps.org/doi/10.1103/PhysRevLett.57.2641].

[98] B. R. Casserberg, *The Spins and Moments of* ^{110}*In and* ^{112}*In*, PhD thesis, Princeton Univ., 1968.

[99] J. Van Cauteren, M. Rots and G. De Doncker, Hyperfine Interactions **34**, 439 (1987), [https://doi.org/10.1007/BF02072751].

[100] J. Eberz *et al.*, Zeitschrift für Physik A Atomic Nuclei **323**, 119 (1986), [https://doi.org/10.1007/BF01294563].

[101] E. Thuriere, *Etude de la Structure Nucleaire des Isotopes 107 et 115 de l'Indium, et des Correlations dans l'Etat Fondamental des Noyaux Cibles de Cadmium, A l'Aide des Reactions Cd(*^{3}*He, d)In*, PhD thesis, Paris Univ., 1970.

[102] W. Hesselink, B. Kooistra, L. Put, R. Siemssen and S. V. D. Werf, Nuclear Physics A **226**, 229 (1974), [https://doi.org/10.1016/0375-9474(74)90404-7].

[103] M. Conjeaud, S. Harar and E. Thuriere, Nuclear Physics A **129**, 10 (1969), [https://doi.org/10.1016/0375-9474(69)90905-1].

[104] A. Ekström *et al.*, The European Physical Journal A **44**, 355 (2010), [https://doi.org/10.1140/epja/i2010-10945-7].

[105] J. Vanhorenbeeck *et al.*, Phys. Rev. C **39**, 1528 (1989), [https://link.aps.org/doi/10.1103/PhysRevC.39.1528].

[106] D. Seweryniak *et al.*, Nuclear Physics A **589**, 175 (1995), [https://doi.org/10.1016/0375-9474(95)00060-E].

[107] B. W. Filippone, C. N. Davids, R. C. Pardo and J. Äystö, Phys. Rev. C **29**, 2118 (1984), [https://link.aps.org/doi/10.1103/PhysRevC.29.2118].

[108] R. Barden *et al.*, Zeitschrift für Physik A Atomic Nuclei **329**, 319 (1988), [https://doi.org/10.1007/BF01290237].

[109] D. De Frenne and A. Negret, Nuclear Data Sheets **109**, 943 (2008), [https://doi.org/10.1016/j.nds.2008.03.002].

[110] J. Szerypo *et al.*, Nuclear Physics A **507**, 357 (1990), [https://doi.org/10.1016/0375-9474(90)90297-Y].

[111] A. Gelman *et al.*, *Bayesian data analysis* (CRC press, 2013).

[112] M. D. Hoffman and A. Gelman, Journal of Machine Learning Research **15**, 1593 (2014), [http://jmlr.org/papers/v15/hoffman14a.html].

[113] J. Salvatier, T. V. Wiecki and C. Fonnesbeck, PeerJ Computer Science **2**, e55 (2016), [https://doi.org/10.7717/peerj-cs.55].

[114] G. Ulm *et al.*, Zeitschrift für Physik A Atoms and Nuclei **321**, 395 (1985), [https://doi.org/10.1007/BF01411970].

[115] G. F. Koster, Phys. Rev. **86**, 148 (1952), [https://link.aps.org/doi/10.1103/PhysRev.86.148].

[116] C. Belfrage *et al.*, Zeitschrift für Physik A Atoms and Nuclei **316**, 15 (1984), [https://doi.org/10.1007/BF01415655].

[117] R. F. Bishop, Theoretica chimica acta **80**, 95 (1991), [https://doi.org/10.1007/BF01119617].

[118] P. Virtanen *et al.*, Nature Methods **17**, 261 (2020), [https://doi.org/10.1038/s41592-019-0686-2].

[119] T. Togashi, Y. Tsunoda, T. Otsuka, N. Shimizu and M. Honma, Phys. Rev. Lett. **121**, 062501 (2018), [https://link.aps.org/doi/10.1103/PhysRevLett.121.062501].

[120] M. Hammen *et al.*, Phys. Rev. Lett. **121**, 102501 (2018), [https://link.aps.org/doi/10.1103/PhysRevLett.121.102501].

[121] G. Guastalla *et al.*, Phys. Rev. Lett. **110**, 172501 (2013), [https://link.aps.org/doi/10.1103/PhysRevLett.110.172501].

[122] MINIBALL and HIE-ISOLDE Collaborations, D. Rosiak *et al.*, Phys. Rev. Lett. **121**, 252501 (2018), [https://link.aps.org/doi/10.1103/PhysRevLett.121.252501].

[123] P. Gysbers *et al.*, Nature Physics **15**, 428 (2019), [https://doi.org/10.1038/s41567-019-0450-7].

[124] S. R. Stroberg, H. Hergert, S. K. Bogner and J. D. Holt, Annual Review of Nuclear and Particle Science **69**, 307 (2019), [https://doi.org/10.1146/annurev-nucl-101917-021120].

[125] R. Casten, *Nuclear Structure from a Simple Perspective* (Oxford University Press, Oxford, UK, 1990).

[126] K. Heyde, Hyperfine Interactions **43**, 15 (1988), [https://doi.org/10.1007/BF02398284].

[127] W. D. Myers and K.-H. Schmidt, Nuclear Physics A **410**, 61 (1983), [https://doi.org/10.1016/0375-9474(83)90401-3].

[128] C. V. Weiffenbach and R. Tickle, Phys. Rev. C **3**, 1668 (1971).

[129] T. H. R. Skyrme, The Philosophical Magazine: A Journal of Theoretical Experimental and Applied Physics **1**, 1043 (1956), [https://doi.org/10.1080/14786435608238186].

[130] A. B. Migdal, *Theory of finite Fermi systems and applications to atomic nuclei*Interscience monographs and texts in physics and astronomy ; vol.19 (Interscience, London, 1967).

[131] J. Stone and P.-G. Reinhard, Progress in Particle and Nuclear Physics **58**, 587 (2007), [https://doi.org/10.1016/j.ppnp.2006.07.001].

[132] S. A. Fayans, Journal of Experimental and Theoretical Physics Letters **68**, 169 (1998), [https://doi.org/10.1134/1.567841].

[133] S. Fayans, S. Tolokonnikov, E. Trykov and D. Zawischa, Nuclear Physics A **676**, 49 (2000), [https://doi.org/10.1016/S0375-9474(00)00192-5].

[134] E. E. Saperstein, S. Kamerdzhiev, S. Krewald, J. Speth and S. V. Tolokonnikov, EPL (Europhysics Letters) **103**, 42001 (2013), [https://doi.org/10.1209/0295-5075/103/42001].

[135] E. E. Saperstein *et al.*, Physics of Atomic Nuclei **77**, 10331056 (2014), [http://dx.doi.org/10.1134/S1063778814080122].

[136] E. E. Saperstein, S. Kamerdzhiev, D. S. Krepish, S. V. Tolokonnikov and D. Voitenkov, Journal of Physics G: Nuclear and Particle Physics **44**, 065104 (2017), [https://doi.org/10.1088/1361-6471/aa65f5].

[137] Saperstein, E. E., Kamerdzhiev, S., Krepish, D. S., Tolokonnikov, S. V. and Voitenkov, D., EPJ Web Conf. **182**, 02109 (2018), [https://doi.org/10.1051/epjconf/201818202109].

[138] I. Towner, Physics Reports **155**, 263 (1987), [https://doi.org/10.1016/0370-1573(87)90138-4].

[139] S. P. Kamerdzhiev, O. I. Achakovskiy, S. V. Tolokonnikov and M. I. Shitov, Physics of Atomic Nuclei **82**, 366 (2019), [https://doi.org/10.1134/S1063778819040100].

[140] D. T. Yordanov *et al.*, Phys. Rev. C **98**, 011303 (2018), [https://link.aps.org/doi/10.1103/PhysRevC.98.011303].

[141] D. T. Yordanov *et al.*, Communications Physics **3**, 107 (2020), [https://doi.org/10.1038/s42005-020-0348-9].

[142] J. Eberz *et al.*, Zeitschrift für Physik A Atomic Nuclei **326**, 121 (1987), [https://doi.org/10.1007/BF01283586].

[143] N. Stone, Atomic Data and Nuclear Data Tables **90**, 75 (2005), [https://doi.org/10.1016/j.adt.2005.04.001].

[144] K. Heyde, M. Waroquier and P. Van Isacker, Phys. Rev. C **22**, 1267 (1980), [https://link.aps.org/doi/10.1103/PhysRevC.22.1267].

[145] P. Doornenbal *et al.*, Phys. Rev. C **90**, 061302 (2014), [https://link.aps.org/doi/10.1103/PhysRevC.90.061302].

[146] D. Radford *et al.*, Nuclear Physics A **746**, 83 (2004), [https://doi.org/10.1016/j.nuclphysa.2004.09.056], Proceedings of the Sixth International Conference on Radioactive Nuclear Beams (RNB6).

[147] D. Radford *et al.*, Nuclear Physics A **752**, 264 (2005), [https://doi.org/10.1016/j.nuclphysa.2005.02.040], Proceedings of the 22nd International Nuclear Physics Conference (Part 2).

[148] J. M. Allmond *et al.*, Phys. Rev. C **84**, 061303 (2011), [https://link.aps.org/doi/10.1103/PhysRevC.84.061303].

[149] J. M. Allmond *et al.*, Phys. Rev. C **92**, 041303 (2015), [https://link.aps.org/doi/10.1103/PhysRevC.92.041303].

[150] A. Banu *et al.*, Phys. Rev. C **72**, 061305 (2005), [https://link.aps.org/doi/10.1103/PhysRevC.72.061305].

[151] P. Doornenbal *et al.*, Phys. Rev. C **78**, 031303 (2008), [https://link.aps.org/doi/10.1103/PhysRevC.78.031303].

[152] R. Kumar *et al.*, Phys. Rev. C **81**, 024306 (2010), [https://link.aps.org/doi/10.1103/PhysRevC.81.024306].

[153] A. Jungclaus *et al.*, Physics Letters B **695**, 110 (2011), [https://doi.org/10.1016/j.physletb.2010.11.012].

[154] J. Cederkäll *et al.*, Phys. Rev. Lett. **98**, 172501 (2007), [https://link.aps.org/doi/10.1103/PhysRevLett.98.172501].

[155] G. J. Kumbartzki *et al.*, Phys. Rev. C **93**, 044316 (2016), [https://link.aps.org/doi/10.1103/PhysRevC.93.044316].

[156] C. Vaman *et al.*, Phys. Rev. Lett. **99**, 162501 (2007), [https://link.aps.org/doi/10.1103/PhysRevLett.99.162501].

[157] V. M. Bader *et al.*, Phys. Rev. C **88**, 051301 (2013), [https://link.aps.org/doi/10.1103/PhysRevC.88.051301].

[158] R. Kumar *et al.*, Phys. Rev. C **96**, 054318 (2017), [https://link.aps.org/doi/10.1103/PhysRevC.96.054318].

[159] P. Möller, A. Sierk, T. Ichikawa and H. Sagawa, Atomic Data and Nuclear Data Tables **109-110**, 1 (2016), [https://doi.org/10.1016/j.adt.2015.10.002].

[160] D. Berdichevsky and F. Tondeur, Zeitschrift für Physik A Atoms and Nuclei **322**, 141 (1985), [https://doi.org/10.1007/BF01412027].

[161] C. M. Ricketts *et al.*, Nuclear Instruments and Methods in Physics Research Section B: Beam Interactions with Materials and Atoms **463**, 375 (2020), [https://doi.org/10.1016/j.nimb.2019.04.054].

[162] B. S. Cooper *et al.*, Hyperfine Interactions **240**, 52 (2019), [https://doi.org/10.1007/s10751-019-1586-7].

[163] K. Shinyama and S. Fujita, International Journal of the Society of Materials Engineering for Resources **13**, 75 (2006), [https://doi.org/10.5188/ijsmer.13.75].

[164] D. Manura and D. Dahl, *SIMION (R) 8.0 User Manual*, 2008.

[165] M. L. Vestal, C. R. Blakley, P. W. Ryan and J. H. Futrell, Review of Scientific Instruments **47**, 15 (1976), [https://aip.scitation.org/doi/pdf/10.1063/1.1134474].

[166] D. Manura, Simion collision model HS1, 2005.

[167] A. R. Vernon *et al.*, Scientific Reports **10**, 12306 (2020), [https://doi.org/10.1038/s41598-020-68218-5].

[168] S. A. Aseyev *et al.*, AIP Conference Proceedings **329**, 339 (1995), [https://aip.scitation.org/doi/pdf/10.1063/1.47578].

[169] G. Drake, Quantum defect theory and analysis of high-precision helium term energies, , Advances In Atomic, Molecular, and Optical Physics Vol. 32, pp. 93 – 116, Academic Press, 1994, https://doi.org/10.1016/S1049-250X(08)60012-9.

[170] S. George, G. Guppy and J. Verges, Journal of the Optical Society of America B **7**, 249 (1990), [https://doi.org/10.1364/JOSAB.7.000249].

[171] D. R. Hartree, Mathematical Proceedings of the Cambridge Philosophical Society **24**, 426437 (1928), [https://doi.org/10.1017/S0305004100015954].

[172] W. C. Martin, Journal of the Optical Society of America **70**, 784 (1980), [https://doi.org/10.1364/JOSA.70.000784].

[173] J. Neijzen and A. Dnszelmann, Physica B+C **114**, 241 (1982), [https://doi.org/10.1016/0378-4363(82)90043-2].

[174] K. M. Lynch *et al.*, Phys. Rev. C **97**, 024309 (2018), [https://link.aps.org/doi/10.1103/PhysRevC.97.024309].

[175] G. J. Farooq-Smith *et al.*, Phys. Rev. C **96**, 044324 (2017), [https://link.aps.org/doi/10.1103/PhysRevC.96.044324].